Master thesis

Spectral Properties of Excited Hubbard Clusters: A Nonequilibrium Green Functions Approach

by

Jan-Philip Joost

Kiel, December 2017

Institut für Theoretische Physik und Astrophysik
der Christian-Albrechts-Universität zu Kiel

Erster Gutachter:	Prof. Dr. Michael Bonitz
Zweiter Gutachter:	Prof. Dr. Wolfgang J. Duschl

Abstract

The understanding of carrier multiplication effects in nanoscale graphene structures is essential for various applications including solar energy harvesting. In this work, a new approach is presented to study the correlated nonequilibrium dynamics in finite graphene clusters, such as nanoribbons. The systems are described by an extended Hubbard model that takes into account the overlap of adjacent orbitals and hopping between up to third nearest neighbors. The model is solved by the nonequilibrium Green functions (NEGF) approach which can be combined with different selfenergy approximations, e.g. the second Born (SOA) and GW selfenergy, to take into account electronic correlations. Various numerical improvements have been made to the existing implementation of the NEGF approach to drastically reduce the computational effort of the calculations. As a result, the description allows to predict the correlated nonequilibrium dynamics of excited graphene nanostructures of arbitrary geometry containing up to 100 carbon atoms for up to 25 fs.
In the scope of this work, first, the NEGF approach is compared to exact solutions such as the Bethe ansatz for spectral properties of one-dimensional Hubbard systems. In that regard, especially the performance of the generalized Kadanoff–Baym ansatz (GKBA) is discussed. It is shown that, even in the ground state, the GKBA is not suited to describe spectral properties, e.g. the photoemission spectrum, correctly.
In the second part, the response of finite graphene clusters after an optical laser pulse excitation is studied. The observed carrier multiplication rates strongly depend on the ratio of the laser frequency to the bandgap of the considered system. Finally, it is shown that a mean field approach is not sufficient to correctly describe carrier multiplication processes in graphene nanostructures.

Kurzfassung

Das Verständnis von Trägermultiplikationseffekten in Graphenstrukturen im Nanobereich ist essentiell für verschiedene Anwendungen einschließlich der Solarenergiegewinnung. In dieser Arbeit wird ein neuer Ansatz vorgestellt, um die korrelierte Nichtgleichgewichtsdynamik in endlichen Graphenclustern, wie zum Beispiel Nanobändern, zu untersuchen. Die Systeme werden durch ein erweitertes Hubbard-Modell beschrieben, das die Überlappung benachbarter Orbitale und das Springen zwischen benachbarten Gitterplätzen berücksichtigt. Dabei werden erste, zweite und dritte Nachbarn mit einbezogen. Das Modell wird durch den Nichtgleichgewichts-Greenfunktionen-Ansatz (NEGF) gelöst, der mit verschiedenen Selbstergienäherungen wie der zweiten Bornschen Näherung (SOA) und der GW-Selbstenergie kombiniert werden kann, um Elektronenkorrelationen zu berücksichtigen. Verschiedene numerische Verbesserungen wurden an der bestehenden Implementierung des NEGF-Ansatzes vorgenommen, um den Rechenaufwand der Simulationen drastisch zu reduzieren. Als Folge dessen erlaubt die Methode die Vorhersage der korrelierten Nichtgleichgewichtsdynamik von angeregten Graphen-Nanostrukturen beliebiger Geometrie mit bis zu 100 Kohlenstoffatomen für bis zu 25 fs. Im Rahmen dieser Arbeit wird zunächst der NEGF-Ansatz bezüglich der spektralen Eigenschaften eindimensionaler Hubbard-Systeme mit exakten Lösungen wie dem Bethe-Ansatz verglichen. In dieser Hinsicht wird insbesondere die Leistung des generalisierten Kadanoff–Baym-Ansatzes (GKBA) diskutiert. Es zeigt sich, dass der GKBA selbst im Grundzustand nicht geeignet ist, um spektrale Eigenschaften wie das Photoemissionsspektrum korrekt zu beschreiben. Im zweiten Teil wird die Verhalten von endlichen Graphenclustern nach einer optischen Laserpulsanregung untersucht. Die beobachteten Trägermultiplikationsraten hängen stark vom Verhältnis der Laserfrequenz zur Bandlücke des betrachteten Systems ab. Schließlich wird gezeigt, dass ein Mean-Field-Ansatz nicht ausreicht, um Trägermultiplikationsvorgänge in Graphen-Nanostrukturen korrekt zu beschreiben.

Table of Contents

1 Introduction

Since its first discovery in 2004 [1] the interest in graphene has grown rapidly. As the first truly two-dimensional material it exhibits a list of unique mechanical, optical and electronic properties. Among them are the large carrier mobility and the low optical absorbance. This makes graphene a promising material for future high-speed opto-electronic devices. To this day, first graphene-based solar cells [2–5] and ultrafast photodetectors [6] have been realized. Another interesting field of application is given by the topic of future nanoelectronics. Today's silicon-based computational devices could be improved using graphene nanostructures to further miniaturize the basic electronic components [7].
However, due to its vanishing bandgap homogeneous monolayer graphene is not suited for application in solar cells or nanoelectronics [8]. The attempts to create semiconducting graphene materials that exhibit a finite bandgap range from stacking single graphene layers [9] to substrate-induced [10, 11] or strain-induced bandgaps [12, 13]. The most promising approach, however, is to obtain a bandgap through lateral confinement in finite graphene nanostructures [14, 15].
Therefore, understanding these finite graphene nanostructures is of high interest in current research. Due to the recently developed new synthesization methods of interesting finite structures, such as graphene nanoribbons (GNRs) [16–20], the number of experiments increased drastically over the last years [21–27]. Therefore, an accurate theoretical description of these systems in nonequilibrium and especially of their time-resolved spectral properties is needed. However, until now no suitable approach exists because of the high challenges that such finite systems present. A convenient theory has to describe finite systems including up to 100 carbon atoms. It has to take into account the finite overlap of the atomic orbitals and describe moderate electronic correlations. Additionally, the two-dimensional geometry of the graphene honeycomb lattice has to be modeled. Finally, the theory has to be able to describe the correlated nonequilibrium dynamics of the system for up to several femtoseconds within a reasonable amount of computational time. Thus, one has to find a model that allows for an accurate description of the system and at the same time reduces the numerical complexity of the problem.
One possible approach is to describe the system using single-particle Kohn–Sham orbitals. According to the Hohenberg–Kohn theorem [28], in equilibrium all observables can be expressed as functionals of the single-particle density matrix. A generalization to nonequilibrium results in the time-dependent density functional theory (TDDFT) [29]. This approach was successfully applied to describe local currents in GNRs [30]. However, the accuracy of the TDDFT crucially depends on the, in general, unknown exchange-correlation potential v_{xc}. To take into account moderate correlations, v_{xc} has to be provided by other methods. In the case of finite graphene clusters only basic approaches such as the local density approximation (LDA), which is known to underestimate the bandgap [14], are numerically feasible.
Another approach that additionally allows to take into account strong correlations is to describe the finite graphene systems in the Hubbard model [31, 32]. As a simplistic description of solid state systems the Hubbard model greatly reduces the numerical effort for the simulation of large finite clusters. At the same time, it can be extended to include the finite overlap between orbitals of adjacent atoms. The exact solution of the Hubbard model can be obtained by the method of exact diagonalization [33]. However, the numerical

effort scales exponentially with the number of atoms in the system. Therefore, other methods have to be applied that provide a solution in an acceptable amount of time.
A different wavefunction-based approach is given by the density matrix renormalization group (DMRG) [34] method and the generalized time-dependent DMRG (t-DMRG). In order to access larger systems the size of the Hilbert space is reduced to the most relevant effective space. However, this methods is mainly restricted to the description of one-dimensional lattice systems. Therefore, it is not suited to describe the two-dimensional honeycomb lattice of graphene nanoclusters.
The dynamical mean-field theory (DMFT)[35] is another way to describe the dynamics in Hubbard lattices. The approach becomes exact in the limit of infinite dimensions (i.e. for an infinite number of nearest neighbors), because the lattice is mapped to a local impurity model. However, in the honeycomb lattice each atom has only three nearest neighbors. Additionally, the DMFT provides good results for large interaction strengths but becomes erroneous for moderate coupling. Thus, the DMFT is not applicable to finite graphene systems.
A method that overcomes all above-mentioned problems is the nonequilibrium Green functions (NEGF) approach [36, 37]. It is not restricted to any specific lattice geometry and can describe nonequilibrium systems at weak and moderate interaction strength. Additionally, it can treat arbitrary excitations and external fields. The information of all n-particle observables are contained in the many-particle Green function $G^{(n)}$. The time evolution of $G^{(n)}$ is given by the coupled Martin–Schwinger hierarchy equations. All single-particle observables and important spectral properties such as the photoemission spectrum can be accessed through the two-time single-particle Green function G. Its equations of motion are given by the lowest hierarchy equations, the Kadanoff–Baym equations (KBEs). Decoupling the KBEs from the higher hierarchy equations leads to the selfenergy Σ which includes mean field and correlation effects. Depending on the choice of the selfenergy approximation different physical effects such as screening (GW approximation) or particle-particle collisions (T-matrix in the particle-particle channel) can be included in the description.
In this thesis, first the validity of the NEGF approach is tested for one-dimensional lattice systems in the standard Hubbard model where a special focus is laid on spectral properties. The results of the NEGF approach in the ground state and for time-dependent excitations are compared to exact solutions. Later, the NEGF method is used to solve the extended Hubbard model in order to study carrier multiplication processes in finite graphene nanostructures.

1.1 Outline

- **1: Introduction**

- **2: Nonequilibrium many-body theory**
  First, the exact solution of the time-dependent Schrödinger equation is presented. After that the concept of the second quantization is introduced, which is the foundation of the NEGF formalism. Additionally, the Schwinger–Keldysh-contour is discussed which allows for the description of time dependent expectation values.

The single-particle Green function is introduced and its equations of motion, the KBEs, are derived by decoupling the Martin–Schwinger hierarchy. For the selfenergy the Hartree–Fock and various other higher order approximations are presented. Furthermore, the real-time components of the contour quantities and the generalized Kadanoff–Baym ansatz (GKBA) are described. Finally, the Hubbard model is introduced and solved for simple limiting cases.

- **3: Numerical implementation**
  After discussing the generation of the initial state of the propagation, the time propagation scheme for the NEGF approach is presented. Additionally, some details are given on the numerical improvements that were achieved by the implemented propagation algorithms and integration methods. Finally, two methods are introduced to exactly solve the Hubbard model for small systems.

- **4: Results I: Method benchmarks**
  The validity of the NEGF approach is tested for one-dimensional lattice systems in the standard Hubbard model. First, ground state results for the photoemission spectrum and the energy dispersion are compared to exact solutions. Additionally, the performance of the GKBA concerning spectral properties is discussed. Finally, the problem of unphysical damping due to artificial energy levels is analyzed for different excitations.

- **5: Graphene**
  The properties, lattices structure and tight-binding band structure of graphene are presented. Furthermore, a specific class of finite systems, the so-called graphene nanoribbons, is discussed in detail. Additionally, the important effect of carrier multiplication is explained. Finally, the Hubbard model is extended to describe finite graphene systems by taking into account hopping and orbital overlap up to third nearest neighbors.

- **6: Results II: Laser excitations of finite graphene clusters**
  The NEGF method is used to solve the extended Hubbard model in order to study the dynamics in finite graphene nanostructures excited by a laser pulse. First, the response of the systems on different polarizations of the laser pulse is investigated. Additionally, carrier multiplication processes are studied for various finite systems. Finally, the influence of damping and correlations on the carrier multiplication effects is discussed.

- **7: Conclusions & Outlook**

2 Nonequilibrium many-body theory

In this section, two different frameworks to describe quantum many-body systems are presented. First, the wavefunction-based approach is introduced that focuses on the solution of the time-dependent Schrödinger equation. In the second part, the nonequilibrium Green functions method that is based on the second quantization is derived. Finally, the standard Hubbard model is presented.

2.1 Exact solution of the TDSE

The state of a quantum mechanical system can be represented by a state vector $|\psi(t)\rangle$ which is an element of a single-particle Hilbert space $\mathcal{H}$. One widely used way to describe the time evolution of such a system is the Schrödinger picture (S). In this formalism the entire time information is attributed to the state vectors, i.e. $\frac{\mathrm{d}}{\mathrm{d}t}|\psi(t)\rangle \neq 0$, whereas the operators of observables are constant in time[1]: $\frac{\mathrm{d}}{\mathrm{d}t}\hat{A}_\mathrm{S} \equiv 0$. The dynamics of the states $|\psi(t)\rangle$ can be described by an equation of motion, the time-dependent Schrödinger equation (TDSE):

$$\mathrm{i}\hbar\frac{\partial}{\partial t}|\psi(t)\rangle = \hat{H}_\mathrm{S}|\psi(t)\rangle\ , \tag{2.1-E1}$$

where $\hat{H}_\mathrm{S}$ denotes the Hamiltonian of the system.
In order to find a formal solution for the TDSE it proves useful to introduce the unitary time evolution operator [38]

$$\hat{U}(t,t_0) := \begin{cases} \mathcal{T}\left\{\mathrm{e}^{-\frac{\mathrm{i}}{\hbar}\int_{t_0}^{t}\mathrm{d}\bar{t}\,\hat{H}_\mathrm{S}(\bar{t})}\right\} & \text{if} \quad t \geq t_0 \\ \bar{\mathcal{T}}\left\{\mathrm{e}^{+\frac{\mathrm{i}}{\hbar}\int_{t}^{t_0}\mathrm{d}\bar{t}\,\hat{H}_\mathrm{S}(\bar{t})}\right\} & \text{if} \quad t < t_0\,, \end{cases} \tag{2.1-E2}$$

for the time-dependent Hamiltonian $\hat{H}_\mathrm{S}(t)$. Additionally, $\mathcal{T}$ is the causal time-ordering operator that arranges following operators chronologically, i.e.

$$\mathcal{T}\left\{\hat{A}(t_{P(k)})\hat{A}(t_{P(k-1)})\ldots\hat{A}(t_{P(1)})\right\} = \hat{A}(t_k)\hat{A}(t_{k-1})\ldots\hat{A}(t_1)\,. \tag{2.1-E3}$$

with time arguments $t_1 \leq t_2 \leq \ldots \leq t_k$ and for arbitrary operators $\hat{A}$ and permutations P of $\mathbb{N}_{\leq k}$. Accordingly, $\bar{\mathcal{T}}$ denotes the anticausal time-ordering operator which sorts operators in anti-chronological order, i.e. it obeys Eq. (2.1-E3) for time arguments $t_1 \geq t_2 \geq \ldots \geq t_k$. At first glance, the exponential in Eq. (2.1-E2) contains only one operator, the Hamiltonian $\hat{H}_\mathrm{S}(t)$. However, the purpose of $\mathcal{T}$ becomes apparent when looking at the Taylor expansion of the exponential function:

$$\mathcal{T}\left\{\mathrm{e}^{-\frac{\mathrm{i}}{\hbar}\int_{t_0}^{t}\mathrm{d}\bar{t}\,\hat{H}_\mathrm{S}(\bar{t})}\right\} := \sum_{n=0}^{\infty}\frac{(-\frac{\mathrm{i}}{\hbar})^n}{n!}\int_{t_0}^{t}\mathrm{d}t_1\int_{t_0}^{t}\mathrm{d}t_2\ldots\int_{t_0}^{t}\mathrm{d}t_n\,\mathcal{T}\left\{\hat{H}_\mathrm{S}(t_1)\hat{H}_\mathrm{S}(t_2)\ldots\hat{H}_\mathrm{S}(t_n)\right\}\,.$$

[1] If they do not have an explicit time-dependence like a time-dependent potential.

Here, the time-ordering operator $\mathcal{T}$ is necessary to sort the product of Hamiltonians $\hat{H}_\mathrm{S}(t)$ for different times.
As mentioned above, the time evolution operator is unitary, i.e. $\left(\hat{U}(t_1,t_2)\right)^\dagger = \hat{U}(t_2,t_1)$. Looking at Eq. (2.1-E2) one finds additional useful relations

$$\begin{aligned}\hat{U}(t_1,t_2)\hat{U}(t_2,t_3) &= \hat{U}(t_1,t_3)\,,\\ \hat{U}(t_1,t_2)\hat{U}(t_2,t_1) &= \hat{U}(t_1,t_1) = \mathbb{1}\,.\end{aligned} \tag{2.1-E4}$$

With this operator $\hat{U}$ it is now possible to write down a formal solution for Eq. (2.1-E1):

$$|\psi(t)\rangle = \hat{U}(t,t_0)\,|\psi(t_0)\rangle = \mathcal{T}\left\{\mathrm{e}^{-\frac{\mathrm{i}}{\hbar}\int_{t_0}^{t}\mathrm{d}\bar{t}\,\hat{H}_\mathrm{S}(\bar{t})}\right\}|\psi(t_0)\rangle\ , \tag{2.1-E5}$$

where t_0 is the initial time and $t > t_0$.

A simple way to handle the time dependence of the Hamiltonian is to break up the total time evolution operator into N small intervals of duration Δt in which the Hamiltonian is assumed to be nearly constant [39]:

$$\hat{U}(t,t_0) = \hat{U}(t_0+n\Delta t, t_0+(n-1)\Delta t)\cdot\ldots\cdot\hat{U}(t_0+\Delta t,t_0)\,, \tag{2.1-E6}$$

where $\Delta t = (t-t_0)/N$. As the intervals are chosen in such a way that the Hamiltonian is not dependent on time on any interval the time evolution operator becomes

$$\hat{U}(t+\Delta t,t) = \mathrm{e}^{-\frac{\mathrm{i}}{\hbar}\hat{H}_\mathrm{S}(t)\Delta t}\,. \tag{2.1-E7}$$

By diagonalizing $\hat{H}_\mathrm{S}$ with $\hat{D}(t) = \hat{Q}^\dagger(t)\hat{H}_\mathrm{S}(t)\hat{Q}(t)$, where $\hat{Q}$ is a unitary operator and $\hat{D}$ is a diagonal matrix containing the eigenenergies of $\hat{H}_\mathrm{S}$, Eq. (2.1-E7) becomes

$$\hat{U}(t+\Delta t,t) = \hat{Q}(t)\mathrm{e}^{-\frac{\mathrm{i}}{\hbar}\hat{D}(t)\Delta t}\hat{Q}^\dagger(t)\,. \tag{2.1-E8}$$

However, in practice the problem is often solved by using the Taylor expansion to approximate the exponential function in Eq. (2.1-E7):

$$\mathrm{e}^{-\frac{\mathrm{i}}{\hbar}\hat{H}_\mathrm{S}(t)\Delta t} = \hat{1} - \frac{\mathrm{i}}{\hbar}\hat{H}_\mathrm{S}(t)\Delta t + \cdots\,. \tag{2.1-E9}$$

This way, the time evolution of a state vector $|\psi(t)\rangle$ for a system with an arbitrary time-dependent Hamiltonian $\hat{H}_\mathrm{S}(t)$ can be solved. A description of the numerical details is given in Sec. 3.4.

2.1.1 The Lanczos propagation

Since the size of the Hilbert space $\mathcal{H}$ grows exponentially with system-size, it is numerically impossible to apply the above mentioned method of directly propagating the state vector to larger systems. To solve this problem, the idea of the Lanczos approach is to diagonalize the Hamiltonian on a small subspace of the d-dimensional Hilbert space, the L-dimensional Krylov space [40]

$$\mathcal{K}^L(|\phi_0\rangle) = \mathrm{span}\left(|\phi_0\rangle\,,\hat{H}_\mathrm{S}\,|\phi_0\rangle\,,\hat{H}_\mathrm{S}^2\,|\phi_0\rangle\,,\ldots,\hat{H}_\mathrm{S}^{L-1}\,|\phi_0\rangle\right)\,, \tag{2.1-E10}$$

where $\hat{H}_\mathrm{S}$ is the Hamiltonian of the system and $|\phi_0\rangle$ is a given initial state.
The orthonormal Lanczos basis $\{|\phi_0\rangle, \ldots, |\phi_{L-1}\rangle\}$ of $\mathcal{K}^L(|\phi_0\rangle)$ can be constructed by the following iterative scheme. Starting from a normalized initial vector $|\phi_0\rangle$ a second vector $|\phi_1\rangle$ can be generated by orthogonalizing $\hat{H}_\mathrm{S}|\phi_0\rangle$ to $|\phi_0\rangle$ and subsequent normalization:

$$b_1|\phi_1\rangle = |\tilde{\phi}_1\rangle = \hat{H}_\mathrm{S}|\phi_0\rangle - |\phi_0\rangle\langle\phi_0|\hat{H}_\mathrm{S}|\phi_0\rangle = \hat{H}_\mathrm{S}|\phi_0\rangle - a_0|\phi_0\rangle\ , \tag{2.1-E11}$$

with $a_0 = \langle\phi_0|\hat{H}_\mathrm{S}|\phi_0\rangle$ and the normalization $b_1^2 = \langle\tilde{\phi}_1|\tilde{\phi}_1\rangle$. In the next step a third vector $|\phi_2\rangle$ is created that is orthogonal to $|\phi_0\rangle$ and $|\phi_1\rangle$,

$$b_2|\phi_2\rangle = |\tilde{\phi}_2\rangle = \hat{H}_\mathrm{S}|\phi_1\rangle - \sum_{i=0}^{1}|\phi_i\rangle\langle\phi_i|\hat{H}_\mathrm{S}|\phi_i\rangle = \hat{H}_\mathrm{S}|\phi_1\rangle - a_1|\phi_1\rangle - b_1|\phi_0\rangle\ , \tag{2.1-E12}$$

where $a_1 = \langle\phi_1|\hat{H}_\mathrm{S}|\phi_1\rangle$ and $b_2^2 = \langle\tilde{\phi}_2|\tilde{\phi}_2\rangle$. Starting from Eqs. (2.1-E11) and (2.1-E12) it is possible to construct an iterative scheme to generate the remaining basis vectors,

$$b_{n+1}|\phi_{n+1}\rangle = |\tilde{\phi}_{n+1}\rangle = \hat{H}_\mathrm{S}|\phi_n\rangle - a_n|\phi_n\rangle - b_n|\phi_{n-1}\rangle\ , \tag{2.1-E13}$$

with $a_n = \langle\phi_n|\hat{H}_\mathrm{S}|\phi_n\rangle$ and the normalization $b_{n+1}^2 = \langle\tilde{\phi}_{n+1}|\tilde{\phi}_{n+1}\rangle$.
In the basis of the Krylov subspace the Hamiltonian is represented by a tridiagonal matrix [41]

$$\hat{H}_{\mathcal{K}^L(|\phi_0\rangle)} = \begin{pmatrix} a_0 & b_1 & 0 & 0 & & 0 & 0 \\ b_1 & a_1 & b_2 & 0 & \cdots & 0 & 0 \\ 0 & b_2 & a_2 & b_3 & & 0 & 0 \\ 0 & 0 & b_3 & a_3 & & 0 & 0 \\ & \vdots & & & \ddots & \vdots & 0 \\ 0 & 0 & 0 & 0 & & a_{L-1} & b_L \\ 0 & 0 & 0 & 0 & \cdots & b_L & a_L \end{pmatrix}. \tag{2.1-E14}$$

This iterative Lanczos technique is often used to get the ground state and the corresponding ground state energy of a system as the extremal eigenenergies converge very fast with increasing L [42]. For this, the only requirement is that the arbitrary initial state $|\phi_0\rangle$ has a final overlap with the ground state.
To propagate a state vector $|\psi\rangle$ with the Lanczos approach, the Hamiltonian in Eq. (2.1-E7) can be expressed by the Hamiltonian in Krylov space $\hat{H}_{\mathcal{K}^L(|\phi_0\rangle)}$,

$$\mathrm{e}^{-\frac{\mathrm{i}}{\hbar}\hat{H}_\mathrm{S}(t)\Delta t} = \mathrm{e}^{-\frac{\mathrm{i}}{\hbar}\hat{V}(t)\hat{H}_{\mathcal{K}^L(|\phi_0\rangle)}(t)\hat{V}^\dagger(t)\Delta t}\,, \tag{2.1-E15}$$

where $\hat{V}(t) = (\phi_0, \ldots, \phi_{L-1})$ is a $d\times L$ matrix constructed from columns ϕ_k representing $|\phi_k\rangle$. Similar to Eq. (2.1-E8) one can diagonalize $\hat{H}_{\mathcal{K}^L(|\phi_0\rangle)}$ with $\hat{D}'(t) = \hat{Q}'^\dagger(t)\hat{H}_{\mathcal{K}^L(|\phi_0\rangle)}(t)\hat{Q}'(t)$, where $\hat{Q}'$ is a unitary operator and $\hat{D}'$ is a diagonal matrix containing the eigenenergies of $\hat{H}_{\mathcal{K}^L(|\phi_0\rangle)}$. By defining $\hat{U}'(t) \coloneqq \hat{V}(t)\hat{Q}'(t)$ one gets [43]

$$\hat{U}(t+\Delta t, t) = \hat{U}'(t)\mathrm{e}^{-\frac{\mathrm{i}}{\hbar}\hat{D}'(t)\Delta t}\hat{U}'^\dagger(t)\,. \tag{2.1-E16}$$

In practice the advantage of this approach compared to Eq. (2.1-E8) is that the diagonalization process is less costly due to the low dimensional Krylov subspace. However, in order to perform the propagation, a new Krylov subspace has to be constructed for every time step starting with the current state vector $|\psi(t)\rangle$ as the new initial state. More details on the numerical aspects of this method are given in Sec. 3.4.

2.2 Nonequilibrium Green functions approach

2.2.1 Second quantization

In the previous chapter the state of a quantum mechanical system is determined by a state vector or wavefunction $|\psi\rangle$ in a Hilbert space $\mathcal{H}$, observables A are given by corresponding operators $\hat{A} : \mathcal{H} \to \mathcal{H}$ and the dynamics of the state is determined by the TDSE.
A different formalism to describe a many-body quantum system is the second quantization, in which the full information of the many-particle state is given by the occupation numbers of the single-particle orbitals. One advantage of this approach is that it inherently takes into account the indistinguishability of particles in quantum mechanics which leads to a symmetric wavefunction for bosons and an antisymmetric wavefunction for fermions [36].

To demonstrate the connection between both formalisms it is convenient to consider a state of N identical particles $|\psi_N\rangle$ that is an element of the N-particle Hilbert space $\mathcal{H}_N$ which is defined as the direct product of single-particle Hilbert spaces

$$\mathcal{H}_N = \underbrace{\mathcal{H}_1 \otimes \mathcal{H}_1 \otimes \ldots \otimes \mathcal{H}_1}_{\text{N times}} . \tag{2.2-E1}$$

The original N-particle state $|\psi_N\rangle$ contains all information about every particle but as particles in quantum mechanics are indistinguishable it is convenient to introduce a symmetric and anti-symmetric N-particle state $|\psi_N\rangle^{\pm}$ for bosonic (upper sign) and fermionic (lower sign) particles, respectively. With this, the N-particle state can be expressed in terms of the occupation numbers n_i

$$|\psi_N\rangle^{\pm} := |n_1, n_2, \ldots\rangle \quad \text{with} \quad n_i = 0, 1, 2, \ldots \quad \text{and} \quad i = 1, 2, \ldots . \tag{2.2-E2}$$

These states are elements of the symmetric and anti-symmetric Hilbert subspaces $\mathcal{H}_N^{\pm}$. Now, it is possible to define the symmetric and anti-symmetric Fock space $\mathcal{F}^{\pm}$ for states of all particle numbers as the direct sum of all symmetric and anti-symmetric Hilbert spaces $\mathcal{H}_N^{\pm}$, respectively:

$$\mathcal{F}^{\pm} = \bigoplus_{n=0}^{\infty} \mathcal{H}_n^{\pm} , \tag{2.2-E3}$$

where $\mathcal{H}_0$ includes the vacuum state $|0\rangle = |0, 0, \ldots\rangle$ without any particles.
Each state in this Fock space $\mathcal{F}$ is determined by the complete set of occupation numbers. Thus, every Fock operator $\hat{A}^{\mathcal{F}} : \mathcal{F} \to \mathcal{F}$ has to change the occupation of the state. This leads to the introduction of the canonical creation (annihilation) operator $\hat{c}_i^{\dagger}$ ($\hat{c}_i$) as a

convenient basis to express Fock operators. As their names suggest, the action of these operators is to create or annihilate a single particle in the orbital i of a given Fock state:

$$\begin{aligned}\hat{c}_i^\dagger \left|n_1, n_2, \ldots, n_i, \ldots\right\rangle &= (\pm 1)^\alpha \sqrt{n_i + 1} \left|n_1, n_2, \ldots, n_i + 1, \ldots\right\rangle \cdot \begin{cases} 1 & \text{for bosons} \\ \delta_{n_i,0} & \text{for fermions} \end{cases}, \\ \hat{c}_i \left|n_1, n_2, \ldots, n_i, \ldots\right\rangle &= (\pm 1)^\alpha \sqrt{n_i} \left|n_1, n_2, \ldots, n_i - 1, \ldots\right\rangle \cdot \begin{cases} 1 - \delta_{n_i,0} & \text{for bosons} \\ \delta_{n_i,1} & \text{for fermions} \end{cases}. \end{aligned} \tag{2.2-E4}$$

Here, $\alpha = \sum_{j=1}^{i-1} n_j$ accounts for the (anti-)symmetric states and the Kronecker delta δ enforces the Pauli principle for Fermions[2]. This way, the N-particle subspace of $\mathcal{F}$ is connected to the $N+1$ particle subspace by $\hat{c}_i^\dagger$ and to the $N-1$ particle subspace by $\hat{c}_i$.

From Eq. (2.2-E4) the commutator (anti-commutator) relations for bosons (fermions) can be derived:

$$\begin{aligned}\left[\hat{c}_i^\dagger, \hat{c}_j^\dagger\right]_\mp &= 0\,, \\ \left[\hat{c}_i, \hat{c}_j\right]_\mp &= 0\,, \\ \left[\hat{c}_i, \hat{c}_j^\dagger\right]_\mp &= \delta_{i,j}\,, \end{aligned} \tag{2.2-E5}$$

where $(-)$ denotes the commutator and $(+)$ the anti-commutator.
Starting from the vacuum state $|0\rangle$ any state $|n_1, n_2, \ldots\rangle$ in $\mathcal{F}$ can be created by applying the creation operator:

$$\left|n_1, n_2, \ldots\right\rangle = \left(\prod_i \frac{1}{\sqrt{n_i!}}\right) \left(\hat{c}_1^\dagger\right)^{n_1} \left(\hat{c}_2^\dagger\right)^{n_2} \ldots \left|0\right\rangle \qquad \begin{cases} n_i \in \mathbb{N}_0 & \text{for bosons} \\ n_i \in \{0, 1\} & \text{for fermions} \end{cases} \tag{2.2-E6}$$

Now it is possible to define arbitrary Fock operators in the basis of the canonical creator and annihilator. The general single-particle operator $\hat{A}_1^{\mathcal{F}}$ and two-particle operator $\hat{A}_2^{\mathcal{F}}$ in second quantization take the form,

$$\hat{A}_1^{\mathcal{F}} = \sum_{i,j} \left\langle i \left| \hat{A}_1 \right| j \right\rangle \hat{c}_i^\dagger \hat{c}_j =: \sum_{i,j} A_{ij} \hat{c}_i^\dagger \hat{c}_j\,, \tag{2.2-E7}$$

$$\hat{A}_2^{\mathcal{F}} = \sum_{i,j,k,l} \left\langle ij \left| \hat{A}_2 \right| kl \right\rangle \hat{c}_i^\dagger \hat{c}_j^\dagger \hat{c}_k \hat{c}_l =: \sum_{i,j,k,l} A_{ijkl} \hat{c}_i^\dagger \hat{c}_j^\dagger \hat{c}_k \hat{c}_l\,, \tag{2.2-E8}$$

where A_{ij} and A_{ijkl} are the corresponding matrix elements. These equations are valid for bosonic and fermionic particles.
With this, the generic time-dependent many-body Hamiltonian of a quantum system in second quantization is given by

$$\hat{H}(t) = \underbrace{\sum_{i,j} h_{ij}^{(0)} \hat{c}_i^\dagger \hat{c}_j}_{\hat{H}^0} + \underbrace{\frac{1}{2} \sum_{i,j,k,l} w_{ijkl} \hat{c}_i^\dagger \hat{c}_j^\dagger \hat{c}_k \hat{c}_l}_{\hat{W}} + \underbrace{\sum_{i,j} f_{ij}(t) \hat{c}_i^\dagger \hat{c}_j}_{\hat{F}(t)}\,, \tag{2.2-E9}$$

[2] Additionally, the annihilation operator can not act on empty orbitals, i.e. occupation numbers can not be negative.

containing the single particle part $\hat{H}^0$, the interaction part W and the time-dependent external single-particle excitation $\hat{F}(t)$.

2.2.2 The Heisenberg picture

Until now, the time dependence of a quantum mechanical system was described in the Schrödinger picture (S), i.e. the system's state vector $|\psi\rangle$ evolves in time while operators $\hat{A}$ of observables are stationary. Another way to take the time dynamics into account is the Heisenberg picture (H). In this picture the operators evolve in time, i.e. $\frac{\mathrm{d}}{\mathrm{d}t}\hat{A}_\mathrm{H} \neq 0$, whereas the states are time-independent: $\frac{\mathrm{d}}{\mathrm{d}t}|\psi_\mathrm{H}\rangle \equiv 0$. Both formalisms are mathematically equivalent[3], however, the Heisenberg picture is crucial for the derivation of the nonequilibrium Green functions (NEGF) approach.
The transformation between the Schrödinger and Heisenberg picture is done by the time evolution operator $\hat{U}$ that was defined in Eq. (2.1-E2). The states and operators transform as

$$|\psi_\mathrm{H}\rangle = \hat{U}(t_0,t)\,|\psi_\mathrm{S}(t)\rangle\ , \quad \hat{A}_\mathrm{H}(t) = \hat{U}(t_0,t)\hat{A}_\mathrm{S}\hat{U}(t,t_0)\,. \tag{2.2-E10}$$

While the time evolution of the time-dependent states in the Schrödinger picture is described by the TDSE (Eq. (2.1-E1)), the equation of motion for the dynamic operators in the Heisenberg picture is the Heisenberg equation [44],

$$\frac{\mathrm{d}\hat{A}_\mathrm{H}(t)}{\mathrm{d}t} = \frac{\mathrm{i}}{\hbar}\left[\hat{H}_\mathrm{H}(t), \hat{A}_\mathrm{H}(t)\right]_- + \left(\frac{\partial \hat{A}_\mathrm{S}}{\partial t}\right)_\mathrm{H}\ , \tag{2.2-E11}$$

with the time-dependent Hamiltonian in the Heisenberg picture $\hat{H}_\mathrm{H}(t)$.

2.2.3 The Schwinger–Keldysh contour

To develop the nonequilibrium Green functions approach it is useful to define a statistical ensemble in order to obtain statistically averaged expectation values of observables. The grand canonical ensemble (GCE) is defined by the temperature $T = (k_\mathrm{B}\beta)^{-1}$, the volume V and the chemical potential μ of the system, whereas the particle number N is allowed to vary. Thus, the GCE is a suitable choice for the ensemble, as creator and annihilator in second quantization require a changing particle number. The grand canonical density matrix describes the quantum statistical ensemble [36]:

$$\begin{aligned} \hat{\rho}_\mathrm{GCE} &= \frac{1}{Z_0}\mathrm{e}^{-\beta(\hat{H}-\mu\hat{N})}\,, \\ Z_0 &= \mathrm{Tr}\left(\mathrm{e}^{-\beta(\hat{H}-\mu\hat{N})}\right)\,, \end{aligned} \tag{2.2-E12}$$

[3] In a third equivalent formalism, the Dirac or interaction picture (I), both operators and states are allowed to be time-dependent.

where $\mathrm{Tr}(\cdot)$ denotes the trace over $\mathcal{F}$ and $\hat{N} = \sum_i \hat{c}_i^\dagger \hat{c}_i$ is the particle number operator. In the following, it is assumed that the system is in equilibrium for times $t \leq t_0$, then the average of an operator $\hat{A}$ can be expressed as

$$\langle \hat{A} \rangle (t \leq t_0) = \mathrm{Tr}\left(\hat{\rho}_\mathrm{S}(t \leq t_0) \hat{A}_\mathrm{S} \right) , \tag{2.2-E13}$$

where $\hat{\rho}_\mathrm{S}(t \leq t_0)$ is the equilibrium density operator in the Schrödinger picture.
For times $t > t_0$, where the system is excited out of equilibrium, the time evolution operator $\hat{U}$ can be used to construct the nonequilibrium density operator

$$\hat{\rho}_\mathrm{S}(t) = \hat{U}(t, t_0) \hat{\rho}_\mathrm{S}(t_0) \hat{U}(t_0, t) . \tag{2.2-E14}$$

Inserting Eq. (2.2-E14) into Eq. (2.2-E13) and using the definition $\rho_\mathrm{H} \equiv \rho_\mathrm{S}(t_0)$ leads to an expression for the average of an operator $\hat{A}$ in nonequilibrium,

$$\begin{aligned} \langle \hat{A} \rangle (t) &= \mathrm{Tr}\left(\hat{\rho}_\mathrm{H} \hat{U}(t_0, t) \hat{A}_\mathrm{S} \hat{U}(t, t_0) \right) \\ &= \mathrm{Tr}\left(\hat{\rho}_\mathrm{H} \hat{A}_\mathrm{H}(t) \right) , \end{aligned} \tag{2.2-E15}$$

where the cyclic property of the trace has been used to change the position of $\hat{U}$ and $\hat{A}_\mathrm{S}$. Using the definition of $\hat{U}$ (Eq. (2.1-E2)) the average becomes

$$\langle \hat{A} \rangle (t) = \mathrm{Tr}\left(\hat{\rho}_\mathrm{H} \bar{\mathcal{T}} \left\{ \mathrm{e}^{-\frac{\mathrm{i}}{\hbar} \int_t^{t_0} \mathrm{d}\bar{t}\, \hat{H}(\bar{t})} \right\} \hat{A}_\mathrm{S} \mathcal{T} \left\{ \mathrm{e}^{-\frac{\mathrm{i}}{\hbar} \int_{t_0}^{t} \mathrm{d}\bar{t}\, \hat{H}(\bar{t})} \right\} \right) . \tag{2.2-E16}$$

To get further insight into the underlying physics of this equation it is helpful to look at the acting of the operators on a ket-vector under the trace (from right to left). First, the state is propagated in chronological order on the real time axis from t_0 to t by the time evolution operator $\hat{U}(t, t_0)$. Second, the operator $\hat{A}_\mathrm{S}$ acts at the time t and third, the state is propagated back on the real time axis from time t to t_0 in anti-chronological order by $\hat{U}(t_0, t)$.
This whole process motivates the introduction of a time contour $\mathcal{C}$. The idea of such a time contour is depicted in Fig. 2.2-F1 and was first presented by Keldysh [45] and Schwinger [46]. To distinguish the real time arguments of the propagation, $\mathcal{C}$ is split into a causal ($\mathcal{C}_-$) and an anticausal ($\mathcal{C}_+$) branch for the forward and backward propagation, respectively. Additionally, times on the contour are denoted $z \in \mathcal{C}$. With this, Eq. (2.2-E16) can be written as

$$\langle \hat{A} \rangle (t) = \mathrm{Tr}\left(\hat{\rho}_\mathrm{H} \mathcal{T}_\mathcal{C} \left\{ \mathrm{e}^{-\frac{\mathrm{i}}{\hbar} \int_{\mathcal{C}_+} \mathrm{d}\bar{z}\, \hat{H}(\bar{z})} \right\} \hat{A}_\mathrm{S} \mathcal{T}_\mathcal{C} \left\{ \mathrm{e}^{-\frac{\mathrm{i}}{\hbar} \int_{\mathcal{C}_-} \mathrm{d}\bar{z}\, \hat{H}(\bar{z})} \right\} \right) , \tag{2.2-E17}$$

where $\mathcal{T}_\mathcal{C}$ is the time ordering superoperator on $\mathcal{C}$ that moves operators at earlier times on the contour to the right and operators at later times to the left, much like its real time counterpart defined in Eq. (2.1-E3). By introducing the notation $\hat{A}_\mathrm{S}\big|_z$ to specify at which time on the contour the operator $\hat{A}_\mathrm{S}$ acts, one can further simplify Eq. (2.2-E17) and finds:

$$\langle \hat{A} \rangle (z) = \mathrm{Tr}\left(\hat{\rho}_\mathrm{H} \mathcal{T}_\mathcal{C} \left\{ \mathrm{e}^{-\frac{\mathrm{i}}{\hbar} \int_\mathcal{C} \mathrm{d}\bar{z}\, \hat{H}(\bar{z})} \hat{A}_\mathrm{S}\big|_z \right\} \right) . \tag{2.2-E18}$$

This equation describes the general time dependent ensemble average of a given observable. However, the generation of a correlated initial state at time t_0 is still an important topic to address. There are two common ways to create such an interacting initial state:

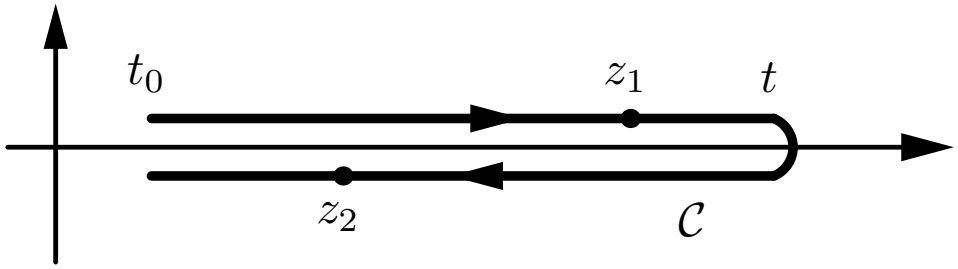

Figure 2.2-F1 – Schematic illustration of the time contour $\mathcal{C}$ that consists of a causal and an anticausal branch. Here, the time z_2 is later than z_1 on $\mathcal{C}$. However, their projections on the real time axis are arranged in opposite order. Both branches lie on top of each other on the real time axis, the spacing between the branches is only an illustrative help. The graphic is taken from Ref. [47].

i.) adding a third vertical branch of complex time arguments to the contour,
ii.) starting from a non-interacting state and switch on the interaction adiabatically.

The first approach is based on the observation that the canonical density operator can be expressed as a time evolution operator in imaginary time:

$$\mathrm{e}^{-\beta\hat{H}_\mathrm{S}(t_0)} = \mathrm{e}^{+\frac{\mathrm{i}}{\hbar}\hat{H}_\mathrm{S}(t_0)[t_0-(t_0-\mathrm{i}\hbar\beta)]} \equiv \hat{U}_0(t_0-\mathrm{i}\hbar\beta, t_0)\,. \tag{2.2-E19}$$

Inserting this expression into Eq. (2.2-E18) extends $\mathcal{C}$ by a third branch ranging along the imaginary axis from t_0 to $t_0 - \mathrm{i}\hbar\beta$. Since this approach is not part of this work, the reader is referred to Ref. [38] for further insight into this method.

The second way, the so-called adiabatic switching method, is used in the calculations of this work and will be outlined in more detail. The Hamiltonian of a quantum system in second quantization is shown in Eq. (2.2-E9). For the purpose of this method an adiabatic switching function $f_\mathrm{AS} : \mathbb{R} \to [0,1]$ is added to the interaction part $\hat{W}$ to switch on the interaction, leading to a generalized Hamiltonian

$$\hat{H}_\mathrm{AS}(t) = \underbrace{\sum_{i,j} h_{ij}^{(0)} \hat{c}_i^\dagger \hat{c}_j}_{\hat{H}^0} + \underbrace{\frac{1}{2} f_\mathrm{AS}(t) \sum_{i,j,k,l} w_{ijkl} \hat{c}_i^\dagger \hat{c}_j^\dagger \hat{c}_l \hat{c}_k}_{\hat{W}_\mathrm{AS}} + \underbrace{\sum_{i,j} f_{ij}(t) \hat{c}_i^\dagger \hat{c}_j}_{\hat{F}(t)}\,, \tag{2.2-E20}$$

where the monotonically increasing switching function $f_\mathrm{AS}(t)$ has to satisfy the following relations:

$$\lim_{t\to-\infty} f_{AS}(t) = 0 \quad \text{and} \quad f_\mathrm{AS}(t) = 1 \quad \text{for all} \quad t \geq t_0\,. \tag{2.2-E21}$$

The main assumption of the adiabatic switching method is that the fully interacting density operator $\hat{\rho}_\mathrm{H}$ can be expressed through the non-interacting density operator $\hat{\rho}_0$ corresponding to the single particle Hamiltonian $\hat{H}_0$. For this purpose, a new time evolution operator $\hat{U}_\mathrm{AS}$ can be defined corresponding to the adiabatic switching Hamiltonian $\hat{H}_\mathrm{AS}$. This way the correlated density operator can be expressed as

$$\hat{\rho}_\mathrm{H} = \hat{U}_\mathrm{AS}(t_0, -\infty)\hat{\rho}_0 \hat{U}_\mathrm{AS}(-\infty, t_0)\,. \tag{2.2-E22}$$

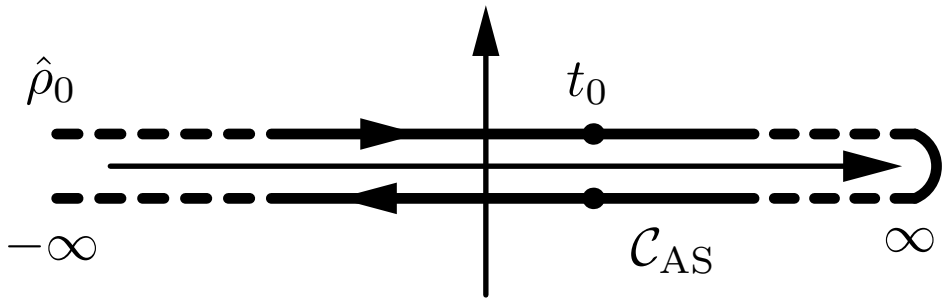

Figure 2.2-F2 – Schematic illustration of the time contour $\mathcal{C}_{\mathrm{AS}}$ that consists of a causal and an anticausal branch like the contour $\mathcal{C}$ depicted in Fig. 2.2-F1. Additionally, both branches are extended to $\pm\infty$ on the real time axis. For $t \to -\infty$ the system is in the noninteracting ground state. Towards t_0 the interaction is switched on adiabatically. The graphic is taken from Ref. [47].

The theoretical foundation of the adiabatic switching method is the *Gell-Mann-Low theorem* [48, 49] which brings some limitations and requirements for the validity of the method. First, the non-interacting ground state $\hat{H}_0$ has to be nondegenerate. Second, the interacting state of the system after the switch-on is an eigenstate of the fully interacting Hamiltonian. However, it is not guaranteed to be the ground state [50]. Thus, in practice, the switch-on has to be performed slowly enough to ensure that the final state is, indeed, the ground state. Last, the interaction is supposed to be switched off again for $t \to \infty$. However, since this does not influence the proceeding propagation, it can be neglected in practice. The numerical realization of this approach is described in Sec. 3.1.2.
Using Eqs. (2.2-E22) and (2.2-E18) one gets

$$\langle \hat{A} \rangle(z) = \mathrm{Tr}\left(\hat{\rho}_0 \hat{U}_{\mathrm{AS}}(-\infty, t_0) \mathcal{T}_{\mathcal{C}} \left\{ \mathrm{e}^{-\frac{\mathrm{i}}{\hbar}\int_{\mathcal{C}} \mathrm{d}\bar{z}\, \hat{H}(\bar{z})} \hat{A}_{\mathrm{S}}\big|_z \right\} \hat{U}_{\mathrm{AS}}(t_0, -\infty) \right) . \tag{2.2-E23}$$

Again, the cyclic property of the trace was used to rearrange the time evolution operators. Additional to the extension of the time contour to $-\infty$ through the adiabatic switching method, it is convenient to also extend $\mathcal{C}$ to $+\infty$ which makes it universal for any choice of t[4]. The final time contour $\mathcal{C}_{\mathrm{AS}}$ is depicted in Fig. 2.2-F2. Using $\mathcal{C}_{\mathrm{AS}}$, Eq. (2.2-E23) can be further simplified and leads to

$$\langle \hat{A} \rangle(z) = \mathrm{Tr}\left(\hat{\rho}_0 \mathcal{T}_{\mathcal{C}_{\mathrm{AS}}} \left\{ \mathrm{e}^{-\frac{\mathrm{i}}{\hbar}\int_{\mathcal{C}_{\mathrm{AS}}} \mathrm{d}\bar{z}\, \hat{H}_{\mathrm{AS}}(\bar{z})} \hat{A}_{\mathrm{S}}\big|_z \right\} \right) , \tag{2.2-E24}$$

where the time ordering superoperator $\mathcal{T}_{\mathcal{C}_{\mathrm{AS}}}$ arranges all operators chronologically on the adiabatic switching contour $\mathcal{C}_{\mathrm{AS}}$. With this, a universal description is found that allows for the combination of time evolution and ensemble averaging of operators in a simple way.

[4] The group property of the time evolution operator allows for the extension of $\mathcal{C}$ to $+\infty$. A prove can be found in Ref. [38].

2.2.4 Green functions and the Martin–Schwinger hierarchy

The time-dependent expectation value of an operator can be accessed in different ways. First, in wavefunction-based approaches, described in Sec. 2.1, where the state vector $|\psi(t)\rangle$ is propagated by the TDSE, the expectation value of an operator $\hat{A}$ is given by

$$\langle \hat{A} \rangle(t) = \langle \psi(t) | \, \hat{A} \, | \psi(t) \rangle \ . \tag{2.2-E25}$$

A second method was presented in the last section. Starting from an initial state described by the density matrix ρ_0, the time dependent ensemble average of an operator can be calculated from Eq. (2.2-E24). The latter approach will, in the following, lead to the introduction of the nonequilibrium Green function.
For this, the operator in Eq. (2.2-E24) has to be expressed in second quantization. The general form of a single particle operator in second quantization was given in Eq. (2.2-E7). In the Heisenberg picture it has the form

$$\hat{A}_{1,\mathrm{H}}(t) = \sum_{i,j} A_{ij} \hat{c}^\dagger_{i,\mathrm{H}}(t) \hat{c}_{j,\mathrm{H}}(t) \, . \tag{2.2-E26}$$

Taking the ensemble average leads to

$$\langle \hat{A}_1 \rangle(t) = \langle \hat{A}_{1,\mathrm{H}} \rangle(t) = \sum_{i,j} A_{ij} \langle \hat{c}^\dagger_{i,\mathrm{H}}(t) \hat{c}_{j,\mathrm{H}}(t) \rangle = \sum_{i,j} A_{ij} \rho_{ij}(t) \, , \tag{2.2-E27}$$

where $\rho_{ij} = \langle \hat{c}^\dagger_i \hat{c}_j \rangle$ is the one-particle density matrix. This means that in order to calculate all one-particle nonequilibrium observables it is sufficient to know ρ_{ij}.
The idea of the NEGF is to generalize the single-time product of $\hat{c}^\dagger(t)$ and $\hat{c}(t)$ to two contour times z and z'. The resulting operator is given by

$$\hat{G}^{(1)}_{ij}(z, z') \coloneqq -\frac{\mathrm{i}}{\hbar} \mathcal{T}_\mathcal{C} \left\{ \hat{c}_{i,\mathrm{H}}(z) \hat{c}^\dagger_{j,\mathrm{H}}(z') \right\} \, , \tag{2.2-E28}$$

where the factor $-\frac{\mathrm{i}}{\hbar}$ and the time-ordering superoperator $\mathcal{T}_\mathcal{C}$ were added and the position of the creation and annihilation operator was swapped for convenience. Now, averaging this expression leads to the well known contour-ordered, single-particle nonequilibrium Green function

$$G^{(1)}_{ij}(z, z') \coloneqq -\frac{\mathrm{i}}{\hbar} \left\langle \mathcal{T}_\mathcal{C} \left\{ \hat{c}_{i,\mathrm{H}}(z) \hat{c}^\dagger_{j,\mathrm{H}}(z') \right\} \right\rangle \, . \tag{2.2-E29}$$

For a better understanding of this expression, Eq. (2.2-E28) can be inserted into Eq. (2.2-E24) to show the averaging explicitly

$$G^{(1)}_{ij}(z, z') = \mathrm{Tr} \left(\hat{\rho}_0 \mathcal{T}_{\mathcal{C}_\mathrm{AS}} \left\{ \mathrm{e}^{-\frac{\mathrm{i}}{\hbar} \int_{\mathcal{C}_\mathrm{AS}} \mathrm{d}\bar{z} \, \hat{H}_\mathrm{AS}(\bar{z})} \hat{c}_{i,\mathrm{S}} \big|_z \hat{c}^\dagger_{j,\mathrm{S}} \big|_{z'} \right\} \right) \, . \tag{2.2-E30}$$

Until now, only one-particle operators are considered but analogous to Eqs. (2.2-E28) and (2.2-E29) it is possible to define the N-particle correlator

$$\hat{G}^{(N)}_{i_1 \ldots i_N j_1 \ldots j_N}(z_1, \ldots, z_N, z'_1, \ldots, z'_N) \coloneqq \\ \frac{1}{(\mathrm{i}\hbar)^N} \mathcal{T}_\mathcal{C} \left\{ \hat{c}_{i_1}(z_1) \ldots \hat{c}_{i_N}(z_N) \hat{c}^\dagger_{j_N}(z'_N) \ldots \hat{c}^\dagger_{j_1}(z'_1) \right\} \tag{2.2-E31}$$

and the corresponding N-particle Green function

$$G^{(N)}_{i_1\dots i_N j_1\dots j_N}(z_1,\dots,z_N,z'_1,\dots,z'_N) = \frac{1}{(\mathrm{i}\hbar)^N}\left\langle \mathcal{T}_\mathcal{C}\left\{\hat{c}_{i_1}(z_1)\dots\hat{c}_{i_N}(z_N)\hat{c}^\dagger_{j_N}(z'_N)\dots\hat{c}^\dagger_{j_1}(z'_1)\right\}\right\rangle . \tag{2.2-E32}$$

with $2N$ contour arguments. The knowledge about $G^{(N)}$ enables the calculation of any N-particle observable. However, for this an equation of motion for $G^{(N)}$ has to be found. As every operator in second quantization can be expressed in the basis of the canonical creator and annihilator it is crucial to take a look at the time evolution of these two operators in the Heisenberg picture. Starting from the Heisenberg equation (cf. Eq. (2.2-E11)) and using the commutator relations of Eq. (2.2-E5) one arrives at [47]

$$\mathrm{i}\hbar\frac{\mathrm{d}\hat{c}_i(z)}{\mathrm{d}z} = \sum_j\left(h^{(0)}_{ij}(z)+f_{ij}(z)\right)\hat{c}_j(z)+\sum_{j,k,l}w_{ijkl}(z)\hat{c}^\dagger_j(z)\hat{c}_k(z)\hat{c}_l(z)\,, \tag{2.2-E33}$$

$$-\mathrm{i}\hbar\frac{\mathrm{d}\hat{c}^\dagger_i(z)}{\mathrm{d}z} = \sum_j\hat{c}^\dagger_j(z)\left(h^{(0)}_{ji}(z)+f_{ji}(z)\right)+\sum_{j,k,l}\hat{c}^\dagger_j(z)\hat{c}^\dagger_k(z)\hat{c}_l(z)w_{jkli}(z)\,, \tag{2.2-E34}$$

for contour times z and a Hamiltonian defined in Eq. (2.2-E9). Using these relations the equations[5] of motion for the N-particle Green function can be derived which couple $G^{(N)}$ to $G^{(N-1)}$ and $G^{(N+1)}$:

$$\begin{aligned}
&\sum_l\left[\mathrm{i}\hbar\frac{\mathrm{d}}{\mathrm{d}z_k}\delta_{i_k,l}-h^{(0)}_{i_k l}(z_k)\right]G^{(N)}_{i_1\dots l\dots i_N j_1\dots j_N}(z_1,\dots,z_N,z'_1,\dots,z'_N)\\
&=\pm\mathrm{i}\hbar\sum_{l,m,n}\int_\mathcal{C}\mathrm{d}\bar{z}\,w_{i_k lmn}(z_k,\bar{z})G^{(N+1)}_{i_1\dots m\dots i_N n j_1\dots j_N l}(z_1,\dots,z_N,\bar{z},z'_1,\dots,z'_N,\bar{z}^+)\\
&\quad+\sum_{p=1}^{N}(\pm1)^{k+p}\delta_{i_k,j_p}\delta_\mathcal{C}(z_k,z'_p)G^{(N-1)}_{i_1\dots\cancel{i_k}\dots i_N j_1\dots\cancel{j_p}\dots j_N}(z_1,\dots,\cancel{z_k},\dots,z_N,z'_1,\dots,\cancel{z'_p},\dots,z'_N)\,,
\end{aligned} \tag{2.2-E35}$$

$$\begin{aligned}
&\sum_l G^{(N)}_{i_1\dots i_N j_1\dots l\dots j_N}(z_1,\dots,z_N,z'_1,\dots,z'_N)\left[-\mathrm{i}\hbar\frac{\overleftarrow{\mathrm{d}}}{\mathrm{d}z'_k}\delta_{l,j_k}-h^{(0)}_{l j_k}(z'_k)\right]\\
&=\pm\mathrm{i}\hbar\sum_{l,m,n}\int_\mathcal{C}\mathrm{d}\bar{z}\,G^{(N+1)}_{i_1\dots i_N n j_1\dots l\dots j_N m}(z_1,\dots,z_N,\bar{z}^-,z'_1,\dots,z'_N,\bar{z})w_{lmj_k n}(\bar{z},z'_k)\\
&\quad+\sum_{p=1}^{N}(\pm1)^{k+p}\delta_{i_p,j_k}\delta_\mathcal{C}(z_p,z'_k)G^{(N-1)}_{i_1\dots\cancel{i_p}\dots i_N j_1\dots\cancel{j_k}\dots j_N}(z_1,\dots,\cancel{z_p},\dots,z_N,z'_1,\dots,\cancel{z'_k},\dots,z'_N)\,.
\end{aligned} \tag{2.2-E36}$$

Here, a generalized two-time interaction

$$w_{ijkl}(z,\bar{z}) \coloneqq w_{ijkl}(z)\delta_\mathcal{C}(z,\bar{z}) \tag{2.2-E37}$$

is introduced, together with the times $z^\pm = z\pm\epsilon, \epsilon\ll 1$, to enforce the correct time ordering of the operators on the contour. The differential operator $\frac{\overleftarrow{\mathrm{d}}}{\mathrm{d}z'_k}$ is acting to its left

[5] There are two sets of equations, one for each time dimension.

what is denoted by the arrow.
A detailed derivation and introduction of Eqs. (2.2-E35) and (2.2-E36), which are well-known as the Martin–Schwinger hierarchy [51], can be found in Refs. [36, 38, 52]. The complete hierarchy is a coupled system of integro-differential equations and its solution gives access to all observables of the studied system. Due to the coupling of the individual equations, the hierarchy can, in principle, be solved exactly in an recursive manner starting from the zero-particle Green function $G^{(0)} := \mathbb{1}$. However, in practice the effort for the full solution scales exponentially with the particle number which makes it impossible to solve the problem with numerical methods.
Fortunately, as show in Eq. (2.2-E27), it is sufficient to know $G^{(1)}$ to calculate all single-particle observables. Therefore, if one is predominantly interested in those quantities, it is convenient to focus on an equation of motion for the single-particle Green function, $G^{(1)}_{ij}(z,z') =: G_{ij}(z,z')$, which from now on is simply referred to as Green function. The dynamics of G are described by the first hierarchy equation which is coupled to the two-particle Green function $G^{(2)}$:

$$\begin{aligned}\sum_l \left[\mathrm{i}\hbar\frac{\mathrm{d}}{\mathrm{d}z}\delta_{i,l} - h^{(0)}_{il}(z)\right] G_{lj}(z,z') &= \delta_{i,j}\delta_{\mathcal{C}}(z,z') \\ &\pm \mathrm{i}\hbar\sum_{l,m,n}\int_{\mathcal{C}}\mathrm{d}\bar{z}\, w_{ilmn}(z,\bar{z})G^{(2)}_{mnjl}(z,\bar{z},z',\bar{z}^+)\,,\end{aligned} \tag{2.2-E38}$$

$$\begin{aligned}\sum_l G_{il}(z,z')\left[-\mathrm{i}\hbar\frac{\overleftarrow{\mathrm{d}}}{\mathrm{d}z'}\delta_{l,j} - h^{(0)}_{lj}(z')\right] &= \delta_{i,j}\delta_{\mathcal{C}}(z,z') \\ &\pm \mathrm{i}\hbar\sum_{l,m,n}\int_{\mathcal{C}}\mathrm{d}\bar{z}\, G^{(2)}_{inlm}(z,\bar{z}^-,z',\bar{z})w_{lmjn}(\bar{z},z')\,.\end{aligned} \tag{2.2-E39}$$

These equations are the well-known Keldysh–Kadanoff–Baym equations [53]. It is apparent that even the determination of G alone requires the solution of the full hierarchy due to the coupling to $G^{(2)}$[6]. In order to solve this problem, the hierarchy equations have to be decoupled by expressing $G^{(2)}$ in terms of G. For this purpose, it is useful to introduce the single-particle selfenergy Σ [36–38, 52] which is implicitly defined as

$$\pm\mathrm{i}\hbar\sum_{l,m,n}\int_{\mathcal{C}}\mathrm{d}\bar{z}\, w_{ilmn}(z,\bar{z})G^{(2)}_{mnjl}(z,\bar{z},z',\bar{z}^+) =: \sum_l\int_{\mathcal{C}}\mathrm{d}\bar{z}\,\Sigma_{il}(z,\bar{z})G_{lj}(\bar{z},z')\,, \tag{2.2-E40}$$

$$\pm\mathrm{i}\hbar\sum_{l,m,n}\int_{\mathcal{C}}\mathrm{d}\bar{z}\, G^{(2)}_{inlm}(z,\bar{z}^-,z',\bar{z})w_{lmjn}(\bar{z},z') =: \sum_l\int_{\mathcal{C}}\mathrm{d}\bar{z}\, G_{il}(z,\bar{z})\Sigma_{lj}(\bar{z},z')\,. \tag{2.2-E41}$$

Using these relations, Eqs. (2.2-E38) and (2.2-E39) can be transformed into the formally closed KBEs for the one-particle Green function G:

$$\begin{aligned}\sum_l \left[\mathrm{i}\hbar\frac{\mathrm{d}}{\mathrm{d}z}\delta_{i,l} - h^{(0)}_{il}(z)\right] G_{lj}(z,z') &= \delta_{i,j}\delta_{\mathcal{C}}(z,z') \\ &+\sum_l\int_{\mathcal{C}}\mathrm{d}\bar{z}\,\Sigma_{il}(z,\bar{z})G_{lj}(\bar{z},z')\,,\end{aligned} \tag{2.2-E42}$$

[6] $G^{(2)}$ couples to $G^{(3)}$ and so on.

$$\sum_l G_{il}(z,z')\left[-\mathrm{i}\hbar\frac{\overleftarrow{\mathrm{d}}}{\mathrm{d}z'}\delta_{l,j} - h^{(0)}_{lj}(z')\right] = \delta_{i,j}\delta_{\mathcal{C}}(z,z') + \sum_l \int_{\mathcal{C}} \mathrm{d}\bar{z}\, G_{il}(z,\bar{z})\Sigma_{lj}(\bar{z},z')\,. \tag{2.2-E43}$$

The integral term on the right hand side of the equation is often referred to as collision integral. It is the reason for the (in general) non-Markovian structure of the KBE, since the time evolution of G depends on its own history.

2.2.5 Selfenergy approximations

If the selfenergy Σ contains the full N-particle information of the system, Eqs. (2.2-E42) and (2.2-E43) are exact. However, since that is the case only in special model systems, many-body approximations (MBA) have to be developed to truncate the Martin–Schwinger hierarchy. For this purpose Σ can be split into two parts:

$$\Sigma_{ij}(z,z') = \Sigma^{\mathrm{HF}}_{ij}(z,z') + \Sigma^{\mathrm{corr}}_{ij}(z,z')\,, \tag{2.2-E44}$$

where mean-field and exchange effects are described by the Hartree–Fock selfenergy Σ^{HF} and correlation effects are included in the correlation part of the selfenergy Σ^{corr}. While the derivation of Σ^{HF} is straightforward, the correct description of correlations turns out to be a challenging task. In the following, the Hartree–Fock selfenergy as well as some correlation including higher order schemes will be introduced.

2.2.5.1 Hartree–Fock

The idea of the Hartree–Fock (HF) approximation is to express the two-particle Green function $G^{(2)}$ as the product of two one-particle Green functions

$$G^{(2),\mathrm{HF}}_{i_1 i_2 j_1 j_2}(z_1,z_2,z_1',z_2') = G_{i_1 j_1}(z_1,z_1')G_{i_2 j_2}(z_2,z_2') \pm G_{i_1 j_2}(z_1,z_2')G_{i_2 j_1}(z_2,z_1')\,, \tag{2.2-E45}$$

where the first term describes the propagation of two independent particles that are added at times z_1' and z_2' and removed at z_1 and z_2. The second term accounts for the indistinguishability of particles in quantum mechanics. This way, the Hartree–Fock Green function includes mean-field and exchange effects.
To get an expression for the selfenergy, Eq. (2.2-E45) has to be inserted into Eq. (2.2-E42)[7].

[7] Inserting Eq. (2.2-E45) into Eq. (2.2-E43) gives the same result.

This leads to the KBE in Hartree–Fock approximation

$$\begin{aligned}\sum_l \left[\mathrm{i}\hbar\frac{\mathrm{d}}{\mathrm{d}z}\delta_{i,l} - h_{il}^{(0)}(z)\right] G_{lj}(z,z') \\ &= \delta_{i,j}\delta_{\mathcal{C}}(z,z') \\ &\quad \pm \mathrm{i}\hbar\sum_{l,m,n}\int_{\mathcal{C}}\mathrm{d}\bar{z}\, w_{ilmn}(z,\bar{z})G_{mj}(z,z')G_{nl}(\bar{z},\bar{z}^+) \\ &\quad + \mathrm{i}\hbar\sum_{l,m,n}\int_{\mathcal{C}}\mathrm{d}\bar{z}\, w_{ilmn}(z,\bar{z})G_{ml}(z,\bar{z}^+)G_{nj}(\bar{z},z') \\ &= \delta_{i,j}\delta_{\mathcal{C}}(z,z') \\ &\quad \pm \mathrm{i}\hbar\sum_{l,m,n}\int_{\mathcal{C}}\mathrm{d}\bar{z}\mathrm{d}\bar{\bar{z}}\,\delta_{\mathcal{C}}(z,\bar{\bar{z}})w_{ilmn}(z,\bar{z})G_{nl}(\bar{z},\bar{z}^+)G_{mj}(\bar{\bar{z}},z') \\ &\quad + \mathrm{i}\hbar\sum_{l,m,n}\int_{\mathcal{C}}\mathrm{d}\bar{z}\, w_{ilmn}(z,\bar{z})G_{ml}(z,\bar{z}^+)G_{nj}(\bar{z},z')\,. \end{aligned} \tag{2.2-E46}$$

Comparing with Eq. (2.2-E40) results in the well-known definition of the Hartree–Fock selfenergy

$$\begin{aligned}\Sigma_{ij}^{\mathrm{HF}}(z,z') &= \pm\mathrm{i}\hbar\delta_{\mathcal{C}}(z,z')\sum_{k,l}\int_{\mathcal{C}}\mathrm{d}\bar{z}\, w_{ikjl}(z,\bar{z})G_{lk}(\bar{z},\bar{z}^+) \\ &\quad +\mathrm{i}\hbar\sum_{k,l} w_{iklj}(z,z')G_{lk}(z,z'^+)\,. \end{aligned} \tag{2.2-E47}$$

An illustration of this expression is shown in terms of Feynman diagrams in Fig. 2.2-F3. The first diagram corresponds to the first term of Eq. (2.2-E47), the so-called Hartree selfenergy, and describes the interaction of a particle with the mean-field. The exchange contribution appears in the second diagram, the so-called Fock selfenergy, as a self-interaction.
Using the definition of the interaction w (cf. Eq. (2.2-E37)) reveals that, due to the contour delta function, the Hartree–Fock selfenergy is time-local. Thus, it does not include any correlation effects, as the contour integral in Eq. (2.2-E42) vanishes. Additionally, in terms of a perturbative expansion, it includes only first order terms of the interaction w. The Hartree–Fock approximation is frequently used in many-body physics as the above mentioned properties result in equations that are numerically easy to handle. However, it has been shown [54–56] that it provides poor results when correlation effects play an important role in the system of interest. Therefore, it is necessary to develop higher order approximations that take correlations into account.

2.2.5.2 Higher order approximations

When looking for self-consistent solutions of the KBEs beyond the Hartree–Fock approximation, it is important to verify that a given many-body approximation is conserving, i.e. that the systems total energy, particle number and momentum are preserved. It has been shown by *Baym* [58] that a selfenergy approximation is conserving if

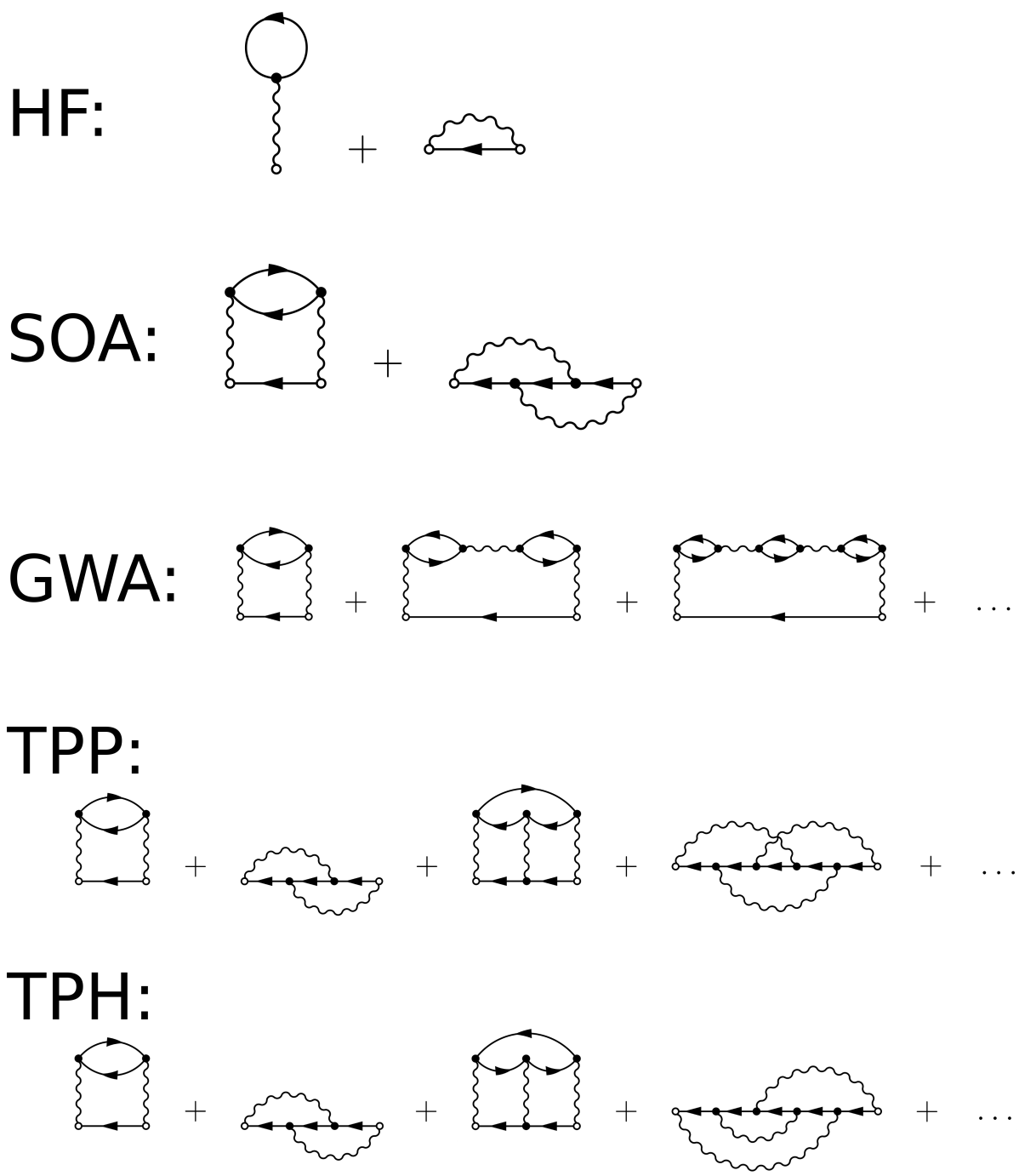

Figure 2.2-F3 – Diagrammatic representation of the Hartree–Fock (HF) approximation, the second Born or second order approximation (SOA), the GW approximation (GWA) and the T-matrix in the particle-particle- (TPP) and particle-hole-channel (TPH). For the last four approximations only the correlation part is depicted and the HF diagrams have to be added to get the full selfenergy, cf. Eq. (2.2-E44). For GWA, TPP and TPH only the first few diagrams are shown. Straight lines correspond to Green functions and curved lines to interactions. Filled dots stand for integrals and sums. The prefactors and signs are neglected for convenience and can be found in Ref. [57].

i.) both Eqs. (2.2-E42) and (2.2-E43) lead to the same approximate solution for G, and
ii.) the approximation for $G^{(2)}$ satisfies the following symmetry relation,

$$G^{(2)}_{i_1 i_2 j_1 j_2}(z_1, z_2, z_1', z_2') = G^{(2)}_{i_2 i_1 j_2 j_1}(z_2, z_1, z_2', z_1') \,. \tag{2.2-E48}$$

The first condition is met by most approximations used in many-particle physics [58]. The second condition is easily verified if the dependence of $G^{(2)}$ on G in a given approximation is known. Taking a look at Eq. (2.2-E45), it is obvious that $G^{(2),\mathrm{HF}}$ satisfies ii.) and, thus, the Hartree–Fock approximation is conserving.
Another important quality of a many-body approximation, which was just recently studied in detail [59–62], is the positive semidefinite property (PSD). In practice, it is mandatory to guarantee the stability of Eqs. (2.2-E42) and (2.2-E43) and a positive spectral function. The Hartree–Hock selfenergy is PSD, but not all conserving approximations, like for instance the fluctuation exchange (FLEX) approximation [63], have this property. However, higher order approximations beyond Hartree–Fock that were found to be both, conserving and PSD, are the second Born or second order approximation (SOA), the GW approximation (GWA) and the T-matrix in the particle-particle- (TPP) and particle-hole-channel (TPH).

Here, a brief overview on those four higher order schemes will be given[8]. To write the selfenergies in a compact way, it is convenient to define some new quantities

$$G^{\mathrm{H}}_{ijkl}(z, z') \coloneqq G_{ik}(z, z') G_{jl}(z, z') \,, \tag{2.2-E49}$$
$$G^{\mathrm{F}}_{ijkl}(z, z') \coloneqq G_{il}(z', z) G_{jk}(z, z') \,, \tag{2.2-E50}$$

where $G^{\mathrm{H}}_{ijkl}(z, z')$ is a Hartree-like and $G^{\mathrm{F}}_{ijkl}(z, z')$ is a Fock-like two-particle Green function. All selfenergies presented here have to be understood as correlation selfenergies, i.e. they have to be inserted for Σ^{corr} in Eq. (2.2-E44) to give the full selfenergy.

Second order approximation (SOA): The SOA is the most simple approach to add correlations to the selfenergy. The idea is to describe the scattering event between two particles by considering only the first term in the Born series [38]. This results in the following expression for the SOA selfenergy

$$\Sigma^{\mathrm{SOA}}_{ij}(z, z') = \pm (\mathrm{i}\hbar)^2 \sum_{m,n,p,q,r,s} \Big(G^{\mathrm{H}}_{mpnq}(z, z') w_{ispm}(z) w_{qnjr}(z') G_{rs}(z', z) \\ \pm w_{iqrm}(z) G_{m,n}(z, z') w_{nsjp}(z') G^{\mathrm{F}}_{prsq}(z', z) \Big) \,. \tag{2.2-E51}$$

It includes all terms up to second order in the interaction w but no higher order terms. Thus, it is a reasonable approach when the interaction strength is low. A diagrammatic representation is shown in Fig. 2.2-F3. More details can be found in Refs. [38, 55, 56].

[8] In the following the definition of the interaction w in Eq. (2.2-E37) is used to get back to a one-time interaction.

***GW* approximation (GWA):** The GWA is a more sophisticated approach that takes the screened interaction between particles into account. The selfenergy is given by

$$\Sigma_{ij}^{\mathrm{GWA}}(z,z') = \mathrm{i}\hbar \sum_{k,l} W_{ikjl}(z,z') G_{lk}(z,z') \,, \tag{2.2-E52}$$

where W is defined recursively as

$$W_{ijkl}(z,z') = \pm\mathrm{i}\hbar \sum_{m,n,p,q} \int_{\mathcal{C}} \mathrm{d}\bar{z}\, w_{ipml}(z) G^{\mathrm{F}}_{mnpq}(z,\bar{z}) W_{qjkn}(\bar{z},z') \,. \tag{2.2-E53}$$

Since W depends on itself in Eq. (2.2-E53), the GWA is a resummation approach that contains contributions up to infinite order in w. It has shown good results for systems near half filling, where screening effects are important [64]. Furthermore, it is frequently used for bandstructure and photoemission calculations [65, 66]. The first three diagrams of the GWA are depicted in Fig. 2.2-F3. For more information and a derivation of above equations the reader is referred to [57].

Particle-particle *T*-matrix (TPP): The TPP is another resummation approach that can be seen as an extension to the SOA as it considers the full Born series instead of just the first term. Therefore, it also contains terms of all orders in w. The selfenergy is defined as

$$\Sigma_{ij}^{\mathrm{TPP}}(z,z') = \mathrm{i}\hbar \sum_{k,l} T^{\mathrm{pp}}_{ikjl}(z,z') G_{lk}(z',z) \,, \tag{2.2-E54}$$

where T^{pp} is given by

$$\begin{aligned} T^{\mathrm{pp}}_{ijkl}(z,z') = {} & \pm\mathrm{i}\hbar \sum_{m,n,p,q} w_{ijmn}(z) G^{\mathrm{H}}_{mnpq}(z,z') w_{pqkl}(z') \\ & + \mathrm{i}\hbar \sum_{m,n,p,q} w_{ijmn}(z) G^{\mathrm{H}}_{mnpq}(z,z') w_{pqlk}(z') \\ & + \mathrm{i}\hbar \sum_{m,n,p,q} \int_{\mathcal{C}} \mathrm{d}\bar{z}\, w_{ijmn}(z) G^{\mathrm{H}}_{mnpq}(z,\bar{z}) T^{\mathrm{pp}}_{pqkl}(\bar{z},z') \,. \end{aligned} \tag{2.2-E55}$$

It describes multiple scattering events between two particles (or two holes) and is justified in the case of nearly empty or nearly filled bands where the correct treatment of scattering effects is important. The first four diagrams are shown in Fig. 2.2-F3. An in depth derivation of the particle-particle T-matrix can be found in [47].

Particle-hole *T*-matrix (TPH): The TPH approach is similar to the TPP with the only difference being that it describes multiple scattering events between a particle and a hole instead of particles of the same type. The resulting selfenergy is

$$\Sigma_{ij}^{\mathrm{TPH}}(z,z') = \mathrm{i}\hbar \sum_{k,l} G_{kl}(z,z') T^{\mathrm{ph}}_{iljk}(z,z') \,, \tag{2.2-E56}$$

with T^{ph} being defined as

$$\begin{aligned} T^{\mathrm{ph}}_{ijkl}(z,z') &= \pm \mathrm{i}\hbar \sum_{m,n,p,q} w_{ipml}(z) G^{\mathrm{F}}_{mnpq}(z,z') w_{pjkn}(z') \\ &\quad + \mathrm{i}\hbar \sum_{m,n,p,q} w_{ipml}(z) G^{\mathrm{F}}_{mnpq}(z,z') w_{qjnk}(z') \\ &\quad + \mathrm{i}\hbar \sum_{m,n,p,q} \int_{\mathcal{C}} \mathrm{d}\bar{z}\, w_{ipml}(z) G^{\mathrm{F}}_{mnpq}(z,\bar{z}) T^{\mathrm{ph}}_{qjkn}(\bar{z},z') \,. \end{aligned} \tag{2.2-E57}$$

Again, due to the resummation, the selfenergy contains an infinite number of terms. The first four can be seen in Fig. 2.2-F3. For further details the reader is referred to [64].

2.2.6 Real-time components of contour quantities

In the form given in Eqs. (2.2-E42) and (2.2-E43) the KBEs can not be handled numerically. Therefore, it is necessary to find a more suited representation of the Green function in order to propagate it in practice. Looking back at the time contour defined in Sec. 2.2.3, there are four different ways to order two time arguments on the two different branches. A vivid illustration of the procedure is shown in Fig. 2.2-F4. This way, it is possible to express the Green function as a 2×2-matrix containing four different real-time components[9]:

$$\boldsymbol{G_{ij}}(z_1,z_2) = \begin{pmatrix} G^{\mathrm{c}}_{ij}(t_1,t_2) & G^{<}_{ij}(t_1,t_2) \\ G^{>}_{ij}(t_1,t_2) & G^{\mathrm{a}}_{ij}(t_1,t_2) \end{pmatrix} , \tag{2.2-E58}$$

where the components are defined as

$$G^{\mathrm{c}}_{ij}(t_1,t_2) = \frac{1}{\mathrm{i}\hbar} \left\langle \mathcal{T} \left\{ \hat{c}_i(t_1) \hat{c}^\dagger_j(t_2) \right\} \right\rangle , \tag{2.2-E59}$$

$$G^{<}_{ij}(t_1,t_2) = \pm \frac{1}{\mathrm{i}\hbar} \left\langle \hat{c}^\dagger_j(t_2) \hat{c}_i(t_1) \right\rangle , \tag{2.2-E60}$$

$$G^{>}_{ij}(t_1,t_2) = \frac{1}{\mathrm{i}\hbar} \left\langle \hat{c}_i(t_1) \hat{c}^\dagger_j(t_2) \right\rangle , \tag{2.2-E61}$$

$$G^{\mathrm{a}}_{ij}(t_1,t_2) = \frac{1}{\mathrm{i}\hbar} \left\langle \bar{\mathcal{T}} \left\{ \hat{c}_i(t_1) \hat{c}^\dagger_j(t_2) \right\} \right\rangle . \tag{2.2-E62}$$

Here, $G^<$ and $G^>$ are referred to as the less and greater Green function while G^{c} and G^{a} are the causal and anticausal component, respectively. They are defined as

$$G^{\mathrm{c}}_{ij}(t_1,t_2) := \Theta(t_1,t_2) G^{>}_{ij}(t_1,t_2) + \Theta(t_2,t_1) G^{<}_{ij}(t_1,t_2), \tag{2.2-E63}$$

$$G^{\mathrm{a}}_{ij}(t_1,t_2) := \Theta(t_2,t_1) G^{>}_{ij}(t_1,t_2) + \Theta(t_1,t_2) G^{<}_{ij}(t_1,t_2), \tag{2.2-E64}$$

where Θ is the Heaviside step function with $\Theta(t_1,t_2) = 1$ if $t_1 > t_2$ and $\Theta(t_1,t_2) = 0$ otherwise. Since G^{c} and G^{a} can be expressed by $G^<$ and $G^>$, the matrix in Eq. (2.2-E58)

[9] This is an advantage of the adiabatic switching method introduced in Sec. 2.2.3. Using the second presented method to generate a ground state, which results in a third contour branch in imaginary time, leads to nine different ways to order two time arguments and, thus, in a 3×3-matrix.

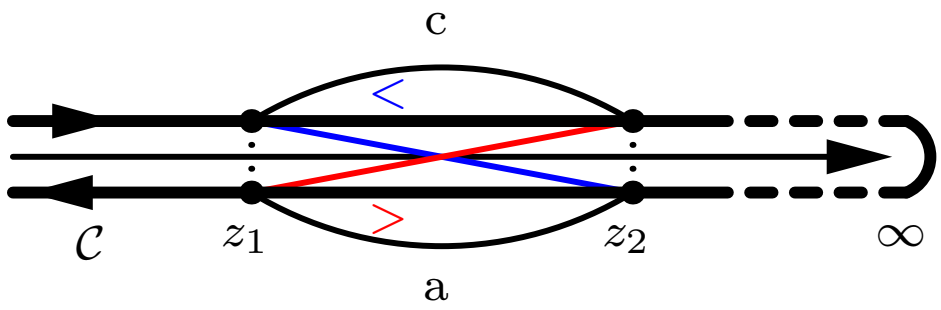

Figure 2.2-F4 – Illustration of the time ordering on the contour: There are four different ways to order two time arguments on the two contour branches. In the case of the causal (anticausal) component both time arguments are placed on the causal (anticausal) branch, indicated by "c" ("a"). If they lie on different branches, they can form the greater component (red), if z_1 is on the anticausal and z_2 is on the causal branch, and the less component (blue) otherwise. The graphic is taken from Ref. [47].

is overcomplete, as it effectively only depends on two components. This finding can be used to transform $\boldsymbol{G_{ij}}$ by so-called Keldysh rotations [67] to get a representation that is best suited for computational demands. In this work, the following Green function matrix was used[10]

$$\boldsymbol{G_{ij}}(z_1, z_2) = \begin{pmatrix} G^{\mathrm{R}}_{ij}(t_1, t_2) & G^{<}_{ij}(t_1, t_2) \\ 0 & G^{\mathrm{A}}_{ij}(t_1, t_2) \end{pmatrix} , \tag{2.2-E65}$$

where G^{R} and G^{A} are the retarded and advanced Green function, respectively. They are defined as

$$\begin{aligned} G^{\mathrm{R}}_{ij}(t_1, t_2) &:= G^{\mathrm{c}}_{ij}(t_1, t_2) - G^{<}_{ij}(t_1, t_2) = G^{>}_{ij}(t_1, t_2) - G^{\mathrm{a}}_{ij}(t_1, t_2) \,, \\ G^{\mathrm{A}}_{ij}(t_1, t_2) &:= G^{\mathrm{c}}_{ij}(t_1, t_2) - G^{>}_{ij}(t_1, t_2) = G^{<}_{ij}(t_1, t_2) - G^{\mathrm{a}}_{ij}(t_1, t_2) \,. \end{aligned} \tag{2.2-E66}$$

Using the definitions of G^{c} and G^{a} in Eqs. (2.2-E63) and (2.2-E64) leads to a more compact expression

$$G^{\mathrm{R/A}}_{ij}(t_1, t_2) = \Theta(t_{1/2}, t_{2/1}) \left(G^{\gtrless}_{ij}(t_1, t_2) - G^{\lessgtr}_{ij}(t_1, t_2) \right) , \tag{2.2-E67}$$

where Θ is the Heaviside step function introduced above.
All these thoughts do not only apply to the Green function but to all two-time contour ordered functions in Keldysh space, like the selfenergy Σ [37]. Hence, it is possible to transform the KBEs into a real-time form to propagate the components of $\boldsymbol{G}$. To do so, there are special rules on how to calculate the components of a product of two two-time

[10] This representation, suggested by Langreth and Wilkens [68], can be obtained by doing a linear transformation of the form $\boldsymbol{G}_{\mathrm{LW}} := \boldsymbol{LMGL}^{-1}$ with $\boldsymbol{L} = \begin{pmatrix} 1 & 0 \\ 1 & 1 \end{pmatrix}$ and $\boldsymbol{M} = \begin{pmatrix} 1 & 0 \\ 0 & -1 \end{pmatrix}$.

contour quantities $\boldsymbol{B}$ and $\boldsymbol{C}$, the so-called Langreth–Wilkins rules [68]:

$$\boldsymbol{BC} = \begin{pmatrix} B^{\mathrm{R}} & B^{<} \\ 0 & B^{\mathrm{A}} \end{pmatrix} \cdot \begin{pmatrix} C^{\mathrm{R}} & C^{<} \\ 0 & C^{\mathrm{A}} \end{pmatrix} = \begin{pmatrix} B^{\mathrm{R}}C^{\mathrm{R}} & B^{\mathrm{R}}C^{<} + B^{<}C^{\mathrm{A}} \\ 0 & B^{\mathrm{A}}C^{\mathrm{A}} \end{pmatrix} . \tag{2.2-E68}$$

This schematic notation can be understood using the example of the less and greater components of rank two tensors $\boldsymbol{B}$ and $\boldsymbol{C}$

$$\begin{aligned} \left\{ \sum_k \int_{\mathcal{C}} \mathrm{d}\bar{z}\, B_{ik}(z,\bar{z}) C_{kj}(\bar{z},z') \right\}^{\gtrless} &= \sum_k \int_{t_\mathrm{s}}^{\infty} \mathrm{d}\bar{t}\, B^{\mathrm{R}}_{ik}(t,\bar{t}) C^{\gtrless}_{kj}(\bar{t},t') \\ &\quad + \sum_k \int_{t_\mathrm{s}}^{\infty} \mathrm{d}\bar{t}\, B^{\gtrless}_{ik}(t,\bar{t}) C^{\mathrm{A}}_{kj}(\bar{t},t') \,. \end{aligned} \tag{2.2-E69}$$

The time t_s in the integral boundaries corresponds to the starting time z_s on the contour $\mathcal{C}$, i.e. in the case of adiabatic switching $t_0 \to -\infty$.
All two-time contour quantities $\boldsymbol{B}$ with two basis indices obey the spatial and time transposition symmetry

$$B^{\gtrless}_{ij}(t_1,t_2) = -\left[B^{\gtrless}_{ji}(t_2,t_1)\right]^* . \tag{2.2-E70}$$

Additionally, there are further useful relations for the real-time components of the Green function

$$G^{\mathrm{R}}_{ij}(t_1,t_2) = \left[G^{\mathrm{A}}_{ji}(t_2,t_1)\right]^* , \tag{2.2-E71}$$

$$G^{>}_{ij}(t,t) - G^{<}_{ij}(t,t) = \pm\frac{\mathrm{i}}{\hbar}\delta_{i,j} \,. \tag{2.2-E72}$$

Using the Langreth–Wilkins rules presented in Eqs. (2.2-E68) and (2.2-E69), it is now possible to transform not only the KBEs (Eqs. (2.2-E42) and (2.2-E43)) but also the expressions for the selfenergy approximations discussed in Sec. 2.2.5 into equations for the respective real-time quantities. The transformation of the KBEs into equations of motion for the real-time components of the Green function leads to the following expressions. For the less and greater component the equations become

$$\begin{aligned} \sum_l \left[\mathrm{i}\hbar\frac{\mathrm{d}}{\mathrm{d}t}\delta_{i,l} - h^{(0)}_{il}(t) \right] G^{\gtrless}_{lj}(t,t') = \\ \sum_l \int_{t_\mathrm{s}}^{\infty} \mathrm{d}\bar{t} \left\{ \Sigma^{\mathrm{R}}_{il}(t,\bar{t}) G^{\gtrless}_{lj}(\bar{t},t') + \Sigma^{\gtrless}_{il}(t,\bar{t}) G^{\mathrm{A}}_{lj}(\bar{t},t') \right\} \quad \text{and} \end{aligned} \tag{2.2-E73}$$

$$\begin{aligned} \sum_l G^{\gtrless}_{il}(t,t') \left[-\mathrm{i}\hbar\frac{\overleftarrow{\mathrm{d}}}{\mathrm{d}t'}\delta_{l,j} - h^{(0)}_{lj}(t') \right] = \\ \sum_l \int_{t_\mathrm{s}}^{\infty} \mathrm{d}\bar{t} \left\{ G^{\mathrm{R}}_{il}(t,\bar{t}) \Sigma^{\gtrless}_{lj}(\bar{t},t') + G^{\gtrless}_{il}(t,\bar{t}) \Sigma^{\mathrm{A}}_{lj}(\bar{t},t') \right\} . \end{aligned} \tag{2.2-E74}$$

It is apparent that the time diagonal part $\delta_{i,j}\delta_{\mathcal{C}}(z,z')$ on the right hand side of the equation has vanished. This is because, for the less and greater component, the two contour times

z and z' are, by definition, located on different branches, i.e. $z \neq z'$. For the retarded and advanced component one gets

$$\sum_l \left[\mathrm{i}\hbar \frac{\mathrm{d}}{\mathrm{d}t} \delta_{i,l} - h_{il}^{(0)}(t) \right] G_{lj}^{\mathrm{R/A}}(t,t') = \delta_{i,j}\delta(t,t') + \sum_l \int_{t_\mathrm{s}}^{\infty} \mathrm{d}\bar{t}\, \Sigma_{il}^{\mathrm{R/A}}(t,\bar{t}) G_{lj}^{\mathrm{R/A}}(\bar{t},t') \quad \text{and} \tag{2.2-E75}$$

$$\sum_l G_{il}^{\mathrm{R/A}}(t,t') \left[-\mathrm{i}\hbar \frac{\overleftarrow{\mathrm{d}}}{\mathrm{d}t'} \delta_{l,j} - h_{lj}^{(0)}(t') \right] = \delta_{i,j}\delta(t,t') + \sum_l \int_{t_\mathrm{s}}^{\infty} \mathrm{d}\bar{t}\, G_{il}^{\mathrm{R/A}}(t,\bar{t}) \Sigma_{lj}^{\mathrm{R/A}}(\bar{t},t') \,, \tag{2.2-E76}$$

where the time diagonal part does not vanish. These equations are a numerically accessible representation of the KBEs and, in practice, allow to propagate the Green function in time. In the next section, an approximation to these equations is introduced that lowers the numerical effort required by reducing the propagation to the time diagonal part.

2.2.7 The generalized Kadanoff–Baym ansatz

The idea of the generalized Kadanoff–Baym ansatz (GKBA) is to reduce the numerical complexity of the KBEs by restricting the propagation to the time diagonal and reconstructing all non-time-diagonal values from the density matrix n of the system. For this purpose, one can define two new quantities

$$\mathcal{R}_{ij}^{\gtrless}(t_1,t_2) := \tilde{\Theta}(t_1,t_2) G_{ij}^{\gtrless}(t_1,t_2) \,, \tag{2.2-E77}$$

$$\mathcal{A}_{ij}^{\gtrless}(t_1,t_2) := -\tilde{\Theta}(t_2,t_1) G_{ij}^{\gtrless}(t_1,t_2) \,, \tag{2.2-E78}$$

where $\tilde{\Theta}$ is the modified Heaviside function that is defined in such a way that $\tilde{\Theta}(t_1,t_2) = 1$ if $t_1 \geq t_2$ and $\tilde{\Theta}(t_1,t_2) = 0$ otherwise. With this, the less and greater Green function can be expressed as

$$G_{ij}^{\gtrless}(t_1,t_2) = \mathcal{R}_{ij}^{\gtrless}(t_1,t_2) - \mathcal{A}_{ij}^{\gtrless}(t_1,t_2) \,. \tag{2.2-E79}$$

It can be shown that $\mathcal{R}^{\gtrless}$ and $\mathcal{A}^{\gtrless}$ obey the following relations [47]

$$\begin{aligned} \mathcal{R}_{ij}^{\gtrless}(t_1,t_2) = {} & \pm \sum_k G_{ik}^{\mathrm{R}}(t_1,t_2) \mathfrak{n}_{kj}^{\gtrless}(t_2) \\ & + \sum_{k,l} \int_{t_2}^{t_1} \mathrm{d}\bar{t}_1 \int_{t_\mathrm{s}}^{t_2} \mathrm{d}\bar{t}_2\, G_{ik}^{\mathrm{R}}(t_1,\bar{t}_1) \Sigma_{kl}^{\mathrm{R}}(\bar{t}_1,\bar{t}_2) G_{lj}^{\gtrless}(\bar{t}_2,t_2) \\ & + \sum_{k,l} \int_{t_2}^{t_1} \mathrm{d}\bar{t}_1 \int_{t_\mathrm{s}}^{t_2} \mathrm{d}\bar{t}_2\, G_{ik}^{\mathrm{R}}(t_1,\bar{t}_1) \Sigma_{k,l}^{\gtrless}(\bar{t}_1,\bar{t}_2) G_{lj}^{\mathrm{A}}(\bar{t}_2,t_2) \,, \end{aligned} \tag{2.2-E80}$$

$$\begin{aligned}\mathcal{A}^{\gtrless}_{ij}(t_1,t_2) &= \pm\sum_k \mathfrak{n}^{\gtrless}_{ik}(t_1)G^{\mathrm{A}}_{kj}(t_1,t_2) \\ &\quad -\sum_{k,l}\int_{t_\mathrm{s}}^{t_1}\mathrm{d}\bar{t}_1\int_{t_1}^{t_2}\mathrm{d}\bar{t}_2\, G^{\gtrless}_{ik}(t_1,\bar{t}_1)\Sigma^{\mathrm{A}}_{kl}(\bar{t}_1,\bar{t}_2)G^{\mathrm{A}}_{lj}(\bar{t}_2,t_2) \\ &\quad -\sum_{k,l}\int_{t_\mathrm{s}}^{t_1}\mathrm{d}\bar{t}_1\int_{t_1}^{t_2}\mathrm{d}\bar{t}_2\, G^{\mathrm{R}}_{ik}(t_1,\bar{t}_1)\Sigma^{\gtrless}_{k,l}(\bar{t}_1,\bar{t}_2)G^{\mathrm{A}}_{lj}(\bar{t}_2,t_2)\,,\end{aligned} \tag{2.2-E81}$$

where the notation

$$\begin{aligned}\mathfrak{n}^{<}_{ij}(t) &= -\mathrm{i}\hbar G^{<}_{ij}(t,t) = n_{ij}(t) \qquad \text{and} \\ \mathfrak{n}^{>}_{ij}(t) &= -\mathrm{i}\hbar G^{>}_{ij}(t,t) = n_{ij}(t) - \delta_{i,j}\end{aligned} \tag{2.2-E82}$$

was introduced for the density matrix. A detailed derivation of Eqs. (2.2-E80) and (2.2-E81) exceeds the scope of this thesis and can be found in [47]. By using those relations for $\mathcal{R}^{\gtrless}$ and $\mathcal{A}^{\gtrless}$ in Eq. (2.2-E79), one finds a new expression for the less and greater Green function:

$$\begin{aligned}G^{\gtrless}_{ij}(t_1,t_2) &= \pm\sum_k\left[G^{\mathrm{R}}_{ik}(t_1,t_2)\mathfrak{n}^{\gtrless}_{kj}(t_2) - \mathfrak{n}^{\gtrless}_{ik}(t_1)G^{\mathrm{A}}_{kj}(t_1,t_2)\right] \\ &\quad +\sum_{k,l}\int_{t_2}^{t_1}\mathrm{d}\bar{t}_1\int_{t_\mathrm{s}}^{t_2}\mathrm{d}\bar{t}_2\, G^{\mathrm{R}}_{ik}(t_1,\bar{t}_1)\Sigma^{\mathrm{R}}_{kl}(\bar{t}_1,\bar{t}_2)G^{\gtrless}_{lj}(\bar{t}_2,t_2) \\ &\quad +\sum_{k,l}\int_{t_2}^{t_1}\mathrm{d}\bar{t}_1\int_{t_\mathrm{s}}^{t_2}\mathrm{d}\bar{t}_2\, G^{\mathrm{R}}_{ik}(t_1,\bar{t}_1)\Sigma^{\gtrless}_{k,l}(\bar{t}_1,\bar{t}_2)G^{\mathrm{A}}_{lj}(\bar{t}_2,t_2) \\ &\quad +\sum_{k,l}\int_{t_\mathrm{s}}^{t_1}\mathrm{d}\bar{t}_1\int_{t_1}^{t_2}\mathrm{d}\bar{t}_2\, G^{\gtrless}_{ik}(t_1,\bar{t}_1)\Sigma^{\mathrm{A}}_{kl}(\bar{t}_1,\bar{t}_2)G^{\mathrm{A}}_{lj}(\bar{t}_2,t_2) \\ &\quad +\sum_{k,l}\int_{t_\mathrm{s}}^{t_1}\mathrm{d}\bar{t}_1\int_{t_1}^{t_2}\mathrm{d}\bar{t}_2\, G^{\mathrm{R}}_{ik}(t_1,\bar{t}_1)\Sigma^{\gtrless}_{k,l}(\bar{t}_1,\bar{t}_2)G^{\mathrm{A}}_{lj}(\bar{t}_2,t_2)\,.\end{aligned} \tag{2.2-E83}$$

This equation is exact as long as the exact advanced and retarded Green functions are used. However, since it is still an integral equation a numerical solution remains complicated. A simple approximation is to neglect the integral terms, which is known as the GKBA [69]

$$G^{\gtrless}_{ij}(t_1,t_2) \approx \pm\sum_k\left[G^{\mathrm{R}}_{ik}(t_1,t_2)\mathfrak{n}^{\gtrless}_{kj}(t_2) - \mathfrak{n}^{\gtrless}_{ik}(t_1)G^{\mathrm{A}}_{kj}(t_1,t_2)\right]\,. \tag{2.2-E84}$$

Here, the non-time-diagonal values of $G^{\gtrless}$ only depend on the density matrix n and the propagator functions $G^{\mathrm{R/A}}$. However, these propagators obey Eqs. (2.2-E75) and (2.2-E76) which are of similar complexity as the KBEs for $G^{\gtrless}$. Thus, in order to reduce the numerical effort various approximate expression for the propagators were developed that differ in the description of correlations [70]. In this thesis, the propagators are approximated on the Hartree–Fock level which leads to

$$\begin{aligned}G^{\mathrm{HF,R}}_{ij}(t_1,t_2) &= -\mathrm{i}\Theta(t_1,t_2)\left[\exp\left(-\frac{\mathrm{i}}{\hbar}\int_{t_2}^{t_1}\mathrm{d}\bar{t}\, h^{\mathrm{eff}}(\bar{t})\right)\right]_{ij}\,, \\ G^{\mathrm{HF,A}}_{ij}(t_1,t_2) &= +\mathrm{i}\Theta(t_2,t_1)\left[\exp\left(-\frac{\mathrm{i}}{\hbar}\int_{t_2}^{t_1}\mathrm{d}\bar{t}\, h^{\mathrm{eff}}(\bar{t})\right)\right]_{ij}\,.\end{aligned} \tag{2.2-E85}$$

Here, h^{eff} is the effective Hartree–Fock Hamiltonian which only depends on the density matrix n. Therefore, the non-time-diagonal part of $G^{\gtrless}$ can now be constructed entirely from the time-diagonal density matrix.
An advantage of the GKBA in the form of Eq. (2.2-E84) is that it maintains the causal time structure of the KBEs. This ensures the conservation of total energy, momentum and density when combined with a conserving approximation for the selfenergy. Furthermore, it is known that the GKBA cures certain damping induced artifacts that emerge in the full two-time solution of the KBEs [54]. For the sake of completeness, it should be noted that the original Kadanoff–Baym ansatz [37, 71] has a slightly different form,

$$G_{ij}^{<}(t_1,t_2) \;\approx\; \pm\sum_k f_{ik}\left(\frac{t_1+t_2}{2}\right)\left(G_{kj}^{\mathrm{R}}(t_1,t_2)-G_{kj}^{\mathrm{A}}(t_1,t_2)\right)\,, \tag{2.2-E86}$$

with the Wigner distribution function f that depends on the center-of-mass time. This version violates the causal time structure and is only viable for systems near equilibrium.

2.2.8 Accessible observables

It was shown in Sec. 2.2.4 that it is sufficient to know the one-particle Green function to obtain all single-particle observables of a system. In the following, some important quantities and their connection to the Green function will be displayed.
One of the most important quantities, when looking at nonequilibrium processes, is the time-dependent single-particle density matrix that is given directly by the less Green function

$$n_{ij}(t) = -\mathrm{i}\hbar G_{ij}^{<}(t,t)\,. \tag{2.2-E87}$$

Additionally, if one has access to the full density matrix, a discrete Fourier transform leads to the momentum distribution in k-space

$$n_k(t) = \frac{1}{N_{\mathrm{s}}}\sum_{ij}\mathrm{e}^{-\mathrm{i}k(i-j)}n_{ij}(t)\,, \tag{2.2-E88}$$

where N_{s} is the basis size.
The total energy of the system can be obtained by summing up the individual contributions that correspond to the different parts of the Hamiltonian defined in Eq. (2.2-E9).

- The kinetic energy $E_{\mathrm{kin}}(t)$ that corresponds to the single-particle Hamiltonian $\hat{H}_0$ is given by

$$E_{\mathrm{kin}}(t) = \Re\left[\mathrm{Tr}\left(h^{(0)}n(t)\right)\right]\,. \tag{2.2-E89}$$

- The potential energy $E_{\mathrm{pot}}(t)$ that corresponds to the excitation part of the Hamiltonian $\hat{F}(t)$ is given by

$$E_{\mathrm{pot}}(t) = \Re\left[\mathrm{Tr}\left(f(t)n(t)\right)\right]\,. \tag{2.2-E90}$$

- The interaction energy $E_{\mathrm{int}}(t)$ that corresponds to the interaction part of the Hamiltonian $\hat{W}$ can be split into a Hartree–Fock and a correlation contribution

$$E_{\mathrm{int}}(t) = E_{\mathrm{HF}}(t) + E_{\mathrm{corr}}(t). \tag{2.2-E91}$$

- The Hartree–Fock energy $E_{\mathrm{HF}}(t)$ that corresponds to the Hartree–Fock selfenergy $\Sigma^{\mathrm{HF}}(t)$ (cf. Eq. (2.2-E47)) is given by

$$E_{\mathrm{HF}}(t) = \frac{1}{2}\Re\left[\mathrm{Tr}\left(\Sigma^{\mathrm{HF}}(t)n(t)\right)\right] , \tag{2.2-E92}$$

- The correlation energy $E_{\mathrm{corr}}(t)$ that corresponds to the correlation selfenergy $\Sigma^{\mathrm{corr}}(t)$ in its approximate realization (cf. Eq. (2.2-E44) and Sec. 2.2.5.2) is given by

$$E_{\mathrm{corr}}(t) = \frac{1}{2}\Im\left[\mathrm{Tr}\left(I^{(2),<}(t,t)\right)\right] . \tag{2.2-E93}$$

  where $I^{(2),<}(t,t)$ is the time-diagonal collision integral that originates from the right-hand side of Eq. (2.2-E73) and its trace is defined as

$$\mathrm{Tr}\left(I^{(2),<}(t,t)\right) = \sum_{kl}\int_{t_{\mathrm{s}}}^{t} \mathrm{d}\bar{t}\left\{G^{>}_{lk}(t,\bar{t})\Sigma^{<}_{kl}(\bar{t},t) - G^{<}_{lk}(t,\bar{t})\Sigma^{>}_{kl}(\bar{t},t)\right\}. \tag{2.2-E94}$$

Finally, the total energy $E_{\mathrm{tot}}(t)$ is given by

$$E_{\mathrm{tot}}(t) = E_{\mathrm{kin}}(t) + E_{\mathrm{pot}}(t) + E_{\mathrm{HF}}(t) + E_{\mathrm{corr}}(t)\,. \tag{2.2-E95}$$

Since the Green function was defined as a two-time quantity (cf. Eq. (2.2-E28)), it also gives access to the spectral properties of a system. The local spectral function is given by performing a Fourier transform with respect to the relative time,

$$A_i(\omega) \;=\; \mathrm{i}\hbar\int \mathrm{d}t\,\mathrm{d}t'\,\mathrm{e}^{-\mathrm{i}\omega(t-t')}\left[G^{>}_{ii}(t,t') - G^{<}_{ii}(t,t')\right] . \tag{2.2-E96}$$

The sum over all local contributions of the spectral function results in the density of states (DOS) of the system. Combining the spatial transform in Eq. (2.2-E88) with the temporal one in Eq. (2.2-E96) results in an expression for the full energy dispersion relation

$$A(\omega,k) \;=\; \frac{\mathrm{i}\hbar}{N_s}\sum_{ij}\mathrm{e}^{-\mathrm{i}k(i-j)}\int \mathrm{d}t\,\mathrm{d}t'\,\mathrm{e}^{-\mathrm{i}\omega(t-t')}\left[G^{>}_{ij}(t,t') - G^{<}_{ij}(t,t')\right] . \tag{2.2-E97}$$

However, the most important quantity in this thesis is the time-resolved photoemission spectrum [72, 73]

$$A^{<}(\omega,T) \;=\; -\mathrm{i}\hbar\sum_{i}\int \mathrm{d}t\,\mathrm{d}t'\,\mathcal{S}_\kappa(t-T)\mathcal{S}_\kappa(t'-T)\mathrm{e}^{-\mathrm{i}\omega(t-t')}G^{<}_{ii}(t,t')\,, \tag{2.2-E98}$$

as it allows for direct comparison with photoemission experiments. Here, $\mathcal{S}$ is a Gaussian function to simulate the probe pulse that is used in corresponding experiments

$$\mathcal{S}_\kappa(t) \;=\; \frac{1}{\kappa\sqrt{2\pi}}\exp\left(-\frac{t^2}{2\kappa^2}\right) . \tag{2.2-E99}$$

More information on photoemission experiments can be found in Sec. 5.3.

2.3 Hubbard model

The Hubbard model was introduced in 1963 by *John Hubbard*[11] in a series of articles [31, 76, 77] to describe the Mott metal-insulator transition in narrow-energy bands of solid state systems. Despite the simplistic nature of the Hubbard model it was applied to a variety of systems since it qualitatively captures the properties and underlying physical processes in solids [32].
The central idea of the Hubbard model is illustrated in Fig. 2.3-F1. It is best explained by looking at the orbitals of the single atoms that form a solid state lattice. The outermost orbitals overlap and form a band that allows electrons to move between the atoms, while the inner orbitals are considered frozen as their overlap is negligible. This way, the solid can be reduced to a lattice with sites at the positions of the atoms. Each of those sites can be occupied by only two electrons due to Pauli blocking.
The tunneling between the outer shells can be understood as the hopping between two different lattice sites. It is described by the hopping amplitude J that represents the probability of an hopping process to take place and the hopping matrix t that contains information about which sites are connected. In the standard Hubbard model, which is presented here, only hopping between adjacent sites is taken into account.
Another assumption of the Hubbard model is that the long range Coulomb potential of the outer electrons is shielded by the frozen inner shells. Thus, the potential is considered to be fallen off at adjacent sides, so that only an on-site interaction U remains which originates from two electrons on the same lattice site.
In order to map the Hubbard model to a physical system, the hopping and interaction parameter have to be chosen appropriately. While the hopping amplitude J and matrix elements t_{ij} can usually be determined accurately through density-functional theory [78], the effective on-site interaction U is often more difficult to estimate, for example by comparing theoretical predictions with experimental results. An exception to this are ultracold atoms in optical lattices which allow to precisely adjust the on-site interaction. More information on this type of systems can be found in Ref. [79].
Although the Hubbard model is a simplistic description of solid state systems, it is by no means easy to solve analytically. In fact, there are only very few special limiting cases for which analytical solutions can be found. Two of them, the so called tight-binding limit for a vanishing interaction $U = 0$ and the Hubbard dimer that contains only two sites, will be presented in this section. Another case that is not discussed here is the infinite one-dimensional Hubbard chain that can be solved analytically within the so-called Bethe ansatz.
It should be noted that the Hubbard model can be improved in various ways to allow for hopping processes beyond nearest neighbors and a long-range (non-local) potential [73, 80–82]. In this thesis, an extended Hubbard model is presented in Sec. 5.4 to better meet the requirements for a sophisticated description of graphene.

[11] It was independently developed by Gutzwiller [74] and Kanamori [75] around the same time.

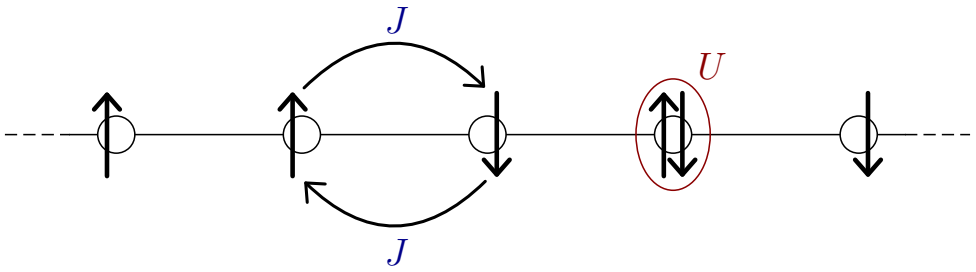

Figure 2.3-F1 – Illustration of the one-dimensional Hubbard model. The solid is reduced to individual lattice sites which can be occupied by up to two electrons. In the standard Hubbard model, electrons can only hop between adjacent sites with a probability J. Only electrons on the same lattice site can interact with each other. The interaction strength is determined by U.

2.3.1 The Hubbard Hamiltonian

Following the assumptions introduced above, the generic Hamiltonian defined in Eq. (2.2-E9) can be transformed into the Hubbard Hamiltonian in second quantization. For that, one has to distinguish between spatial and spin coordinates, $\{i\} \to \{i, \sigma\}$, where i denotes the lattice site position and $\sigma \in \{\uparrow\downarrow\}$ the electronic spin. With this, the matrix elements in Eq. (2.2-E9) become

$$\begin{aligned} h^{(0)}_{ij,\alpha\beta} &= -Jt_{ij}\delta_{\alpha,\beta} - \mu\delta_{i,j}\delta_{\alpha,\beta} \\ &= -J\delta_{\langle i,j\rangle}\delta_{\alpha,\beta} - \mu\delta_{i,j}\delta_{\alpha,\beta}\,, \\ w_{ijkl,\alpha\beta\gamma\delta} &= U\delta_{i,j}\delta_{i,k}\delta_{i,l}\delta_{\alpha,\gamma}\delta_{\beta,\delta}\bar{\delta}_{\alpha,\beta}\,, \\ f_{ij,\alpha\beta}(t) &= f_{i,\alpha}(t)\delta_{i,j}\delta_{\alpha,\beta}\,. \end{aligned} \tag{2.3-E1}$$

Here, μ is the chemical potential, $\bar{\delta}_{\alpha,\beta} \coloneqq 1 - \delta_{\alpha,\beta}$ accounts for the Pauli principle and, since in the standard Hubbard model only hopping between neighboring sites is allowed, t_{ij}[12] was replaced by $\delta_{\langle i,j\rangle}$, where $\delta_{\langle i,j\rangle} := 1$ if the sites i, j are nearest neighbors and $\delta_{\langle i,j\rangle} := 0$ otherwise. Furthermore, all time-dependent excitations considered in this work are on-site ($\delta_{i,j}$) and spin-conserving ($\delta_{\alpha,\beta}$). Using these expressions for the matrix elements

[12] In the common literature the amplitude J is included into the hopping matrix t_{ij}. In this work, the separation is chosen to allow for a convenient notation also in the case of the extended Hubbard model presented in Sec. 5.4.

in Eq. (2.2-E9) leads to the full Hubbard Hamiltonian

$$\begin{aligned}\hat{H}(t) &= -J\sum_{i,j}\sum_{\alpha,\beta}\delta_{\langle i,j\rangle}\delta_{\alpha,\beta}\hat{c}^{\dagger}_{i,\alpha}\hat{c}_{j,\beta} + \frac{U}{2}\sum_{i,j,k,l}\sum_{\alpha,\beta,\gamma,\delta}\delta_{i,j}\delta_{i,k}\delta_{i,l}\delta_{\alpha,\gamma}\delta_{\beta,\delta}\hat{c}^{\dagger}_{i,\alpha}\hat{c}^{\dagger}_{j,\beta}\hat{c}_{l,\delta}\hat{c}_{k,\gamma}\bar{\delta}_{\alpha,\beta} \\ &\quad + \sum_{i,j}\sum_{\alpha,\beta} f_{i,\alpha}(t)\delta_{i,j}\delta_{\alpha,\beta}\hat{c}^{\dagger}_{i,\alpha}\hat{c}_{j,\beta} - \mu\sum_{i,j}\sum_{\alpha,\beta}\delta_{i,j}\delta_{\alpha,\beta}\hat{c}^{\dagger}_{i,\alpha}\hat{c}_{j,\beta} \\ &= -J\sum_{\langle i,j\rangle}\sum_{\alpha}\hat{c}^{\dagger}_{i,\alpha}\hat{c}_{j,\alpha} + \frac{U}{2}\sum_{i}\sum_{\alpha\neq\beta}\hat{c}^{\dagger}_{i,\alpha}\hat{c}^{\dagger}_{i,\beta}\hat{c}_{i,\beta}\hat{c}_{i,\alpha} \\ &\quad + \sum_{i}\sum_{\alpha} f_{i,\alpha}(t)\hat{c}^{\dagger}_{i,\alpha}\hat{c}_{i,\alpha} - \mu\sum_{i}\sum_{\alpha}\hat{c}^{\dagger}_{i,\alpha}\hat{c}_{i,\alpha}\,, \end{aligned} \tag{2.3-E2}$$

where $\sum_{\langle i,j\rangle}$ denotes the summation over all neighboring sites i, j. This expression can be further simplified by using

$$\begin{aligned}\sum_{i}\sum_{\alpha\neq\beta}\hat{c}^{\dagger}_{i,\alpha}\hat{c}^{\dagger}_{i,\beta}\hat{c}_{i,\beta}\hat{c}_{i,\alpha} &= \sum_{i}\left\{\hat{c}^{\dagger}_{i,\uparrow}\hat{c}^{\dagger}_{i,\downarrow}\hat{c}_{i,\downarrow}\hat{c}_{i,\uparrow} + \hat{c}^{\dagger}_{i,\downarrow}\hat{c}^{\dagger}_{i,\uparrow}\hat{c}_{i,\uparrow}\hat{c}_{i,\downarrow}\right\} \\ &= 2\sum_{i}\hat{c}^{\dagger}_{i,\uparrow}\hat{c}_{i,\uparrow}\hat{c}^{\dagger}_{i,\downarrow}\hat{c}_{i,\downarrow} = 2\sum_{i}\hat{n}^{\uparrow}_{i}\hat{n}^{\downarrow}_{i}\,, \end{aligned} \tag{2.3-E3}$$

where the last anticommutator relation for fermions in Eq. (2.2-E5) was used. By defining $\hat{n}^{\alpha}_{i} := \hat{c}^{\dagger}_{i,\alpha}\hat{c}_{i,\alpha}$, Eq. (2.3-E2) becomes

$$\hat{H}(t) = -J\sum_{\langle i,j\rangle}\sum_{\alpha}\hat{c}^{\dagger}_{i,\alpha}\hat{c}_{j,\alpha} + U\sum_{i}\hat{n}^{\uparrow}_{i}\hat{n}^{\downarrow}_{i} + \sum_{i}\sum_{\alpha} f_{i,\alpha}(t)\hat{n}^{\alpha}_{i} - \mu\sum_{i}\sum_{\alpha}\hat{n}^{\alpha}_{i}\,, \tag{2.3-E4}$$

which is known as the generalized time dependent Hubbard Hamiltonian. Additionally, as in this work the adiabatic switching method is used to turn on interactions (cf. Secs. 2.2.3 and 3.1.2), the Hamiltonian has to be modified further. By introducing a time-dependent interaction

$$U(t) := f_{\mathrm{AS}}(t)U\,, \tag{2.3-E5}$$

that includes the adiabatic switching function introduced in Eq. (2.2-E21), the final Hubbard Hamiltonian becomes

$$\hat{H}(t) = -J\sum_{\langle i,j\rangle}\sum_{\alpha}\hat{c}^{\dagger}_{i,\alpha}\hat{c}_{j,\alpha} + U(t)\sum_{i}\hat{n}^{\uparrow}_{i}\hat{n}^{\downarrow}_{i} + \sum_{i} f_{i}(t)\hat{n}_{i} - \mu\sum_{i}\hat{n}_{i}\,. \tag{2.3-E6}$$

Here, it was used that all excitations in this work are spin independent, i.e. $f_{i,\alpha}(t) \to f_{i}(t)$. Furthermore, the notation $\hat{n}_{i} = \hat{n}^{\uparrow}_{i} + \hat{n}^{\downarrow}_{i}$ was introduced.

2.3.2 The tight-binding limit

An interesting limiting case of the Hubbard model is the so called tight-binding (TB) limit. As the name suggests, it describes electrons that are tightly bound to their corresponding atom and do not interact with other electrons. This is realized by setting the interaction

parameter to zero, i.e. $U = 0$. For simplicity, we further set $\mu = 0$ and $f_i(t) = 0$. Under these conditions, Eq. (2.3-E6) becomes the tight-binding Hamiltonian

$$\hat{H}_{\mathrm{TB}} = -J \sum_{\langle i,j \rangle} \sum_{\alpha} \hat{c}^{\dagger}_{i,\alpha} \hat{c}_{j,\alpha} \,, \tag{2.3-E7}$$

for which the energy dispersion can be found analytically. In the following, this will be demonstrated for the geometry of the one-dimensional Hubbard chain. In this case, the canonical operators in reciprocal space can be written as [83]

$$\hat{c}^{\dagger}_{i,\sigma} = \frac{1}{N} \sum_{i} \mathrm{e}^{-\mathrm{i}ki} \hat{c}^{\dagger}_{k,\sigma} \,, \tag{2.3-E8}$$

$$\hat{c}_{i,\sigma} = \frac{1}{N} \sum_{i} \mathrm{e}^{\mathrm{i}ki} \hat{c}_{k,\sigma} \,. \tag{2.3-E9}$$

Here, N is the total number of lattice sites and k is the momentum that can take the values $k = \frac{2\pi n}{N} - \pi$ with $n \in \{0, 1, \ldots, N-1\}$, assuming periodic boundary conditions. Inserting those definitions into Eq. (2.3-E7), the Hamiltonian becomes

$$\begin{aligned}
\hat{H}_{\mathrm{TB}} &= -J \sum_{\langle i,j \rangle} \sum_{\sigma} \hat{c}^{\dagger}_{i,\sigma} \hat{c}_{j,\sigma} \\
&= -\frac{J}{N} \sum_{k,k'} \sum_{\langle i,j \rangle} \sum_{\sigma} \mathrm{e}^{-\mathrm{i}ki} \mathrm{e}^{\mathrm{i}k'j} \hat{c}^{\dagger}_{k,\sigma} \hat{c}_{k',\sigma} \\
&= -\frac{J}{N} \sum_{k,k'} \sum_{i} \sum_{\sigma} \mathrm{e}^{-\mathrm{i}ki} \underbrace{\left(\mathrm{e}^{\mathrm{i}k'(i+1)} + \mathrm{e}^{\mathrm{i}k'(i-1)} \right)}_{\mathrm{e}^{\mathrm{i}k'i}\left(\mathrm{e}^{\mathrm{i}k'} + \mathrm{e}^{-\mathrm{i}k}\right)} \hat{c}^{\dagger}_{k,\sigma} \hat{c}_{k',\sigma} \\
&= -J \sum_{k,k'} \sum_{\sigma} \underbrace{\left(\mathrm{e}^{\mathrm{i}k'} + \mathrm{e}^{-\mathrm{i}k'} \right)}_{2\cos(k')} \underbrace{\frac{1}{N} \sum_{i} \mathrm{e}^{-\mathrm{i}i(k-k')}}_{\delta_{k,k'}} \hat{c}^{\dagger}_{k,\sigma} \hat{c}_{k',\sigma} \\
&= -2J \sum_{k} \sum_{\sigma} \cos(k) \hat{c}^{\dagger}_{k,\sigma} \hat{c}_{k,\sigma} = \sum_{k} \sum_{\sigma} \epsilon_k \hat{n}^{\sigma}_{k} \,,
\end{aligned} \tag{2.3-E10}$$

where the energy dispersion relation ϵ_k was introduced as

$$\epsilon_k \coloneqq -2J \cos(k) \,. \tag{2.3-E11}$$

With this expression, the energy bandwidth of the one-dimensional chain in the tight-binding limit can be defined. Since $\cos : [-\pi, \pi) \to [-1, 1]$, the range of possible energies is between $-2J$ and $2J$, resulting in a total bandwidth of $4J$[13]. In Fig. 2.3-F2 an illustration of the one-dimensional Hubbard chain is presented together with the density-of-states (DOS) that results from the energy dispersion given in Eq. (2.3-E11). Additionally, other lattice geometries and their corresponding DOSs and bandwidths are shown.

[13] Note that this is true only for the infinite chain. In finite systems, the coarse sampling of k results in a smaller bandwidth as the extreme values of the cosine function are not reached. This applies to all systems shown in Fig. 2.3-F2.

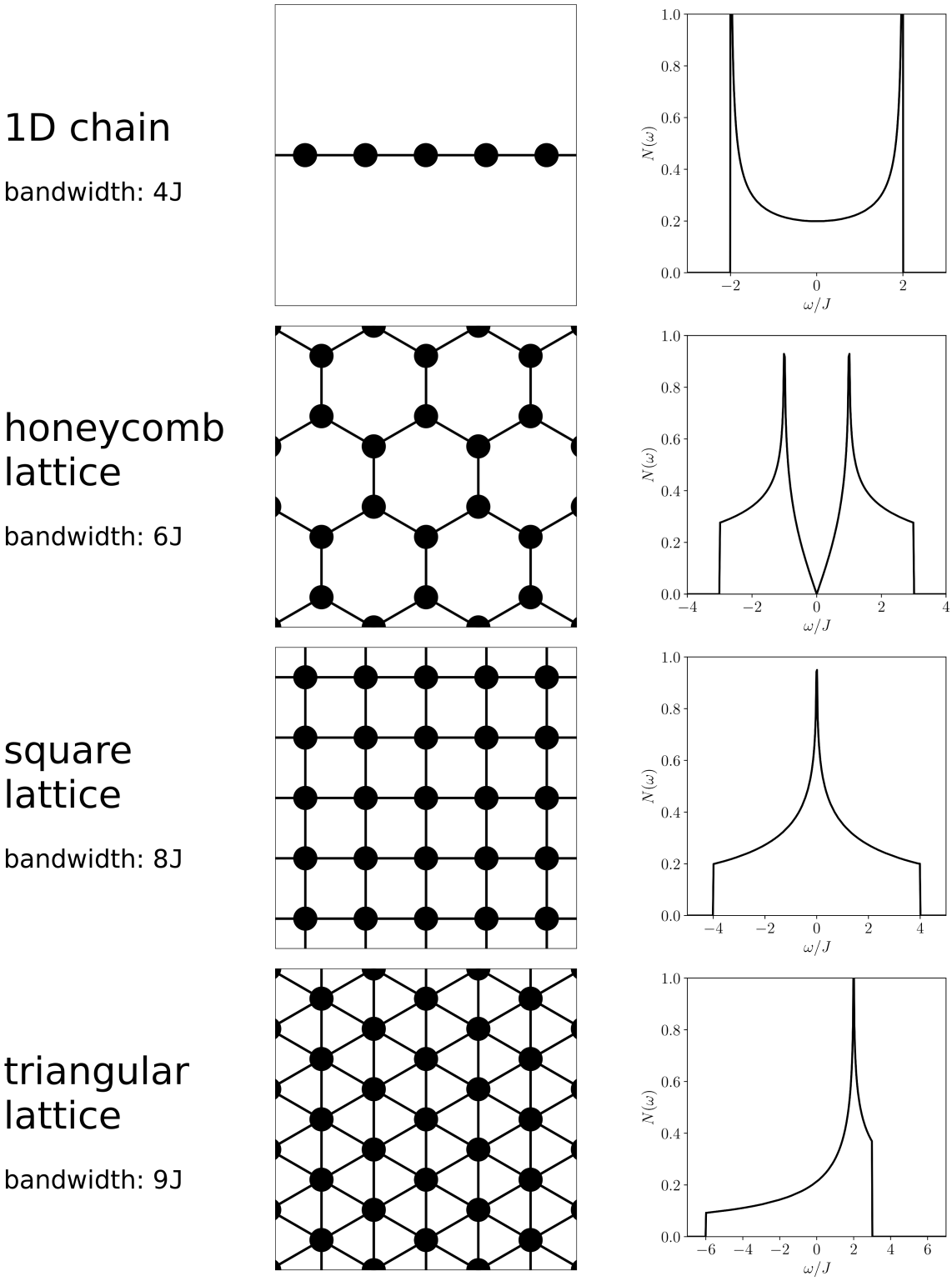

Figure 2.3-F2 – Different lattice geometries for the Hubbard model presented with increasing bandwidth from top to bottom. In the right column, the corresponding density-of-states (DOS) is depicted. The top three lattices show particle-hole symmetry, i.e. $N(\omega) = N(-\omega)$, while the triangular geometry is the only non-bipartite lattice, i.e. $N(\omega) \neq N(-\omega)$ [84]. The honeycomb lattice is the only non-bravais lattice shown here. Instead, it can be understood as a triangular lattice with a two-point basis. Thus, the DOS of the honeycomb lattice loosely resembles two mirrored DOSs of the triangular lattice.

2.3.3 The Hubbard dimer

A system that can be solved analytically due to its sheer simplicity is the Hubbard dimer, a two-site Hubbard chain. It is an interesting system that provides insight into complex effects like the opening of the Mott gap for increasing interaction strength U. Furthermore, as an exactly solvable system it can be used to benchmark approximate approaches like the NEGF.
As an example, the case of half filling ($N = 2$ with $N^{\uparrow} = 1$ and $N^{\downarrow} = 1$) is considered here. Again, we set $\mu = 0$, $f_i(t) = 0$ and $U(t) = U$. In such a system, the possible states are

$$\begin{aligned} |\uparrow,\downarrow\rangle &= \hat{c}^{\dagger}_{2,\downarrow}\hat{c}^{\dagger}_{1,\uparrow}|0\rangle \,, \\ |\downarrow,\uparrow\rangle &= \hat{c}^{\dagger}_{1,\downarrow}\hat{c}^{\dagger}_{2,\uparrow}|0\rangle \,, \\ |\downarrow\uparrow,\cdot\rangle &= \hat{c}^{\dagger}_{1,\downarrow}\hat{c}^{\dagger}_{1,\uparrow}|0\rangle \,, \\ |\cdot,\downarrow\uparrow\rangle &= \hat{c}^{\dagger}_{2,\downarrow}\hat{c}^{\dagger}_{2,\uparrow}|0\rangle \,. \end{aligned} \tag{2.3-E12}$$

In this basis, the Hubbard Hamiltonian of Eq. (2.3-E6) has the form [84]

$$H = \begin{pmatrix} 0 & 0 & -J & -J \\ 0 & 0 & -J & -J \\ -J & -J & U & 0 \\ -J & -J & 0 & U \end{pmatrix} . \tag{2.3-E13}$$

The eigenvalues and corresponding eigenvectors of this 4×4 matrix can calculated by diagonalization:

$$\begin{aligned} E^{\pm} &= \frac{U}{2} \pm \frac{\sqrt{U^2 + 16J^2}}{2} \,, \quad \psi^{\pm} = \left(2 + \frac{1}{2}\left(\frac{E^{\pm}}{J}\right)^2\right)^{-\frac{1}{2}} \begin{pmatrix} \mp 1 \\ \mp 1 \\ \frac{E^{\pm}}{2J} \\ \frac{E^{\pm}}{2J} \end{pmatrix} , \\ E^{0} &= 0 \,, \qquad \psi^{0} = \frac{1}{\sqrt{2}} \begin{pmatrix} -1 \\ 1 \\ 0 \\ 0 \end{pmatrix} , \\ E^{U} &= U \,, \qquad \psi^{U} = \frac{1}{\sqrt{2}} \begin{pmatrix} 0 \\ 0 \\ -1 \\ 1 \end{pmatrix} . \end{aligned} \tag{2.3-E14}$$

The four eigenenergies are depicted in Fig. 2.3-F3 for different values of U. In the tight-binding limit ($U = 0$) the bandwidth of $4J$ corresponds exactly to the value derived in Eq. (2.3-E11) for the one-dimensional chain. For increasing U, however, the bandwidth grows as $E^{-} \to 0$ and $E^{-} \to U$. The two energies E^0 and E^U that are degenerate for

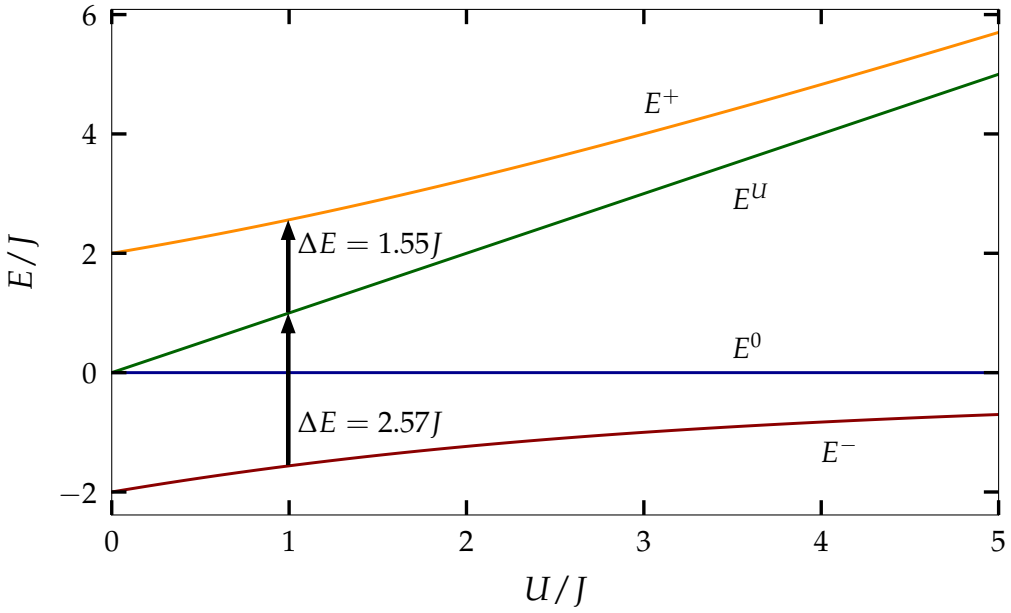

Figure 2.3-F3 – Eigenenergies of the half-filled Hubbard dimer for varying interaction strength U. In the limit $U \to \infty$, $E^- \to E^0 = 0$ and $E^- \to E^U = U$. The two possible dipole excitations from the ground state ψ^- are shown for $U = 1J$.

$U = 0$ move away from each other linearly for increasing interaction. This corresponds to the opening of the Hubbard gap which is crucial for the Mott metal-insulator transition.

As optical laser excitations are an important part of this thesis, the possible optical dipole transitions of the Hubbard dimer will be determined in the following. For this, a dipole moment operator is defined as

$$\hat{d} = -e\hat{r} = -e \begin{pmatrix} 1 & 0 & 0 & 0 \\ 0 & 1 & 0 & 0 \\ 0 & 0 & 0 & 0 \\ 0 & 0 & 0 & 2 \end{pmatrix} , \tag{2.3-E15}$$

where e is the elementary charge. Looking at the ground state ψ^-, one finds that the only possible excitation due to dipole interaction is into the state ψ^U

$$\begin{aligned} \langle \psi^0 | \hat{d} | \psi^- \rangle &= 0 , \\ \langle \psi^U | \hat{d} | \psi^- \rangle &= -e \left(1 + 4 \left(\frac{J}{E^-} \right)^2 \right)^{-\frac{1}{2}} . \\ \langle \psi^+ | \hat{d} | \psi^- \rangle &= 0 . \end{aligned} \tag{2.3-E16}$$

For the state ψ^U one finds that another excitation into the state ψ^+ is possible

$$\langle \psi^+ | \hat{d} | \psi^U \rangle = -e \left(1 + 4 \left(\frac{J}{E^+} \right)^2 \right)^{-\frac{1}{2}} . \tag{2.3-E17}$$

The two possible transitions are shown in Fig. 2.3-F3 at $U = 1J$. Starting at the ground state, the only state that can not be occupied by a dipole excitation is the state ψ^0.

3 Numerical implementation

In the previous section, the Hubbard model and the NEGF approach have been introduced in detail. This part will build on this foundation. First, it will be explained how to generate a non-interacting ground state to start the propagation from and how to perform the adiabatic switching introduced in Sec. 2.2.3. Second, the KBEs and the selfenergies will be expressed in the Hubbard basis which is the form that is used for numerical calculations in practice. Despite the great reduction of computational demands that comes with the choice of the Hubbard model due to a diagonal interaction, it still remains a tremendous numerical task to perform the propagation of the Green functions. Therefore, some numerical improvements in the propagation and integration scheme will be presented, that reduce the computational effort to a manageable amount. In a later section, the numerical implementation of the exact propagation schemes described in Sec. 2.1 is displayed.

3.1 Generation of the initial state

In order to start the propagation of the Green function, first an initial state has to be generated. In Sec. 2.2.3 it has been shown that a correlated initial state can be created by starting from a non-interacting state and adding correlations by using the adiabatic switching method. In the following, first, the generation of a density matrix ρ_0 corresponding to a non-interacting ground state and, later, the numerical realization of the adiabatic switching process will be discussed.

3.1.1 Generation of the non-interacting ground state

The NEGF approach has specific requirements on the underlying ensemble that describes the physical system. On the one hand, the particle number is conserved by all selfenergy approximations considered in Sec. 2.2.5, on the other hand, the canonical operators connect the N-particle space to the $(N \pm 1)$-particle space.
In Sec. 2.2.3 the grand canonical ensemble, which meets these requirements, has been introduced. It is described by the density operator ρ_{GCE} (cf. Eq. (2.2-E12)). The ensemble is determined by the inverse temperature $\beta = (k_{\mathrm{B}}T)^{-1}$ and the chemical potential μ while the particle number is allowed to vary. In order to still describe a system with a certain constant particle number N, one can choose μ in such a way that the average particle number $\langle N \rangle_0$ in the ground state matches the desired N.
In order to find the density matrix ρ_0 that corresponds to the non-interacting ground state of the system, the single particle part $h^{(0)}(t_{\mathrm{s}})$ of the Hamiltonian that occurs in Eq. (2.2-E73) has to be diagonalized. Let B be a matrix that diagonalizes $h^{(0)}(t_{\mathrm{s}})$, then

$$D = B h^0_{ij}(t_{\mathrm{s}}) B^{-1}\,, \tag{3.1-E1}$$

where D is a diagonal matrix which diagonal contains the eigenvalues of $h^{(0)}(t_\mathrm{s})$. Now one can choose μ in such a way that

$$N\left(\beta,\mu,D\right)=\sum_k f(D_{kk}-\mu) \tag{3.1-E2}$$

equals the desired particle number. Here,

$$f\left(D_{kk}-\mu\right)=\frac{1}{\mathrm{e}^{\beta(D_{kk}-\mu)}+1} \tag{3.1-E3}$$

is the Fermi-Dirac distribution. Now, with the matching μ the corresponding density matrix in the Hubbard basis can be calculated by

$$n_{ij}(t_\mathrm{s})=\left[B^{-1}\mathcal{D}(f(D_{11}-\mu),f(D_{22}-\mu),\ldots,f(D_{N_\mathrm{s}N_\mathrm{s}}-\mu))B\right]_{ij}\,. \tag{3.1-E4}$$

Finally, with this initial non-interacting density matrix the Green function can be initialized by (cf. Eq. (2.2-E87))

$$\begin{aligned} G^<_{ij}(t_\mathrm{s},t_\mathrm{s})&=\frac{\mathrm{i}}{\hbar}n_{ij}(t_\mathrm{s})\,,\\ G^>_{ij}(t_\mathrm{s},t_\mathrm{s})&=\frac{\mathrm{i}}{\hbar}\left(n_{ij}(t_\mathrm{s})-\delta_{i,j}\right)\,, \end{aligned} \tag{3.1-E5}$$

which now describes the non-interacting ground state of the system. Starting from this, a Green function that corresponds to an interacting state can be generated using the adiabatic switching method. Numerical details on this are presented in the next section.

3.1.2 Adiabatic switching method

In Sec. 2.2.3 it has been shown that the adiabatic switching method can be used to generate an interacting initial state. This can be done by introducing a time-dependent interaction $U(t)=Uf_\mathrm{AS}(t)$, cf. Eq. (2.3-E5), where $f_\mathrm{AS}(t)$ describes the adiabatic switching. In practice, the switch-on procedure has to be carried out slowly enough to ensure that no additional energy is transferred to the system. Additionally, for numerical reasons it is beneficial if $f_\mathrm{AS}(t)$ is smooth for $\lim_{t\to t_\mathrm{s}} f_\mathrm{AS}(t)=0$ and $\lim_{t\to t_0} f_\mathrm{AS}(t)=1$, i.e. at the start and the end of the switching process. It was found in Ref. [85] that the best choice for $f_\mathrm{AS}(t)$ that fulfills all these requirements is given by

$$\begin{aligned} f^{\tau,t_\mathrm{H}}_\mathrm{AS}(t)=&\exp\left(-\frac{A^\tau_{t_\mathrm{H}}}{t/\left(2t_\mathrm{H}\right)}\exp\left(\frac{B^\tau_{t_\mathrm{H}}}{t/\left(2t_\mathrm{H}\right)-1}\right)\right)\,,\\ B^\tau_{t_\mathrm{H}}:=&\frac{t_\mathrm{H}}{\tau\ln(2)}-\frac{1}{2}\,,\\ A^\tau_{t_\mathrm{H}}:=&\frac{\ln(2)}{2}\mathrm{e}^{2B^\tau_{t_\mathrm{H}}}\,, \end{aligned} \tag{3.1-E6}$$

where $t_\mathrm{H}:=\frac{t_0-t_\mathrm{s}}{2}$ specifies the length of the switching process and τ controls the slope of the function. In Fig. 3.1-F1 the switching function is displayed for different ratios $\frac{\tau}{t_\mathrm{H}}$. In the calculations for this work $\frac{\tau}{t_\mathrm{H}}=\frac{19}{25}$ with $t_\mathrm{H}=12.5$ is used to generate the interacting ground state.

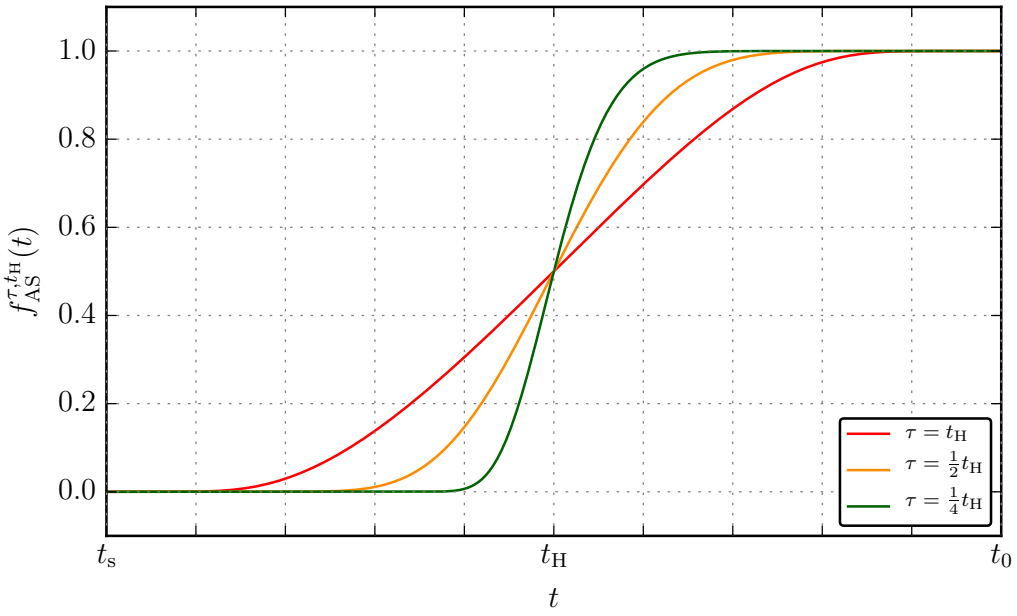

Figure 3.1-F1 – Illustration of the adiabatic switching function (cf. Eq. (3.1-E6)) for $\frac{\tau}{t_{\mathrm{H}}} = 1, \frac{1}{2}, \frac{1}{4}$. For all parameters the function has the limits $\lim_{t\to t_{\mathrm{s}}} f_{\mathrm{AS}}^{\tau,t_{\mathrm{H}}}(t) = 0$ and $\lim_{t\to t_0} f_{\mathrm{AS}}^{\tau,t_{\mathrm{H}}}(t) = 1$ and is asymmetric with respect to t_{H}. The graphic is taken from Ref. [47].

3.2 The time propagation

In this section, the KBEs given in Eqs. (2.2-E73) and (2.2-E74) will be applied to the Hubbard model presented in Sec. 2.3 to result in the equations of motion that are solved to calculate the results presented in Secs. 4 and 6. Additionally, the complete implemented propagation scheme including the calculation of the SOA and GWA selfenergy will be presented here.

3.2.1 Applying the NEGF approach to the Hubbard model

Using the interaction w given by Eq. (2.3-E2), the Hartree–Fock part of the selfenergy (cf. Eq. (2.2-E47)) within the Hubbard model attains the form

$$\begin{aligned}
\Sigma^{\mathrm{HF}}_{ij,\alpha\beta}(z,z') &= -\mathrm{i}\hbar\delta_{\mathcal{C}}(z,z')\sum_{k,l}\sum_{\gamma,\delta}\int_{\mathcal{C}}\mathrm{d}\bar{z}\,U(z)\delta_{\mathcal{C}}(z,\bar{z})\delta_{i,k}\delta_{i,j}\delta_{i,l}\delta_{\alpha,\beta}\delta_{\gamma,\delta}\bar{\delta}_{\alpha,\gamma}G_{lk,\delta\gamma}(\bar{z},\bar{z}^{+}) \\
&\quad +\mathrm{i}\hbar\sum_{k,l}\sum_{\gamma,\delta}U(z)\delta_{\mathcal{C}}(z,z')\delta_{i,k}\delta_{i,l}\delta_{i,j}\delta_{\alpha,\delta}\delta_{\gamma,\beta}\bar{\delta}_{\alpha,\gamma}\delta_{\delta,\gamma}G_{lk,\delta\gamma}(z,z'^{+}) \\
&= -\mathrm{i}\hbar\delta_{\mathcal{C}}(z,z')\delta_{i,j}\delta_{\alpha,\beta}\sum_{\gamma}U(z)\bar{\delta}_{\alpha,\gamma}G_{ii,\gamma\gamma}(z,z^{+}) \\
&\quad +\mathrm{i}\hbar\delta_{\mathcal{C}}(z,z')\delta_{i,j}\underbrace{\bar{\delta}_{\alpha,\beta}\delta_{\alpha,\beta}}_{=0}U(z)G_{ii,\alpha\beta}(z,z'^{+})\,. \qquad (3.2\text{-E1})
\end{aligned}$$

In the last step it is used that the Hubbard Hamiltonian in Eq. (2.3-E6) does not allow for spin flips. This implies that the Green function has to be spin conserving, i.e. $G_{ij,\alpha\beta}(t,t') = G_{ij,\alpha\alpha}(t,t')\delta_{\alpha,\beta}$. Since the same is true for the selfenergy, it is convenient to define

$$G^{\sigma}_{ij}(t,t') \coloneqq G_{ij,\sigma\sigma}(t,t')\,, \tag{3.2-E2}$$

$$\Sigma^{\sigma}_{ij}(t,t') \coloneqq \Sigma_{ij,\sigma\sigma}(t,t')\,. \tag{3.2-E3}$$

As the exchange Fock term in Eq. (3.2-E1) vanishes, one can take advantage of the contour delta and the Kronecker function to incorporate the Hartree–Fock selfenergy into a new effective single-particle Hamiltonian. To do so, one can write Eq. (3.2-E1) as

$$\Sigma^{\mathrm{HF}}_{ij,\alpha\beta}(z,z') = \delta_{\mathcal{C}}(z,z')\delta_{i,j}\delta_{\alpha,\beta}\Sigma^{\mathrm{HF},\alpha}_{i}(z)\,, \tag{3.2-E4}$$

by defining

$$\Sigma^{\mathrm{HF},\uparrow(\downarrow)}_{i}(z) \coloneqq -\mathrm{i}\hbar U(z) G^{\downarrow(\uparrow)}_{ii}(z,z^{+})\,. \tag{3.2-E5}$$

Using Eq. (2.2-E87) and $n^{\sigma}_{i}(t) \coloneqq n^{\sigma}_{ii}(t)$, this can be expressed in real-time space as

$$\Sigma^{\mathrm{HF},\uparrow(\downarrow)}_{i}(t) = U(t) n^{\downarrow(\uparrow)}_{i}(t)\,. \tag{3.2-E6}$$

Looking at Eq. (2.2-E42) and comparing with Eq. (3.2-E4), one finds that one can define an effective single particle Hamiltonian that contains the Hartree(–Fock) contribution of the selfenergy and the excitation $f_i(t)$ for an arbitrary hopping matrix t:

$$\begin{aligned} h^{\mathrm{eff}}_{ij,\alpha\beta}(t) &= -Jt_{ij}\delta_{\alpha,\beta} + \delta_{i,j}\delta_{\alpha,\beta}\sum_{\gamma}\delta_{\alpha,\gamma}\Sigma^{\mathrm{HF},\gamma}_{i}(t) \\ &\quad + \delta_{i,j}\delta_{\alpha,\beta}f_i(t)n_i(t) - \delta_{i,j}\delta_{\alpha,\beta}\mu n_i(t)\,, \end{aligned} \tag{3.2-E7}$$

The equation for one specific spin species is given by

$$h^{\mathrm{eff},\uparrow(\downarrow)}_{ij}(t) = -Jt_{ij} + \delta_{i,j}\Sigma^{\mathrm{HF},\uparrow(\downarrow)}_{i}(t) + \delta_{i,j}f_i(t)n_i(t) - \delta_{i,j}\mu n_i(t)\,. \tag{3.2-E8}$$

With this effective single-particle Hamiltonian, the KBEs in Eqs. (2.2-E73) and (2.2-E74) can be written as

$$\begin{aligned} &\sum_{l}\left[\mathrm{i}\hbar\frac{\mathrm{d}}{\mathrm{d}t}\delta_{i,l} - h^{\mathrm{eff},\sigma}_{il}(t)\right]G^{\sigma,\gtrless}_{lj}(t,t') = \\ &\qquad \sum_{l}\int_{t_{\mathrm{s}}}^{\infty}\mathrm{d}\bar{t}\left\{\Sigma^{\sigma,\mathrm{R}}_{il}(t,\bar{t})G^{\sigma,\gtrless}_{lj}(\bar{t},t') + \Sigma^{\sigma,\gtrless}_{il}(t,\bar{t})G^{\sigma,\mathrm{A}}_{lj}(\bar{t},t')\right\}, \end{aligned} \tag{3.2-E9}$$

$$\begin{aligned} &\sum_{l}G^{\sigma,\gtrless}_{il}(t,t')\left[-\mathrm{i}\hbar\frac{\overleftarrow{\mathrm{d}}}{\mathrm{d}t'}\delta_{l,j} - h^{\mathrm{eff},\sigma}_{lj}(t')\right] = \\ &\qquad \sum_{l}\int_{t_{\mathrm{s}}}^{\infty}\mathrm{d}\bar{t}\left\{G^{\sigma,\mathrm{R}}_{il}(t,\bar{t})\Sigma^{\sigma,\gtrless}_{lj}(\bar{t},t') + G^{\sigma,\gtrless}_{il}(t,\bar{t})\Sigma^{\sigma,\mathrm{A}}_{lj}(\bar{t},t')\right\}, \end{aligned} \tag{3.2-E10}$$

where the selfenergy Σ is redefined as the correlation part $\Sigma \coloneqq \Sigma^{\mathrm{corr}}$ (cf. Eq. (2.2-E44)) since the Hartree–Fock contribution is already considered inside h^{eff}.

Looking at the above form of the KBEs, it is apparent that both equations show no preference with respect to the spin orientation σ. Likewise, the Hubbard Hamiltonian in Eq. (2.3-E6) does not provide any special treatment for a specific type of spin either. Thus, a spin-symmetric initial state will preserve this symmetry for all times and positions, i.e.

$$G_{ij}^{\uparrow,\gtrless}(t,t') = G_{ij}^{\downarrow,\gtrless}(t,t') \quad \forall i,j,t,t' \,. \tag{3.2-E11}$$

Since in this work only systems with spin symmetry are considered, this features can be used to further simplify the equations of motion by neglecting the spin indices and define

$$G_{ij}^{\gtrless}(t,t') \coloneqq G_{ij}^{\uparrow,\gtrless}(t,t') = G_{ij}^{\downarrow,\gtrless}(t,t') \,, \tag{3.2-E12}$$

which also applies for all other quantities like the selfenergy.

3.2.2 The propagation scheme

In order to get access to the full single-particle information of the system, it is necessary to obtain $G^{>}(t,t')$ and $G^{<}(t,t')$ in the complete (t,t')-plane. However, due to Eq. (2.2-E70), $G_{ij}^{\lessgtr}(t,t') = -\left[G_{ji}^{\lessgtr}(t',t)\right]^{*}$, it is sufficient to calculate them only in one half-plane, i.e. each of the two KBEs (Eqs. (3.2-E9) and (3.2-E10)) has to be solved for only one real-time component. In this work, the following equations are used:

$$\sum_l \left[\mathrm{i}\hbar\frac{\mathrm{d}}{\mathrm{d}t}\delta_{i,l} - h_{il}^{\mathrm{eff}}(t)\right] G_{lj}^{>}(t,t') = I_{ij}^{(1),>}(t,t') \,, \tag{3.2-E13}$$

$$\sum_l G_{il}^{<}(t,t') \left[-\mathrm{i}\hbar\frac{\overleftarrow{\mathrm{d}}}{\mathrm{d}t'}\delta_{l,j} - h_{lj}^{\mathrm{eff}}(t')\right] = I_{ij}^{(2),<}(t,t') \,, \tag{3.2-E14}$$

where on the right-hand side the collision integrals $I^{(1),>}$ and $I^{(2),<}$ are introduced. They are defined as

$$\begin{aligned} I_{ij}^{(1),>}(t,t') &\coloneqq \sum_l \int_{t_\mathrm{s}}^{\infty} \mathrm{d}\bar{t} \left\{\Sigma_{il}^{\mathrm{R}}(t,\bar{t})G_{lj}^{>}(\bar{t},t') + \Sigma_{il}^{>}(t,\bar{t})G_{lj}^{\mathrm{A}}(\bar{t},t')\right\} , \\ I_{ij}^{(2),<}(t,t') &\coloneqq \sum_l \int_{t_\mathrm{s}}^{\infty} \mathrm{d}\bar{t} \left\{G_{il}^{\mathrm{R}}(t,\bar{t})\Sigma_{lj}^{<}(\bar{t},t') + G_{il}^{<}(t,\bar{t})\Sigma_{lj}^{\mathrm{A}}(\bar{t},t')\right\} . \end{aligned} \tag{3.2-E15}$$

This way, $G^{<}(t,t')$ is propagated above and $G^{>}(t,t')$ below the time diagonal. For $t = t'$ either one of them can be calculated while the other one can be accessed by the symmetry relation on the time diagonal, Eq. (2.2-E72). Likewise, the collision integral $I^{(1),>}(t,t')$ has to be calculated only for $t > t'$ (denoted by $I^{(1),>}(t > t')$) and $I^{(2),<}(t,t')$ for $t < t'$ (denoted by $I^{(2),<}(t < t')$). On the time-diagonal, the same relation as for the Green function applies. This results in three equations of motion for the full two-time propagation

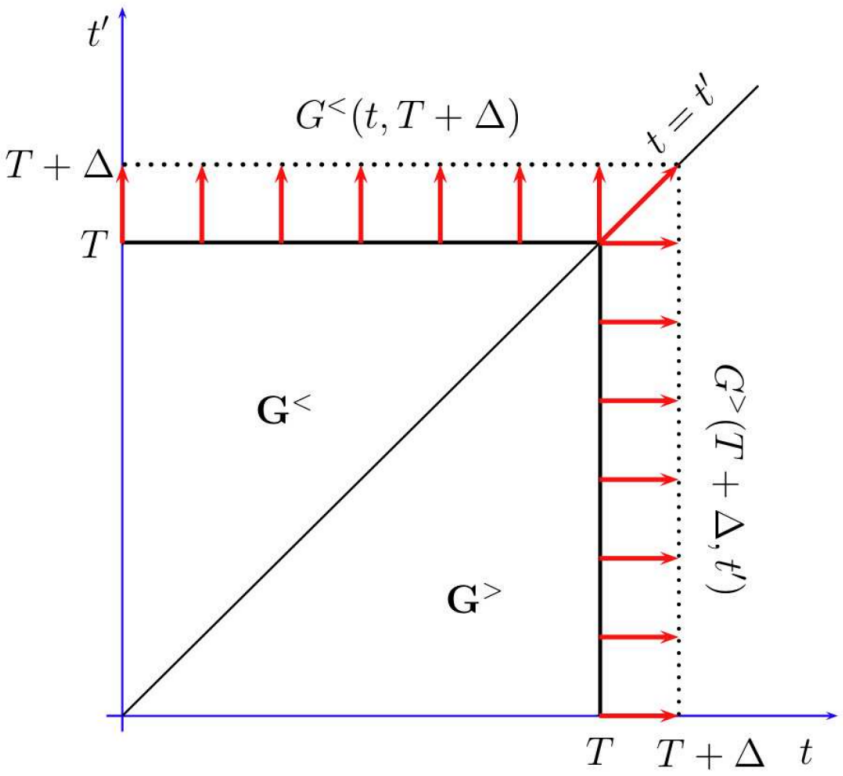

Figure 3.2-F1 – Illustration of the propagation scheme of the real-time components of the Green function. $G^>$ is propagated on the lower half-plane according to Eq. (3.2-E16) while the propagation on the upper half corresponds to $G^<$ and Eq. (3.2-E17). The time-diagonal is described by Eq. (3.2-E18). The graphic is taken from Ref. [86].

of the real-time components of the Green function:

$$\mathrm{i}\hbar\frac{\mathrm{d}}{\mathrm{d}t}G^>_{ij}(t \geq t') = \sum_l h^{\mathrm{eff}}_{il}(t)G^>_{lj}(t \geq t') + I^{(1),>}_{ij}(t \geq t')\,, \tag{3.2-E16}$$

$$-\mathrm{i}\hbar\frac{\mathrm{d}}{\mathrm{d}t'}G^<_{ij}(t \leq t') = \sum_l G^<_{il}(t \leq t')h^{\mathrm{eff}}_{lj}(t') + I^{(2),<}_{ij}(t \leq t')\,, \tag{3.2-E17}$$

$$\mathrm{i}\hbar\frac{\mathrm{d}}{\mathrm{d}t}G^<_{ij}(t,t) = \Big[h^{\mathrm{eff}}(t)G^<(t,t)\Big]_{ij} + I^{(1),>}_{ij}(t,t) - I^{(2),<}_{ij}(t,t)\,. \tag{3.2-E18}$$

An illustration of this propagation scheme is shown in Fig. 3.2-F1. When using the GKBA introduced in Sec. 2.2.7 the propagation along the diagonal stays the same. However, in Eqs. (3.2-E16) and (3.2-E17) the collision integral vanishes due to the Hartree–Fock nature of the propagators defined in Eq. (2.2-E85). Thus, the resulting equations of motion for the off-diagonal propagation in the GKBA approximation have the form

$$\mathrm{i}\hbar\frac{\mathrm{d}}{\mathrm{d}t}G^>_{ij}(t \geq t') = \sum_l h^{\mathrm{eff}}_{il}(t)G^>_{lj}(t \geq t')\,, \tag{3.2-E19}$$

$$-\mathrm{i}\hbar\frac{\mathrm{d}}{\mathrm{d}t'}G^<_{ij}(t \leq t') = \sum_l G^<_{il}(t \leq t')h^{\mathrm{eff}}_{lj}(t')\,. \tag{3.2-E20}$$

In order to solve these equations of motion, the collision integrals that appear in Eq. (3.2-E16) to Eq. (3.2-E20) have to be expressed in terms of $G^<(t<t')$ and $G^>(t>t')$. Using the definition of the advanced and retarded Green function and selfenergy (cf. Eq. (2.2-E66)) one arrives, after some calculations, at the following expressions for the collision integrals at a given time step T:

$$\begin{aligned} I_{ij}^{(1),>}(T>t') &= \int_{t_\mathrm{s}}^{t'} \mathrm{d}\bar{t} \sum_k \left\{ \Sigma_{ik}^>(T>\bar{t}) G_{kj}^<(\bar{t}<t') - \left(\Sigma_{ki}^<(\bar{t}<T) G_{jk}^>(t'>\bar{t})\right)^* \right\} \\ &\quad + \int_{t'}^{T} \mathrm{d}\bar{t} \sum_k \left\{ \Sigma_{ik}^>(T>\bar{t}) G_{kj}^>(\bar{t}>t') + \left(\Sigma_{ki}^<(\bar{t}<T)\right)^* G_{kj}^>(\bar{t}>t') \right\}, \\ I_{ij}^{(2),<}(t<T) &= \int_{t_\mathrm{s}}^{t} \mathrm{d}\bar{t} \sum_k \left\{ G_{ik}^>(t>\bar{t}) \Sigma_{kj}^<(\bar{t}<T) - \left(G_{ki}^<(\bar{t}<t) \Sigma_{jk}^>(T>\bar{t})\right)^* \right\} \\ &\quad + \int_{t}^{T} \mathrm{d}\bar{t} \sum_k \left\{ G_{ik}^<(t<\bar{t}) \Sigma_{kj}^<(\bar{t}<T) + G_{ik}^<(t<\bar{t}) \left(\Sigma_{jk}^>(T>\bar{t})\right)^* \right\}, \end{aligned} \tag{3.2-E21}$$

for the off-diagonal elements and

$$\begin{aligned} I_{ij}^{(1),>}(T,T) &= \int_{t_\mathrm{s}}^{T} \mathrm{d}\bar{t} \sum_k \left\{ \Sigma_{ik}^>(T>\bar{t}) G_{kj}^<(\bar{t}<T) - \left(\Sigma_{ki}^<(\bar{t}<T) G_{jk}^>(T>\bar{t})\right)^* \right\}, \\ I_{ij}^{(2),<}(T,T) &= \int_{t_\mathrm{s}}^{T} \mathrm{d}\bar{t} \sum_k \left\{ G_{ik}^>(T>\bar{t}) \Sigma_{kj}^<(\bar{t}<T) - \left(G_{ki}^<(\bar{t}<T) \Sigma_{jk}^>(T>\bar{t})\right)^* \right\} \\ &= -\left(I_{ji}^{(1),>}(T,T)\right)^*, \end{aligned} \tag{3.2-E22}$$

for the time diagonal. These equation do only depend on $G^<(t<t')$, $G^>(t>t')$, $\Sigma^<(t<t')$ and $\Sigma^>(t>t')$. Therefore, if it is possible to express the selfenergy in terms of the less and greater component of the Green function, the propagation is closed.

In the following, expressions for the SOA and GWA selfenergy that have been introduced for an arbitrary basis in Sec. 2.2.5.2 will be presented, since both are used frequently in the scope of this work[14]. The most simple selfenergy approximation beyond the Hartree–Fock level is the SOA. The less and greater components in the Hubbard basis are given by[15]

$$\begin{aligned} \Sigma_{ij}^{\mathrm{SOA},>}(T>t') &= \hbar^2 U(T) U(t') G_{ij}^>(T>t') G_{ij}^>(T>t') G_{ji}^<(t'<T) \\ &= \hbar^2 U(T) U(t') G_{ij}^>(T>t') G_{ji}^{\mathrm{F},<}(t'<T), \\ \Sigma_{ij}^{\mathrm{SOA},<}(t<T) &= \hbar^2 U(t) U(T) G_{ij}^<(t<T) G_{ij}^<(t<T) G_{ji}^>(T>t) \\ &= \hbar^2 U(t) U(T) G_{ij}^<(t<T) G_{ij}^{\mathrm{F},<}(t<T). \end{aligned} \tag{3.2-E23}$$

where the real-time components of the two-particle Fock-like Green function (cf. Eq. (2.2-E50)) are introduced that are defined as

$$G_{ij}^{\mathrm{F},\gtrless}(t \gtrless t') = G_{ij}^{\gtrless}(t \gtrless t') G_{ji}^{\lessgtr}(t' \lessgtr t). \tag{3.2-E24}$$

[14] Mind that, again, the selfenergies shown here only contain the correlation part of the total selfenergy. The HF part is included in the effective Hamiltonian h^{eff}.

[15] Σ^{SOA} can also be expressed in terms of the Hartree-like Green function G^{H}. The following description in terms of G^{F} is chosen to compare with the GWA selfenergy.

From a numerical point of view the SOA selfenergy is easy to calculate since no integration over a time argument has to be performed.
A more sophisticated selfenergy approximation is the GWA. However, as explained in Sec. 2.2.5.2, it is an resummation approach that contains contributions up to infinite order of the interaction. Therefore, it is a lot more challenging than the SOA from a numerical perspective. The real-time components of the GWA selfenergy are given by

$$\begin{aligned} \Sigma_{ij}^{\mathrm{GWA},>}(T > t') &= \mathrm{i}\hbar W_{ji}^{<,\uparrow\uparrow}(t' < T) G_{ij}^{>}(T > t')\,, \\ \Sigma_{ij}^{\mathrm{GWA},<}(t < T) &= \mathrm{i}\hbar W_{ij}^{<,\uparrow\uparrow}(t < T) G_{ij}^{<}(t < T)\,. \end{aligned} \tag{3.2-E25}$$

The less component of the same-spin screened interaction $W^{<,\uparrow\uparrow}$ has to be calculated in an iterative manner. For this, it is convenient to define the retarded and advanced component of the two-particle Fock-like Green function

$$G_{ij}^{\mathrm{F,R}}(t > t') = G_{ij}^{>}(t > t') G_{ji}^{<}(t' < t) - \left(G_{ji}^{<}(t' < t)\right)^* \left(G_{ij}^{>}(t > t')\right)^*\,, \tag{3.2-E26}$$

$$G_{ij}^{\mathrm{F,A}}(t < t') = G_{ij}^{<}(t < t') G_{ji}^{>}(t' > t) - \left(G_{ji}^{>}(t' > t)\right)^* \left(G_{ij}^{<}(t < t')\right)^*\,. \tag{3.2-E27}$$

Now, the same-spin screened interaction is given by

$$\begin{aligned} W_{ij}^{<,\uparrow\uparrow}(t < T) = &- \mathrm{i}\hbar U(t) G_{ij}^{\mathrm{F},<}(t < T) U(T) \\ &- \mathrm{i}\hbar U(t) \sum_k \int_{t_\mathrm{s}}^{t} \mathrm{d}\bar{t}\, G_{ik}^{\mathrm{F,R}}(t > \bar{t}) W_{kj}^{<,\uparrow\downarrow}(\bar{t} < T) \\ &- \mathrm{i}\hbar U(t) \sum_k \int_{t_\mathrm{s}}^{t} \mathrm{d}\bar{t}\, \left(G_{ki}^{\mathrm{F},<}(\bar{t} < t)\right)^* W_{kj}^{\mathrm{A},\uparrow\downarrow}(\bar{t} < T) \\ &- \mathrm{i}\hbar U(t) \sum_k \int_{t}^{T} \mathrm{d}\bar{t}\, G_{ik}^{\mathrm{F},<}(t < \bar{t}) W_{kj}^{\mathrm{A},\uparrow\downarrow}(\bar{t} < T)\,. \end{aligned} \tag{3.2-E28}$$

It depends on the different-spin screened interaction

$$\begin{aligned} W_{ij}^{<,\uparrow\downarrow}(t < T) = &- \mathrm{i}\hbar U(t) G_{ij}^{\mathrm{F},<}(t < T) U(T) \\ &- \mathrm{i}\hbar U(t) \sum_k \int_{t_\mathrm{s}}^{t} \mathrm{d}\bar{t}\, G_{ik}^{\mathrm{F,R}}(t > \bar{t}) W_{kj}^{<,\uparrow\uparrow}(\bar{t} < T) \\ &- \mathrm{i}\hbar U(t) \sum_k \int_{t_\mathrm{s}}^{t} \mathrm{d}\bar{t}\, \left(G_{ki}^{\mathrm{F},<}(\bar{t} < t)\right)^* W_{kj}^{\mathrm{A},\uparrow\uparrow}(\bar{t} < T) \\ &- \mathrm{i}\hbar U(t) \sum_k \int_{t}^{T} \mathrm{d}\bar{t}\, G_{ik}^{\mathrm{F},<}(t < \bar{t}) W_{kj}^{\mathrm{A},\uparrow\uparrow}(\bar{t} < T)\,, \end{aligned} \tag{3.2-E29}$$

that, again, contains the same-spin screened interaction $W^{<,\uparrow\uparrow}$. Additionally, these two coupled equations depend on the advanced components of the same- and different-spin screened interaction that are given by

$$\begin{aligned} W_{ij}^{\mathrm{A},\uparrow\uparrow}(t < T) &= -\mathrm{i}\hbar U(t) G_{ij}^{\mathrm{F,A}}(t < T) U(T) \\ &\quad + \mathrm{i}\hbar U(t) \sum_k \int_{t}^{T} \mathrm{d}\bar{t}\, G_{ik}^{\mathrm{F,A}}(t < \bar{t}) W_{kj}^{\mathrm{A},\uparrow\downarrow}(\bar{t} < T)\,, \end{aligned} \tag{3.2-E30}$$

$$W_{ij}^{\mathrm{A},\uparrow\downarrow}(t < T) = \mathrm{i}\hbar U(t) \sum_k \int_{t}^{T} \mathrm{d}\bar{t}\, G_{ik}^{\mathrm{F,A}}(t < \bar{t}) W_{kj}^{\mathrm{A},\uparrow\uparrow}(\bar{t} < T)\,. \tag{3.2-E31}$$

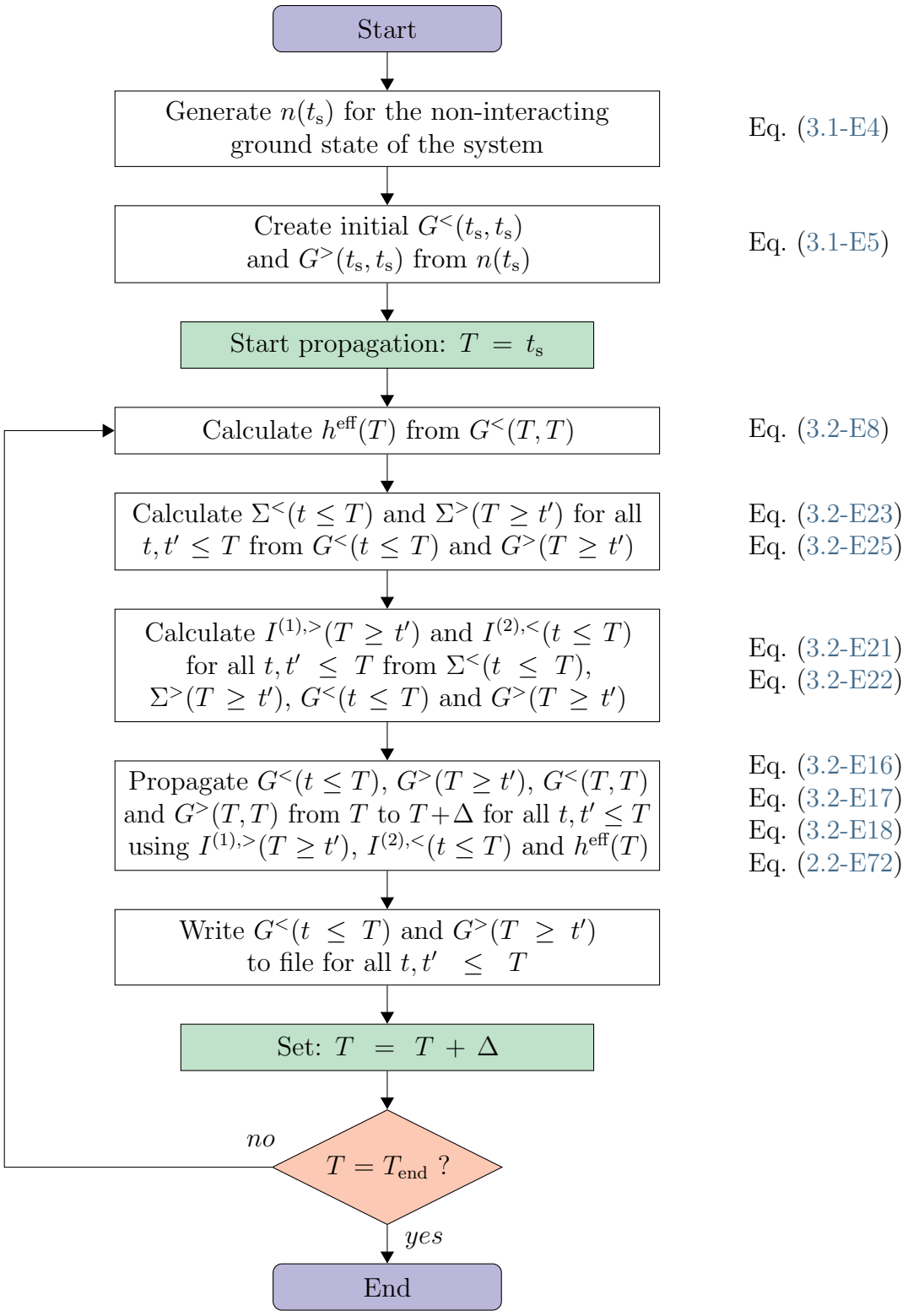

Figure 3.2-F2 – Illustration of the propagation scheme used in this work to propagate the real-time components of the Green function on the two-time plane depicted in Fig. 3.2-F1.

In order to solve this system of coupled equations numerically, first, the two advanced components of the screened interaction can be calculated. On the time diagonal a solution can be immediately found for both:

$$W_{ij}^{\mathrm{A},\uparrow\uparrow}(T,T) = -\mathrm{i}\hbar U(t) G_{ij}^{\mathrm{F,A}}(t<T) U(T)\,, \tag{3.2-E32}$$

$$W_{ij}^{\mathrm{A},\uparrow\downarrow}(T,T) = 0, \tag{3.2-E33}$$

Next, Eqs. (3.2-E30) and (3.2-E31) can be solved simultaneously in an iterative way for every time t starting from the diagonal. After that, Eqs. (3.2-E28) and (3.2-E29) can be iterated until convergence for every time step t, this time starting at t_s. This way, the less and greater component of the GWA selfenergy can be computed according to Eq. (3.2-E25). A detailed derivation of these equations and the corresponding expressions for other selfenergies can be found in Ref. [57].

With the selfenergies given in Eqs. (3.2-E23) and (3.2-E25) the propagation scheme for the real-time components of the Green function is closed. First, the density matrix $n(t_\mathrm{s})$ that corresponds to the non-interacting ground state of the system at the time t_s is generated using Eq. (3.1-E4). With this density matrix the less and greater components of the Green functions can be initialized as shown in Eq. (3.1-E5). At this point the propagation starts. For a given time step T, first, the effective single-particle Hamiltonian h^eff (cf. Eq. (3.2-E8)) and the chosen selfenergy (cf. Eqs. (3.2-E23) and (3.2-E25)) can be calculated from the Green functions. Now all quantities are known to determine the collision integrals $I^{(1),>}$ and $I^{(2),<}$ via Eqs. (3.2-E21) and (3.2-E22). Next, the components of the Green function can be propagated one time step further to $T+\Delta$ using Eq. (3.2-E16) to Eq. (3.2-E18), where Δ is the time step size. Finally, the newly generated Green function can be written to a file and the propagation of the next time step begins. A vivid illustration of this propagation scheme is depicted in Fig. 3.2-F2.

3.3 Numerical improvements

Although the use of the Hubbard model greatly reduces the numerical demands of propagating the KBEs, the solution of the propagation scheme presented in the previous section still remains to be a challenging task. Thus, in order to handle large systems and long propagation times that are needed for the systems investigated in this work, it is essential to optimize the whole process of propagation in the best way possible. Taking a closer look at the propagation scheme, it becomes apparent that there are three main aspects that critically influence the performance of the propagation and, thus, have to be addressed. First, the equations of motion (cf. Eq. (3.2-E16) to Eq. (3.2-E18)) have to be propagated using an efficient algorithm. Second, the calculation of the time integrals appearing in the collision integrals and the GWA selfenergy has to be done accurately. And third, the matrix multiplications that are part of almost every equation in the propagation scheme have to be optimized.
This section will feature all numerical improvements that were implemented in the scope of this work and which made the calculations for the results of this thesis possible in the first place.

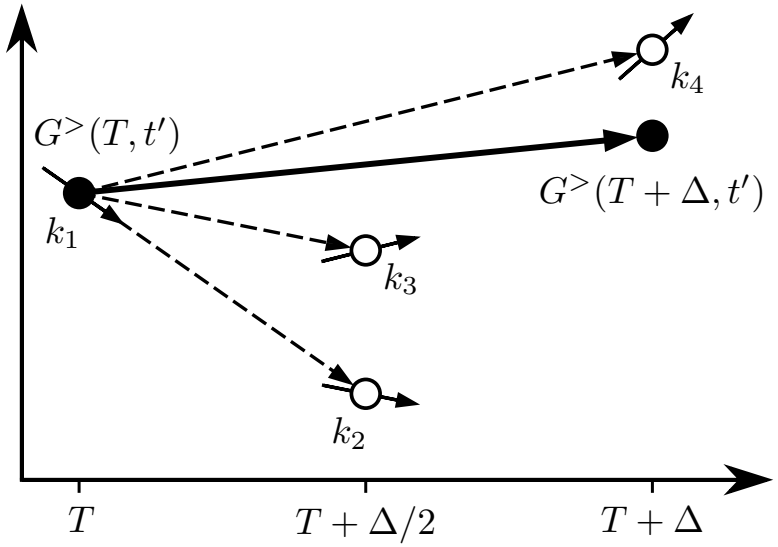

Figure 3.3-F1 – Illustration of the forth-order Runge–Kutta method (RK4). The propagation of $G^>$ is described by Eq. (3.3-E2). For each propagation step four additional intermediate time steps have to be calculated to obtain the slopes $k_1, \ldots, k_4$.

3.3.1 Propagation algorithms

There are a lot of different numerical procedures to solve ordinary differential equations [87]. The most simple first-order approach is the so-called Euler method which results in the following expression for the propagation of $G^>$[16]:

$$G^>_{ij}(T+\Delta \geq t') \;=\; G^>_{ij}(T \geq t') + \Delta \cdot \frac{\mathrm{d}}{\mathrm{d}t} G^>_{ij}(t \geq t')\Big|_{t=T,\, G^>_{ij}(t\geq t')=G^>_{ij}(T\geq t')} \tag{3.3-E1}$$

where the second term on the right-hand side can be understood as the derivative of $G^>$ at time t. The expression $t = T$ denotes that the explicitly time dependent terms like an external potential should be evaluated at the time T and $G^>_{ij}(t \geq t') = G^>_{ij}(T \geq t')$ reveals at which time $G^>$ has to be used in the right hand side of Eq. (3.2-E16). The advantage of this separate notation will become evident shortly. As a first order procedure the Euler method has a local error term of $\mathcal{O}(\Delta^2)$. Therefore, it does not meet the high requirements for a propagation method that is suitable for long propagation times.
A more sophisticated approach is the forth-order Runge–Kutta method (RK4) [88]. It requires the evaluation of four additional intermediate time steps for each propagation step. However, this is rewarded by a local error term of $\mathcal{O}(\Delta^5)$. In this method the greater Green function at the time $T + \Delta$ is given by

$$G^>_{ij}(T+\Delta \geq t') \;=\; G^>_{ij}(T \geq t') + \frac{\Delta}{6}\left(k_{ij,1} + 2k_{ij,2} + 2k_{ij,3} + k_{ij,4}\right), \tag{3.3-E2}$$

[16] The focus of this part lies on the equation of motion for $G^>$, i.e. Eq. (3.2-E16). However, all results also apply for the propagation of $G^<$.

where the slopes $k_{ij,1}, \ldots, k_{ij,4}$ are given by

$$\begin{aligned}
k_{ij,1} &= \frac{\mathrm{d}}{\mathrm{d}t} G^{>}_{ij}(t \geq t') \Big|_{t=T,\, G^{>}_{ij}(t\geq t')=G^{>}_{ij}(T\geq t')}, \\
k_{ij,2} &= \frac{\mathrm{d}}{\mathrm{d}t} G^{>}_{ij}(t \geq t') \Big|_{t=T+\frac{\Delta}{2},\, G^{>}_{ij}(t\geq t')=G^{>}_{ij}(T\geq t')+\frac{\Delta}{2}k_{ij,1}}, \\
k_{ij,3} &= \frac{\mathrm{d}}{\mathrm{d}t} G^{>}_{ij}(t \geq t') \Big|_{t=T+\frac{\Delta}{2},\, G^{>}_{ij}(t\geq t')=G^{>}_{ij}(T\geq t')+\frac{\Delta}{2}k_{ij,2}}, \\
k_{ij,4} &= \frac{\mathrm{d}}{\mathrm{d}t} G^{>}_{ij}(t \geq t') \Big|_{t=T+\Delta,\, G^{>}_{ij}(t\geq t')=G^{>}_{ij}(T\geq t')+\Delta k_{ij,3}}.
\end{aligned} \tag{3.3-E3}$$

An illustration of the procedure is shown in Fig. 3.3-F1. The first step to calculate $k_{ij,1}$ is the same as in the Euler method. After that the remaining slopes are calculated consecutively as depicted in Fig. 3.3-F1. Here, the above introduced notation is advantageous. For the calculation of $k_{ij,2}$ and $k_{ij,3}$, for instance, the derivative is taken at the same explicit time but for different Green functions. After the slopes at all four intermediate time steps are determined $G^{>}$ can be propagated by Eq. (3.3-E2).
In Figs. 3.3-F2 and 3.3-F3 the quality of both presented procedures, the Euler and the RK4 method, is directly compared. Fig. 3.3-F2 shows the oscillating density on a single site of a Hubbard dimer after an instantaneous excitation at $t = 0$ within the HF approximation. In such a system the amplitude of the oscillation should be constant like in the case of RK4 [89]. The Euler method, however, shows a significant deviation for the same time step size.
The same observation can be made in Fig. 3.3-F3. Here, the total energy of the same system after the instantaneous excitation is shown. As the HF selfenergy approximation is conserving, the total energy should be constant. Again, the RK4 method shows a far better result than Euler.

It is important to note that the RK4 method becomes unstable when h^{eff} attains very high values due to strong excitations [86]. In this case, one can define two propagators $\mathcal{U}$ and $\mathcal{V}$ that include the effective single-particle Hamiltonian:

$$\mathcal{U}_{ij}(T) := \left[\exp\left(-\frac{\mathrm{i}}{\hbar} h^{\mathrm{eff}}(T)\Delta\right)\right]_{ij}, \tag{3.3-E4}$$

$$\mathcal{V}_{ij}(T) := \left[\left(h^{\mathrm{eff}}(T)\right)^{-1}\left(\mathbb{1} - \exp\left(-\frac{\mathrm{i}}{\hbar} h^{\mathrm{eff}}(T)\Delta\right)\right)\right]_{ij}. \tag{3.3-E5}$$

With these, the three equations of motion in Eq. (3.2-E16) to Eq. (3.2-E18) can be transformed to

$$G^{<}_{ij}(t \leq T+\Delta) = \sum_l \left\{ G^{<}_{il}(t \leq T)\mathcal{U}^{*}_{jl}(T) - I^{(1),<}_{il}(t \leq T)\mathcal{V}^{*}_{jl}(T) \right\}, \tag{3.3-E6}$$

$$G^{>}_{ij}(T+\Delta \geq t') = \sum_l \left\{ \mathcal{U}_{il}(T) G^{>}_{lj}(T \geq t') - \mathcal{V}_{il}(T) I^{(2),>}_{lj}(T \geq t') \right\}, \tag{3.3-E7}$$

$$G^{<}_{ij}(T+\Delta, T+\Delta) = \sum_{lm} \left\{ \mathcal{U}_{il}(T) \Big[G^{<}_{lm}(T, T) + \mathcal{W}_{lm}(T) \Big] \mathcal{U}^{*}_{jm}(T) \right\}, \tag{3.3-E8}$$

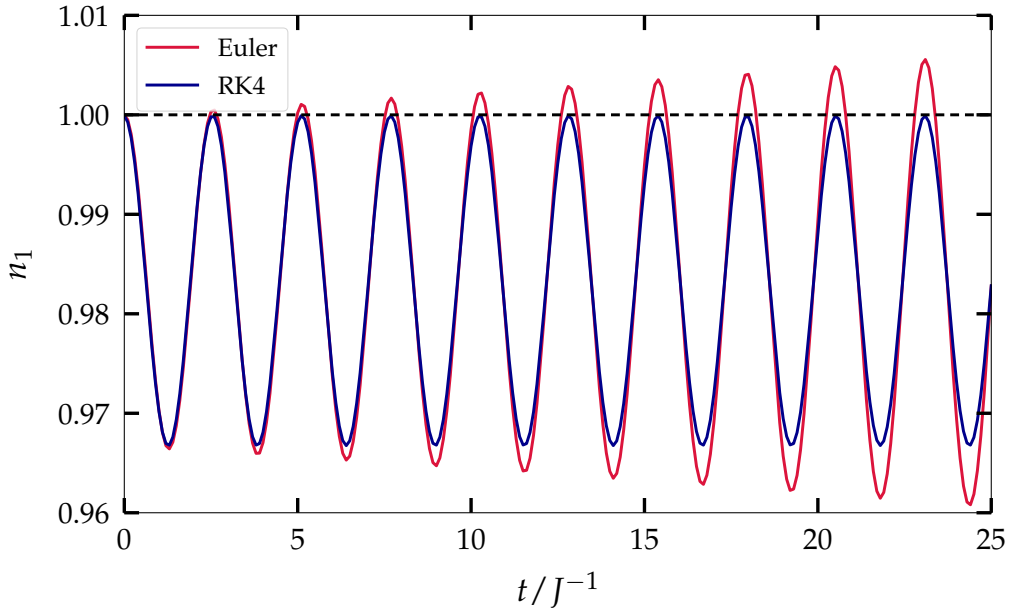

Figure 3.3-F2 – Density on a single site of a Hubbard dimer after an instantaneous excitation at $t = 0$. The amplitude of the oscillation should remain constant over the complete propagation. The Euler method shows huge deviations from the correct result while the RK4 method is in very good agreement. Both calculations are performed within the HF approximation and for the same time step size of $\Delta = 0.025 J^{-1}$. The interaction is set to $U = 1J$.

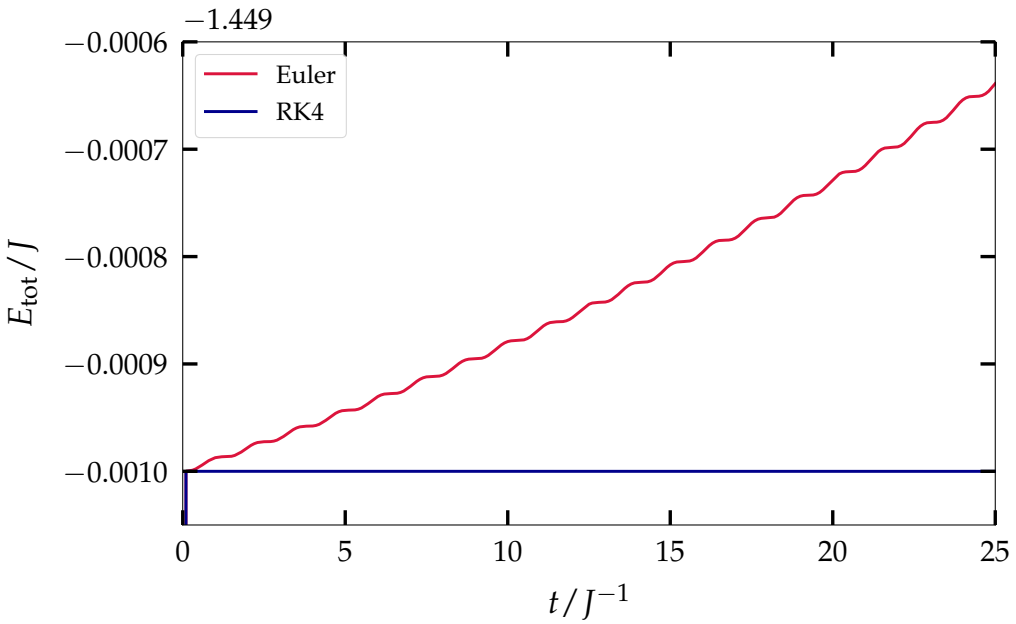

Figure 3.3-F3 – Total energy of a one-dimensional chain after an instantaneous excitation at $t = 0$. The calculations are performed for the same system and parameters as in Fig. 3.3-F2. Thus, the total energy should be constant. The RK4 method shows a better conservation of energy than the Euler method for the same time step size.

where

$$\begin{aligned} \mathcal{W}_{lm}(T) &:= \sum_{n=0}^{\infty} w_{lm}^{(n)}(T)\,, \\ w_{lm}^{(n)}(T) &:= \frac{\mathrm{i}\Delta}{n+1}\left[\left[h^{\mathrm{eff}}(T),\, w^{(n-1)}(T)\right]_-\right]_{lm}\,, \\ w_{lm}^{(0)}(T) &:= \mathrm{i}\Delta\left(I_{lm}^{(1),<}(T,\,T) - I_{lm}^{(2),>}(T,\,T)\right)\,. \end{aligned} \tag{3.3-E9}$$

In the case of the GKBA, again, the terms that contain the collision integral in Eqs. (3.3-E6) and (3.3-E7) vanish. These new equations of motion have the advantage that they are stable even for strong excitations. However, the downside is that it is not trivial to find higher order propagation algorithms for this set of equations. An exception is a second order method that uses one additional intermediate step. Starting at time T, the Green function is propagated to $T + \frac{\Delta}{2}$ with the above equations. At this time, the effective Hamiltonian and the collision integrals are calculated. Finally, the main propagation step is executed, starting again from T, but this time propagating to $T + \Delta$ and using the effective Hamiltonian and collision integrals obtained in the intermediate step. It can be shown that this procedure has an local error term of $\mathcal{O}(\Delta^3)$ and is therefore a second order method [86]. Algorithms of higher order are more complex and need to extrapolate values to achieve a better error term [56].
However, in this work the RK4 method is used since it is an excellent choice for the weak excitations considered in the simulations for the results presented in Secs. 4 and 6.

3.3.2 Numerical integration techniques

The numerical propagation scheme described in Sec. 3.2.2 and depicted in Fig. 3.2-F2 contains a lot of time integrals, especially when using resummation selfenergies like the GWA. Additionally, as the Green function is an oscillating quantity the integrands exhibit strong oscillations as shown in Fig. 3.3-F4. Thus, it is crucial to use algorithms that can solve them both fast and accurately.
In general, a variety of numerical methods exists to evaluate integral expressions. Assuming a function $f : [a, b] \to \mathbb{C}, x \mapsto f(x)$ with $a, b \in \mathbb{R}$ then the one-dimensional integral expression is given by [90]

$$I(f) = \int_a^b \mathrm{d}x\, f(x)\,. \tag{3.3-E10}$$

This integral can be approximated by a quadrature rule that only depends on the values of N discrete sampling points,

$$I(f) \;\approx\; (N-1)h \sum_{i=0}^{N-1} f_i w_i^d\,, \tag{3.3-E11}$$

where $f_i := f(x_i)$, $h := \frac{x_{N-1}-x_0}{N-1}$, $N \in \mathbb{N}$ and $i \in [0, N-1]$. The weight factors w_i^d of order d depend on the chosen quadrature method. As the non-Markovian structure of the propagation scheme requires an equidistant grid of data points, i.e. $x_i = a + i\frac{b-a}{N-1}$, only methods with equidistant stepping are applicable. Under these circumstances a convenient

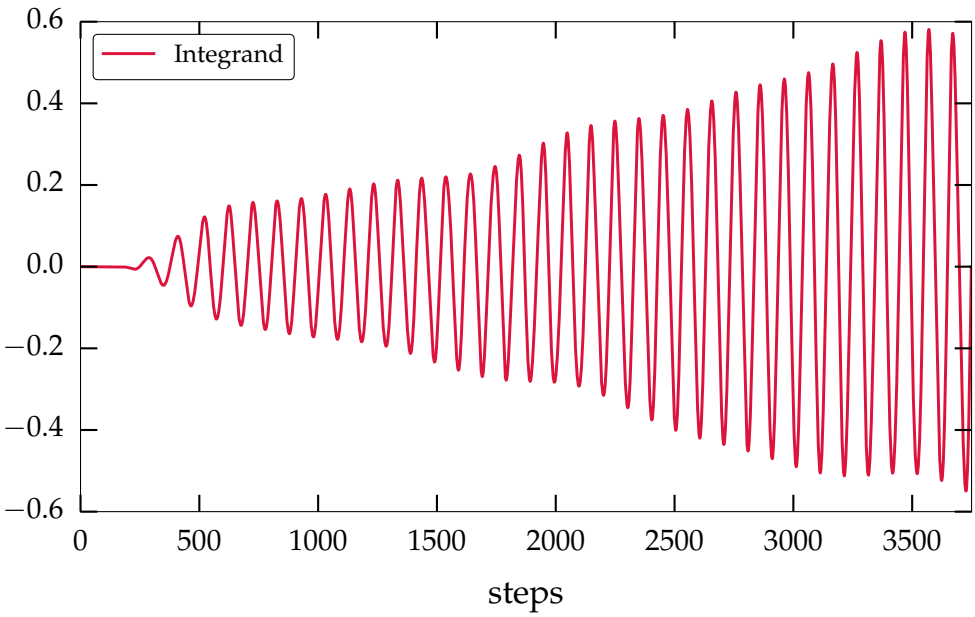

Figure 3.3-F4 – An example for a typical integrand that has to be integrated to calculate the collision integrals (cf. Eqs. (3.2-E21) and (3.2-E22)) and the resummation selfenergies (cf. Eq. (3.2-E25)) in the propagation scheme depicted in Fig. 3.2-F2.

choice for a high order integration scheme is given by the so-called Newton–Cotes (NC) formulas for which the order of integration is given by the number of sampling points, i.e. $d = N - 1$. The general idea of this approach is to interpolate the sampling points by a polynomial of order d which can be integrated analytically. The universal weight factors for the closed Newton–Cotes integration are given by [47]

$$w^d_{i,\mathrm{NC}} \;:=\; \int_0^1 \mathrm{d}\hat{x} \prod_{\substack{j=0 \\ j\neq i}}^{d} \frac{\hat{x}d - j}{i - j}\,. \tag{3.3-E12}$$

An advantage of the NC integration is that the weights can be calculated before the start of the propagation. Thus, there is no additional numerical overhead during the propagation compared to a trivial linear integration. The error of the NC integration is of the order $\mathcal{O}\left(h^{d+2}\left|f^{(d+1)}\right|\right)$, if d is odd and of the order $\mathcal{O}\left(h^{d+3}\left|f^{(d+2)}\right|\right)$, if d is even. Since $d = N - 1$, it is, in principle, possible to vastly reduce the numerical error for integrals over a large number of sampling points. However, in practice it turns out that for $d \geq 8$ some of the weight factors become negative which results in numerical cancellation effects due to summation with alternating sign [91]. Additionally, a well known problem of high order, equidistant integration schemes is the so-called Runge phenomenon which will be addressed later in this section. Therefore, it is convenient to restrict the order of integration formulas to $d \leq 7$.

In order to nevertheless calculate integrals with a large number of sampling points, two different approaches can be applied. In Fig. 3.3-F5 both are illustrated for an integral over $N = 11$ sampling points. The idea of the first approach, shown in Fig. 3.3-F5(a), is to divide the integration interval into subintervals in such a way that the minimal occurring integration order is optimal. In the case of $N = 11$ the interval can be split into two

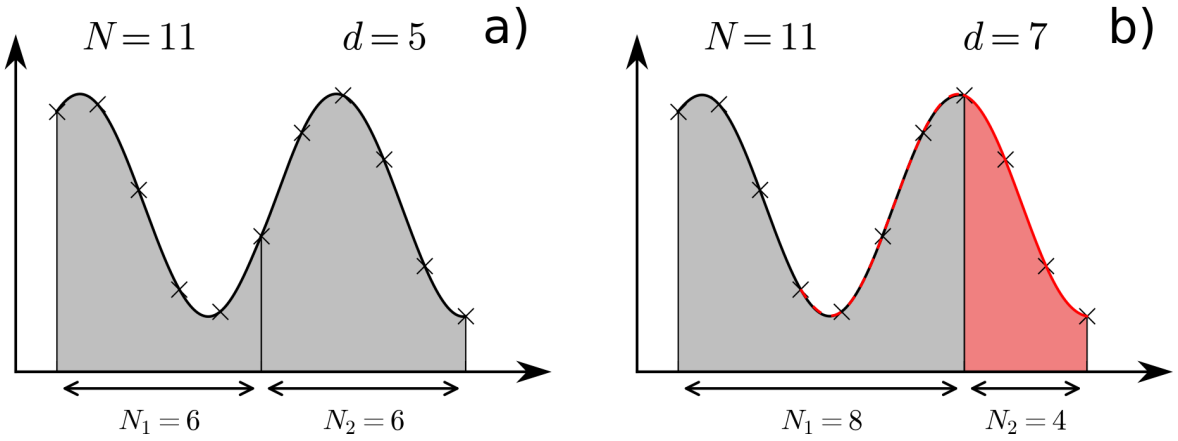

Figure 3.3-F5 – Illustration of the two different ways to handle integrals over a large number of sampling points. Left: The interval is divided into equal subintervals to achieve a optimal total order, here $d = 5$. Right: The interval is divided into subintervals of the highest order $d = 7$. The remaining part is also considered in the highest order by reusing points of the adjacent interval for the interpolation.

subintervals containing six sampling points each[17]. This results in a total integration order of $d = 5$. More details about this optimal order scheme can be found in [47].
For the second approach, depicted in Fig. 3.3-F5(b), the integration interval is split into subintervals that correspond to the highest considered order, i.e. $d = 7$ for the NC integration. The remaining part can also be integrated using the highest integration order by reusing points of the adjacent subinterval. For this the calculation of the weight factors has to be adjusted by changing the integration boundaries in Eq. (3.3-E12) to account for the fact that the integration is not performed over all considered sampling points. This way, the total integration order is $d = 7$.
Both approaches have advantages and disadvantages. The optimal order scheme achieves only low integration orders for integrals of short to intermediate length but guaranties positive weight factors. With the second approach, integrals of all lengths can be calculated in the highest integration order but for the cost of partly negative weight factors.

Even with these sophisticated techniques to handle integrals with a large number of sampling points there still remains a fundamental problem. To obtain the collision integral, even at later time steps, one has to calculate short integrals over only a few sampling points. This is shown in Fig. 3.3-F6 for the first term of Eq. (3.2-E21). Since the integration order for the NC approach is given by $d = N - 1$ it is apparent that the resulting error for such integrals is significantly higher than for the longer integrals. However, since the integrands are highly oscillating (cf. Fig. 3.3-F4), integrals of all lengths are of the same order of magnitude. Thus, even errors in short integrals have a huge negative impact on the propagation.
Fortunately, there is a way to solve this problem at later time steps. Because the Green function is calculated on the complete two-time plane, it is possible to extend the occurring short integrals, much like in the second approach described above. This

[17] The central point is contained in both subintervals.

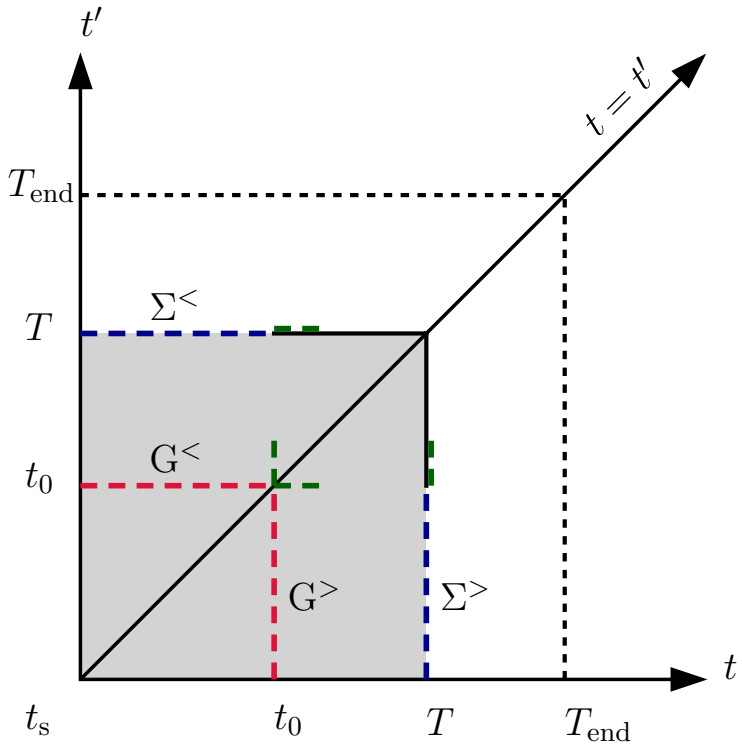

Figure 3.3-F6 – Illustration of the less and greater component of the Green function (red) and selfenergy (blue) that are used in the integration from t_s to t and t_s to t' in Eq. (3.2-E21) for $t = t' = t_0$ at the time T. Even at later time steps small integrals have to be evaluated. To solve this problem the integrals can be extended (green) because the Green function at a time T is known for all $t, t' < T$ (gray).

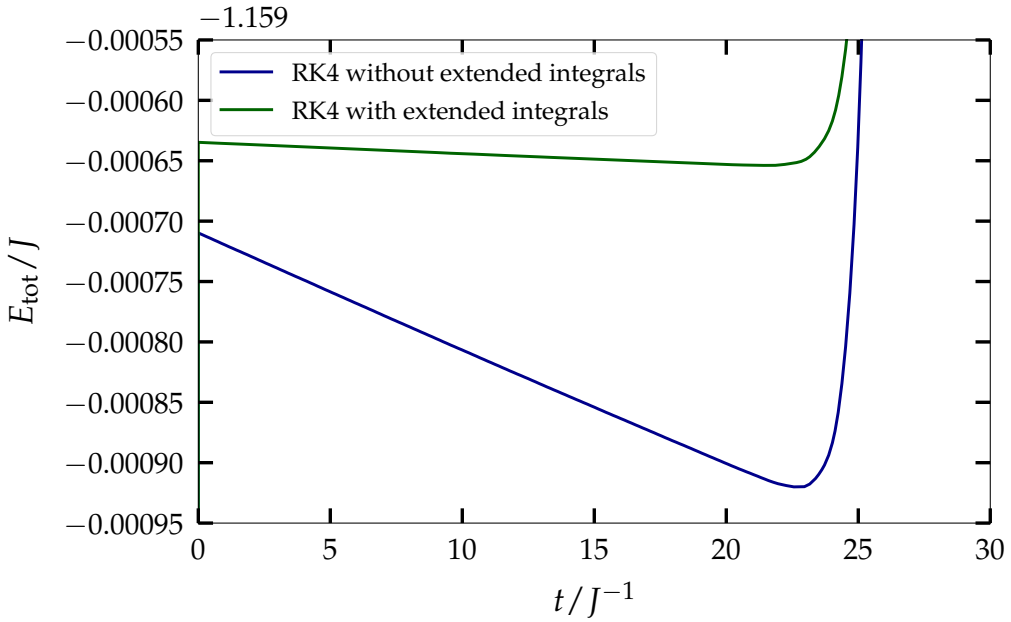

Figure 3.3-F7 – Total energy of a Hubbard dimer after an instantaneous excitation at $t = 0$. The calculations are performed within the conserving SOA selfenergy and for a time step size of $\Delta = 0.005 J^{-1}$. Thus, the total energy should be constant. Using extended integrals results in a better conservation of energy. Both calculations diverge at $t = 25 J^{-1}$.

is illustrated in Fig. 3.3-F6 by the green dashed lines. The result of this procedure is demonstrated in Fig. 3.3-F7 where the same system as in Fig. 3.3-F3 is shown but for the SOA selfenergy. Again, the total energy should be constant as the selfenergy approximation is conserving. It is apparent that the use of the extended integrals significantly improves the energy conservation. However, both calculations diverge at $t = 25J^{-1}$ due to the Runge phenomenon that will be discussed in the following.

The Runge phenomenon is a well known problem in numerical analysis [92, 93]. It describes the oscillations that occur at the edges of an interval when using polynomial interpolation as in the NC formulas. It is demonstrated in Fig. 3.3-F8 for the Runge function

$$f_{\text{Runge}}(x) = \frac{1}{1+x^2}\,. \tag{3.3-E13}$$

Using an interpolation polynomial of tenth order results in significant oscillating at the edges of the interval. The common solution to his problem is to use a non-equidistant distribution of the sampling points, the so-called Chebyshev nodes [94] . However, this approach is not applicable here since the propagation scheme enforces an equidistant grid. Another method is to introduce redundancy by allowing the order d of the quadrature rule to be smaller than $N-1$ as in the NC case [95]. This way, the polynomials used for the integration are no longer generated by interpolation but by regression. Fitting a polynomial of ninth order to the eleven sampling points in Fig. 3.3-F8 greatly reduces the artificial oscillations compared to the tenth order interpolation. The weight factors of this least squares (LS) approach are given by [95]

$$w^d_{i,\text{LS}} \;\coloneqq\; \sum_{j=0}^{d-1} q_j(x_i) \int_0^1 \mathrm{d}\hat{x}\, q_j(\hat{x})\,, \tag{3.3-E14}$$

with the orthogonal polynomials

$$q_n(x) \;=\; \frac{1}{||p_n||_u} p_n(x)\,. \tag{3.3-E15}$$

Here, $||f||_u \coloneqq \sqrt{u(f,f)}$ is the norm with the discrete scalar product

$$u(f,g) \;=\; \sum_{j=0}^{N-1} f(x_j) g(x_j)\,. \tag{3.3-E16}$$

The polynomials can be obtained by solving the recurrence relation

$$p_n(x) = (x-\alpha_n)p_{n-1}(x) - \beta_n p_{n-2}(x), \qquad n = 2,3,\ldots,N-1 \tag{3.3-E17}$$

with the coefficients

$$\alpha_n(x) = \frac{u(xp_{n-1}, p_{n-1})}{u(p_{n-1}, p_{n-1})}, \qquad \beta_n(x) = \frac{u(xp_{n-1}, p_{n-2})}{u(p_{n-2}, p_{n-2})}$$

and the initial values $p_{-1}(x) = 0$ and $p_0(x) = 1$. The advantage of this method is displayed in Fig. 3.3-F9. While the calculation using the NC integration with seventh

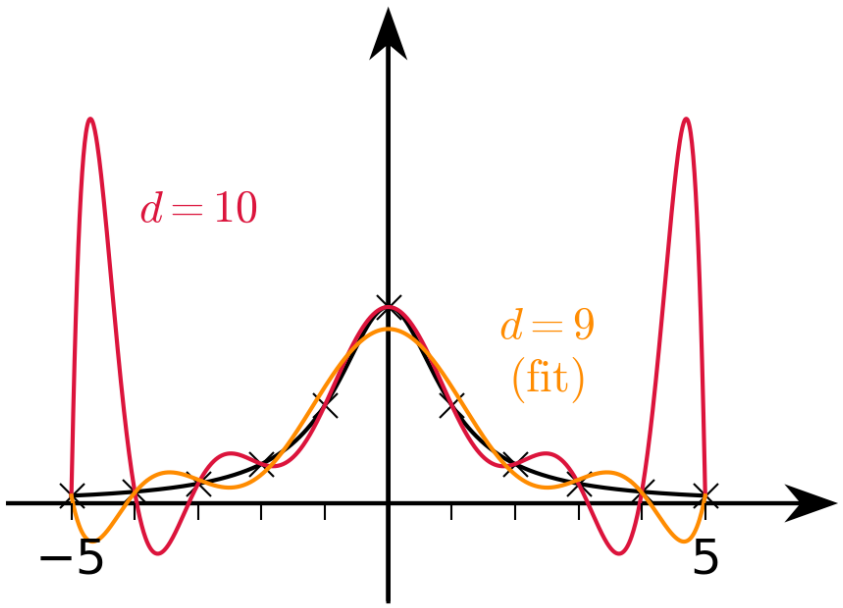

Figure 3.3-F8 – The Runge function (black) given in Eq. (3.3-E13) is sampled at eleven equidistant points. An interpolation polynomial of tenth order (red) shows strong oscillations at the edges of the interval. Fitting a polynomial of ninth order (orange) to the same sampling points greatly reduces the oscillations.

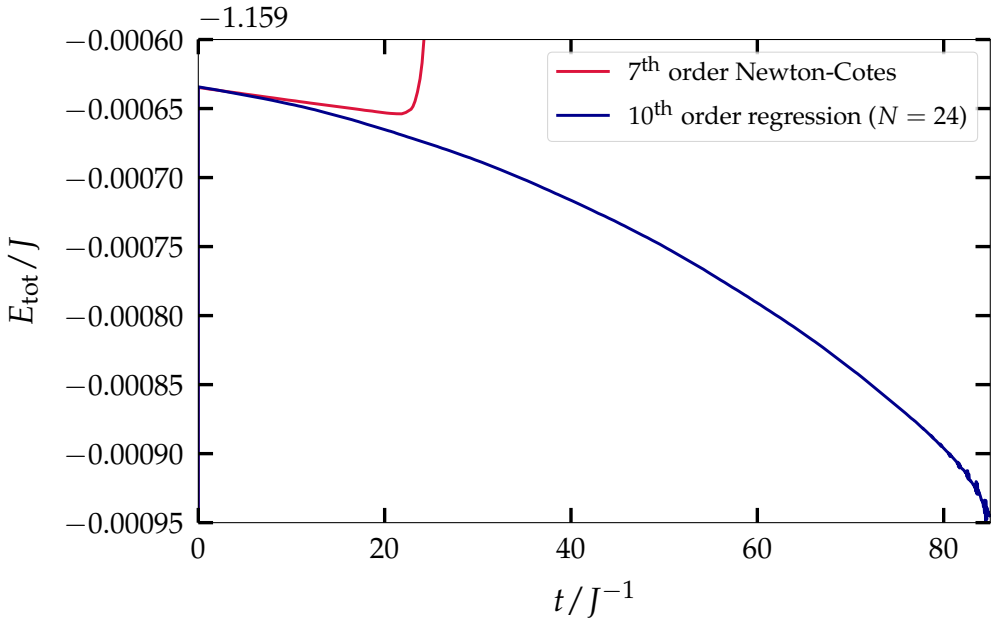

Figure 3.3-F9 – Same system and parameters as in Fig. 3.3-F7. For NC integration with seventh order interpolation polynomials the calculation diverges at $t = 25J^{-1}$. The propagation time can be extended to $t \approx 80J^{-1}$ at the cost of a slightly worse energy conservation by fitting tenth order polynomials to blocks of $N = 24$ sampling points.

order interpolation polynomials diverges at around $t = 25J^{-1}$, the propagation can be extended to $t \approx 80J^{-1}$ by fitting tenth order polynomials to blocks of $N = 24$ sampling points. It should be noted that the increased stability of the propagation comes at the cost of a slightly worse energy conservation. However, this is often negligible in practice as seen in Fig. 3.3-F9.
Another useful regression-based quadrature rule that should be mentioned here is the method of Fourier extension (FE) [96]. Since the integrands occurring in the calculations are highly oscillating, as shown in Fig. 3.3-F4, it is beneficial to use oscillating basis functions, namely sine and cosine, instead of polynomials for the regression. More details on this approach can be found in Ref. [97].
In practice, most of the time the NC method is used since it shows the best energy conservation of all three quadrature rules described above. However, the two regression methods are useful to access longer propagation times when the NC integration fails.

3.3.3 Computational demands and parallelization

As explained in the previous chapter, it is important to solve the time integrals accurately. However, as the weight factors can be determined before the start of the calculation the main numerical effort of the solution of the time integrals is given by the sum in Eq. (3.3-E11). From a performance perspective, another crucial part of the propagation scheme is the huge number of matrix multiplications. In general, each of these matrix multiplications of the form

$$C_{ij}(t,t') = \sum_k \int_{t_1}^{t_2} \mathrm{d}\bar{t}\, A_{ik}(t,\bar{t}) B_{kj}(\bar{t},t') \tag{3.3-E18}$$

can be parallelized with respect to i, j, t and t'. In theory, this can be utilized to massively speed-up the simulation on an appropriate architecture. Therefore, all calculations in this work have been performed on graphics processing units (GPUs) on accelerator cards of the types

- NVIDIA®Tesla®K20m
- NVIDIA®Tesla®P100
- NVIDIA®GeForce®GTX TITAN
- NVIDIA®GeForce®GTX TITAN Black.

The underlying architecture of GPUs differs severely from the one of normal CPUs. Thus, in order to utilize the tremendous processing power of the accelerator cards listed above, one has to take these differences into account when implementing numerical algorithms. One important restriction of GPUs compared to CPUs is the limited bandwidth. In the case of the above mentioned matrix multiplication, this can be addressed by tiling. An illustration of this procedure is shown in Fig. 3.3-F10. In order to use the limited

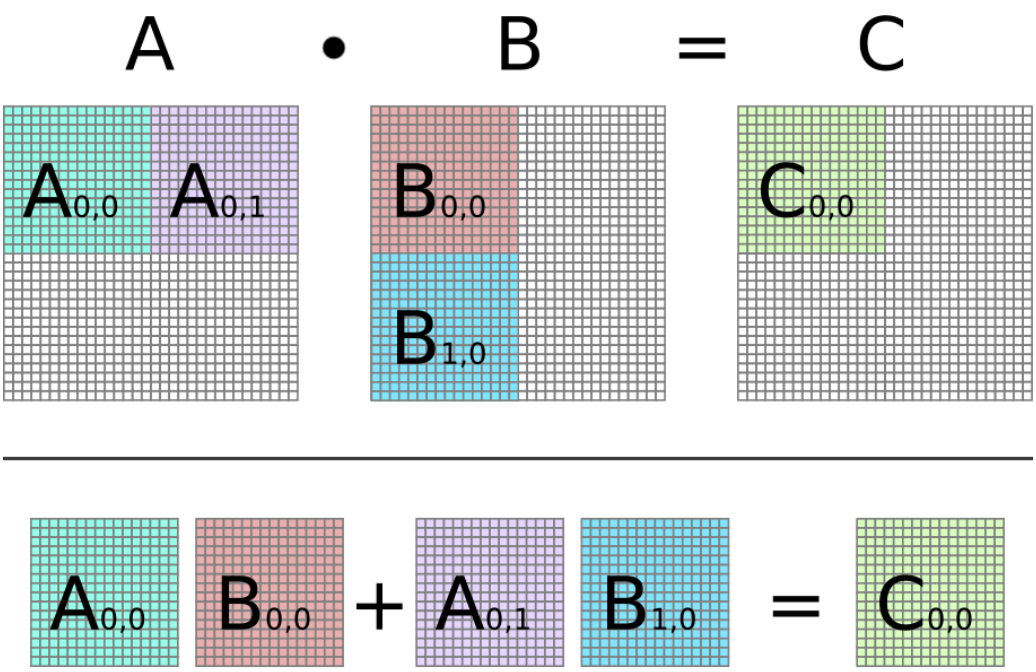

Figure 3.3-F10 – Illustration of the matrix multiplication AB = C implemented on a GPU using tiling. In order to make the matrix multiplication more efficient, the matrices are split into tiles and multiplied seperately as shown in the bottom. This way, the limited bandwidth can be used more efficiently. The Graphic is taken from Ref. [99].

bandwidth more efficiently, the matrices can be split into multiple tiles which are multiplied seperately[18].

After discussing the propagation algorithm, the integration techniques and the topic of parallelization, one can now derive how the memory demands and the computational performance of the propagation scheme presented in chapter Sec. 3.2.2 scales with the basis size N_s and the number of propagation steps N_t. The memory demand of the calculation depends mainly on the storage of the less and greater Green function on the two-time plane. Although, in principle, one has to calculate both components only on one half-plane, it turns out to be advantageous for the calculations on the GPU to save them on the complete plane. Because the Green function is stored as a double-precision complex number of 16 Bytes, the total required memory during the calculation is given by

$$M(N_\mathrm{s}, N_t) = 16\,\mathrm{Bytes} \cdot 2 \cdot N_\mathrm{s}^2 \cdot N_t^2\,. \tag{3.3-E19}$$

The performance scaling of the calculation is determined by the number of coupled integrations and matrix multiplications in the complete propagation scheme. It can be shown that for all higher order selfenergies the total performance scaling is of the order

$$P(N_\mathrm{s}, N_t) \propto \mathcal{O}\left(N_\mathrm{s}^3 \cdot N_t^3\right)\,. \tag{3.3-E20}$$

[18] The speed-up of this approach is due to the efficient use of so-called shared memory. A detailed description of the characteristics of the GPU architecture would exceed the scope of this thesis. The reader is referred to Ref. [98].

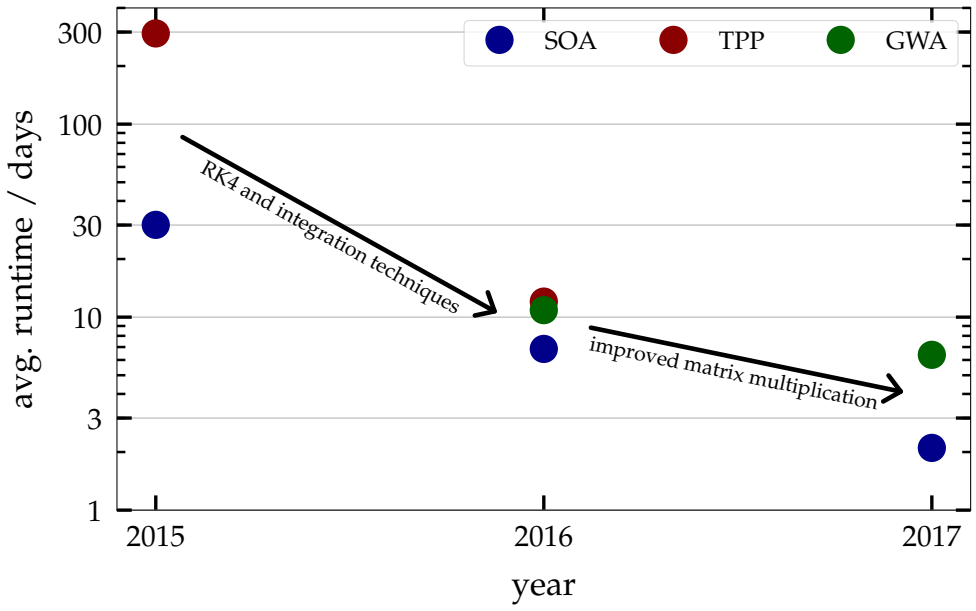

Figure 3.3-F11 – Comparison of the average computation time to propagate a system of 30 sites for a time of $110J^{-1}$ using different selfenergy approximations. The numerical improvements have greatly reduced the required computation time.

Nevertheless, it is important to note that both, the memory and the performance scaling, can be drastically reduced when using the GKBA propagation scheme together with the SOA selfenergy. In this case, the scaling becomes

$$M^{\mathrm{SOA}}_{\mathrm{GKBA}}(N_\mathrm{s}, N_t) \propto \mathcal{O}\left(N_\mathrm{s}^2 \cdot N_t\right) , \tag{3.3-E21}$$

$$P^{\mathrm{SOA}}_{\mathrm{GKBA}}(N_\mathrm{s}, N_t) \propto \mathcal{O}\left(N_\mathrm{s}^3 \cdot N_t^2\right) . \tag{3.3-E22}$$

Thus, the GKBA combined with the SOA selfenergy is an important tool to describe systems that require a long propagation time. However, in this thesis mainly the full two-time propagation scheme is used.

To summarize the topic of computational demands, a few examples of actual simulations and the improvements over the last years are presented in the following. The most demanding simulations performed in the scope of this thesis have been done for systems of 30 Hubbard sites and a propagation time of $110J^{-1}$. For the GWA selfenergy such simulations would typically take around seven days to complete and use up to 300GB of RAM each. Using the SOA selfenergy reduces the time of the calculation to about two days while the memory consumption stays the same. Fig. 3.3-F11 shows how long simulations for this system would have taken before the numerical improvements presented in this chapter were implemented. It is safe to say that this thesis would not have been possible two years ago since the systems sizes and propagation times were not accessible in a reasonable amount of computation time. Even one year ago it would have been far more demanding with all calculations taking at least twice as much time as today.
While the main limitation in the past has always been the available computation time, the recent numerical improvements have let to a new situation. At the current stage, simulations are restricted by their large memory consumption. However, in the long run

the computational performance will always be the limiting factor due to its cubic scaling with respect to the basis size and the number of time steps (cf. Eq. (3.3-E20)) while the amount of memory shows only a quadratic dependence (cf. Eq. (3.3-E19)).

3.4 Exact propagation methods

In order to test the accuracy of the NEGF approach, it is important to compare to exact solutions for selected model systems. Therefore, in the following, the exact wave-function-based methods presented in Sec. 2.1 will be discussed in the scope of the Hubbard model. Using the wave function of the system it is possible to generate the exact single-particle Green function which allows for the best possible comparison with the NEGF approach. Starting from an initial state $|\psi(t_0)\rangle$ of a given system, the time evolution of the exact wave function $|\psi(t)\rangle$ can be expressed by the time evolution operator $\hat{U}(t, t_0)$:

$$|\psi(t)\rangle = \hat{U}(t, t_0)\,|\psi(t_0)\rangle\,. \tag{3.4-E1}$$

In the calculations performed for this work the propagations starts from the interacting ground state of the system as discussed in Sec. 2.2.3. However, for the exact methods no adiabatic switching is needed. Instead, the initial wave function that describes the interacting ground state can be generated using the iterative Lanczos technique presented in Sec. 2.1.1.

Starting from the initial state, there are at least two ways to implement the propagation numerically. The first approach is to directly propagate the Schrödinger equation given in Eq. (2.1-E1) which leads to the following equation of motion for the state vector:

$$\frac{\mathrm{d}}{\mathrm{d}t}\,|\psi(t)\rangle = -\frac{\mathrm{i}}{\hbar}\hat{H}(t)\,|\psi(t)\rangle\,. \tag{3.4-E2}$$

Here, $\hat{H}$ is the Hubbard Hamiltonian (cf. Eq. (2.3-E4)) given in the N-particle Hilbert space for $N = N^{\uparrow} + N^{\downarrow}$ and $N^{\uparrow} = N^{\downarrow}$[19]. This differential equation can be solved by appropriate numerical algorithms. In this work, the Runge–Kutta Dormand–Prince 5 method is used that provides an adaptive step size control to limit the numerical error. This approach is applicable for both time-dependent and time-independent Hamiltonians. Further, it shows only linear scaling with respect to the number of time steps. However, although in every propagation step only one matrix-vector-multiplication has to be performed, the approach is limited to system sizes of $N_\mathrm{s} \leq 12$. This is due to the exponential scaling of the Hilbert space with respect to the number of Hubbard sites and particles. Only the fact that the Hamiltonian is typically very sparse allows to even reach system sizes above $N_\mathrm{s} = 8$.

The second approach is based on the Lanczos propagation presented in Sec. 2.1.1 where the time evolution operator in Eq. (3.4-E1) is expressed in the low-dimensional Krylov space (cf. Eq. (2.1-E16)). In contrast to the direct method described above the success of this approach depends on the time dependence of the Hamiltonian. The propagation is numerically exact if the Hamiltonian is time independent, i.e. it is exact for an arbitrary

[19] All systems considered in this work are symmetric with respect to the spin.

time step size Δ [43]. Therefore, the Lanczos propagation is the method of choice to calculate ground state systems or instantaneous excitations where the numerical effort is constant for all propagation times. However, for time dependent systems the time step size has to be small enough to resolve the changes in the Hamiltonian. In this case, the Lanczos method is far more costly than the direct approach since the Krylov space has to be generated seperately for every single time step. In general, the Lanczos propagation is applicable to systems of the same size as the direct approach due to the exponential scaling of the Hilbert space with respect to the number of Hubbard sites and particles.

3.4.1 Exact Green functions

When propagating the wave function with one of the two approaches presented above, it is possible to generate the exact single-particle Green function [43]. Starting from an initial state $|\psi(t_0)\rangle$, the less component of the Green function has the form

$$G_{ij}^{<}(t,t') = \frac{\mathrm{i}}{\hbar} \langle\psi(t_0)| \hat{c}_j^\dagger(t')\hat{c}_i(t) |\psi(t_0)\rangle \tag{3.4-E3}$$

$$= \frac{\mathrm{i}}{\hbar} \underbrace{\langle\psi(t_0)| \hat{U}(t_0,t)\hat{c}_j^\dagger(t')\hat{U}(t',t_0)}_{\langle\Psi_j(t')|} \underbrace{\hat{U}(t_0,t)\hat{c}_i\hat{U}(t,t_0) |\psi(t_0)\rangle}_{|\Psi_i(t)\rangle} . \tag{3.4-E4}$$

In order to calculate the exact less component of the Green function for all basis indices i,j and in the complete two-time plane t,t' the following four-step procedure has to be executed. First, the system's initial state $|\psi(t_0)\rangle$ has to be computed. In this work, the initial state is the interacting ground state of the system and is generated by the iterative Lanczos technique (cf. Sec. 2.1.1). Second, the wave function

$$|\psi(t)\rangle = \hat{U}(t,t_0) |\psi(t_0)\rangle \tag{3.4-E5}$$

is propagated and stored on a equidistant grid up to a time T_{end} using one of the methods described above. Third, for every time t on the grid and every site i a new state

$$|\Psi_i^{<}(t)\rangle = \hat{U}(t_0,t)\hat{c}_i |\psi(t)\rangle \tag{3.4-E6}$$

is generated. This corresponds to a propagation backwards in time in the $(N-1)$-particle Hilbert space. Finally, using the states $|\Psi_i(t)\rangle$, the less Green function can be created for all sites i,j and times t,t':

$$G_{ij}^{<}(t,t') = \frac{\mathrm{i}}{\hbar}\langle\Psi_j^{<}(t')|\Psi_i^{<}(t)\rangle . \tag{3.4-E7}$$

The greater component of the Green function can be generated in the same way with

$$G_{ij}^{>}(t,t') = -\frac{\mathrm{i}}{\hbar}\langle\Psi_i^{>}(t)|\Psi_j^{>}(t')\rangle , \tag{3.4-E8}$$

where

$$|\Psi_i^{>}(t)\rangle = \hat{U}(t_0,t)\hat{c}_i^\dagger |\psi(t)\rangle \tag{3.4-E9}$$

is propagated in the $(N+1)$-particle Hilbert space.
The most time consuming step is the back propagation in Eqs. (3.4-E6) and (3.4-E9) that has to be done for every time step on the grid. However, in case of a time independent Hamiltonian the exact Green function can be calculated for all sites and all times in a linear amount of time using the Lanczos propagation scheme, since the back propagation can be done in a single propagation step. For time dependent systems the calculation of the exact Green function shows a quadratic scaling with the number of time steps as Eqs. (3.4-E6) and (3.4-E9) have to be propagated within a linearly increasing number of steps. However, it is possible to create a propagation scheme that, even for a time dependent Hamiltonian, scales linearly with respect to the number of time steps.
Assuming a simple Euler propagation scheme for Eq. (3.4-E2) the propagation of the wave function can be expressed as

$$|\psi(t+\Delta)\rangle = \hat{P}_{\Delta}(t)\,|\psi(t)\rangle\ , \tag{3.4-E10}$$

where the propagator $\hat{P}$ is given by

$$\hat{P}_{\Delta}(t) = \hat{1} - \frac{\mathrm{i}}{\hbar}\Delta\hat{H}(t). \tag{3.4-E11}$$

To perform the back propagation in a constant amount of time the propagators P can be multiplied during the forward propagation to create the backward propagator at a given time T[20]:

$$\hat{P}_{\text{back}}(T) = \hat{P}_{-\Delta}(t_1)\hat{P}_{-\Delta}(t_2)\ldots\hat{P}_{-\Delta}(T), \qquad t_1 < t_2 < \ldots < T. \tag{3.4-E12}$$

However, the downside of this approach is that $\hat{P}_{\text{back}}$ becomes non-sparse for long propagation times. Thus, the calculation of exact Green functions for time dependent Hamiltonians is limited to system sizes of $N_{\text{s}} = 8$.

[20]Here, the notation $\hat{P}_{-\Delta}$ denotes the backwards propagation ($\Delta \to -\Delta$).

4 Results I: Method benchmarks

In this section, the validity of the NEFG approach in general and the performance of the individual selfenergy approximations in particular are studied by comparing results for the one-dimensional Hubbard chain with exact methods. As the main focus of this work lies on the correct description of finite graphene structures within the Hubbard model and the NEGF, all studied systems are considered at half filling which corresponds to the case of non-doped graphene. The first part of this section will focus on the ground state of the Hubbard chain while in the second part different excitations are considered.

4.1 Ground state results

The correct description of the ground state is of utmost importance since it is the foundation for the accurate simulation of nonequilibrium processes. Therefore, in this part the spectral properties of the one dimensional Hubbard chain are calculated for different selfenergy approximations within the NEGF approach and compared to both, results from the exact methods presented in Sec. 3.4 for small clusters and results of the Bethe ansatz solution [100, 101] for the infinite chain. Furthermore, the Mott metal-insulator transition, i.e. the opening of the Hubbard gap for increasing interaction strength, is compared for various selfenergies. This is especially important because the correct simulation of the bandgap is crucial for an accurate description of the nonequilibrium processes in graphene nanostructures [14, 102]. Additionally, the performance of the GKBA will be studied in particular. It was shown in the past that the GKBA is a useful tool to describe strong excitations as it does not suffer from artificial damping effects [47, 56, 103]. However, it will be shown that the GKBA fails to correctly reproduce even the spectral properties of systems at the ground state.

4.1.1 Testing against exact results

An important property for the analysis of graphene nanostructures is the photoemission spectrum given in Eq. (2.2-E98). Thus, it is reasonable to look at this quantity when benchmarking the NEGF against exact results. In Figs. 4.1-F1 and 4.1-F2 the photoemission spectrum of an eight-site Hubbard chain at half filling is calculated for the HF, SOA, TPP, TPH and GWA selfenergy (cf. Sec. 2.2.5) and compared to the result of an exact Lanczos calculation. As the system is in the ground state, only states below the Fermi energy $\omega_{\mathrm{F}} = 0$ are occupied.
In Fig. 4.1-F1 the on-site interaction is $U = 1J$. The main features of the exact spectrum are four major peaks between $\omega \approx -0.4J$ and $\omega \approx -1.9J$ and some satellites at $\omega < -2J$. It is apparent that all selfenergy approximations roughly reproduce the correct positions of the four main peaks. However, the spectral weight of the individual peaks, especially for the second and third at $\omega \approx -1J$ and $\omega \approx -1.5J$, is estimated differently. While the HF approximation incorrectly predicts a homogeneous distribution of spectral weight, the TPH and GWA selfenergies show the best agreement with the exact spectrum, especially for the

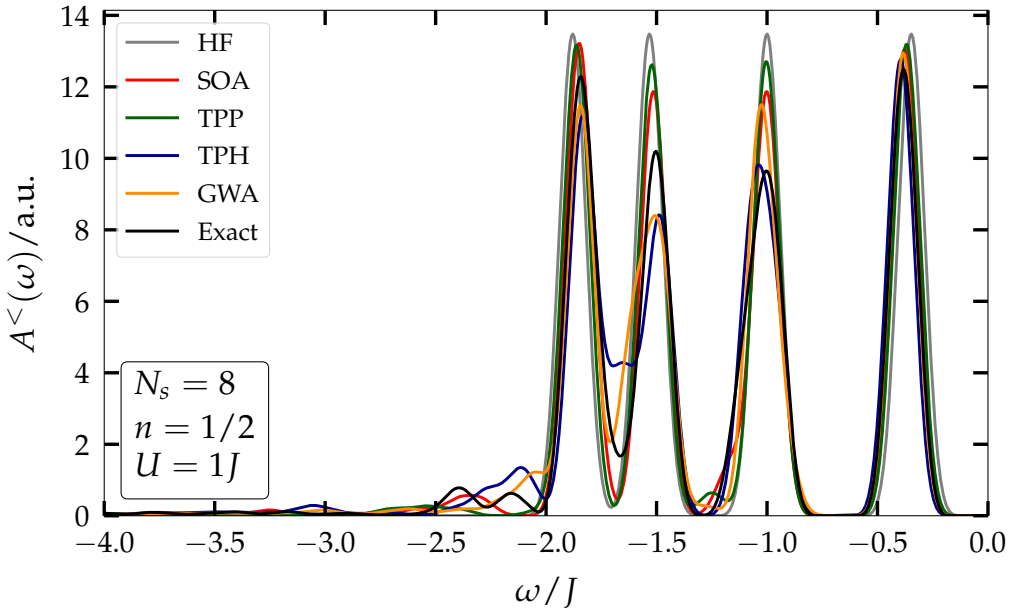

Figure 4.1-F1 – Ground state photoemission spectrum (cf. Eq. (2.2-E98)) of a one-dimensional Hubbard chain of $N_s = 8$ sites at half filling and an on-site interaction of $U = 1J$. The width of the probe pulse is set to $\kappa = 12.5J^{-1}$. The full two-time NEGF results for the different selfenergy approximations are compared to the solution of the exact Green function (cf. Sec. 3.4.1) in black.

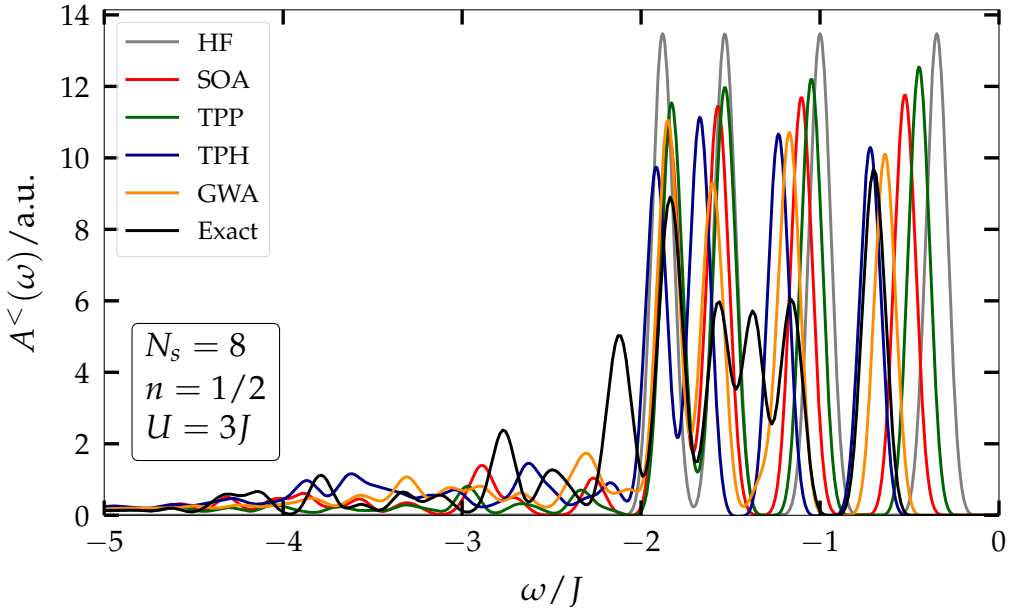

Figure 4.1-F2 – Ground state photoemission spectrum (cf. Eq. (2.2-E98)) of a one-dimensional Hubbard chain of $N_s = 8$ sites at half filling and an on-site interaction of $U = 3J$. The width of the probe pulse is set to $\kappa = 12.5J^{-1}$. The full two-time NEGF results for the different selfenergy approximations are compared to the solution of the exact Green function (cf. Sec. 3.4.1) in black.

second and third peak. It should be noted that apart from HF all selfenergy approximations correctly predict the existence of satellites for $\omega < -2J$. However, the exact positions and weights of all occurring satellites are reproduce by none of the considered approximations. The system in Fig. 4.1-F2 has an increased on-site interaction of $U = 3J$. The most striking difference of the exact spectrum compared to the case of $U = 1J$ is that the two peaks at $\omega \approx -1J$ and $\omega \approx -1.5J$ have split into three peaks. Additionally, the first peak has shifted from $\omega \approx -0.4J$ to $\omega \approx -0.7J$ and the satellites at $\omega < -2J$ are far more dominant at this higher interaction. The results of the NEGF approach differ to some extent from the exact results. Comparing the findings for $U = 1J$ and $U = 3J$ it is apparent that the HF selfenergy predicts the same photoemission spectrum for both cases. This is due to the fact that HF only considers mean field effects which solely result in a shift of the spectrum but not in a redistribution of the spectral weight. The mean field shift is not shown here since the Fermi energy is set to $\omega_\mathrm{F} = 0$. Again, the TPH and GWA selfenergies show the best agreement with the exact result. Especially the shift of the first peak, which corresponds to the opening of the Hubbard gap, is captured well by these two selfenergy approximations. However, the NEGF approach does neither correctly reproduce the splitting of the second and third peak nor the positions and weights of the satellites. To understand these findings, one has to look at the bandwidth of the considered system. In Sec. 2.3.2 it was found that the bandwidth of the ideal one-dimensional Hubbard chain is $4J$. It is known that to NEGF approach is only valid for interaction strengths below the bandwidth of the system at hand [103]. Therefore, the agreement with the exact spectrum is far better for the case of $U = 1J$ than for $U = 3J$ which is already near the bandwidth of the one-dimensional chain. However, even for the case of high interactions the important feature of the shift of the first peak is predicted accurately by both the TPH and GWA selfenergy. This is not surprising since in the considered case of half filling the effects of particle hole collisions (TPH) and electron screening (GWA) are most important. In summary, to correctly describe the photoemission spectrum of even such a simple system as a eight site Hubbard chain at moderate interaction, it is essential to take into account correlation effects. The pure mean field treatment does not capture any of the effects appearing at higher interaction strengths. Thus, the HF selfenergy approximation will not be considered in the remainder of this section.

Another important spectral property to look at is the energy dispersion. It can be calculated from the two-time components of the Green function using Eq. (2.2-E97). The energy dispersion of a $N_\mathrm{s} = 40$ site Hubbard chain at half filling and for an on-site interactions of $U = 1J$ and $U = 3J$ is shown in Fig. 4.1-F3 within the first Brillouin zone ($k \in [\pi, \pi)$). The colormap corresponds to the NEGF calculation using the SOA selfenergy while the black lines mark the results of the exact Bethe ansatz solution for the infinite one dimensional Hubbard chain. The dashed lines correspond to the elemental excitations of so-called holons and antiholons and can be understood as the addition or removal of a spinless particle carrying the charge $\mp e$. These elemental excitations have to be distinguished from physical excitations that have to be consistent with given selection rules [32]. The full lines mark the boundaries of the continuum of so-called spin-charge scattering states. This two-particle excitation results in a change of the charge and the spin of the system by $\pm e$ and $\pm\frac{1}{2}$, respectively. Thus, this excitation is especially important for photoemission experiments where an electron carrying the charge $-e$ and the spin $\frac{1}{2}$ is removed from the system. More information on the Bethe ansatz and the calculation of these excitations can be found in Ref. [32].

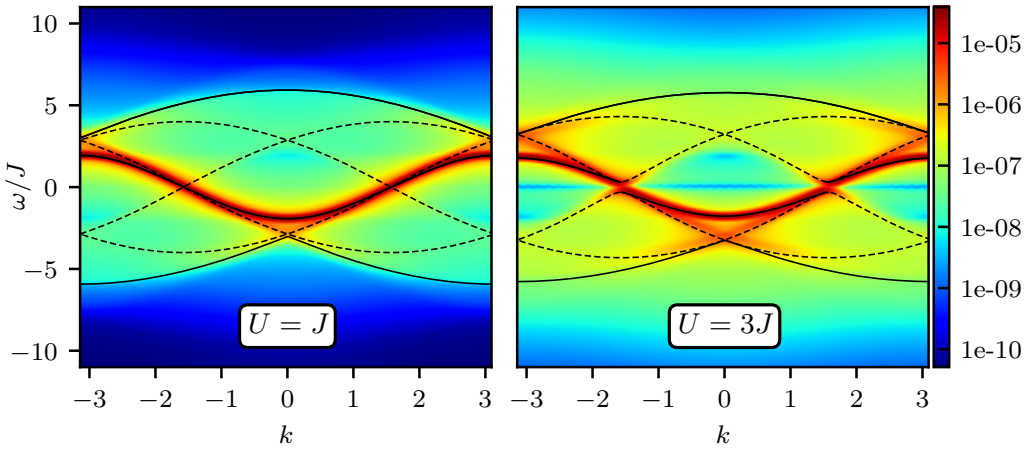

Figure 4.1-F3 – Ground state energy dispersion relation (cf. Eq. (2.2-E97)) of a one-dimensional Hubbard chain of $N_\mathrm{s} = 40$ sites at half filling and an on-site interaction of $U = 1J$ (left) and $U = 3J$ (right). The propagation time after the adiabatic switching is $T_\mathrm{end} = 50J^{-1}$. The colormap corresponds to the full two-time NEGF results using the SOA selfenergy. The solution of the exact Bethe ansatz [32] for the infinite chain is displayed by the black lines. The dashes correspond to the (anti)holon bands while the full lines mark the spin-charge scattering continuum.

For the infinite chain in the tight binding approximation ($U = 0$) we have found that the energy dispersion is given by a cosine (cf. Eq. (2.3-E11)). Looking at Fig. 4.1-F3, it is apparent that for an interaction of $U = 1J$ the SOA calculation still shows a cosine dependence as the main feature of the dispersion. This is in excellent agreement with the exact solution. Additionally, the SOA selfenergy reproduces the weak (anti)holon bands and the boundaries of the spin-charge scattering continuum. The area of this continuum corresponds to the satellites found in Figs. 4.1-F1 and 4.1-F2 for $\omega < 0$. Since the HF approximation takes into account only mean field effects, it does not allow for the two-particle excitations that create the scattering continuum and thus, as discussed before, does not reproduce the satellites.
In the case of $U = 3J$, the scattering states become more pronounced compared to the cosine contribution, which corresponds to the transfer of spectral weight from the main peaks to the satellites in Fig. 4.1-F2. However, the most important feature is the opening of the bandgap, the so-called Hubbard gap, at the Fermi energy $\omega_\mathrm{F} = 0$. Although the SOA calculation correctly predicts the existence of a gap for $U = 3J$, it seems to underestimate the width of the bandgap compared to the exact results. Because the correct description of the bandgap is essential for the accurate modeling of graphene nanostructures, the following part will focus on the Hubbard gap in detail. However, to summarize, even for this high interaction the SOA results for a finite Hubbard chain of $N_\mathrm{s} = 40$ sites are in good agreement with the Bethe ansatz solution for the infinite chain.

4.1.2 The Hubbard gap

The opening of the bandgap can be analyzed best by looking at the density of states $A(\omega)$ that can be calculated by summing over all local contributions of the spectral function

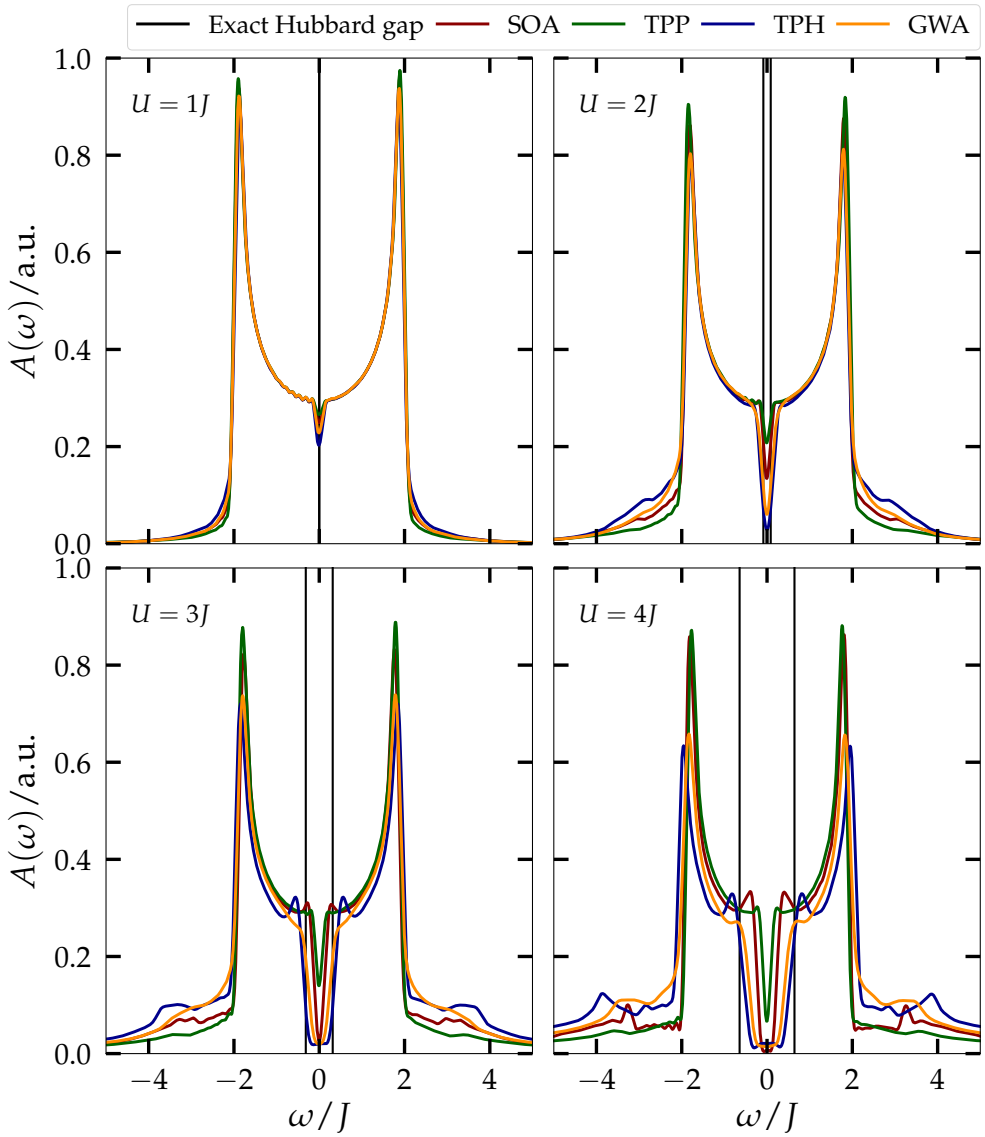

Figure 4.1-F4 – Density of states (cf. Eq. (2.2-E96)) of a one-dimensional Hubbard chain of $N_s = 40$ sites at half filling and an on-site interaction of $U = 1J$ (top left), $U = 2J$ (top right), $U = 3J$ (bottom left) and $U = 4J$ (bottom right). The propagation time after the adiabatic switching is $T_{end} = 50J^{-1}$. The colored lines correspond to the full two-time propagation of the KBEs using different selfenergy approximations. The black vertical lines display the width of the Hubbard gap for the infinite chain given by the exact Bethe ansatz [32].

(cf. Eq. (2.2-E96)). Alternatively, it can be obtained from the dispersion relation through a summation over all k. In Fig. 4.1-F4 the density of states (DOS) of a $N_s = 40$ sites Hubbard chain is shown for various values of the on-site interaction U and different selfenergy approximations. Additionally, the Hubbard gap for the infinite chain predicted by the exact Bethe ansatz solution is depicted as two black vertical lines.
As shown in Fig. 2.3-F2, the infinite Hubbard chain in the tight-binding limit ($U = 0$) does not have a bandgap. Looking at Fig. 4.1-F4 the DOS for $U = 1J$ shows a similar shape compared to the tight-binding case. All selfenergy approximations predict only

a slight dip of the DOS at the Fermi energy but no complete opening of the bandgap. Likewise, the Bethe ansatz does not show a noticeable Hubbard gap. For $U = 2J$ first differences between the particular selfenergies appear with TPP showing the smallest bandgap and TPH the largest. However, it is hard to say which approximation shows the best agreement with the exact solution as the deviations are still small. Looking at $U = 3J$ and $U = 4J$ the width of the gap further increases and it emerges that the TPH and GWA selfenergy best reproduce the exact bandgap while SOA and especially TPP underestimate its width. Additionally, for $\omega < -2J$ and $\omega > 2J$ the scattering continuum becomes more pronounced as already seen in Fig. 4.1-F3.

Until now, the results of the NEFG approach for finite Hubbard clusters have been compared to the exact solution for the infinite chain. Furthermore, looking at Fig. 4.1-F4 it is difficult to determine the exact width of the bandgap for the Green function calculations since the spectrum is broadened due to the finite propagation time and width of the probe pulse (cf. Eq. (2.2-E99)). To make a direct quantitative comparison between the NEGF approach and the exact solution possible, the results for the finite systems have to be extrapolated towards the infinite limit. Thus, the DOS for systems between $N_\mathrm{s} = 2$ and $N_\mathrm{s} = 40$ are calculated for all considered selfenergies. Afterwards, the edge of the upper and lower Hubbard subbands are determined by fitting Gaussian functions to the spectrum. The bandgap is then given by the difference between the center of the lowest peak in the upper subband and the highest peak in the lower subband. It is found that the size of the bandgap $E_\mathrm{gap}^{N_\mathrm{s}}$ for a system of N_s sites obeys the relation

$$E_\mathrm{gap}^{N_\mathrm{s}} - E_\mathrm{gap}^{\infty} \quad \propto \quad \frac{1}{N_\mathrm{s}}. \tag{4.1-E1}$$

Extrapolating the results for the different system sizes to $N_\mathrm{s} \to \infty$ allows for a direct comparison with the exact gap of the Bethe ansatz which can be evaluated analytically by [104]

$$E_\mathrm{gap}^{\infty}/J \quad = \quad \frac{16}{U/J} \int_1^\infty \mathrm{d}x \frac{\sqrt{(x^2-1)}}{\sinh(2\pi x/(U/J))}. \tag{4.1-E2}$$

The results for the four selfenergy approximations that take into account correlations are presented in Fig. 4.1-F5. The HF approximation does not show an opening of the bandgap as already shown in Figs. 4.1-F1 and 4.1-F2 and is therefore not considered here. The SOA is the most basic extension to the HF selfenergy that contains all terms up to the second order of the interaction. However, it severely underestimates the width of the bandgap, especially for strong interactions. The three more complex selfenergy approximations that contain higher order diagrams show completely different results. While the GWA slightly underestimates the exact solution and the TPH approximation predicts a bandgap that is bit too large, the TPP selfenergy shows no gap opening at all in the considered range up to $U = 3J$. This can be explained in terms of the diagrams the different selfenergy approximations include.

In the Hubbard basis the perturbation expansion of the selfenergy contains exactly two third order diagrams. One of them corresponds to particle-hole scattering and is included in the TPH selfenergy, the other one describes particle-particle interaction and is part of the TPP approximation. It can be shown that in the case of half filling, which is considered here, the sum of those two diagrams vanishes in the ground state [105]. Thus,

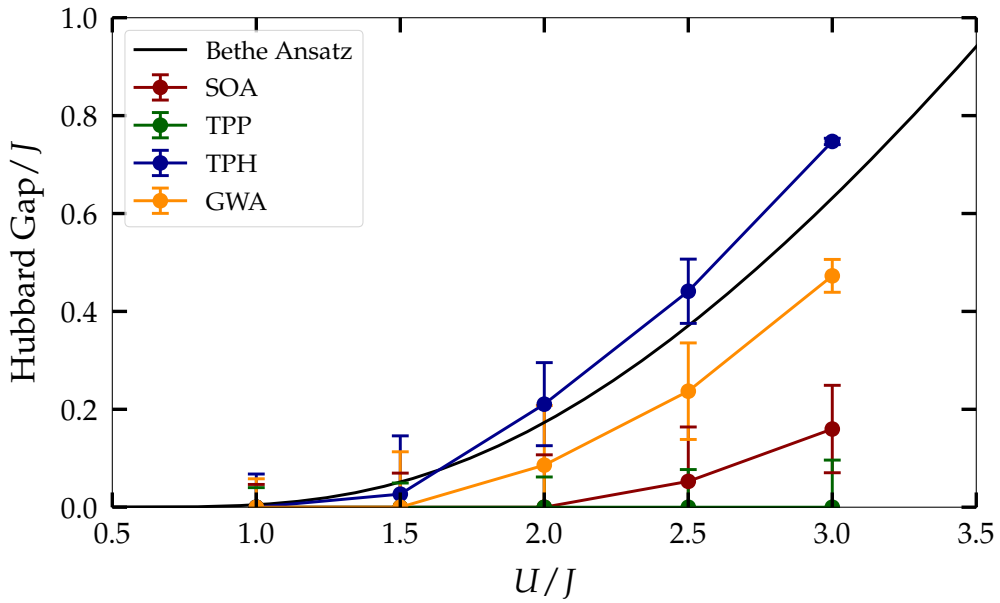

Figure 4.1-F5 – Width of the bandgap of an infinite one-dimensional Hubbard chain as a function of the on-site interaction U. The NEGF results are obtained by extrapolating the bandgaps of smaller systems as described in the text. The error bars show the uncertainty of the interpolation. The black line displays the exact Hubbard gap obtained by the Bethe ansatz (cf. Eq. (4.1-E2)).

the SOA, which only contains contributions up to second order, effectively describes the system correctly up to the third order in the interaction. However, the TPH and TPP approximations do not describe the third order contribution correctly since they each include only one of the third order diagrams which not vanish separately. This is the reason why the TPH overestimates the exact solution for the bandgap and the TPP predicts an even smaller gap than the SOA. In contrast, like the SOA, the GWA contains all second order and no third order contributions. Additionally, it includes fourth and higher order diagrams. Thus, the GWA is a straight improvement over the SOA selfenergy.
Although the TPH selfenergy reproduces the width of the bandgap nicely, the calculations for graphene in section Sec. 6 were mostly done using the SOA and GWA selfenergy because of the wrong third order contribution that the TPH approximation contains.

4.1.3 Spectral deficiencies of the GKBA

It was found in the past that for strongly excited systems the full two-time propagation of the KBEs results in an unphysical damping of the density evolution [56]. If one is only interested in the density dynamics of the system, the GKBA is the method of choice in the case of strong excitations since it does not suffer from the artificial damping. Combined with advanced selfenergy approximations it reproduces the nonequilibrium dynamics of strongly excited systems very accurately [103]. Another advantage of the GKBA is the better numerical scaling with respect to the number of time steps when using the SOA

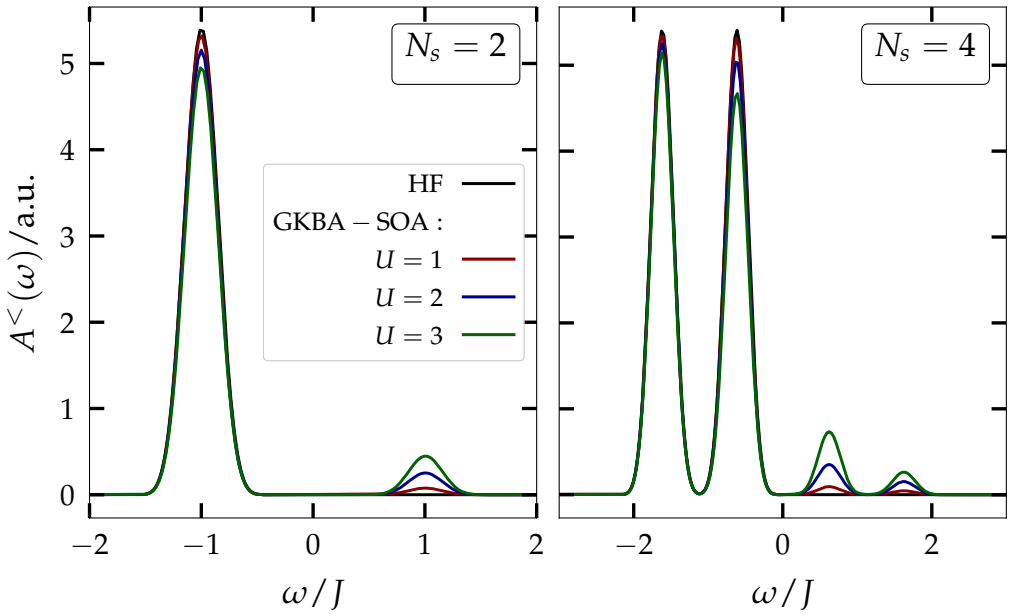

Figure 4.1-F6 – Ground state photoemission spectrum (cf. Eq. (2.2-E98)) of a one-dimensional Hubbard chain of $N_s = 2$ (left) and $N_s = 4$ (right) sites at half filling. The width of the probe pulse is set to $\kappa = 12.5J^{-1}$. The result of the GKBA combined with the SOA selfenergy for $U = 1$ (red), $U = 2J$ (blue) and $U = 3J$ (green) is compared to the HF solution which does not depend on the on-site interaction U.

selfenergy (cf. Eqs. (3.3-E21) and (3.3-E22)). However, since in this thesis the focus is primarily on spectral properties, it is important to analyze the performance of the GKBA in that regard, which is the purpose of this part.
In Fig. 4.1-F6 the photoemission spectrum for two finite Hubbard chains of $N_s = 2$ and $N_s = 4$ sites is shown for the HF approximation and the GKBA propagation combined with the SOA selfenergy. As already discussed, the spectrum of HF does not depend on the interaction U and because the systems are considered in the ground state only states below the Fermi energy $\omega_F = 0$ are occupied. In contrast, the spectrum of the GKBA shows excited states above the Fermi energy that gain spectral weight with increasing interaction U. This would suggest that the system is not in the ground state but in an excited state. However, it was shown in the past that the GKBA does describe other ground state properties like the total energy or the density distribution correctly [54, 106]. In order to find the reason for the incorrect spectral properties in the ground state one has to look at the quantities that enter the calculation of the photoemission spectrum (cf. Eq. (2.2-E98)). The main contribution is a Fourier transform of $G^<_{ii}(t,t')$ perpendicular to the time diagonal in the two-time plane. Thus, the spectral information are primarily influenced by the off-diagonal propagation of the Green function. In both cases, the HF approximation and the GKBA with SOA selfenergy, the off-diagonal dynamics of the less Green function are given by (cf. Eq. (3.2-E20))

$$-\mathrm{i}\hbar\frac{\mathrm{d}}{\mathrm{d}t'}G^<_{ij}(t \leq t') \;=\; \sum_l h^{\mathrm{eff}}_{il}(t')G^<_{lj}(t \leq t')\,. \tag{4.1-E3}$$

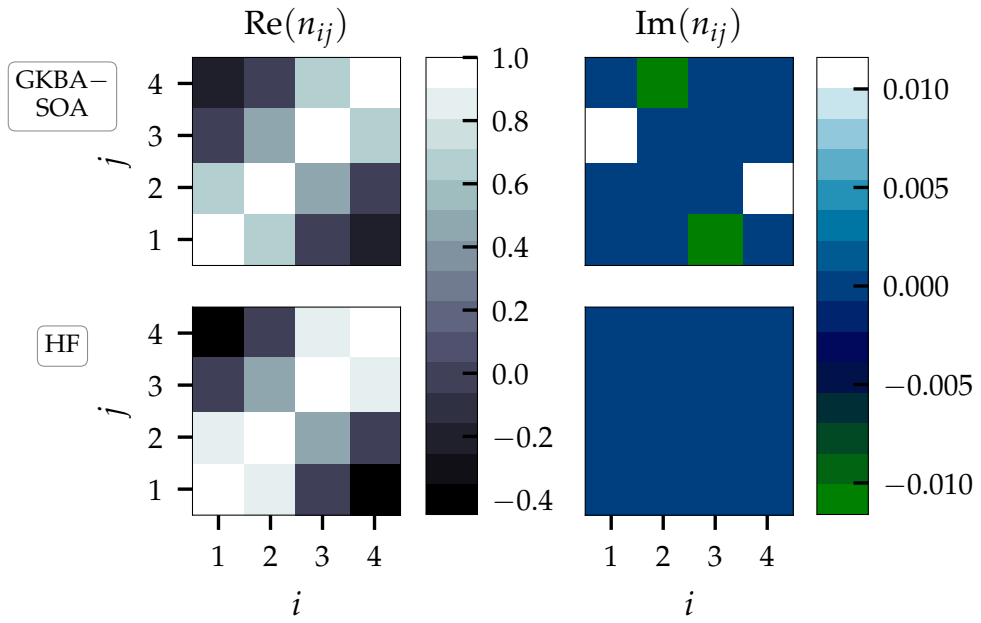

Figure 4.1-F7 – Real (left) and imaginary (right) part of the density matrix for a $N_s = 4$ site Hubbard chain in the ground state at half filling and $U = 3J$. The result of the GKBA combined with the SOA selfenergy (top) is compared to the full two-time propagation using the HF approximation (bottom).

The propagation always starts at the time diagonal, i.e. $t = t'$. In that case the less Green function can be expressed in terms of the density matrix (cf Eq. (2.2-E87)). Thus, because Eq. (4.1-E3) does not depend on the collision integral, the only difference between the full HF and the GKBA propagation can be caused by the density matrix in the ground state. In Fig. 4.1-F7 the real and imaginary part of the density matrix in the ground state are shown for both propagations at an interaction of $U = 3J$ and $N_s = 4$. Both approaches agree for the diagonal elements of the density matrix, i.e. $i = j$. Hence, the effective single-particle Hamiltonian h^{eff} in Eq. (4.1-E3) which only depends on the diagonal $n_i(t)$ (cf. Eq. (3.2-E8)) is the same for both methods. However, the off-diagonal elements of the density matrix differ for both, the real and the imaginary part. Thus, the off-diagonal propagation starts at different initial values of $G^<$ on the time diagonal.
To summarize, the GKBA describes the propagation in off-diagonal direction on the HF level. Thus, the spectral properties do also contain only HF information, since they are determined by the off-diagonal Green function. However, the propagation is started from a density matrix that does not correspond to the HF ground state. This results in an effective mapping of the GKBA-SOA ground state onto the HF photoemission spectrum which causes the artificial excitations to occur above the Fermi energy. Thus, the GKBA is not suited, if one is interested in the spectral properties of a system.

4.2 Dynamical results

After the detailed discussion of the ground state in the last section the following part will focus on systems in nonequilibrium. First, a Hubbard dimer is analyzed under the

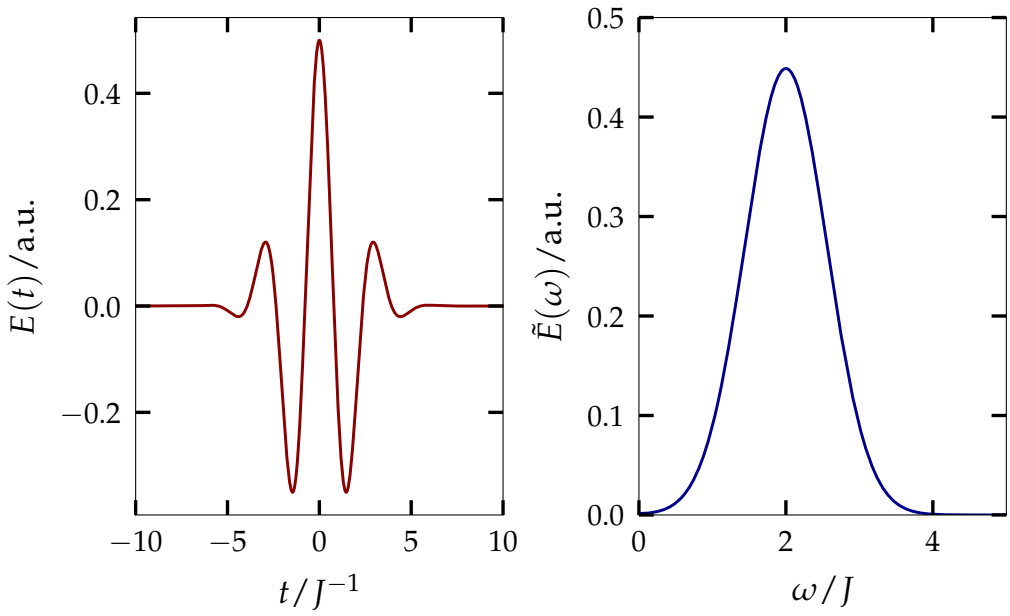

Figure 4.2-F1 – Shape of the laser pulse described by Eq. (4.2-E2) with the parameters $t_0 = 0$, $\omega_0 = 2J$, $\sigma = 1.8J^{-1}$ and $E_0 = 0.5$ in the time (left) and frequency (right) space. A pulse of this form is used to excite the systems in Figs. 4.2-F2, 4.2-F3 and 4.2-F4.

influence of a laser excitation that is later used to excite finite graphene structures (cf. Sec. 6). Additionally, the problem of unphysical damping occurring at strong excitations is addressed in detail.

4.2.1 Laser excitations

Before the finite graphene structures in Sec. 6 are excited by a laser pulse, this type of excitation is tested for a Hubbard dimer which allows to compare the NEGF approach with exact methods.
In this work, the dipole approximation is used which is justified if the wavelength ω of the laser is a lot larger than the size l of the system. The experiments with graphene presented in Sec. 5.3 are performed with optical lasers, i.e. $\omega \approx 400\,\mathrm{nm} - 700\,\mathrm{nm}$ [24]. The typical size of the graphene systems considered in this work is $l \approx 1\,\mathrm{nm} - 10\,\mathrm{nm}$. Thus, the dipole approximation is justified. In this case, an external laser excitation is included into the effective single-particle Hamiltonian in Eq. (3.2-E8) by setting

$$f_i(t) \quad = \quad -\boldsymbol{r}_i \cdot \boldsymbol{E}_{\mathrm{Laser}}\,, \tag{4.2-E1}$$

where $\boldsymbol{r}_i$ is the position of site i in units of the lattice constant of the system and the magnitude of the electric field of the laser pulse $\boldsymbol{E}_{\mathrm{Laser}}$ is given by

$$E_{\mathrm{Laser}}(t) = E_0 \cos\left(\omega_0\,(t - t_0)\right) \mathrm{e}^{-\frac{(t-t_0)^2}{2\sigma^2}}\,. \tag{4.2-E2}$$

In the following calculations a laser frequency of $\omega_0 = 2J$ is used and the standard deviation of the Gaussian is set to $\sigma = 1.8J^{-1}$. The amplitude of the laser excitation E_0 is varied. It

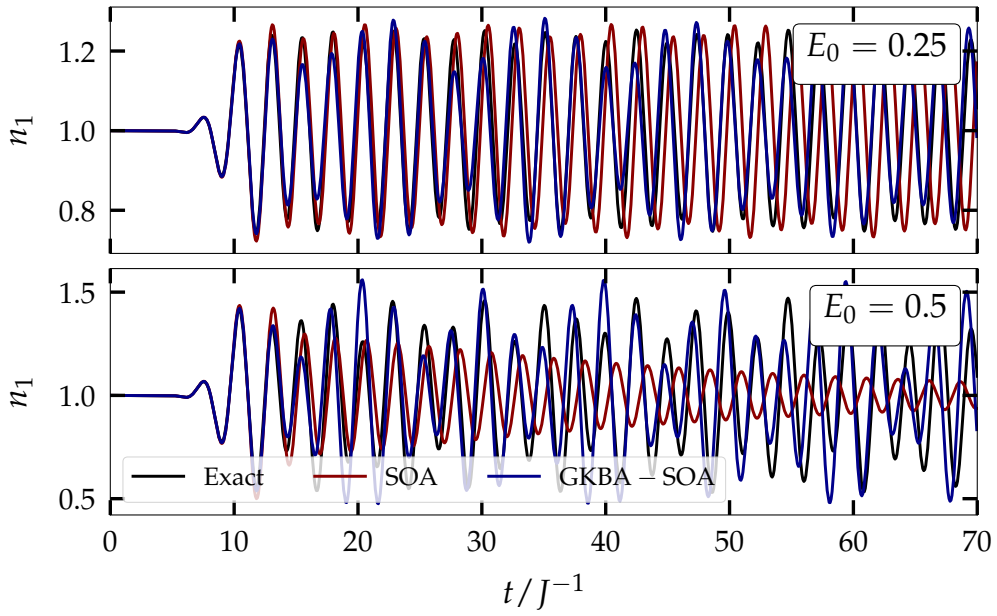

Figure 4.2-F2 – Density on the first site of a Hubbard dimer ($N_s = 2$) at half filling and $U = 1J$. The system is excited at $t_0 = 10J^{-1}$ by a laser pulse given by Eq. (4.2-E2) with an amplitude of $E_0 = 0.25$ (top) and $E_0 = 0.5$ (bottom). The NEGF results using the full two-time propagation (red) and GKBA (blue) combined with the SOA selfenergy are compared to the exact solution (black) described in Sec. 3.4.

is given in units of $Je^{-1}a^{-1}$ where e is the elementary charge and a is the lattice constant of the system. The shape of the corresponding laser pulse in time and frequency space is shown in Fig. 4.2-F1.

To test the performance of the NEGF approach in nonequilibrium, a small system has to be chosen that can be solved within the exact methods presented in Sec. 3.4. Since the laser excitation results in a time dependent Hamiltonian, the numerical demands to calculate the exact Green function are much higher than for the ground state. Therefore, in the following, the Hubbard dimer is considered since it can be solved analytically as shown in Sec. 2.3.3 and the exact Green function is easy to calculate.
In Fig. 4.2-F2 the density on the first site of a Hubbard dimer at $U = 1J$ is shown. The system is excited by a laser pulse depicted in Fig. 4.2-F1 with the maximum being at $t_0 = 10J^{-1}$. The calculations are performed with the full two-time propagation and the GKBA, both using the SOA selfenergy. Additionally, the exact Green function is determined with the Lanczos propagation method (cf. Secs. 2.1.1 and 3.4).
In the case of a small laser amplitude ($E_0 = 0.25$), both NEGF results are in good agreement with the exact solution. The GKBA solution even predicts the correct frequency of the density oscillations induced by the laser pulse while the frequency of the full two-time calculation is slightly too small. However, both NEGF simulations show the correct oscillation amplitude over the complete time frame.
At a higher laser amplitude of $E_0 = 0.5$ the full propagation shows a strong unphysical damping of the oscillation starting at $t \approx 15J^{-1}$. This effect is a well known characteristic of the NEGF for strong excitations and will be studied in more detail in Sec. 4.2.2. As already discussed, the GKBA does not show such artificial damping of the density

dynamics. Instead, it is in good agreement with the exact solution even for such a high laser amplitude.
In general, it is astonishing that doubling the laser amplitude leads to such a dramatic difference in the quality of the full two-time solution. However, as shown in Sec. 4.1.3, the correct prediction of the density dynamics does not imply the accurate description of the spectral properties. Vice versa, it might be possible that the full propagation is able to show the correct spectrum of a system at strong excitations despite the artificial damping. In order to test this, the photoemission spectrum of the same system is shown in Figs. 4.2-F3 and 4.2-F4. The dimer has been solved analytically in Sec. 2.3.3 and its eigenenergies are depicted in Fig. 2.3-F3. For the considered interaction of $U = 1J$ the two possible transitions $\psi^- \to \psi^U$ and $\psi^U \to \psi^+$ require an excitation energy of $2.57\,J$ and $1.55\,J$, respectively. Looking at Fig. 4.2-F1, one can see that the laser frequency is chosen in such a way that both transitions are possible.
For the case of $E_0 = 0.25$ the photoemission spectrum is depicted in Fig. 4.2-F3. Looking at the exact spectrum, the most interesting part are the two peaks at $\omega \approx 1J$ and $\omega \approx 1.5J$. The second one corresponds to the transition from the state ψ^U to the ground state of the $N = 1$ system[21]. The first peak indicates the transition from ψ^+ to an excited state of the $N = 1$ system. Because of this, it appears at a lower energy in the photoemission spectrum. For a small laser amplitude $E_0 = 0.25$ the system gets mainly excited into the state ψ^U which is the reason why the second excitation peak is much higher than the first. The full propagation of the Green function combined with the SOA selfenergy shows excellent agreement with the exact result. The position and height of both, the main peak at $\omega \approx -1J$ and the two excitation peaks, are well reproduced. The GKBA solution shows some deviations for the main peak and especially for the first excitation peak at $\omega \approx 1J$. Comparing with Fig. 4.1-F6 reveals that this peak is the one that already has an unphysical contribution in the ground state.
For $E_0 = 0.5$, both excitation peaks have about the same spectral weight for the exact solution because the system is partially excited to the highest state ψ^+. Again, the GKBA result overestimates the weight of the first excitation peak due to the already insufficient description of the ground state. In stark contrast to the case of a small laser amplitude, here, the full propagation shows a severe broadening of all peaks in the photoemission spectrum. The two excitation peaks of the exact result are merged to one single broadened peak in the solution of the full two-time propagation. This broadening of the peaks corresponds to the unphysical damping of the density oscillations in Fig. 4.2-F2.
Thus, in order to get accurate information about the spectral properties of a system using the NEGF approach, one has to make sure that the considered excitations are weak enough to not result in an unphysical damping of the system. Although the GKBA does deal with the damping problem, using it to get access to spectral information is not an option since it even fails to predict the correct ground state spectrum. To get a better understanding of the effect, the following part focuses on the reasons of the artificial damping.

[21] As this is the photoemission spectrum it shows transitions to the $(N-1)$-particle system. In this case the Hubbard dimer is considered at half filling, i.e. $N = 2$.

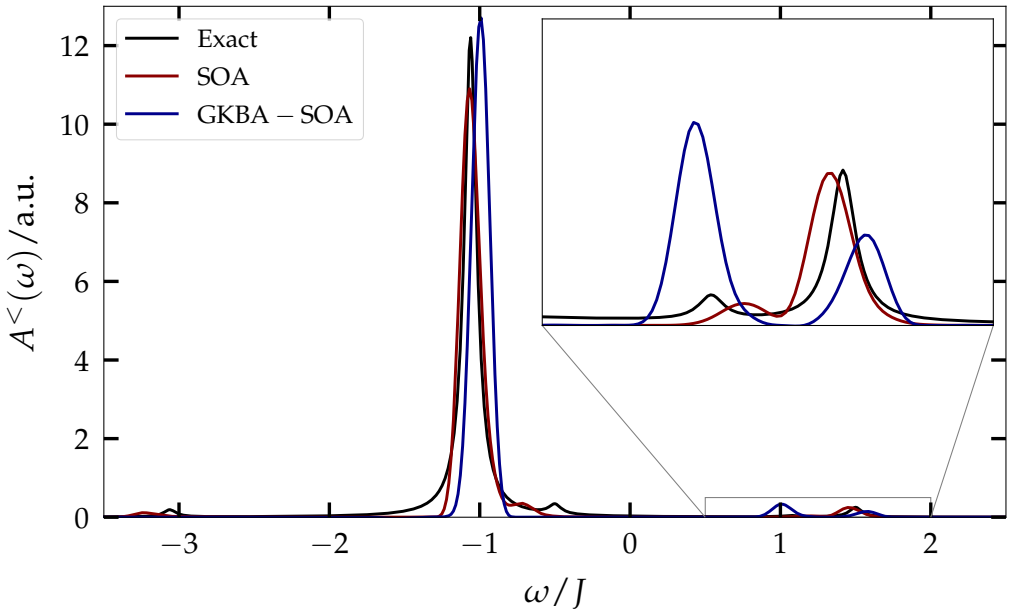

Figure 4.2-F3 – Photoemission spectrum (cf. Eq. (2.2-E98)) of a Hubbard dimer ($N_s = 2$) at half filling and $U = 1J$. The width of the probe pulse is set to $\kappa = 12.5J^{-1}$. The system is excited by a laser pulse given by Eq. (4.2-E2) with an amplitude of $E_0 = 0.25$. The NEGF results using the full two-time propagation (red) and GKBA (blue) combined with the SOA selfenergy are compared to the exact solution (black) described in Sec. 3.4.

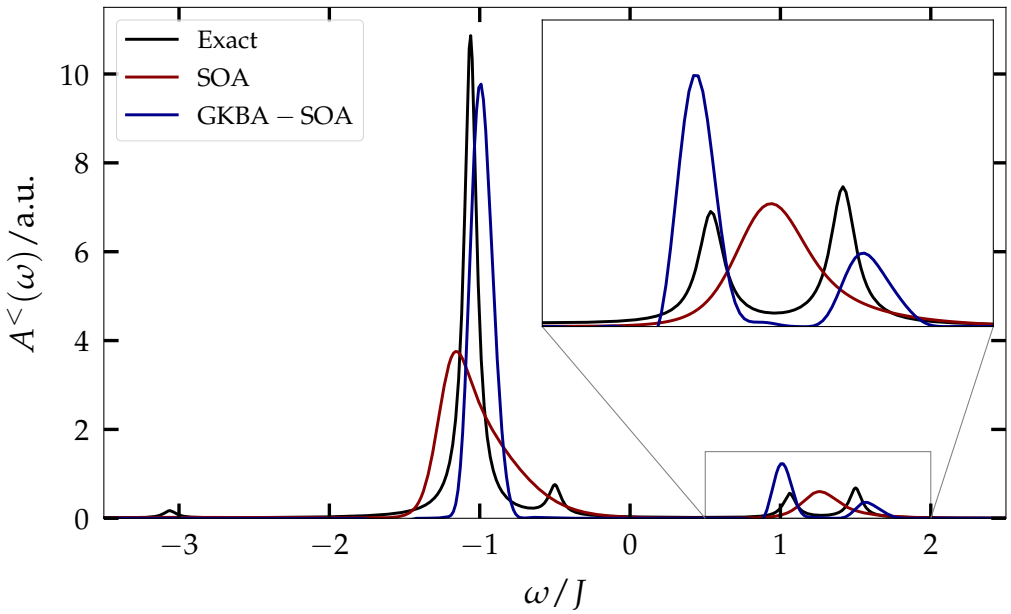

Figure 4.2-F4 – Photoemission spectrum (cf. Eq. (2.2-E98)) of a Hubbard dimer ($N_s = 2$) at half filling and $U = 1J$. The width of the probe pulse is set to $\kappa = 12.5J^{-1}$. The system is excited by a laser pulse given by Eq. (4.2-E2) with an amplitude of $E_0 = 0.5$. The NEGF results using the full two-time propagation (red) and GKBA (blue) combined with the SOA selfenergy are compared to the exact solution (black) described in Sec. 3.4.

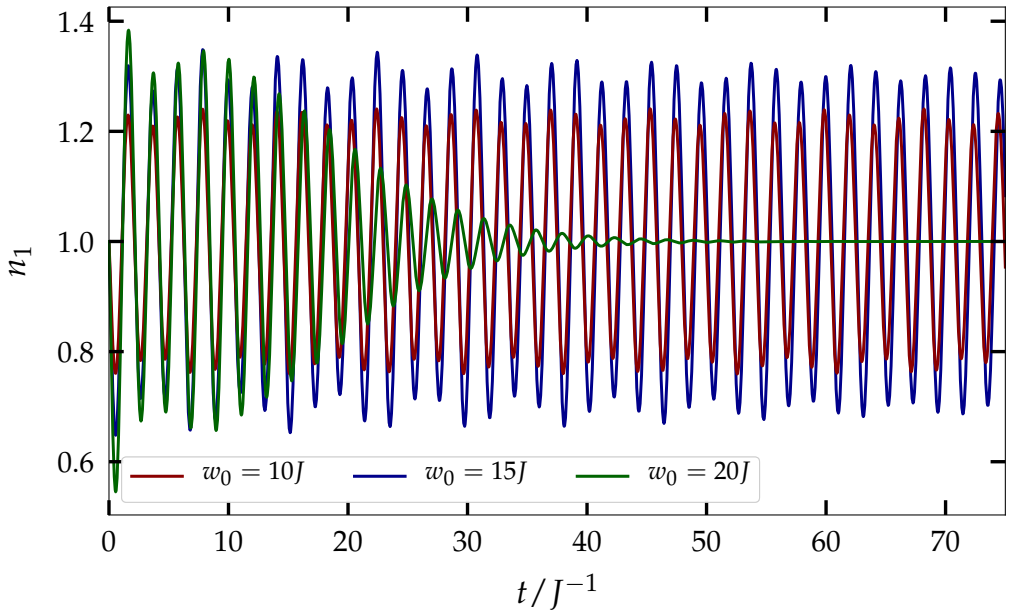

Figure 4.2-F5 – Density on the first site of a Hubbard dimer ($N_s = 2$) at half filling and $U = 2J$. The system is excited at $t_0 = 0$ by a sudden kick of the potential on the first site given by Eq. (4.2-E3). The strength of the excitation is given by w_0. The calculations are performed using the full two-time propagation combined with the SOA selfenergy.

4.2.2 Artificial damping problems

The topic of correlation induced artificial damping of the NEGF dynamics for finite Hubbard systems is well known and was frequently discussed in recent years [89, 107]. It was found that for all selfenergies which include correlation effects the KBEs develop a steady-state solution when propagating a strongly excited system. The reason for this lies in the selfconsistency of the propagation and the many-body approximations. Any correlation including selfenergy leads to the summation of unphysical contributions. In the exact solution all of these terms would cancel each other out. However, when using approximations for the selfenergy, artificial contributions remain and act as an energy reservoir that causes the damping of the dynamics for strong excitations [56].
The following part will focus on the influence of these artificial states on the photoemission spectrum. In Figs. 4.2-F5 and 4.2-F6 a Hubbard dimer at an interaction of $U = 2J$ is excited instantaneously at $t_0 = 0$ by a sudden kick of the potential on the first site:

$$f_i(t) \quad = \quad \delta_{i,1}\tilde{\delta}(t, t_0)\omega_0\,, \tag{4.2-E3}$$

with $\tilde{\delta}(t, t') = 1$ if $t = t'$ and $\tilde{\delta}(t, t') = 0$ otherwise. In Fig. 4.2-F5 the density on the first site is shown up to a propagation time of $t = 75J^{-1}$. The calculations were performed using the full propagation and the SOA selfenergy. For weak excitations, i.e. $\omega_0 = 10J$ and $\omega_0 = 15J$, the amplitude of the density oscillation remains constant except for temporary variations. However, for $\omega_0 = 20J$ the oscillation is strongly damped and an steady state is reached at $t \approx 55J^{-1}$.
The photoemission spectrum of the same setup is depicted in Fig. 4.2-F6 in logarithmic

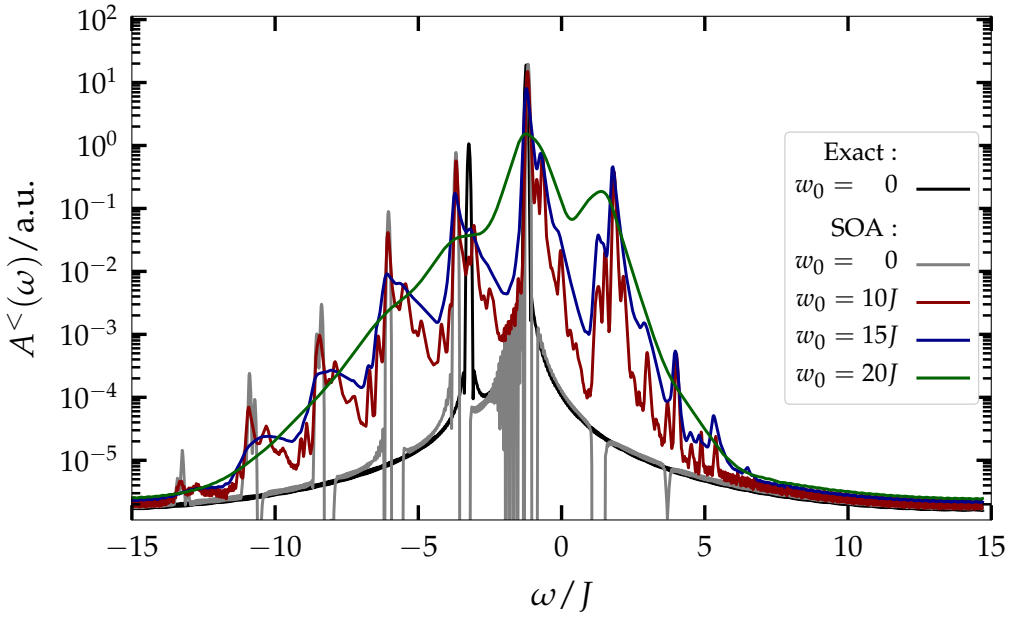

Figure 4.2-F6 – Photoemission spectrum of a Hubbard dimer ($N_s = 2$) at half filling and $U = 2J$ in logarithmic representation. The width of the probe pulse is set to $\kappa = 12.5J^{-1}$. The system is excited by a sudden kick of the potential on the first site given by Eq. (4.2-E3). The strength of the excitation is given by w_0. The NEGF calculations are performed using the full two-time propagation combined with the SOA selfenergy. Additionally, the ground state result is depicted for the NEGF approach (gray) and the exact solution (black) using the Lanczos propagation (cf. Secs. 2.1.1 and 3.4).

representation. Already for the ground state a striking observation can be made. While the exact solution only shows a main peak at $\omega \approx -1J$ and a secondary peak at $\omega \approx -3J$, the NEGF result displays a series of six equidistant and monotonically decreasing peaks between $\omega \approx -1J$ and $\omega \approx -13J$. These artificial contributions emerge due to the selfconsistent nature of the approximate solution.
When the system is excited, peaks occur above the Fermi energy. Furthermore, for weak excitations of $\omega_0 = 10J$ and $\omega_0 = 15J$ spectral weight is transferred to adjacent unphysical states. In the case of $\omega_0 = 20J$ this effect is even more pronounced so that no single peaks can be identified anymore. This redistribution of the spectral weight from physical to artificial states leads to the broadening of the spectrum. It can be understood as the dissipation of energy into unphysical energy levels that results in the damping of the dynamics and the development of a steady-state solution.

5 Graphene

For a long time the existence of graphene was not believed to be possible because the Mermin–Wagner theorem [108] postulates the instability of any 2D crystal at finite temperatures due to thermal fluctuations [109]. Nevertheless, in 2004 A.K. Geim and K.S. Novoselov were able to produce isolated monolayers of graphene by the use of adhesive tape on graphite [1]. For their *groundbreaking experiments regarding the two-dimensional material graphene* both researchers received the Nobel Prize in Physics in 2010 [110].
The unique mechanical, optical and electronic properties of graphene have been studied theoretically long before its first synthesis in 2004 [111–113]. However, especially in the last decade the interest in graphene has grown tremendously. Today the field of application ranges from electrodes in solar cells [2] over ultrafast photodetectors [6] to graphene-based flexible and transparent displays [114, 115]. Additionally, the use of graphene nanostructures in place of silicon in today's computational devices is hoped to increase the miniaturization in the fabrication of semiconductors [7].
This chapter will present the properties of graphene and finite graphene nanostructures, the so-called nanoribbons. Furthermore, the interesting effect of carrier multiplication is introduced that is essential for various applications of graphene, including solar energy harvesting [3–5]. To describe these nonequilibrium effects in finite graphene nanostructures, the Hubbard model introduced in Sec. 2.3 is extended to take into account the overlap of adjacent orbitals and hopping between up to third nearest neighboring sites.

5.1 Properties of graphene

The elementary constituent of graphene is Carbon, the sixth element of the periodic table. As such, it contains six electrons that are in the configuration $1s^2 2s^2 2p^2$ if the carbon is in the ground state. That is, two electrons are close to the nucleus and occupy the inner shell 1s while the other four fill the outer shells of the 2s and 2p orbitals. However, in the presence of other Carbon atoms one electron from the 2s orbital is excited to the 2p orbital in order to form covalent σ-bonds between the atoms. The quantum mechanical superposition of the remaining 2s orbital with n of the 2p states is called sp^n hybridization [116].
The structure of graphene is obtained by the planar sp^2 hybridization. The three hybridized orbitals are oriented in a plane and have mutual angles of 120°. This leads the carbon atoms to arrange in a hexagonal structure, the so-called honeycomb lattice. The remaining unhybridized 2p orbital is oriented perpendicular to the plane. Due to the non-negligible overlap between these orbitals of adjacent atoms, they form the so-called π-bonds [117]. These half-filled bands are responsible for most of graphene's interesting electronic properties.

5.1.1 Lattice structure

As mentioned above, the carbon atoms in graphene form a planar hexagonal lattice due to their sp^2 hybridization. In Fig. 2.3-F2 it was already discussed that the honeycomb lattice is not a Bravais lattice, i.e. two adjacent sites are not equivalent. Instead, it can be seen as a triangular Bravais lattice with a two-atom basis. This is illustrated in Fig. 5.1-F1(a) where the blue and red sites correspond to the A and B triangular sublattice, respectively. All nearest neighbors (NNs) of a site of the A sublattice are part of the B sublattice and vice versa. The vectors that connect a site to its NNs are given by

$$\boldsymbol{\delta_1} = \frac{a}{2}\left(-\sqrt{3}\boldsymbol{e}_x + \boldsymbol{e}_y\right), \tag{5.1-E1}$$

$$\boldsymbol{\delta_2} = \frac{a}{2}\left(\sqrt{3}\boldsymbol{e}_x + \boldsymbol{e}_y\right), \tag{5.1-E2}$$

$$\boldsymbol{\delta_3} = -a\boldsymbol{e}_y, \tag{5.1-E3}$$

where the distance between neighboring carbon atoms is $a = 0.142\,\mathrm{nm}$ [118]. The basis vectors of the triangular lattice are

$$\boldsymbol{a_1} = \frac{\sqrt{3}a}{2}\left(-\boldsymbol{e}_x + \sqrt{3}\boldsymbol{e}_y\right), \tag{5.1-E4}$$

$$\boldsymbol{a_2} = \frac{\sqrt{3}a}{2}\left(\boldsymbol{e}_x + \sqrt{3}\boldsymbol{e}_y\right), \tag{5.1-E5}$$

with the lattice spacing $\tilde{a} = \sqrt{3}a = 0.24\,\mathrm{nm}$ between two sites of the same sublattice [119]. Using the triangular lattice one can define a reciprocal lattice for the honeycomb structure. It is spanned by the basis vectors

$$\boldsymbol{b_1} = \frac{2\pi}{\sqrt{3}a}\left(-\boldsymbol{e}_x + \frac{\boldsymbol{e}_y}{\sqrt{3}}\right), \tag{5.1-E6}$$

$$\boldsymbol{b_2} = \frac{2\pi}{\sqrt{3}a}\left(\boldsymbol{e}_x + \frac{\boldsymbol{e}_y}{\sqrt{3}}\right) \tag{5.1-E7}$$

and is again a hexagonal lattice. The first Brillouin zone (BZ) for the honeycomb lattice of graphene is depicted in Fig. 5.1-F1(b). The points of high symmetry are given by

$$\boldsymbol{M} = \frac{2\pi}{3a}\boldsymbol{e}_y, \tag{5.1-E8}$$

$$\boldsymbol{K} = \frac{2\pi}{3a}\left(-\frac{\boldsymbol{e}_x}{\sqrt{3}} + \boldsymbol{e}_y\right), \tag{5.1-E9}$$

$$\boldsymbol{K'} = \frac{2\pi}{3a}\left(\frac{\boldsymbol{e}_x}{\sqrt{3}} + \boldsymbol{e}_y\right) \tag{5.1-E10}$$

and Γ at the origin. The so-called Dirac points are located at the six corners of the first BZ and are denoted as K and K' alternatingly due to their different chiralities [120]. The electronic properties of graphene are significantly determined by the cone-like form of the band structure around these points, the so-called Dirac cones. Due to the linear dispersion in the vicinity of the Dirac points, low-energy electrons in graphene behave like relativistic massless fermions [111, 113] and can be described by a Dirac equation. For a better understanding of this, the following part focuses on the energy dispersion of graphene within the tight-binding approximation.

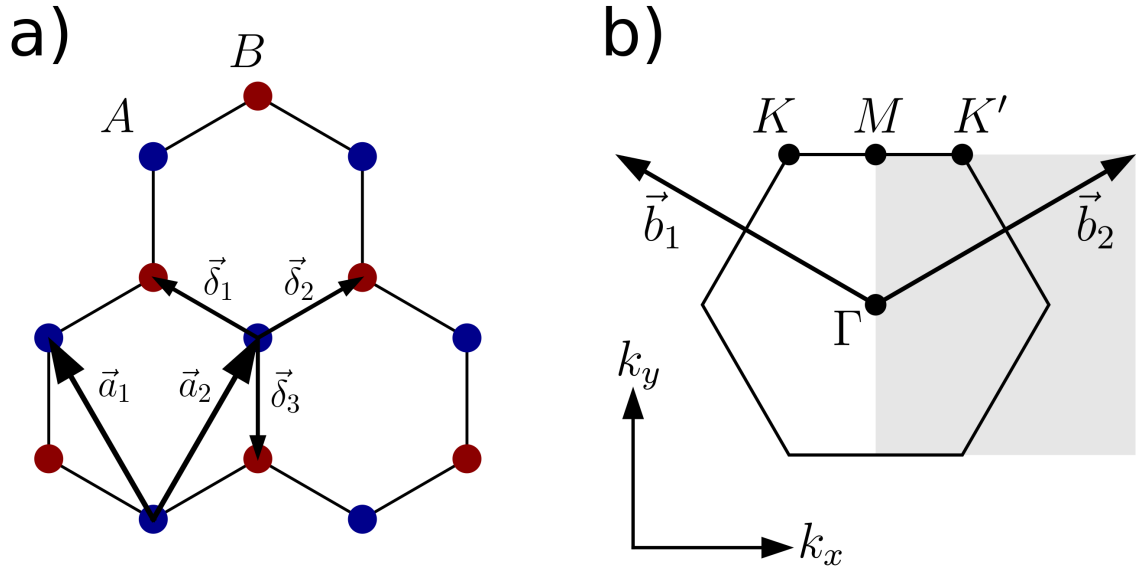

Figure 5.1-F1 – a) Lattice structure of graphene. The honeycomb lattice is not a Bravais lattice. It consists of two triangular Bravais sublattices A (blue) and B (red). Thus, it can be seen as a triangular lattice with a two-point basis. The vectors are given by Eqs. (5.1-E1) to (5.1-E5).
b) First Brillouin zone of graphene. The reciprocal lattice of the honeycomb lattice is again a hexagonal lattice. The basis vectors are given by Eqs. (5.1-E6) and (5.1-E7), the points of high symmetry by Eqs. (5.1-E8) to (5.1-E10), Γ is at the origin. The gray shaded area marks an alternative Brillouin zone.

5.1.2 Tight-binding description

In the graphene lattice three electrons per carbon atom form strong covalent σ-bonds with neighboring atoms while one electron is part of the π-bond that determines the electronic properties of graphene at low energies such as optical excitations [119]. Because the π-orbitals are perpendicular to the graphene plane, they are localized at the atomic positions. Thus, it is a reasonable choice to describe the π-bands in the tight-binding model that was already introduced in Sec. 2.3.2. The σ energy bands are far away from the Fermi energy and are therefore not considered in the following.
If one only allows hopping between adjacent sites, which corresponds to the standard Hubbard model presented in Sec. 2.3, the dispersion relation of the π-electrons of graphene within the tight-binding approximation is given by [117]

$$E(\boldsymbol{k}) = \pm J \sqrt{3 + 2\cos\left(\sqrt{3}k_y a\right) + 4\cos\left(\frac{\sqrt{3}}{2}k_y a\right)\cos\left(\frac{3}{2}k_x a\right)}, \quad \text{(5.1-E11)}$$

where J is the hopping amplitude of the Hubbard model and a is the distance between neighboring carbon atoms. The energy dispersion within the first BZ is depicted in Fig. 5.1-F2(a) where the Dirac cones are clearly visible at the high symmetry points K and K'. In Fig. 5.1-F2(b) a cut through the dispersion relation is shown. Here, it is apparent that the energy dispersion contains two separate bands, the valence and the

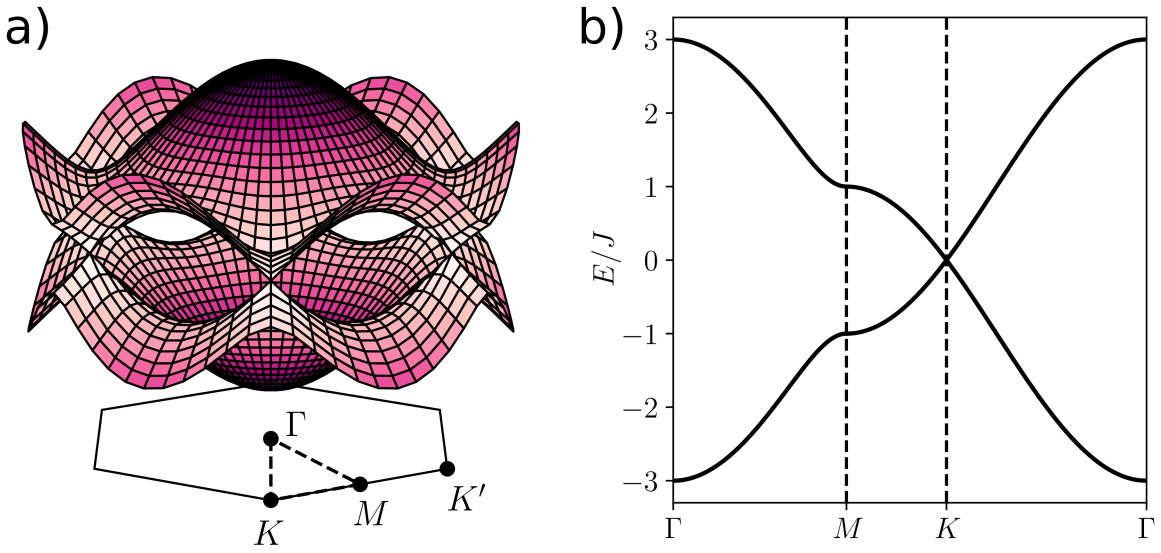

Figure 5.1-F2 – a) Energy dispersion (cf. Eq. (5.1-E11)) of graphene within the tight-binding approximation for only nearest neighbor hopping. The dispersion is shown for $k \leq \frac{8\pi}{5\sqrt{3}}$, i.e. slightly more than the first BZ, to make the Dirac cones at K and K' better visible. The dashed line marks the path for the cut through the dispersion shown in b).
b) Cut through the dispersion marked by the dashed line in a).

conduction band which correspond the minus and plus sign in Eq. (5.1-E11), respectively. The two bands touch only in the symmetry points K and K' and form the Dirac cones. The aforementioned linear dispersion in the vicinity of these points is also clearly visible in Fig. 5.1-F2(b). The symmetry of the two bands corresponds to the particle-hole symmetry that is given because only hopping between nearest neighbors is considered in the derivation of Eq. (5.1-E11) [117]. As expected, the bandwidth of graphene within the tight-binding approximation is $6J$ (cf. Fig. 2.3-F2 for a honeycomb lattice).

5.2 Graphene nanoribbons

Due to its exceptional electronic and transport properties, graphene is a promising candidate material for a lot of future technological applications. However, as graphene is a semimetal, its zero bandgap prevents the realization of next-generation graphene-based nanoelectronics [8]. Therefore, a lot of effort was put into creating semiconducting graphene materials that still exhibit its remarkable transport properties. While some methods focus on substrate-induced [10, 11] or strain-induced bandgaps [12, 13], the most promising approach is obtaining a bandgap through the effect of quantum confinement in finite graphene nanostructures [14, 15].
In this thesis, the focus lies on the so-called graphene nanoribbons (GNR) which are quasi-one-dimensional slices of graphene. Because of their typical width of only a few nanometers they exhibit various remarkable properties such as enhanced electron correlations due to

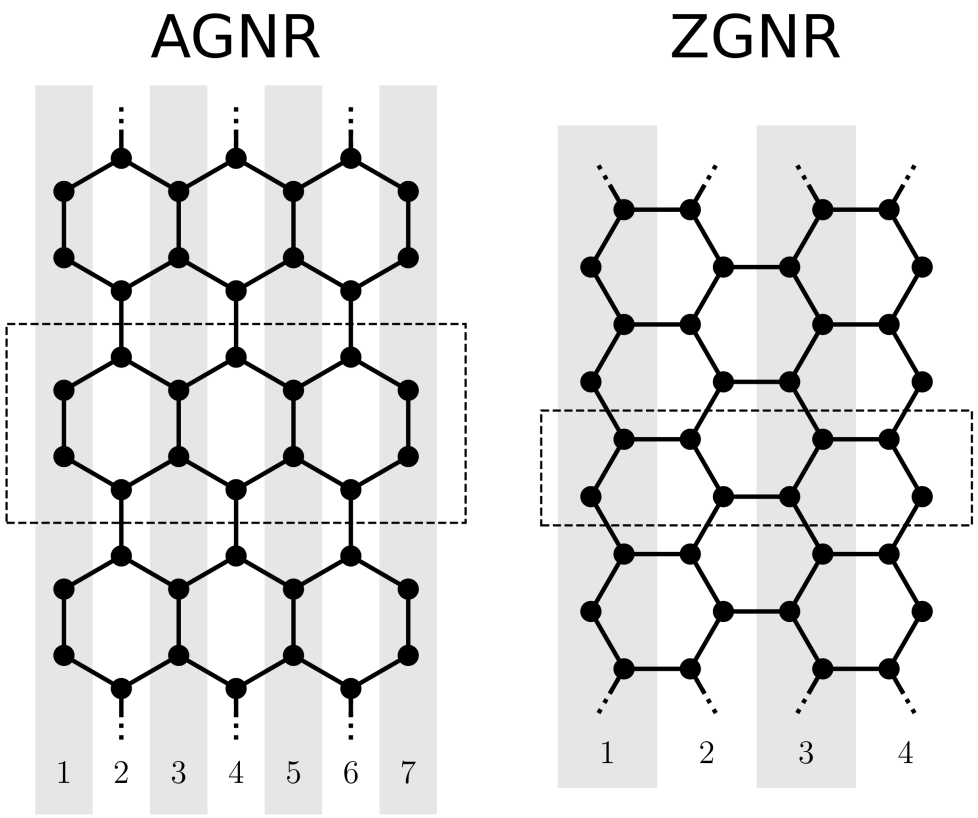

Figure 5.2-F1 – Illustration of the structure of armchair graphene nanoribbons (AGNR) and zigzag graphene nanoribbons (ZGNR). The width N of the graphene ribbons is defined as the number of dimer lines and the number of zigzag lines for AGNR and ZGNR, respectively. The dashed rectangles define the unit cells.

quantum size effects [102].
The electronic properties and especially the low energy spectrum of the π-electrons is strongly influenced by the edge structure of the nanoribbons. Depending on the shape of the edges one distinguishes between armchair graphene nanoribbons (AGNR) and zigzag graphene nanoribbons (ZGNR). An illustration of both types is shown in Fig. 5.2-F1. The width N of the ribbons is defined as the number of dimer lines for AGNR and the number of zigzag lines for ZGNR. It was found that for the two individual types of nanoribbons the bandgap shows a completely different dependence on the width N [121]. While ZGNRs are always metallic, i.e. $E_{\text{gap}} = 0$, AGNRs exhibit a vanishing bandgap only in the case of $N = 3M - 1$, where M is an integer [122][22]. In all other cases AGNRs are found to be semiconducting with a bandgap that can be tuned by their width. Therefore, especially nanoribbons with an armchair edge are interesting for the development of next-generation electronics [20].
Because of their tuneable bandgap, mainly AGNRs are studied in the scope of this work. Thus, in the following the band structure of these type of GNRs is analyzed within the tight-binding approximation. The dangling bonds at the edges are assumed to be

[22] It should be noted that this is true only if the ribbons have a considerable length. In this thesis, AGNRs with a width of $N = 5$ are studied. Although they meet the above condition for a metallic behavior, they were found to have a non-zero bandgap due to there finite length of only a few carbon atoms.

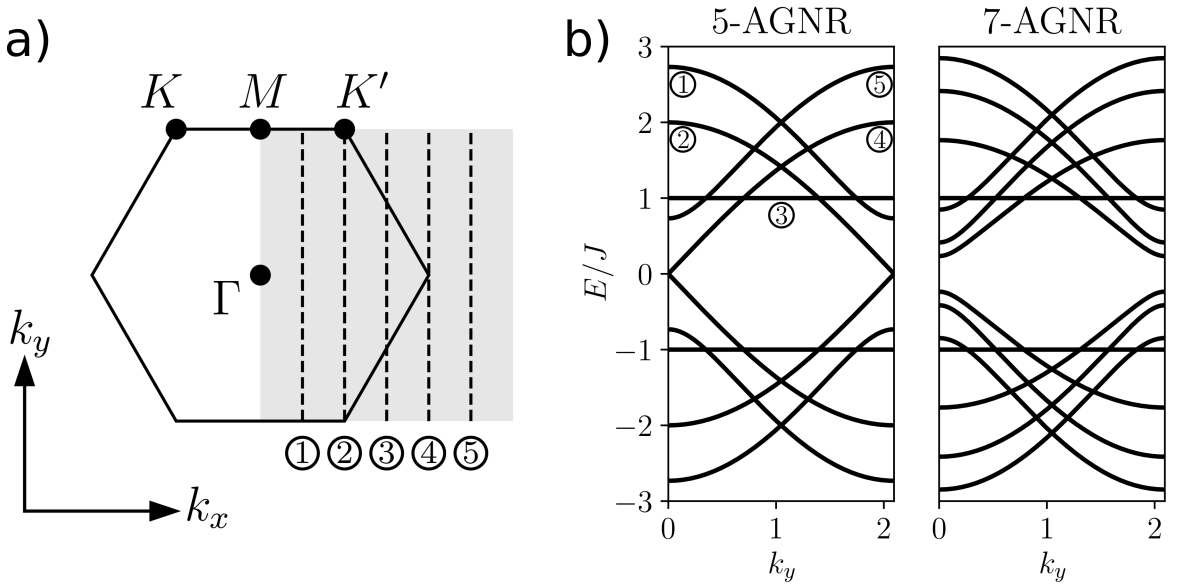

Figure 5.2-F2 – a) Discrete sampling of the first BZ for an armchair GNR of width $N = 5$ (5-AGNR). The gray shaded area marks an alternative BZ (cf. Fig. 5.1-F1(b)). Due to the finite width of the ribbon it is sampled at only five discrete values of k_x given by Eq. (5.2-E1) (dashed lines).
b) Band structure of a 5-AGNR and a 7-AGNR. The individual bands correspond to the discrete values of k_x (cf. Eq. (5.2-E1) and Fig. 5.1-F1(a)). The 5-AGNR is metallic while the 7-AGNR has a non-zero bandwidth and shows semiconducting behavior.

terminated by hydrogen atoms. This way they do not contribute to the energy levels near the Fermi energy and can be neglected.
The energy dispersion of planar graphene within the TB method is given by Eq. (5.1-E11). Due to the finite width of the nanoribbons, the momentum in the corresponding dimension can only attain certain discrete values given by [123]

$$k_x = \frac{2\pi}{\sqrt{3}} \frac{n}{N+1} \qquad n = 1, \ldots, N\,, \tag{5.2-E1}$$

where N is the width of the AGNR, i.e. the number of dimer lines. A vivid illustration for the case of $N = 5$ is shown in Fig. 5.2-F2(a). It it apparent that in this case the K and K' points are sampled which is the reason why, for the considered width of $N = 5$, an AGNR of considerable length is metallic. In Fig. 5.2-F2(b) the corresponding band structure is depicted where one band corresponds to one sampling path at a given k_x. Here, it is obvious that the bandgap of the 5-AGNR vanishes because the Dirac points are included in the sampling paths denoted by 2 and 4. In contrast, the 7-AGNR is semiconducting since for $N = 7$ the discrete k_x, given by Eq. (5.2-E1), do not cut through the Dirac points.

Another type of graphene nanostructures are the so-called carbon nanotubes (CNT)[23]. A CNT can be seen as a rolled up GNR that forms a hollow cylinder. As such, it exhibits

[23] They are named carbon instead of graphene nanotubes for historic reasons. CNTs were studied long before graphene was first produced experimentally in 2004 [124].

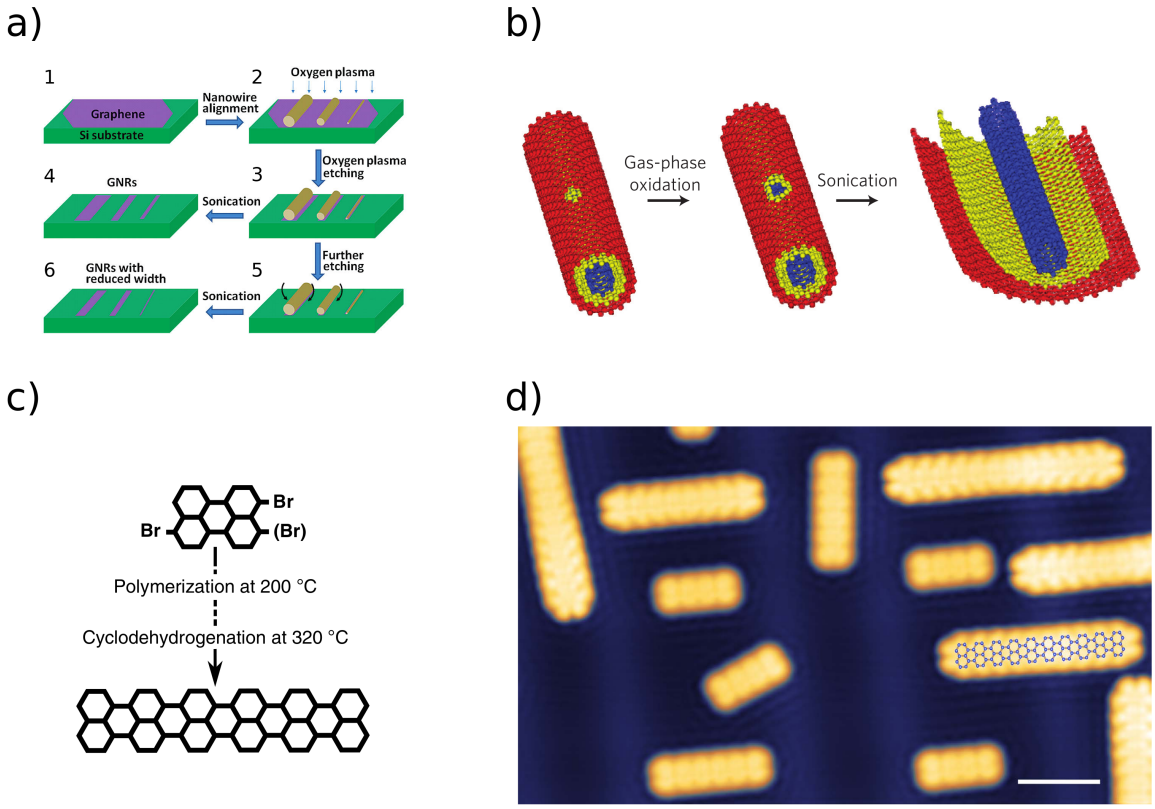

Figure 5.2-F3 – Illustration of different approaches to produce GNRs experimentally. a) Etching graphene with oxygen plasma using silicon nanowires as etch mask. Taken from Ref. [16]. b) Unzipping of multiwalled CNTs by oxidation and sonication. Taken from Ref. [17]. c) Bottom-up approach: starting from the molecular precursor dibromoperylene $C_{20}H_{10}Br_2$, well defined GNRs are created in a two step procedure. Taken from Ref. [19]. d) Scanning tunneling microscopy (STM) image of the 5-AGNRs produced by the procedure shown in c). The white scale bar corresponds to 2 nm. Taken from Ref. [19].

similar properties as a nanoribbon. More information on the topic of CNTs can be found in Ref. [125].

5.2.1 Synthesis of graphene nanoribbons

While the theoretical understanding of graphene nanoribbons advanced over the last decades [14, 121, 123, 126], the production of well-defined GNRs was achieved only recently [19, 20]. Today, there are countless different techniques for the synthesis of nanoribbons with different width and edge structure [18]. Here, we will focus on the three most common approaches that are depicted in Fig. 5.2-F3.

Etching of graphene [16]: Starting from a graphene layer on a silicon substrate, silicon nanowires are aligned onto the graphene to function as a physical etch mask. The unprotected graphene is etched away using an oxygen plasma. After the etching procedure the silicon nanowires can be removed by a brief sonication. The width of the resulting GNRs on the silicon substrate depends on the size of the used nanowires as well as on the duration of the etching and is typically less than 10 nm. An illustration is depicted in Fig. 5.2-F3(a).

Unzipping of CNTs [17]: The first large-scale synthesis of CNTs was realized in 1992 [127] during an arch discharge. Since then a lot of progress was made so that today CNTs are commercially available [128]. Therefore, this approach uses multiwalled CNTs as a precursor to produce GNRs. First, the nanotubes are locally damaged by oxidation in air at around 500 °C. Second, a mechanical sonication in an organic solvent is used to unzip the nanotube along its axis. The width and the edge structure of the resulting GNRs are determined by the type of the CNTs used. Due to the varying size of the available nanotubes the resulting width ranges from 10 nm to 20 nm [18]. An illustration of this procedure is shown in Fig. 5.2-F3(b).

Bottom-up approach [19]: The third approach was developed only in recent years [129, 130] but, at the same time, is the most promising. Starting from a molecular precursor, GNRs of well defined width can be synthesized on a substrate in a two step procedure. In the example depicted in Fig. 5.2-F3(c) and Fig. 5.2-F3(d) the substrate used was Au(111) with the precursor dibromoperylene $C_{20}H_{10}Br_2$. In the first step at 200 °C the bromine is detached through dehologenation. Further heating to 320 °C leads to dehydrogenation resulting in the formation of well defined 5-AGNR with a width well below 1 nm. Here, the choice of the molecular precursor determines the structure of the resulting GNRs.

5.3 Carrier multiplication in graphene

The short-time nonequilibrium dynamics in graphene after an excitation by, for example, a laser pulse are significantly affected by the electron-electron interactions such as Coulomb induced carrier scattering. These scattering events can be distinguished into intraband, interband and Auger processes [131, 132]. Scattering interactions where both carriers remain in their initial band are denoted as intraband, whereas during an interband event both carriers perform a band transition. During the Auger processes one of the scattering electrons changes its band while the other remains in its initial band. Thus, Auger scattering is qualitatively different from all other Coulomb mediated scattering channels since it is the only process that changes the total number N_{CB} of charge carriers in the conduction band. Depending on how N_{CB} is changed, one distinguishes Auger recombination (AR) and impact excitation (IE). The latter describes a scattering process with one electron initially in the valence and one in the conduction band. During the scattering event the transferred energy excites the energetically lower electron from the valence to the conduction band which leads to an increase of the number of charge carriers

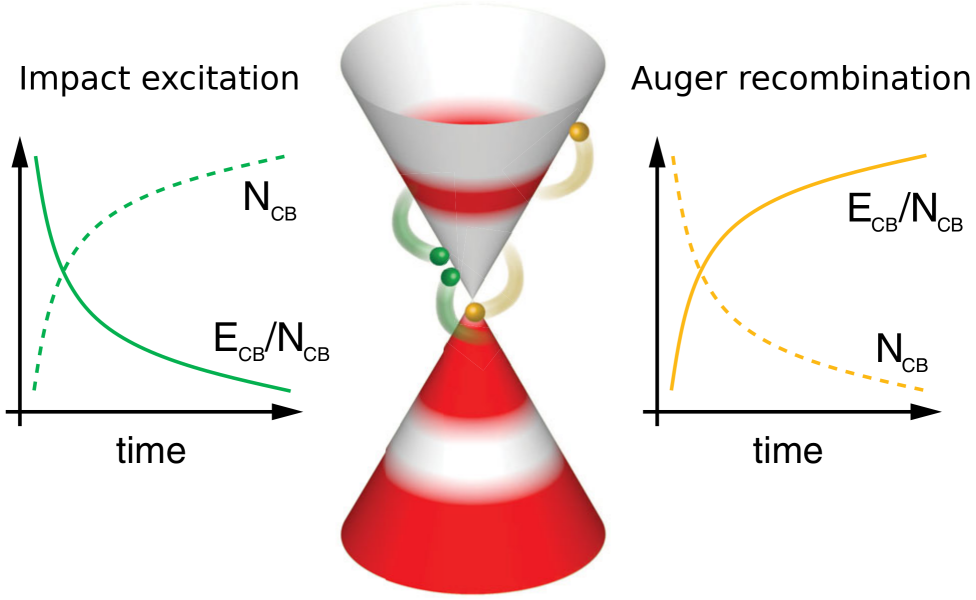

Figure 5.2-F4 – Illustration of the two Auger scattering processes, namely impact excitation (IE) and Auger recombination (AR), in the vicinity of a Dirac cone. In the case of IE (green) an electron-hole pair is generated which leads to an increase of the number of charge carriers in the conduction band N_{CB}. As a consequence the mean energy of electrons in the conduction band $E_{\mathrm{CB}}/N_{\mathrm{CB}}$ is reduced. The reverse process is denoted as AR (yellow). Graphic taken from Ref. [24].

N_{CB}. This can also be described as the creation of an electron-hole pair while the reverse process, the annihilation of an electron-hole pair, is denoted as Auger recombination. Both types of Auger scattering are illustrated in Fig. 5.2-F4.
Of particular interest for the development of photodetectors or photovoltaic devices is the process of impact excitation since it allows for the generation of multiple charge carriers by a single photon, which is often referred to as carrier multiplication (CM) [133]. In conventional semiconductors Auger processes are either energetically forbidden or extremely unlikely and inefficient. In graphene, however, they are permitted and efficient due to the linear shape of the band structure around the Dirac points [131]. Additionally, due to carrier confinement in finite structures such as quantum dots, nanotubes or nanoribbons, the rate of Auger processes is further enhanced while the electron-phonon interaction is reduced [134]. These effects make graphene a promising material for photovoltaic devices since it might improve the efficiency of solar cells beyond the Shockley–Queisser limit [135, 136]. So far, the effect of CM has been predicted in graphene [137] and various graphene nanostructures, namely quantum dots [138], nanotubes [139] and nanoribbons [140]. In the case of monolayer graphene, quantum dots and nanotubes it has also been confirmed experimentally [22, 141, 142].
In 2015 Gierz *et al.* [24] performed femtosecond time- and angle-resolved photoemission spectroscopy (TR-ARPES) measurements on monolayer graphene to measure the density and average kinetic energy of carriers in the conduction band directly. Their results are shown in Fig. 5.3-F1. It was found that in a time window of approximately 26 fs after the excitation by a laser pulse the dynamics of the system is dominated by the process of IE. After that, the state decays through AR and electron-phonon scattering. For homogeneous

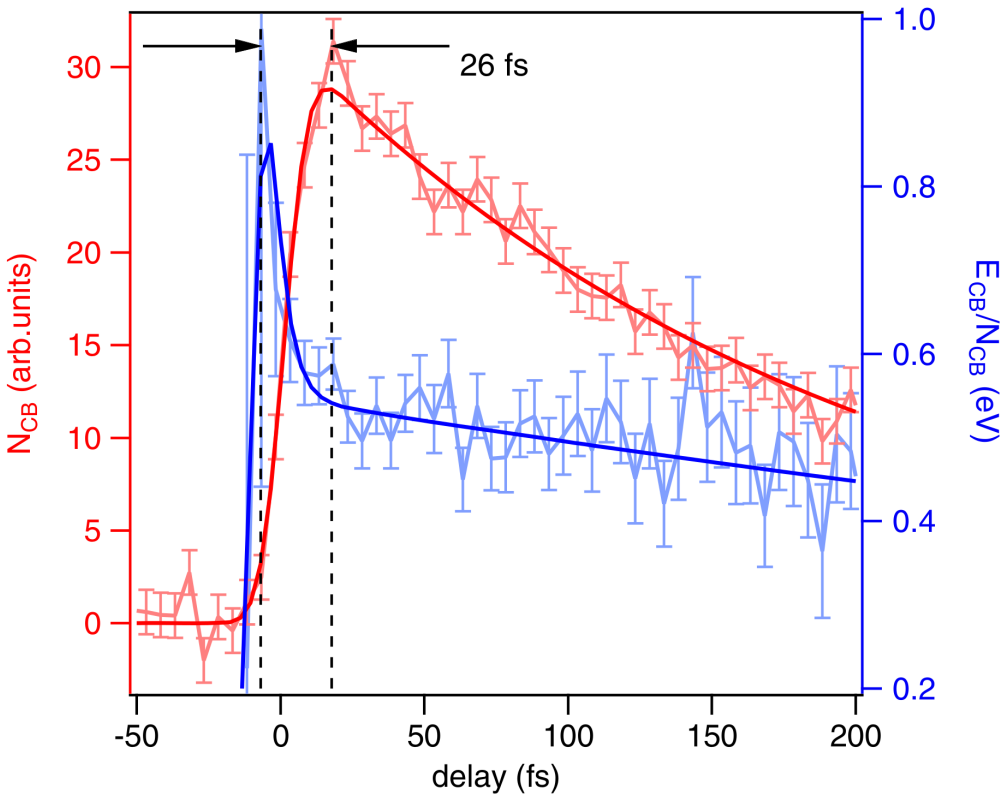

Figure 5.3-F1 – Total number of carriers inside the conduction band (N_{CB}, red) and their average kinetic energy ($E_{\mathrm{CB}}/N_{\mathrm{CB}}$, blue) for graphene after the excitation by a laser pulse. In a windows of 26 fs after the excitation N_{CB} keeps increasing while $E_{\mathrm{CB}}/N_{\mathrm{CB}}$ already decreases which indicates IE. After that, the system thermalizes through AR and electron-phonon scattering. Experimental results of TR-ARPES measurements performed by Gierz *et al.* in Ref. [24].

graphene such behavior was already predicted theoretically by Winzer in 2013 [131] using graphene Bloch equations within the tight-binding approximation. However, until now no theoretical approach exists that can describe the correlated nonequilibrium dynamics of finite graphene nanostructures. In order to create a numerical method that is capable of accurately simulating those systems, in the following part the standard Hubbard model presented in Sec. 2.3 is extended and combined with the NEGF approach.

5.4 Extended Hubbard model for finite graphene nanostructures

Finite graphene nanostructures, especially in nonequilibrium, are extremely complex, inhomogeneous systems that put high requirements on any theory that attempts to describe them accurately. Despite their finite width they can contain up to several hundreds of carbon atoms. Therefore, one has to choose a basis that simultaneously takes into account all important features of the bandstructure and is simple enough to simulate the dynamics of such large systems numerically for several femtoseconds. A convenient approach is given by the Hubbard model that was already presented in Sec. 2.3. Due to its

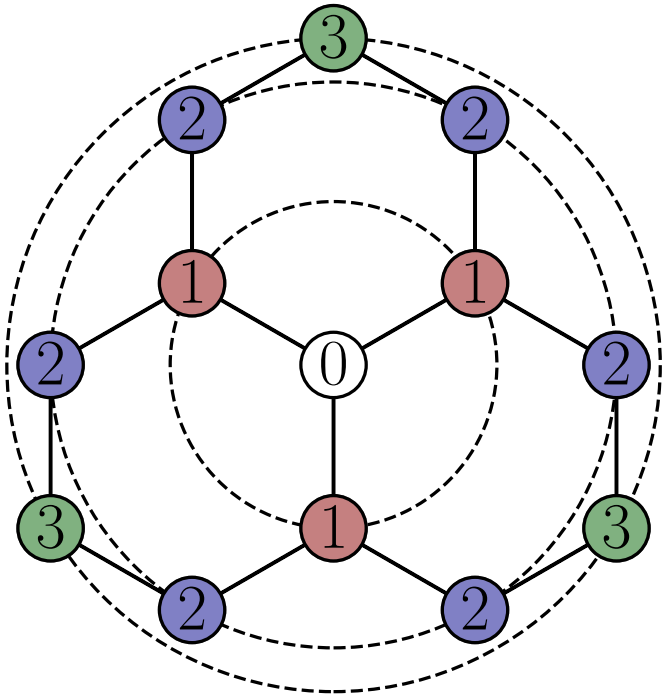

Figure 5.3-F2 – Illustration of the position of neighboring sites in graphene. The three nearest neighbors (1NN) of the white site are marked in red, the six second nearest neighbors (2NN) in blue and the three third nearest neighbors (3NN) in green.

simplistic nature it greatly reduces the numerical effort needed for the description of finite systems compared to more sophisticated basis sets like the Kohn–Sham functions [143]. Nevertheless, it was shown on many occasions that the Hubbard model is able to reproduce both the ground state [144] and transport properties [145] of GNRs and CNTs correctly. However, for this, one has to extent the standard Hubbard model presented in Sec. 2.3 to take into account the orbital overlap and hopping between up to third nearest neighbors[24]. To consider hopping beyond nearest neighbors one has to modify the hopping matrix t that occurs in the single-particle Hamiltonian (cf. Eq. (3.2-E8)). For hopping between up to third nearest neighboring (3NN) sites t is given by

$$t_{ij} = \begin{cases} t_1 \text{ if } (i,j) \text{ is 1NN} \\ t_2 \text{ if } (i,j) \text{ is 2NN} \\ t_3 \text{ if } (i,j) \text{ is 3NN} \\ 0 \text{ else} \end{cases} . \tag{5.4-E1}$$

The parameters t_1, t_2 and t_3 can be determined by fitting the tight-binding band structure to density functional theory (DFT) calculations [146]. The parameter sets that are used in this work are given in Tab. 5.4-T1.
Including the orbital overlap into the Hubbard model can be done in form of an overlap

[24] These improvements do not increase the numerical effort of the simulation.

matrix $\boldsymbol{S}$ that is defined as

$$S_{ij} = \delta_{i,j} + \begin{cases} s_1 \text{ if } (i,j) \text{ is 1NN} \\ s_2 \text{ if } (i,j) \text{ is 2NN} \\ s_3 \text{ if } (i,j) \text{ is 3NN} \\ 0 \text{ else} \end{cases} . \tag{5.4-E2}$$

As the name suggests, $\boldsymbol{S}$ describes the overlap between orbitals on different sites. In the case of orthogonal basis states, the overlap vanishes and $\boldsymbol{S} = \mathbb{1}$. However, in a correct description of graphene the finite overlap of the π-orbitals has to be taken into account. Again, the parameters s_1, s_2 and s_3 that are obtained through a comparison with DFT results are given in Tab. 5.4-T1.
A non-vanishing orbital overlap is well known for the case of molecular orbitals in quantum chemistry [147]. In such a case the Hamiltonian $\boldsymbol{H}$ of the system is described by a generalized eigenvalue problem in a non-orthogonal basis [145]:

$$\boldsymbol{H} |\psi\rangle = E \boldsymbol{S} |\psi\rangle . \tag{5.4-E3}$$

If $\boldsymbol{S}^{-1}$ exists, this can be transformed into a standard eigenvalue problem

$$\underbrace{\boldsymbol{S}^{-1}\boldsymbol{H}}_{\tilde{\boldsymbol{H}}} |\psi\rangle = E |\psi\rangle . \tag{5.4-E4}$$

However, $\tilde{\boldsymbol{H}}$ is not generally Hermitian because the basis is still non-orthogonal. This can be solved by applying the symmetric Löwdin orthogonalization [148]. In a first step a transformation matrix $\boldsymbol{U}$ is defined as

$$\boldsymbol{U} = \boldsymbol{S}^{-\frac{1}{2}} . \tag{5.4-E5}$$

Because $\boldsymbol{S}$ is real and symmetric, one can show that

$$\boldsymbol{U}^\dagger \boldsymbol{S} \boldsymbol{U} = \mathbb{1} . \tag{5.4-E6}$$

Now, the generalized eigenvalue problem in Eq. (5.4-E3) can be transformed as

$$\begin{aligned} \boldsymbol{H} |\psi\rangle &= E \boldsymbol{S} |\psi\rangle \\ \boldsymbol{H} \underbrace{\boldsymbol{U}\boldsymbol{U}^{-1}}_{\mathbb{1}} |\psi\rangle &= E \boldsymbol{S} \underbrace{\boldsymbol{U}\boldsymbol{U}^{-1}}_{\mathbb{1}} |\psi\rangle \\ \underbrace{\boldsymbol{U}^\dagger \boldsymbol{H} \boldsymbol{U}}_{\boldsymbol{H}'} \underbrace{\boldsymbol{U}^{-1} |\psi\rangle}_{|\Psi\rangle} &= E \underbrace{\boldsymbol{U}^\dagger \boldsymbol{S} \boldsymbol{U}}_{\mathbb{1}} \underbrace{\boldsymbol{U}^{-1} |\psi\rangle}_{|\Psi\rangle} . \end{aligned} \tag{5.4-E7}$$

The standard eigenvalue problem in a diagonal basis now reads

$$\boldsymbol{H}' |\Psi\rangle = E |\Psi\rangle , \tag{5.4-E8}$$

where the new Hermitian Hamiltonian $\boldsymbol{H}'$ is given by

$$\boldsymbol{H}' = \boldsymbol{U}^\dagger \boldsymbol{H} \boldsymbol{U} . \tag{5.4-E9}$$

In a last step one can look at the connection between $\boldsymbol{H}'$ and the non-Hermitian Hamiltonian $\tilde{\boldsymbol{H}}$ defined in Eq. (5.4-E4):

Structure	Set	J/eV	t_1/J	t_2/J	t_3/J	s_1	s_2	s_3
2D Graphene	1NN	2.7	1	-	-	-	-	-
	3NN (Reich2002)	2.97	1	0.025	0.111	0.073	0.018	0.026
Graphene ribbons	3NN (Tran2017)	2.756	1	0.026	0.138	0.093	0.079	0.070

Table 5.4-T1 – Various parameter sets for the hopping (cf. Eq. (5.4-E1)) and overlap (cf. Eq. (5.4-E2)) matrix in the extended Hubbard model. For homogeneous graphene the parameters are taken from Reich *et al.* [149] and for GNRs from Tran *et al.* [146].

$$\begin{aligned} \boldsymbol{H}' &= \left(\boldsymbol{S}^{-\frac{1}{2}}\right)^{\dagger} \boldsymbol{H}\boldsymbol{S}^{-\frac{1}{2}} \\ &= \boldsymbol{S}^{-\frac{1}{2}}\boldsymbol{H}\boldsymbol{S}^{-\frac{1}{2}} \\ &= \boldsymbol{S}^{\frac{1}{2}}\underbrace{\boldsymbol{S}^{-1}\boldsymbol{H}}_{\tilde{\boldsymbol{H}}}\boldsymbol{S}^{-\frac{1}{2}} \\ &= \boldsymbol{U}^{-1}\tilde{\boldsymbol{H}}\boldsymbol{U} \end{aligned} \tag{5.4-E10}$$

It is apparent that the Löwdin orthogonalization includes the overlap matrix $\boldsymbol{S}$ in the new defined Hamiltonian. Additionally, a change of basis is performed using the transformation matrix $\boldsymbol{U}$. Thus, a general matrix quantity $\boldsymbol{A}$ can be transformed from the orthogonal to the non-orthogonal basis by the transformation

$$\boldsymbol{A} = \boldsymbol{U}\boldsymbol{A}'\boldsymbol{U}^{-1} \,, \tag{5.4-E11}$$

where $\boldsymbol{A}'$ is given in the orthogonal basis.

To apply this procedure to the Hubbard model and the NEGF approach, one has to define a new effective single particle Hamiltonian in an orthogonal basis

$$h^{\mathrm{eff}'} = \boldsymbol{U}^{\dagger} h^{\mathrm{eff}} \boldsymbol{U} \,, \tag{5.4-E12}$$

where $\boldsymbol{U}$ is given by Eq. (5.4-E5). Since the HF selfenergy is included in h^{eff}, this approach takes into account non-local interactions within the mean field level. However, all contributions beyond HF assume an on-site interaction to keep the numerical effort reasonable. Beside the new defined effective Hamiltonian $h^{\mathrm{eff}'}$ no additional changes have to be made to the propagation scheme of the KBEs. However, the new orthogonal basis in which the propagation of the KBEs is performed does not correspond to the sites of the Hubbard lattice. Therefore, after the calculation one has to transform $G^{<}$ and $G^{>}$ into the non-orthogonal basis of the Hubbard sites via Eq. (5.4-E11).

As already mentioned, the common approach to generate parameter sets for the hopping and overlap matrix is to compare TB calculations of the ground state band structure to more sophisticated DFT results. Because the energy dispersion strongly depends on the lattice structure of graphene (cf. Figs. 5.1-F2 and 5.2-F2), various parameter sets exist

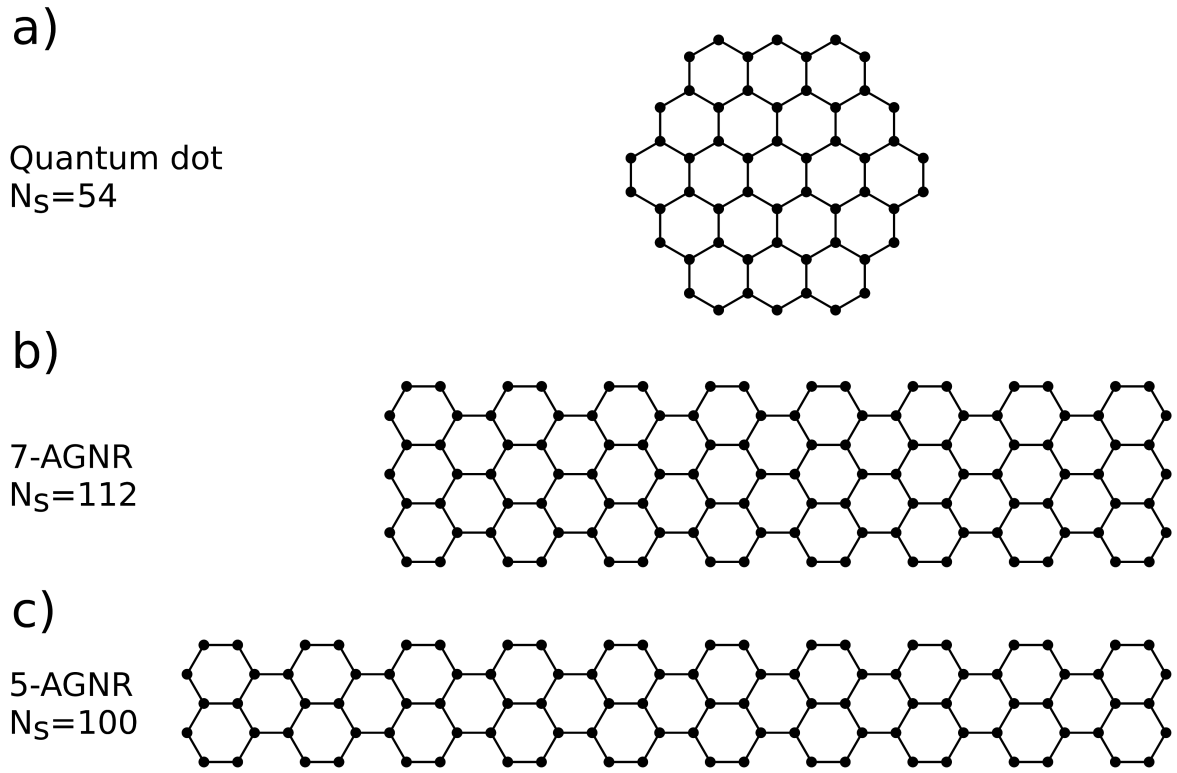

Figure 5.4-F1 – Finite graphene structures that are used to test the implementation of the extended Hubbard model and the parameter sets shown in Tab. 5.4-T1. The result for system a), b) and c) is shown in Figs. 5.4-F2, 5.4-F4 and 5.4-F3, respectively.

that were found to provide good results for either homogeneous or finite systems [146, 149, 150]. The parameter sets used in this work are presented in Tab. 5.4-T1. In addition to the standard Hubbard model that takes into account only nearest neighbor hopping, the set by Reich *et al.* [149] performs well for homogeneous graphene while Tran *et al.* [146] generated a parameter set specifically for finite graphene nanostructures such as GNRs. It should be noted that the parameters are not necessarily monotonic, i.e. for instance $t_1 > t_2$ but $t_2 < t_3$. This might be due to the similar distance of the second and third neighbor to the initial site which is illustrated in Fig. 5.3-F2 by the dashed lines. Additionally, the second neighboring site might be screened to some degree by the first neighbor.

It should be noted that the presented model does not include electron-phonon scattering. However, in the calculations presented in Sec. 6.2 a time frame of about 15 fs after the laser excitation is considered. In this regime relaxation due to electron-phonon processes is negligible as seen in Fig. 5.3-F1. Thus, disregarding such effects is justified here.

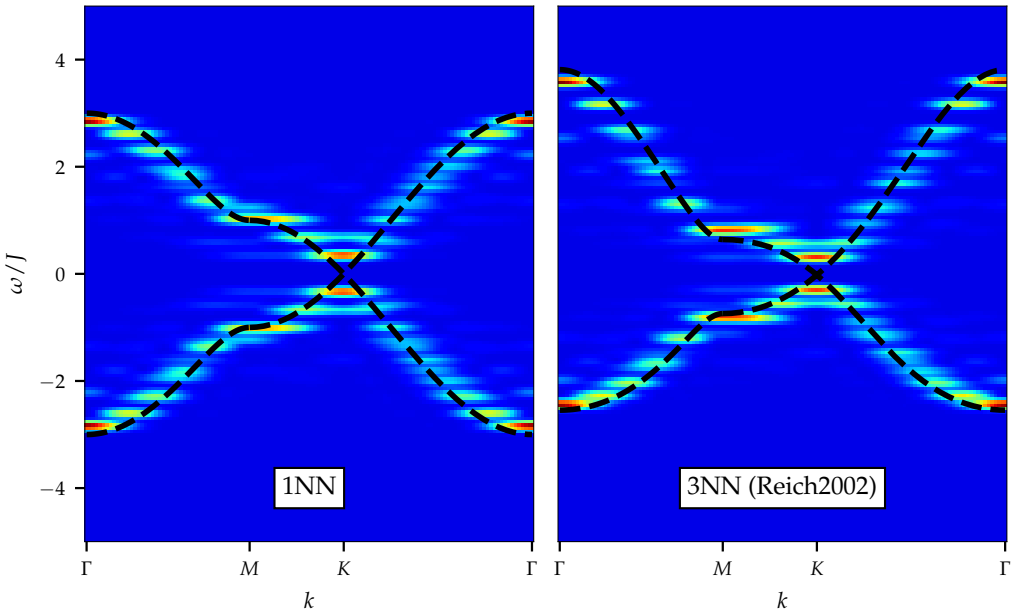

Figure 5.4-F2 – Energy dispersion (cf. Eq. (2.2-E97)) of the system depicted in Fig. 5.4-F1(a). The propagation time after the adiabatic switching is $T_{\text{end}} = 25J^{-1}$. The colormap corresponds to NEGF calculations for $U = 0$ while the black dashed lines represent analytical TB results for infinite homogeneous graphene [149]. The parameter sets are given in Tab. 5.4-T1.

5.4.1 Reproducing ground state properties

In order to test the implementation of the extended Hubbard model and to analyze the effects of the parameter sets including third nearest neighbor interaction on the band structure, in this part the ground state energy dispersion of the systems shown in Fig. 5.4-F1 is calculated using the NEGF approach. The NEGF calculations are performed for $U = 0$ to allow for a comparison with analytical TB results for infinite homogeneous graphene and GNRs with infinite length [149].
The parameter set by Reich *et al.* that performs well for homogeneous graphene is tested on a quantum dot of $N_{\text{s}} = 54$ sites depicted in Fig. 5.4-F1(a). This system was successfully used in the past to describe stopping power effects in homogeneous graphene [151]. The result is shown in Fig. 5.4-F2. If only nearest neighbor hopping is considered, the band structure exhibits a particle-hole symmetry as already shown in Fig. 5.1-F2(b). However, including second nearest neighbor hopping breaks this symmetry. This is due to the fact that graphene can be described as two triangular lattices and second nearest neighbor sites are part of the same sublattice as the initial site[25]. Additionally, the parameter set of Reich *et al.* changes the slope of the bands in the low energy regime around the Dirac points. In general, the NEGF results are in good agreement with the analytical TB dispersion for infinite homogeneous graphene marked as black dashed lines. The small deviations like a non-vanishing bandgap in the NEGF results are due to the finite size of the system.

[25] In the case of a vanishing overlap, including only first and third nearest neighbor hopping results in a symmetric band structure because in that case only hopping between different sublattices is allowed.

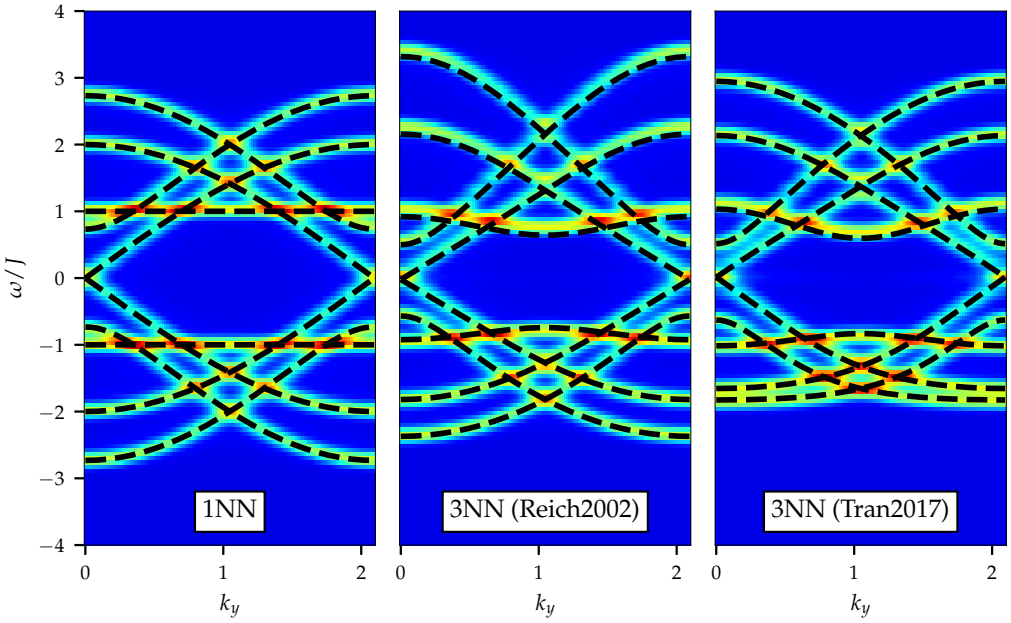

Figure 5.4-F3 – Energy dispersion (cf. Eq. (2.2-E97)) of the system depicted in Fig. 5.4-F1(c). The propagation time after the adiabatic switching is $T_{\text{end}} = 15J^{-1}$. The colormap corresponds to NEGF calculations for $U = 0$ while the black dashed lines represent analytical TB results for an 5-AGNR of infinite length [149]. The parameter sets are given in Tab. 5.4-T1. The individual bands are due to the discrete sampling of the BZ (cf. Fig. 5.2-F2).

In Fig. 5.4-F3 the different parameter sets are compared for an AGNR of $N_{\text{s}} = 100$ sites as depicted in Fig. 5.4-F1(c). The different bands are due to the discrete sampling of the BZ as shown in Fig. 5.2-F2. Again, the extended Hubbard model breaks the particle-hole symmetry for the parameter sets that take into account hopping beyond nearest neighbors. Here, it becomes apparent why it is important to chose the appropriate parameter set for a given system. Although the sets of Reich and Tran roughly agree on most parameters (e.g. t_2, t_3 and s_1), they show huge differences in the band structure. By comparison with DFT results it was found that the parameter set of Tran best describes GNRs [146]. Because the systems considered in this work are finite graphene nanostructures such as quantum dots and GNRs, the parameter set of Tran will be used for all following calculations. In general, the NEGF results are in excellent agreement with the analytic TB calculation for an infinite AGNR of the same width. There are only minor deviations due to finite size effects because the system of $N_{\text{s}} = 100$ sites already is of considerable length.

Until now all calculations within the NEGF approach have been performed for $U = 0$ to compare the results to analytic TB band structures. However, it is well known that the DFT approach that is used to obtain the parameter sets for the extended Hubbard model systematically underestimates the bandgap of finite graphene systems [14]. Using the NEGF approach one can increase the bandgap by including correlations through appropriate selfenergy approximations like SOA or GWA. It has already been shown in Fig. 4.1-F5 that the width of the Hubbard gap depends on the interaction U. Therefore, by adjusting U it is possible to reproduce the correct bandgap for any GNR using the NEGF approach.

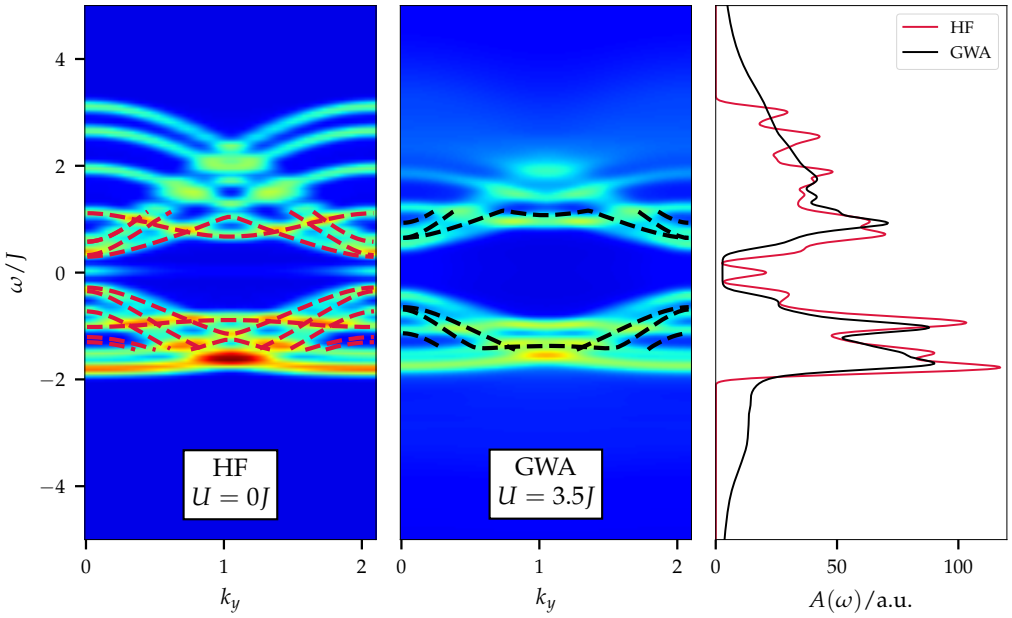

Figure 5.4-F4 – Left and middle panel: Energy dispersion (cf. Eq. (2.2-E97)) of the system shown in Fig. 5.4-F1(b). The propagation time after the adiabatic switching is $T_{\text{end}} = 15J^{-1}$. The colormap corresponds to NEGF calculations using the HF and GWA selfenergy with $U = 0$ and $U = 3.5J$, respectively. The dashed red (black) lines in the left (middle) panel show the results of DFT (GW) calculations by Wang *et al.* [152] for an infinite AGNR of the same width. The right panel shows the DOS for the NEGF results.

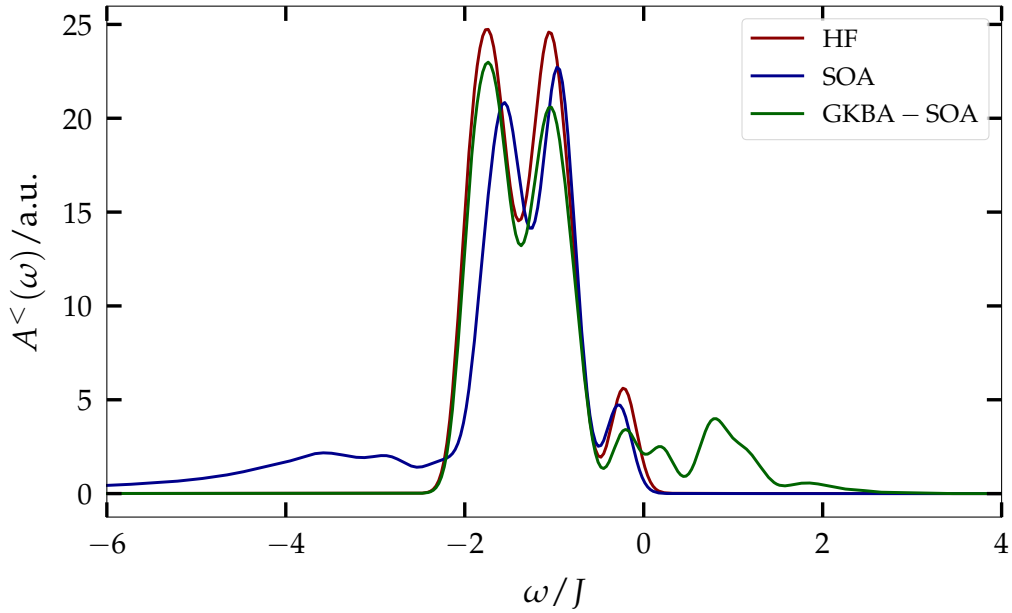

Figure 5.4-F5 – Ground state photoemission spectrum (cf. Eq. (2.2-E98)) of a 5-AGNR containing $N_s = 30$ sites for $U = 3.5J$. The width of the probe pulse is set to $\kappa = 22.5J^{-1}$. As already seen in Sec. 4.1.3 the GKBA shows excitations above the Fermi energy at $\omega = 0$.

In Fig. 5.4-F4 the band structure of a 7-AGNR with $N_s = 112$ (cf. Fig. 5.4-F1(b)) is calculated using the NEGF approach and compared to DFT and GW results by Wang *et al.* [152] for an infinite AGNR of the same width. The band structure for the HF selfenergy and an interaction of $U = 0$ is in perfect agreement with the DFT result. This is hardly surprising since the parameters of the extended Hubbard model were generated to reproduce the DFT results for GNRs in the tight-binding limit. Using the GWA selfenergy combined with an interaction of $U = 3.5J$ significantly increases the bandgap which is best visible in the DOS in the right panel of Fig. 5.4-F4. Especially the bands above the Fermi energy are in good agreement with the GW result of Wang *et al.*, while the lower bands show some deviations. In theory, one could increase the interaction further to achieve an even better agreement. However, on the one hand this would make the propagation numerically more challenging and on the other hand the NEGF approach fails to describe systems correctly for high interactions near the bandwidth of $6J$. Thus, in the following calculations an on-site interaction of $U = 3.5J$ is chosen.

To complete the discussion of the ground state results, the performance of the GKBA is tested within the extended Hubbard model. It was shown in Sec. 4.1.3 that for the standard Hubbard model the GKBA is not suited to describe the spectral properties of ground state systems. In Fig. 5.4-F5 the ground state photoemission spectrum for a 5-AGNR of $N_s = 30$ sites is depicted for an interaction of $U = 3.5J$. While the spectrum of the full two-time propagation combined with the HF and SOA selfenergy shows only peaks at energies below the Fermi energy $\omega_F = 0$, the GKBA again predicts excitations above ω_F. Therefore, the GKBA is not used in the following calculations.

6 Results II: Laser excitations of finite graphene clusters

After the validity and correct implementation of the extended Hubbard model was confirmed for the ground state in the last chapter, the following part addresses the nonequilibrium dynamics of finite graphene nanostructures. The systems are excited by a linearly polarized laser pulse given by Eq. (4.2-E2). Compared to the one-dimensional systems in Sec. 4, here, it is important to consider the orientation of the polarization. Therefore, in a first part the influence of the laser polarization on the dynamics of the excited system is analyzed. The second part focuses on the effect of carrier multiplication in finite graphene nanostructures. Systems of different size and geometry are addressed and various selfenergy approximations are compared.
In all calculations the parameter set of Tran *et al.* is chosen for the extended Hubbard model and the on-site interaction is set to $U = 3.5J$. In this parameter set one unit of time J^{-1} corresponds to 0.23 fs.

6.1 Influence of the polarization

To analyze the effect that the orientation of the linear polarized laser pulse has on the excited system, we look at a 7-AGNR with $N_\mathrm{s} = 112$ sites that is depicted in Fig. 5.4-F1b)[26]. In order to propagate a system of this size for a time of $125J^{-1}$ the HF selfenergy approximation is used. It is assumed that the general dependence on the laser orientation is already included on the mean field level. The laser excitation is described by Eqs. (4.2-E1) and (4.2-E2) with the parameters $E_0 = 0.1$, $\omega_0 = 0.5J$, $\sigma = 4.787J^{-1}$ and $t_0 = 20J^{-1}$. This corresponds to a laser fluence of $0.51\,\mathrm{mJ/cm^2}$. In the following, three different orientations of the polarization are considered. In the first case the electric field vector is oriented perpendicular to the ribbon axis, in the second it is aligned parallel to the axis and the third orientation is diagonal. In all three cases the electric field vector lies in the plane of the lattice.
In Fig. 6.1-F1 the total energy and the density on an exemplary site are shown for the complete simulation. The maximum of the laser potential is reached at $t_0 = 20J^{-1}$. In the inset it is clearly visible that in the case when the laser is polarized along the ribbon axis, the most energy is transferred into the system, while the least energy is absorbed for the perpendicular polarization. As one would expect, the final energy in the diagonal case lies between the results of the two extremal orientations.
The amplitude of the density oscillations depends on the transferred energy. Thus, the parallel polarization results in the strongest oscillation while the perpendicular orientation shows the weakest response of the density. Interestingly, the density oscillations of the parallel and diagonal excitation exhibit a similar frequency whereas the density of the perpendicular polarization shows a completely different behavior.
To find the reason for this strong influence of the polarization on the transferred energy and the density response of the system, in Fig. 6.1-F2 the optical spectrum is shown for the same setups as in Fig. 6.1-F1. It contains information about the energy levels that are

[26] Note that the illustration of the system is rotated by 90° to fit in the plot. In the following graphics the ribbon is assumed to be aligned in vertical direction.

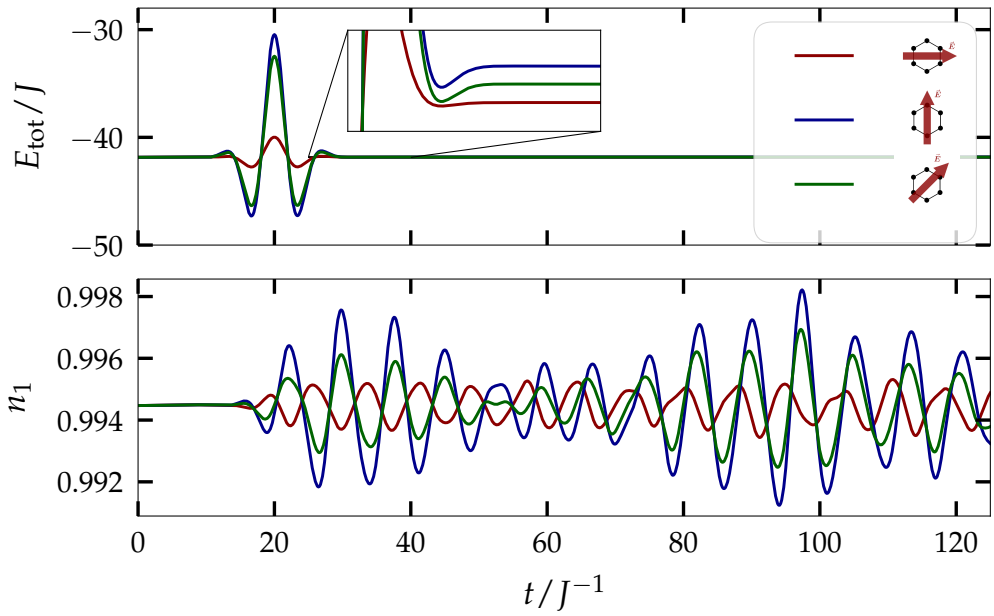

Figure 6.1-F1 – Total energy (top) and density on an exemplary site (bottom) of a 7-AGNR with $N_{\mathrm{s}} = 112$ sites (cf. Fig. 5.4-F1b)) for an interaction of $U = 3.5J$. The system is excited by laser pulses of three different polarizations at $t = 20J^{-1}$. The remaining laser parameters are given in the text. The calculations were performed using the HF selfenergy.

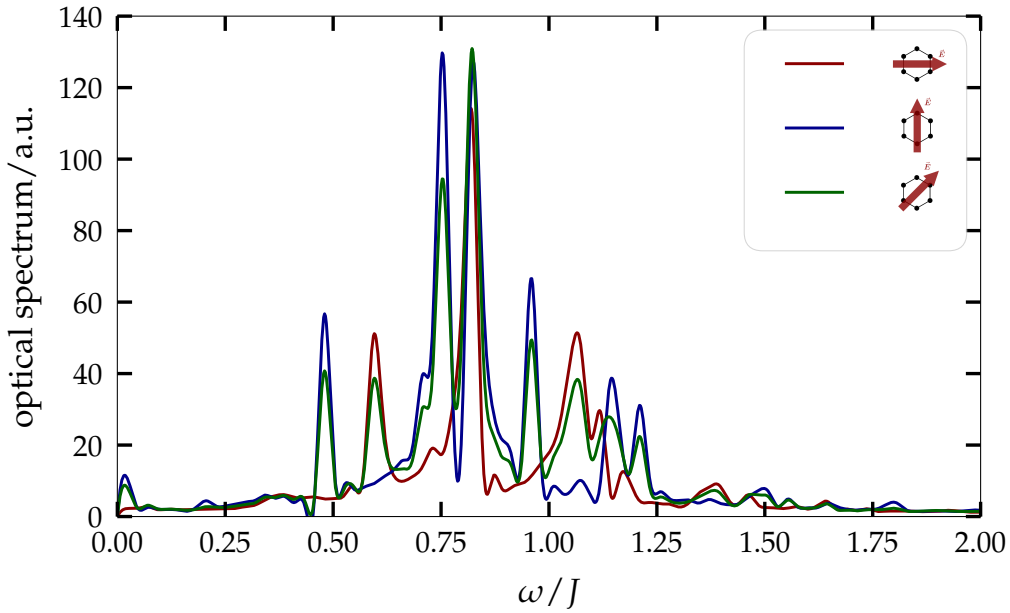

Figure 6.1-F2 – Optical spectrum (cf. Eq. (6.1-E1)) of a 7-AGNR with $N_{\mathrm{s}} = 112$ sites (cf. Fig. 5.4-F1b)) for an interaction of $U = 3.5J$ after the excitation by laser pulses of three different polarizations. The remaining laser parameters are given in the text. The calculations were performed using the HF selfenergy.

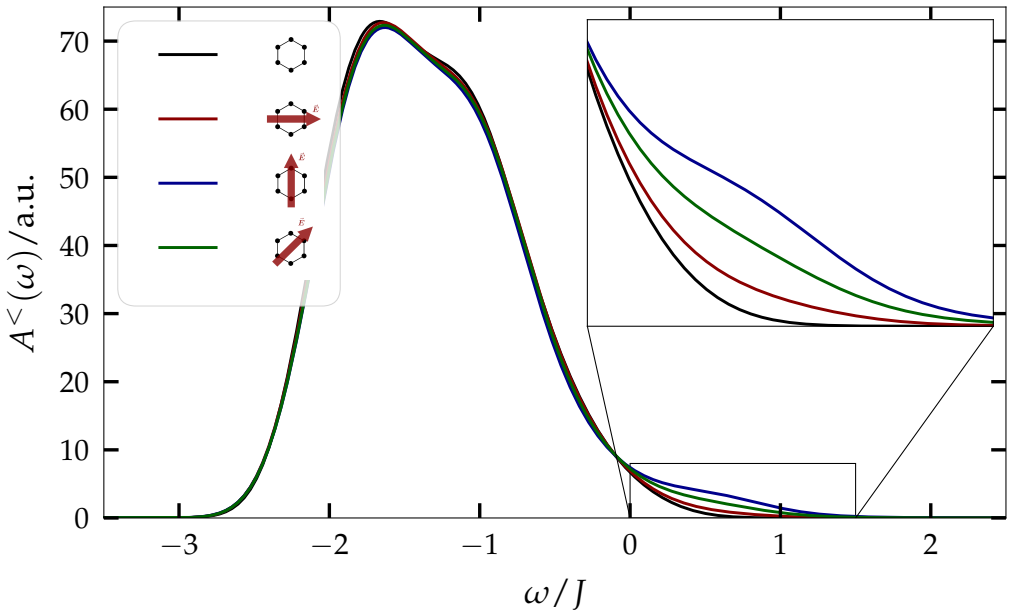

Figure 6.1-F3 – Photoemission spectrum (cf. Eq. (2.2-E98)) of a 7-AGNR with $N_s = 112$ sites (cf. Fig. 5.4-F1b)) for an interaction of $U = 3.5J$ in the ground state and after the excitation by laser pulses of three different polarizations. The remaining laser parameters are given in the text. The calculations were performed using the HF selfenergy. The width of the probe pulse is set to $\kappa = 5J^{-1}$.

excited by the laser pulse and can be accessed by a Fourier transform of the density on all sites:

$$A^{\mathrm{opt}}(\omega) = \sum_{i=1}^{N_s} \left| \int \mathrm{d}t\, \mathrm{e}^{-\mathrm{i}\omega t} n_i(t) \right| . \tag{6.1-E1}$$

Looking at Fig. 6.1-F1, it is apparent that the polarization of the laser pulse determines which energy levels are occupied. The spectrum for the parallel polarization does not show a peak at $\omega \approx 0.6J$ and $\omega \approx 1.1J$. Whereas the excitations at $\omega \approx 0.5J$, $\omega \approx 0.75J$ and $\omega \approx 0.9J$ are not part of the spectrum for a laser pulse polarized perpendicular to the ribbon axis. It is important to note, however, that in the case of the diagonal orientation all contributions are included in the spectrum. The most noteworthy difference between the spectrum of the parallel and perpendicular polarization is the peak at $\omega \approx 0.75J = 2.07\,\mathrm{eV}$. It was found by Denk *et al.* [23] that this peak corresponds to the optical transition between the last valence and the first conduction bands[27]. This transition, apparently, is not induced by light that is polarized perpendicular to the ribbon axis and seems to be the main reason for the weak response of the system.
A similar observation can be made for the photoemission spectrum in Fig. 6.1-F3. Again, while the perpendicular polarization leads to only weak excitations above the Fermi energy $\omega_F = 0$, an orientation of the electric field vector along the ribbon axis results in the transfer of far more spectral weight to the upper band. However, due to the low resolution of the spectrum it is not possible to get information on single excited peaks. Therefore,

[27] However, they find it at 1.9 eV instead of 2.07 eV. This difference might be attributed to the HF selfenergy.

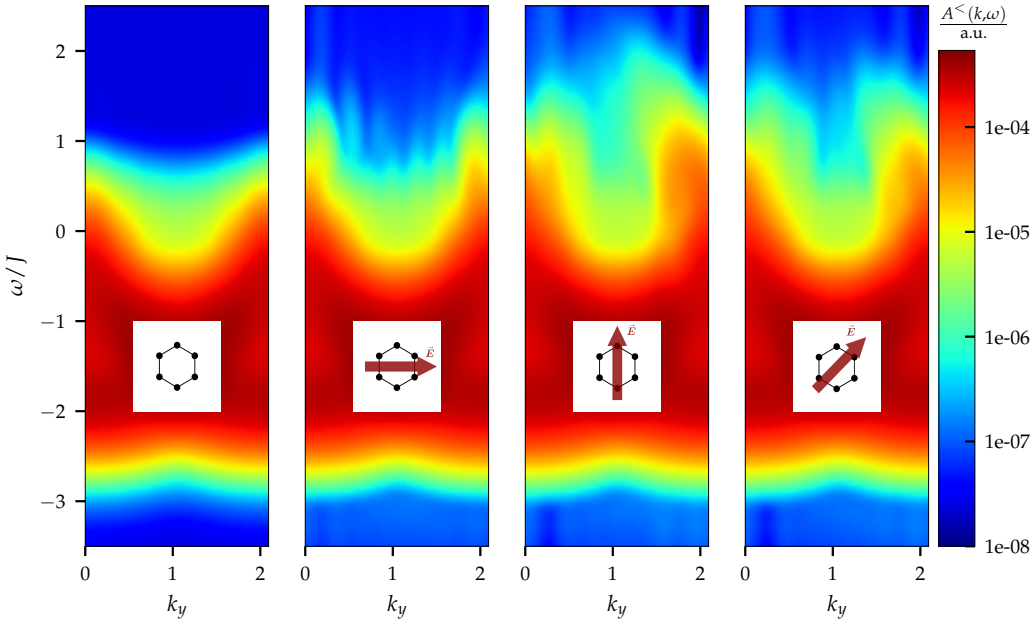

Figure 6.1-F4 – Momentum resolved photoemission spectrum (cf. Eq. (2.2-E97)) of a 7-AGNR with $N_s = 112$ sites (cf. Fig. 5.4-F1b)) for an interaction of $U = 3.5J$ in the ground state and after the excitation by laser pulses of three different polarizations. The remaining laser parameters are given in the text. The calculations were performed using the HF selfenergy. The width of the probe pulse is set to $\kappa = 2.5J^{-1}$. The colormap has a logarithmic scale.

it is favorable to look at the momentum resolved photoemission spectrum in Fig. 6.1-F4. For the perpendicular polarization the excitations are mainly restricted to an area around the Dirac points at $k_y = 0$ and $k_y = \frac{2\pi}{3}$. In contrast, when the laser pulse is polarized parallel to the axis of the nanoribbon also higher bands are occupied and spectral weight is transferred away from the Dirac points.
All results presented above are in good agreement with other findings for GNRs [23] and CNTs [153] that confirm the high anisotropy of such systems. Therefore, in the following part about carrier multiplication all laser pulses are polarized along the ribbon axis.

6.2 Carrier multiplication in graphene nanostructures

The effect of carrier multiplication (CM) in graphene is explained in Sec. 5.3. After an excitation, additional charge carriers can be excited into the conduction band via impact excitation (IE). This effect is interesting for photovoltaic devices in particular, since the efficiency of current solar sells is restricted by the Shockley–Queisser limit. That is because in conventional semiconductors a single photon can excite only one electron due to the inefficiency of CM processes in those materials.
For homogeneous graphene the time-resolved dynamics of IE processes after a laser excitation was first simulated by Winzer [131] using graphene Bloch equations in the tight-binding approximation. Later, Gierz *et al.* confirmed the theoretical observations

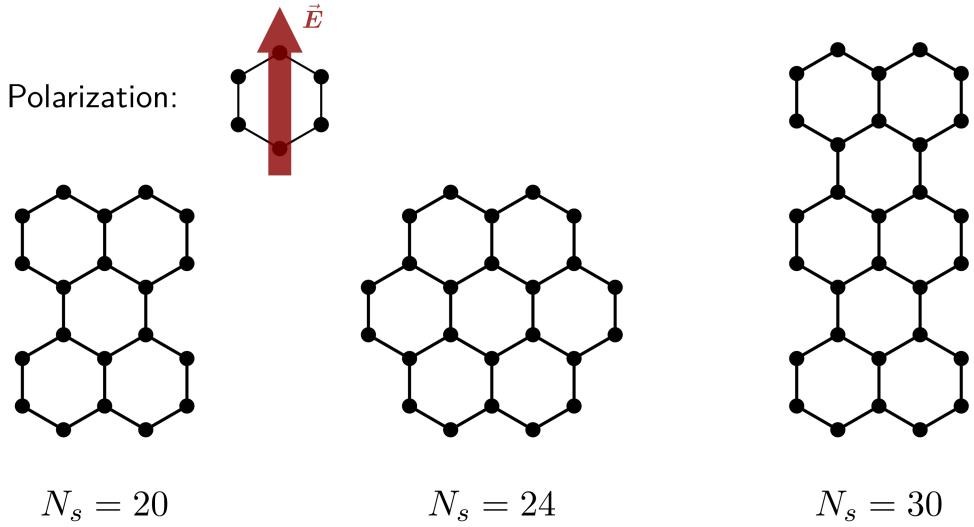

Figure 6.2-F1 – Illustration of the three systems studied in Sec. 6.2. The setups contain two 5-AGNR with $N_\mathrm{s} = 20$ (left) and $N_\mathrm{s} = 30$ (right) sites. Additionally, a quantum dot containing $N_\mathrm{s} = 24$ sites is considered (center). The laser pulse is linearly polarized along the armchair edge of the setups.

experimentally [24]. Until now, the theoretical description of CM effects in finite graphene nanostructures was restricted to the study of single relaxation processes [140] or rough approximations through Langevin dynamics [139] and rate equations [154]. Thus, in this part CM processes in finite graphene structures are studied for the first time by simulating the correlated nonequilibrium dynamics of the systems after a laser excitation. This is achieved by combining the extended Hubbard model and the NEGF approach.

In Fig. 6.2-F1 the three considered systems are displayed, two short 5-AGNR with $N_\mathrm{s} = 20$ and $N_\mathrm{s} = 30$ sites and a quantum dot containing $N_\mathrm{s} = 24$ sites[28]. Although the systems differ only by a few atoms, they exhibit distinct spectral properties due to their finite size and different edge structure. The systems are excited using a laser pulse as presented in Eqs. (4.2-E1) and (4.2-E2) with the parameters $E_0 = 0.1$ and $\sigma = 4.35J^{-1}$. This corresponds to a laser fluence of $0.46\mathrm{mJ/cm^2}$ which is comparable to experimental laser conditions [22, 25]. The laser frequency is set to $\omega_0 = 1.55J$ for the systems with $N_\mathrm{s} = 24$ and $N_\mathrm{s} = 30$ sites and to $\omega_0 = 1.85J$ for the system containing $N_\mathrm{s} = 20$ sites, which corresponds to a wavelength of 290 nm and 243 nm, respectively. This was done to ensure that all setups get excited. The large width of the laser pulse in time results in a sharp peak in frequency space. Because of this and the discrete band structure, the system containing $N_\mathrm{s} = 20$ sites shows no response for a laser frequency of $\omega_0 = 1.55J$. In general, a short wavelength has to be chosen for the laser because the systems considered here exhibit fairly large bandgaps due to their finite size. As discussed in the previous part the laser pulse is linearly polarized along the direction of the armchair edge. This is illustrated in Fig. 6.2-F1. The simulations are performed at zero temperature, $T = 0$, using the

[28] To study CM effects propagation times of $110J^{-1}$, including the adiabatic switching, are needed. Therefore, calculations using numerically expensive selfenergy approximations like SOA or GWA are restricted to small system sizes up to 40 sites. More information on this topic can be found in Sec. 3.3.3.

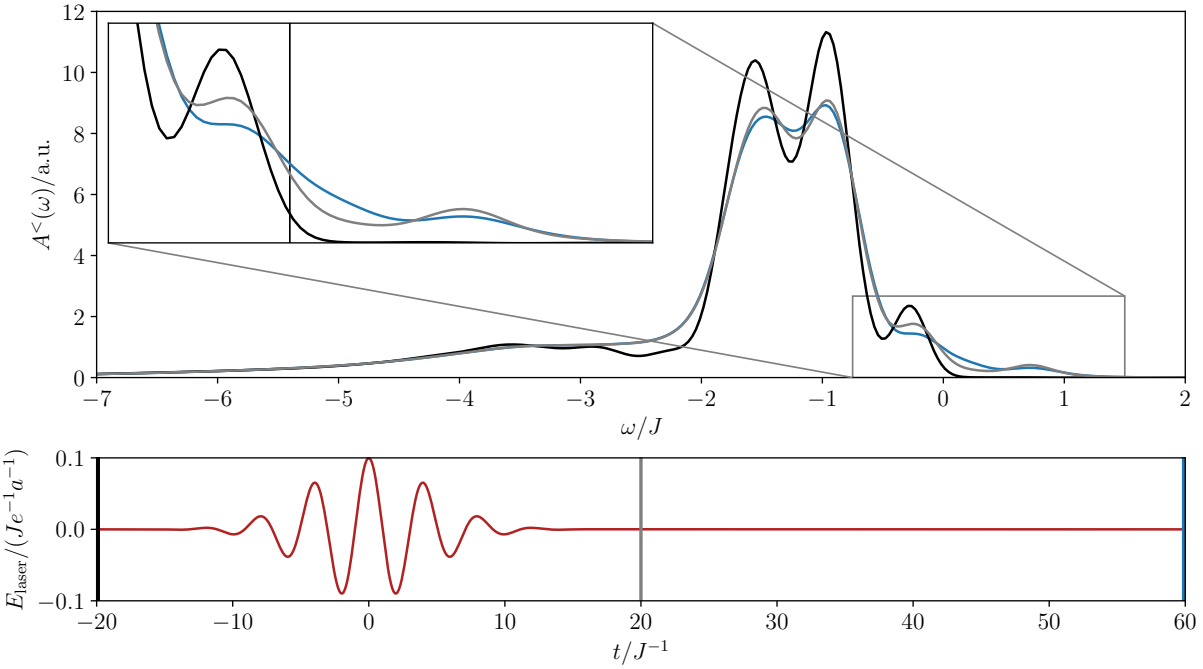

Figure 6.2-F2 – Photoemission spectrum (top) (cf. Eq. (2.2-E98)) of the 5-AGNR containing $N_\mathrm{s} = 30$ sites shown in Fig. 6.2-F1 that is excited by a laser pulse (bottom). The width of the probe pulse is set to $\kappa = 2.5J^{-1}$. The spectrum is shown for the times $t = -20J^{-1}$ (black), $t = 20J^{-1}$ (gray) and $t = 60J^{-1}$ (blue). The calculation is performed using the SOA selfenergy and an interaction of $U = 3.5J$. The system is excited using a laser pulse as presented in Eqs. (4.2-E1) and (4.2-E2) with the parameters $E_0 = 0.1$, $\sigma = 4.35J^{-1}$, $t_0 = 0$ and $\omega_0 = 1.55J$.

parameter set of Tran *et al.* shown in Tab. 5.4-T1 and an on-site interaction of $U = 3.5J$.

The photoemission spectrum of the system containing $N_\mathrm{s} = 30$ sites is shown in the upper panel of Fig. 6.2-F2 for the SOA selfenergy. In the lower panel the amplitude of the electric field of the laser pulse is plotted over the time. The maximum of the laser amplitude is reached at $t = 0$. The black, gray and blue lines denote the times for which the photoemission spectrum is depicted in the upper panel with the respective colors. At $t = -20J^{-1}$ (black), before the interaction with the laser pulse, the system is in the ground state. Thus, only states below the Fermi energy at $\omega_\mathrm{F} = 0$, which is marked by a black vertical line in the inset, are occupied[29]. The main features of the spectrum are three major peaks at $\omega \approx -1.55J$, $\omega \approx -0.95J$ and $\omega \approx -0.25J$, and satellites at $\omega < -2J$. After the laser pulse interacts with the system, at $t = 20J^{-1}$ (gray), a considerable amount of spectral weight is transferred to the upper band. Notably, a peak at $\omega \approx 0.75J$ is strongly occupied, whereas the three major peaks in the lower band all lose spectral weight. Since the laser frequency is set to $\omega_0 = 1.55J$, it can be assumed that the laser mostly excites electrons around the peak at $\omega \approx -0.95J$ to the upper band. At $t = 60J^{-1}$ (black), a long time after the laser interaction, the occupation of the peaks at $\omega \approx -0.25J$ and $\omega \approx 0.75J$ decreases while a new peak emerges at $\omega \approx 0.25J$, the center of both energies.

[29] The small overlap to energies above ω_F, visible in the inset, is due to the finite width of the peaks in the spectrum. It is determined by the width of the Gaussian function in Eq. (2.2-E98) that acts as a probe pulse.

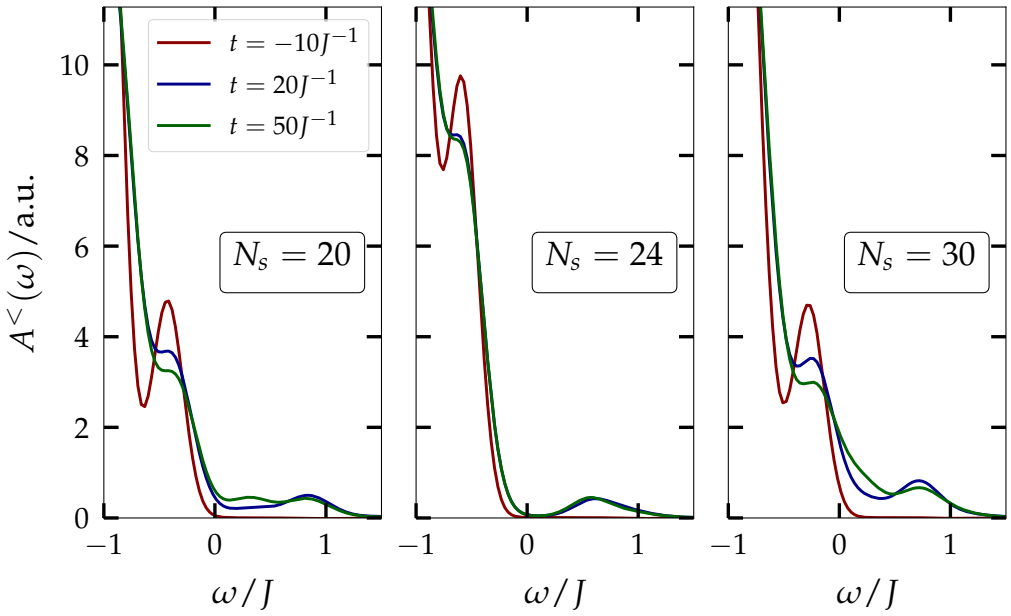

Figure 6.2-F3 – Photoemission spectrum (cf. Eq. (2.2-E98)) around the Fermi energy for all three considered systems depicted in Fig. 6.2-F1 for times before (red), shortly after (blue) and long after (green) the laser excitation at $t_0 = 0$. The remaining laser parameters are given in the text. The width of the probe pulse is set to $\kappa = 2.5J^{-1}$. In all calculations the SOA selfenergy with an interaction of $U = 3.5J$ is used. The section of the spectrum shown corresponds to the region of the inset in Fig. 6.2-F2.

This indicates the existence of IE processes where an electron in the conduction band has enough energy to excite a second electron from the valence over the bandgap. This leads to an increase of charge carriers in the upper band.
Before analyzing this behavior in detail, the photoemission spectrum around the Fermi energy is depicted in Fig. 6.2-F3 for all three considered systems. Again, the SOA selfenergy is used in all calculations. The section of the spectrum shown corresponds to the region of the inset in Fig. 6.2-F2. The three lines denote times before (red), shortly after (blue) and long after (green) the laser excitation. The result for the system of $N_s = 30$ sites was already discussed before.
A similar behavior can be observed for the other short 5-AGNR of $N_s = 20$ sites. Here, the laser excitation leads to the occupation of states at $\omega \approx 0.85J$. After the interaction with the laser pulse, electrons of this energy are able to excite other carriers from the valence to the conduction band and a second peak above the Fermi energy arises at $\omega \approx 0.3J$. In contrast, a similar effect can not be observed for the quantum dot of $N_s = 24$ sites. Admittedly, the laser excites electrons above the bandgap which results in a peak at $\omega \approx 0.6J$. However, after that no CM processes occur which would increase the number of conduction band electrons.
To compare the results for the three different systems quantitatively one can calculate the number of electrons in the conduction band N_{CB} and their energy E_{CB} which are given

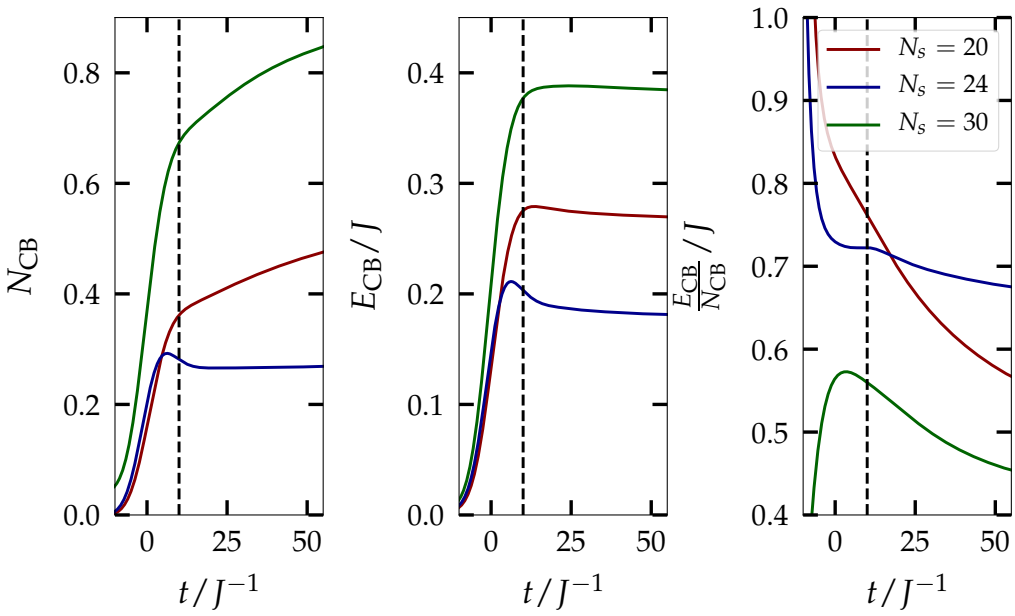

Figure 6.2-F4 – Number N_{CB} (left), total energy E_{CB} (center) and average energy $\frac{E_{\mathrm{CB}}}{N_{\mathrm{CB}}}$ (right) of the carriers in the conduction band (cf. Eqs. (6.2-E1) and (6.2-E2)) for all three considered systems depicted in Fig. 6.2-F1 after a laser excitation at $t_0 = 0$. The remaining laser parameters are given in the text. In all calculations the SOA selfenergy with an interaction of $U = 3.5J$ is used. The dashed black vertical line at $t = 10J^{-1}$ denotes the time after which the laser amplitude becomes negligible.

by[30]

$$N_{\mathrm{CB}} = \int_{\omega_{\mathrm{F}}}^{\infty} A^{<}(\omega)\,\mathrm{d}\omega\,, \tag{6.2-E1}$$

$$E_{\mathrm{CB}} = \int_{\omega_{\mathrm{F}}}^{\infty} \omega A^{<}(\omega)\,\mathrm{d}\omega\,. \tag{6.2-E2}$$

In Fig. 6.2-F4 both quantities together with the resulting average energy of the carriers in the conduction band $\frac{E_{\mathrm{CB}}}{N_{\mathrm{CB}}}$ are shown for the results in Fig. 6.2-F3. The dashed black vertical line at $t = 10J^{-1}$ denotes the point in time after which the laser amplitude becomes negligible. All effects before that time can be attributed to single-particle excitations directly induced by the laser pulse. However, all changes to the particle number and the average energy after that have to be the result of other processes like IE or AR.
As already observed in Fig. 6.2-F3, after the excitation of the system by the laser pulse the particle number in the conduction band increases for the 5-AGNR of $N_{\mathrm{s}} = 20$ and $N_{\mathrm{s}} = 30$ sites whereas for the quantum dot containing $N_{\mathrm{s}} = 24$ sites it remains nearly constant. In the time frame from $t = 10J^{-1}$ to $t = 55J^{-1}$, which equals about 10 fs, N_{CB} increases by 26% for the $N_{\mathrm{s}} = 30$ system and by 32% for the $N_{\mathrm{s}} = 20$ system. At the same time, the total energy of the conduction band carriers E_{CB} remains nearly constant

[30] In general, the photoemission spectrum does not contain any information about the exact particle number. However, by normalizing the spectrum to the total number of particles, Eq. (6.2-E1) can be interpreted as the number of carriers in the conduction band.

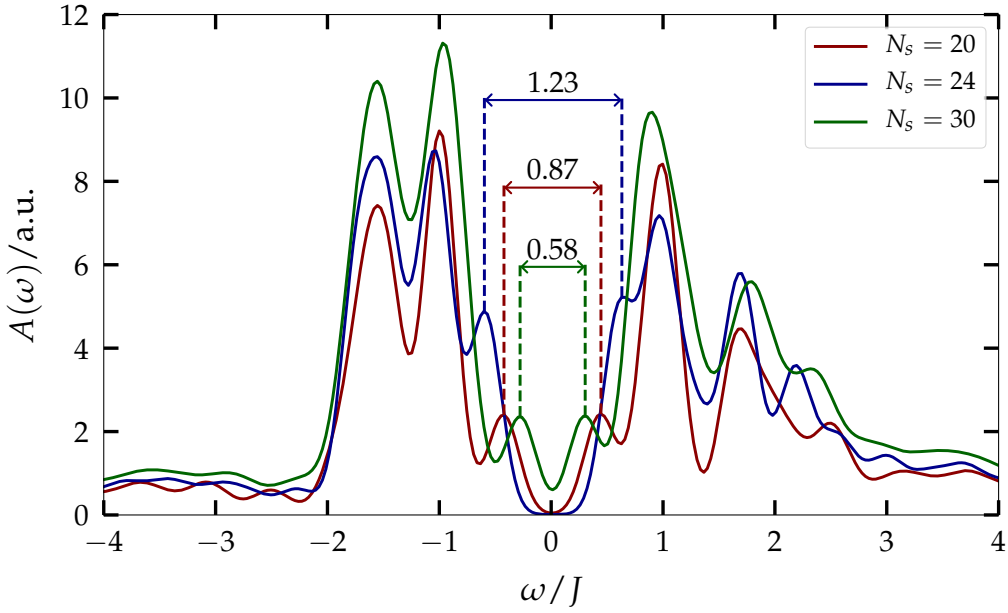

Figure 6.2-F5 – Density of states (DOS) for all three considered systems depicted in Fig. 6.2-F1. The propagation time after the adiabatic switching is $T_{\text{end}} = 10J^{-1}$. The width of the bandgap is estimated by measuring the distance between the highest visible peak of the valence band ($\omega < 0$) and the lowest peak of the conduction band ($\omega > 0$). In all calculations the SOA selfenergy with an interaction of $U = 3.5J$ is used.

after the interaction with the laser pulse[31]. Starting from $t = 10J^{-1}$ the average energy of the conduction band carriers $\frac{E_{\text{CB}}}{N_{\text{CB}}}$ decreases by 19% and 25% for the $N_{\text{s}} = 30$ and $N_{\text{s}} = 20$ site nanoribbons, respectively. For the quantum dot it changes by only 7% over the same period of time. Comparing these results with the expected behavior of the particle number and average energy in the conduction band for the two Auger processes sketched in Fig. 5.2-F4, it is obvious that IE effects play a crucial role in the dynamics of the two nanoribbon systems after the laser excitation. For the quantum dot system, however, these effects seem to be prohibited or very unlikely.

It is known that CM processes are only efficient if the energy of the exciting laser is at least two times the bandgap, i.e. $\omega_0/E_{\text{gap}} > 2$ [134, 142]. To see if this is the case here, one can consider the DOS of the three systems in the ground state. This is shown in Fig. 6.2-F5. The spectrum of the three systems differs most in the crucial area around the Fermi energy. A rough estimation of the bandgap can be determined by measuring the distance between the highest visible peak of the valence band and the lowest peak of the conduction band. This results in the following bandgaps for the systems:

$$E_{\text{gap}}^{N_{\text{s}}=20} = 0.87J\,, \tag{6.2-E3}$$

$$E_{\text{gap}}^{N_{\text{s}}=24} = 1.23J\,, \tag{6.2-E4}$$

$$E_{\text{gap}}^{N_{\text{s}}=30} = 0.58J\,. \tag{6.2-E5}$$

[31] The small decrease of E_{CB} is a statistical effect. Imagine a conduction band electron at an energy of $\omega = 5J$ and a valence band electron at $\omega = -1J$. After an scattering event both carriers are excited at an energy of $\omega = 2J$ above the Fermi energy. Thus, the total energy in the conduction band effectively decreases by the amount of the initial energy of the valence band electron.

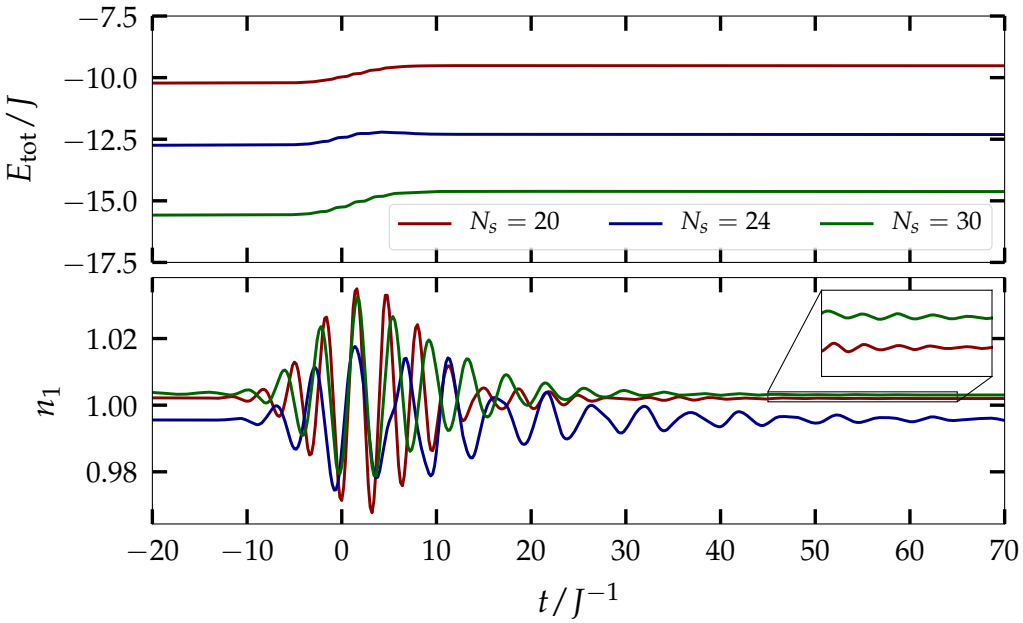

Figure 6.2-F6 – Total energy (top) and density on an exemplary site (bottom) for all three considered systems depicted in Fig. 6.2-F1 that are excited by a laser pulse at $t_0 = 0$. The remaining laser parameters are given in the text. In all calculations the SOA selfenergy with an interaction of $U = 3.5J$ is used.

Although the systems differ only by a few atoms, the different edge structures result in a far larger bandgap for the quantum dot compared to the nanoribbons. Taking into account the different laser frequencies used for the individual systems, one arrives at

$$\omega_0/E_{\mathrm{gap}}^{N_s=20} = 1.85J/0.87J = 2.13 > 2\,, \tag{6.2-E6}$$

$$\omega_0/E_{\mathrm{gap}}^{N_s=24} = 1.55J/1.23J = 1.26 < 2\,, \tag{6.2-E7}$$

$$\omega_0/E_{\mathrm{gap}}^{N_s=30} = 1.55J/0.58J = 2.67 > 2\,. \tag{6.2-E8}$$

This explains why CM effects can only be observed for the two nanoribbon systems. Additionally, this finding confirms $\omega_0/E_{\mathrm{gap}} > 2$ as a requirement for efficient IE processes.

6.2.1 Impact of artificial damping

It was shown in Sec. 4.2.2 that strong excitations result in artificial energy levels when propagating the full two-time KBEs in combination with correlation including selfenergy approximations like SOA or GWA. These artificial states result in an unphysical damping of the density dynamics. Since in the calculations above the SOA selfenergy is used, one has to make sure that the CM effects are not the result of artificial energy levels. In Fig. 6.2-F6 the total energy (top) and the density on an exemplary site (bottom) are depicted for the three setups considered above. The total energy shows that the most energy is transferred to the nanoribbon with $N_s = 30$ sites while the least energy is absorbed by the quantum dot. This is consistent with the observation that the total energy in the conduction band E_{CB} in Fig. 6.2-F4 is highest for the $N_s = 30$ system and lowest for the $N_s = 24$ system.

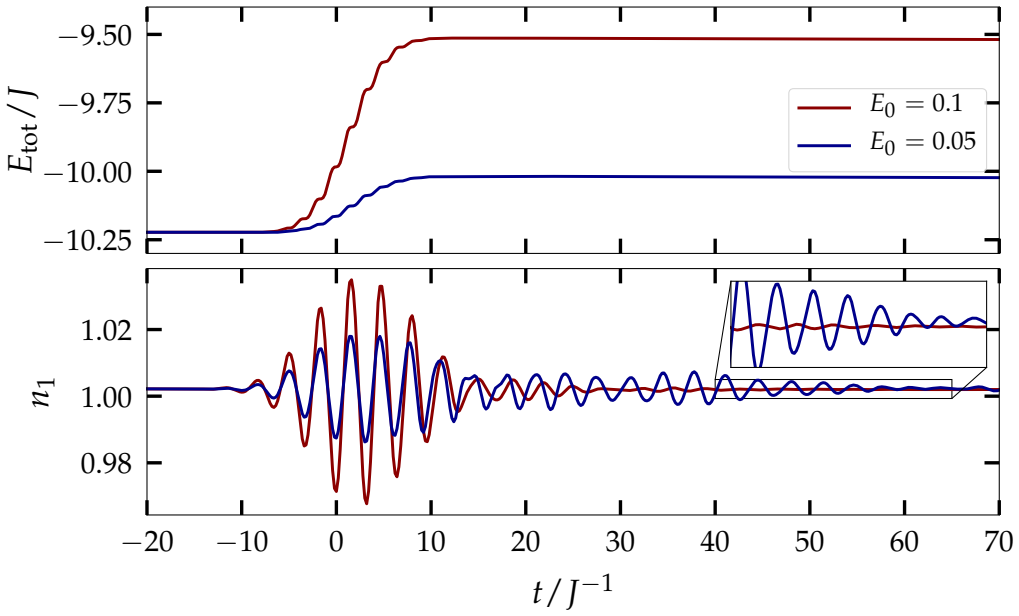

Figure 6.2-F7 – Total energy (top) and density on an exemplary site (bottom) for the 5-AGNR containing $N_{\mathrm{s}} = 20$ sites depicted in Fig. 6.2-F1 that is excited by a laser pulse at $t_0 = 0$. The laser amplitude is set to $E_0 = 0.1$ and $E_0 = 0.05$ while the remaining parameter are fixed to $\sigma = 4.35J^{-1}$ and $\omega_0 = 1.85J$. In both calculations the SOA selfenergy with an interaction of $U = 3.5J$ is used.

Although a small laser amplitude of $E_0 = 0.1$ is used, the oscillations of the density are damped after the laser excitation around $t = 0$, especially for the two nanoribbon systems that show CM effects.

To study the effect of the excitation strength on the CM, another calculation is performed for the 5-AGNR of $N_{\mathrm{s}} = 20$ sites with a laser amplitude of $E_0 = 0.05$. The total energy (top) and the density on an exemplary site (bottom) are shown in Fig. 6.2-F7 for both laser amplitudes, $E_0 = 0.05$ and $E_0 = 0.1$. As expected, the smaller amplitude results in less energy that is transferred to the system. Additionally, the density dynamics is far less damped. Thus, if the CM effects observed in Figs. 6.2-F3 and 6.2-F4 were due to the artificial energy levels as a result of the strong excitation, we would now expect no CM processes to occur in the spectrum.

In Fig. 6.2-F8, again, N_{CB}, E_{CB} and $\frac{E_{\mathrm{CB}}}{N_{\mathrm{CB}}}$ are displayed, this time for the two setups of Fig. 6.2-F7. The carrier number in the conduction band N_{CB} is normalized to $N_0 = N_{\mathrm{CB}}(t = 0)$ for better comparison. For the small laser amplitude of $E_0 = 0.05$ the carrier density in the conduction band is increased by 12% between $t = 10J^{-1}$ and $t = 55J^{-1}$, whereas in the case of $E_0 = 0.1$ an increase of 32% is observed. Over the same time interval, the average energy of conduction band carriers $\frac{E_{\mathrm{CB}}}{N_{\mathrm{CB}}}$ is reduced by 13% and 25% for a laser amplitude of $E = 0.05$ and $E = 0.1$, respectively. Again, E_{CB} decreases slightly in both cases.

In summary, although the CM effects are less significant for the smaller laser amplitude, they still are considerably more pronounced than in the case of the quantum dot shown in Fig. 6.2-F4. Thus, artificial energy levels due to strong excitations can at most increase CM processes. However, such unphysical energy states do not induce CM effects as seen in the case of the quantum dot, which shows damped density dynamics but no CM (cf.

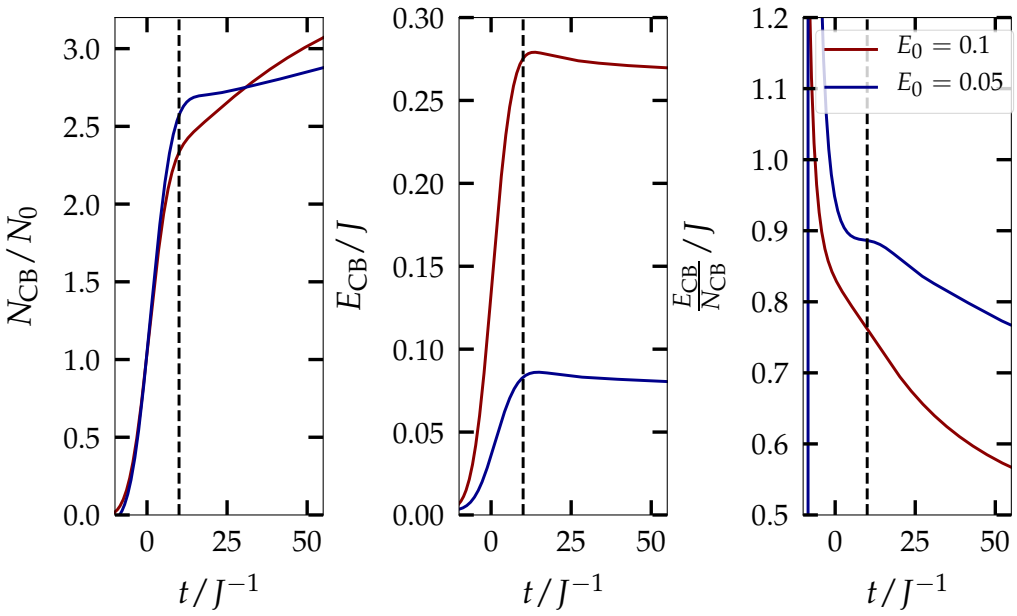

Figure 6.2-F8 – Number N_{CB} (left), total energy E_{CB} (center) and average energy $\frac{E_{CB}}{N_{CB}}$ (right) of the carriers in the conduction band (cf. Eqs. (6.2-E1) and (6.2-E2)) for the 5-AGNR containing $N_s = 20$ sites depicted in Fig. 6.2-F1 that is excited by a laser pulse at $t_0 = 0$ (cf. Fig. 6.2-F7). The laser amplitude is set to $E_0 = 0.1$ and $E_0 = 0.05$ while the remaining parameter are fixed to $\sigma = 4.35J^{-1}$ and $\omega_0 = 1.85J$. In both calculations the SOA selfenergy with an interaction of $U = 3.5J$ is used. The dashed black vertical line at $t = 10J^{-1}$ denotes the time after which the laser amplitude becomes negligible.

Figs. 6.2-F4 and 6.2-F6). Instead, carrier multiplication is observed in the case of a small laser amplitude for the $N_s = 20$ nanoribbon, although the density dynamics show no strong damping.

6.2.2 Significance of correlations

In the calculations above only the SOA selfenergy has been used, because from a numerical point of view it is the least demanding selfenergy approximation that takes into account correlations. In this part, additional calculations are performed for the $N_s = 20$ site nanoribbon system using the HF and the GWA selfenergy to study the influence of correlation effects on the CM processes. In Fig. 6.2-F9 the photoemission spectrum is shown for a small section around the Fermi energy that corresponds to the region of the inset in Fig. 6.2-F2. The data for the SOA selfenergy is taken from Fig. 6.2-F3 and displayed to compare with the results of the two other selfenergy approximations. In general, the spectrum for GWA shows a similar behavior as the data for SOA. First, the laser excites states at $\omega \approx 0.9J$. Second, after the laser interaction, a new peak arises at $\omega \approx 0.4J$ while the first peak loses spectral weight. This, again, can be explained by IE processes. In the case of the HF selfenergy, the laser excitation leads to a peak at $\omega \approx 1J$. However, after that a completely different behavior is observed. Additional peaks emerge

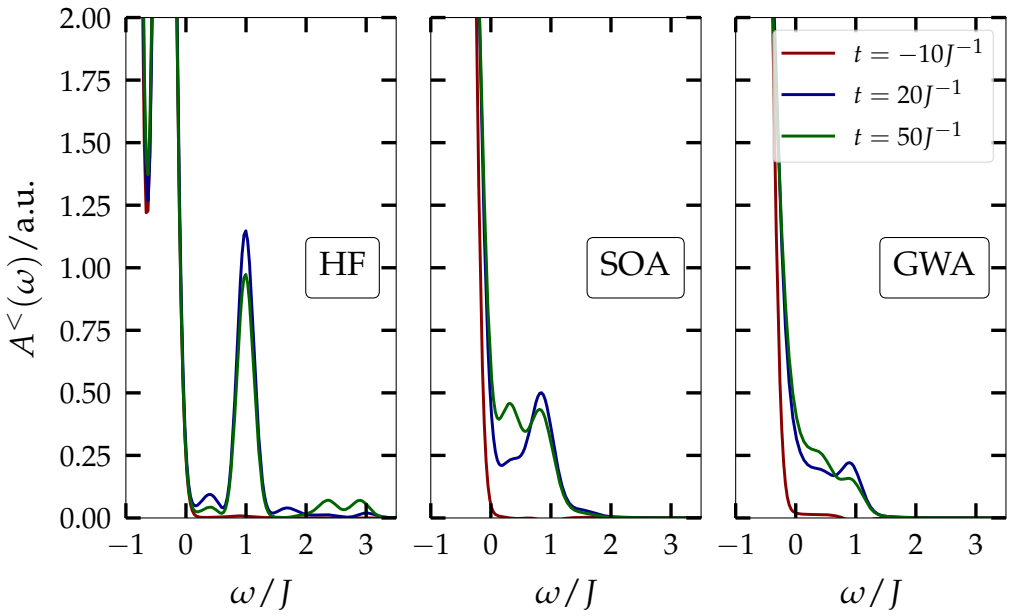

Figure 6.2-F9 – Photoemission spectrum (cf. Eq. (2.2-E98)) around the Fermi energy for the 5-AGNR containing $N_s = 20$ sites depicted in Fig. 6.2-F1 for times before (red), shortly after (blue) and long after (green) the laser excitation at $t_0 = 0$. The remaining laser parameters are given in the text. The width of the probe pulse is set to $\kappa = 2.5J^{-1}$. The calculations are performed using the HF (left), SOA (center) and GWA (right) selfenergy with an interaction of $U = 3.5J$ is used. The section of the spectrum shown corresponds to the region of the inset in Fig. 6.2-F2.

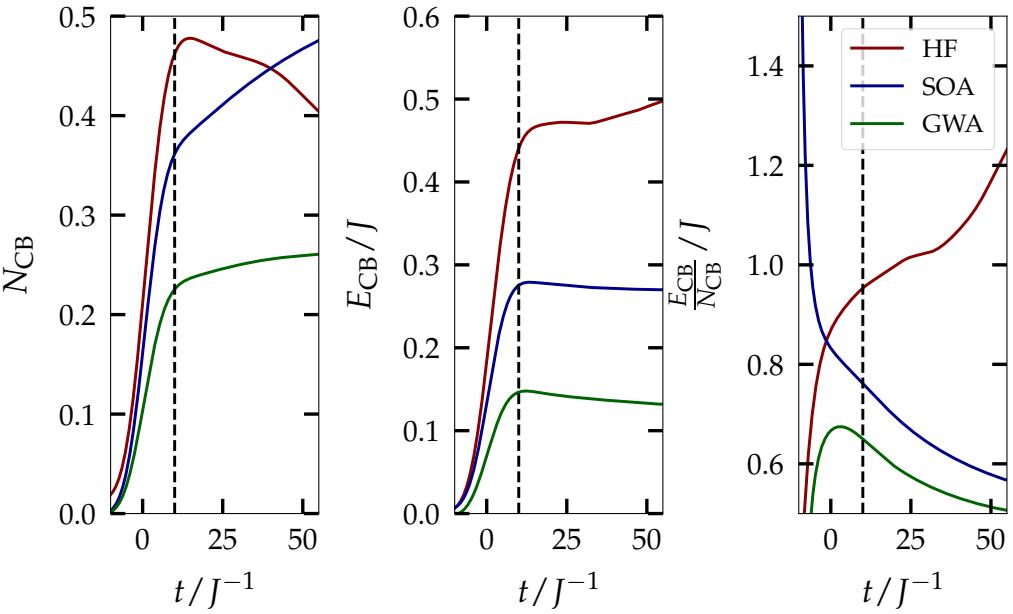

Figure 6.2-F10 – Number N_{CB} (left), total energy E_{CB} (center) and average energy $\frac{E_{CB}}{N_{CB}}$ (right) of the carriers in the conduction band (cf. Eqs. (6.2-E1) and (6.2-E2)) for the 5-AGNR containing $N_s = 20$ sites depicted in Fig. 6.2-F1 after a laser excitation at $t_0 = 0$. The remaining laser parameters are given in the text. The calculations are performed using the HF (red), SOA (blue) and GWA (green) selfenergy with an interaction of $U = 3.5J$ is used. The dashed black vertical line at $t = 10J^{-1}$ denotes the time after which the laser amplitude becomes negligible.

at high energies $\omega \approx 2.4J$ and $\omega \approx 2.9J$. This result corresponds to AR instead of IE processes.
For a more detailed analysis of these results, N_{CB}, E_{CB} and $\frac{E_{\mathrm{CB}}}{N_{\mathrm{CB}}}$ are depicted in Fig. 6.2-F10. It has already been discussed previously that for the SOA selfenergy N_{CB} increases by 32% and $\frac{E_{\mathrm{CB}}}{N_{\mathrm{CB}}}$ decreased by 25% in the time interval between $t = 10J^{-1}$ and $t = 55J^{-1}$. For GWA this changes to an increase by 16% and a decrease by 22%, respectively. As shown in Fig. 4.1-F4, GWA generally produces a larger bandgap than SOA. This could explain the reduced CM rates, since the width of the bandgap has a significant influence on the efficiency of IE effects as explained above. However, since the results of SOA and GWA qualitatively agree, it is likely that all important processes are already well described by the second order diagrams.
For all three considered quantities the HF selfenergy shows the opposite trend to the results of SOA and GWA. This indicates the existence of AR instead of IE processes. However, Auger processes are two-particle excitations which are not included in the mean field picture of the HF selfenergy. Therefore, for the HF selfenergy one would expect the carrier density in the conduction band to remain constant after the laser excitation. The reason for the observed counterintuitive behavior remains unclear. Additional calculations, that are not presented here, have revealed that in the case of the standard Hubbard model the HF approximation shows a similar trend as depicted in Fig. 6.2-F10. Thus, the observed AR effects are not caused by the extended Hubbard model. Furthermore, the calculations were tested to be numerically converged, i.e. the observed behavior is not a numerical artifact. Nonetheless, to correctly describe the CM processes in the studied systems, one has to take into account correlations, since the mean field description of HF does not capture the underlying processes correctly.

7 Conclusions & Outlook

In this thesis, a new approach has been presented to describe the time resolved nonequilibrium dynamics and spectral properties of finite graphene nanoclusters. While for homogeneous graphene similar time resolved simulations were developed many years ago [131, 132], finite graphene systems such as quantum dots, graphene nanoribbons (GNRs) and carbon nanotubes (CNTs) were not accessible until now due to their finite size and increased correlations. Existing approaches for these systems were either restricted to the study of single processes [140] or roughly approximated the dynamics by Langevin [139] or rate equations [154]. However, especially these finite systems are of high interest for applications in next-generation electronics and solar cells due to their non-vanishing bandgap [134].
The new description that has been presented in this thesis is based on an extension of the standard Hubbard model that is solved by the nonequilibrium Green functions (NEGF) approach to include correlations. Due to its simplistic nature the Hubbard model greatly reduces the computational demands of the description of finite systems. Nevertheless, it was often used to great success to describe the ground state [144] as well as the transport properties [145] of graphene.
The NEGF approach is based on the description of quantum many-body systems in second quantization. The resulting equations of motions are the so-called Kadanoff–Baym equations (KBEs) [53] which contain the full many-body information in the selfenergy Σ. Since, in general, the exact selfenergy is not accessible, various approximations exist that take into account different physical processes [57].
The quality of the NEGF method has been tested against exact results for various one-dimensional systems within the standard Hubbard model in Sec. 4. Especially the performance of the different selfenergy approximations to reproduce the exact spectral properties in the ground state has been studied. The GWA and TPH selfenergy approximations are found to predict the size of the Hubbard gap best, while HF and TPP show no bandgap for any considered interaction U up to $U = 3J$.
Additionally, it has been found that the generalized Kadanoff–Baym ansatz (GKBA) [69] which, in the past, was successfully applied to describe the nonequilibrium density dynamics of strongly excited systems [103] does not correctly reproduce the spectral properties of the considered systems. In the ground state at zero temperature the GKBA spectrum contains excited states in the upper Hubbard subband although, in this case, only states below the Fermi energy should be occupied. Due to its insufficient description of the spectral properties, the GKBA can not be used for the simulation of graphene nanostructures if one is interested in quantities such as the photoemission spectrum.
However, it is known that the full two-time propagation of the KBEs results in a damping of the density dynamics for strongly excited systems, if correlations are considered, due to artificial energy states [56]. Therefore, it has been studied in Sec. 4.2.2 how this unphysical damping affects the photoemission spectrum of the system. It has been found that the artificial energy levels become occupied for strongly excited systems which leads to an effective broadening of the peaks and the spectrum in general. Thus, even if one is not interested in the density dynamics of the system, the considered excitation has to be weak enough to not result in an excessive damping of the spectrum.
For the correct description of finite graphene nanostructures the standard Hubbard model

hast to be extended to take into account the overlap of the π-orbitals in the graphene honeycomb lattice. In this work, hopping and overlap between up to third nearest neighbors is considered. The parameter sets are taken from Reich *et al.* [149] for homogeneous graphene and from Tran *et al.* [146] to describe finite graphene systems. Additionally, to determine the on-site interaction U the band structures of a 7-AGNR has been compared to results of Wang *et al.* [152] for the GWA selfenergy. It was found that the width of the selfenergy is well reproduced for $U = 3.5J$.

Graphene is an interesting material for future solar cells due to its efficient impact excitation (IE) processes that lead to high carrier multiplication (CM) rates [2]. In 2015 Gierz *et al.* [24] performed femtosecond time- and angle-resolved photoemission spectroscopy (TR-ARPES) measurements to observe such effects in monolayer graphene. They found that the photoemission spectrum grants easy access to the density and average energy of carriers in the conduction band which allows to measure carrier multiplication processes. The same approach has been used in this thesis for finite graphene nanostructures because the photoemission spectrum is easily accessible through the two-time Green functions.

First, the influence of different laser polarizations on a 7-AGNR has been studied in Sec. 6.1 using the HF selfenergy approximation. The system showed the strongest response when the light was polarized along the direction of the armchair edge. The results are in good agreement with the findings of Denk *et al.* [23] who experimentally observed a high anisotropy for the optical response of similar systems.

For studying CM effects in finite graphene nanostructures three different systems have been considered, two short 5-AGNR with Ns $= 20$ and $N_\mathrm{s} = 30$ sites, and a quantum dot containing $N_\mathrm{s} = 20$ sites. It has been found that after an excitation by a laser pulse the carrier number in the conduction band increased by 26% and 32% in the considered time frame for the two 5-AGNR systems due to IE effects. However, in the case of the quantum dot, after the laser excitation, the carrier density in the upper band remained constant. This is explained by the distinct bandgap of the different systems due to their individual geometry and edge structure. For IE processes to be effective, the frequency of the laser pulse ω_0 has to be at least twice the bandgap E_gap [134, 142], i.e. $\omega_0 > 2E_\mathrm{gap}$, which was found to be true only for the two 5-AGNR systems but not for the quantum dot. Additionally, it has been shown that the observed CM effects are not a result of the artificial energy levels that emerge for strong excitations.

Finally, the influence of correlation effects on the observed CM processes has been analyzed. For that, the calculations described above were repeated using the HF and GWA selfenergy. It has been found that the GWA selfenergy shows the same trends for the number and average energy of conduction band carriers as the SOA selfenergy. This implied that the important IE processes are already well described by the second order terms contained in the SOA selfenergy. However, the CM rates observed in the GWA results are lower than for SOA. This can be explained by the increased bandgap in the case of GWA, which reduces the number of occurring IE processes.

On the other hand it was found that the HF selfenergy does not show CM effects. Instead, Auger relaxation processes have been observed. This is especially interesting because such effects should not be included in a mean field description. At the moment, the reason for this behavior remains unclear.

A lot of work was put into the optimization of the numerical algorithms. For the propagation of the KBEs a fourth order Runge–Kutta method was implemented. Additionally, a lot of different integration techniques have been used to improve the accuracy of the

integral expressions. Finally, the matrix multiplication was optimized to take advantage of the GPU architecture. All in all, the numerical improvements that were achieved over the last two years, made a work of this scope possible in the first place. Today, propagating a system of $N_\mathrm{s} = 30$ sites for a time of $110J^{-1}$ using the GWA selfenergy takes about seven days on a single GPU. Two years ago, the same calculation would have taken up to 300 days on the same hardware.

In summary, the combined approach of the extended Hubbard model and the NEGF method is well-suited to describe the correlated nonequilibrium dynamics of excited finite graphene nanoclusters. Here, it was used to successfully predict CM effects in finite GNRs in a, for the first time, full nonequilibrium context.

Outlook

The presented approach is applicable to various systems. Additionally, it could be extended to even describe strong excitations accurately. Below, possible topics of future research are listed.

- As a mean field approach the HF selfenergy should not contain any Auger processes. Nevertheless, in the simulations relaxation processes are observed that show the behavior of AR. At the moment, the reason for this is unclear. For a better understanding of the occurring processes in general, this should be further analyzed in the future.

- The TPH selfenergy showed good results for the Hubbard gap of the one-dimensional chain. It would be interesting to see how the higher order scattering contributions of the T-matrix influence the description of the CM processes.

- The GKBA is not applicable if one is interested in spectral properties. In order to describe the dynamics and spectral properties of a system even for strong excitations one can implement a consistent second order scheme [57].

- In this work, only linearly polarized laser pulses were considered. In a next step one could study the effect of light with a circular polarization on finite graphene systems.

- CNTs have a similar structure to GNRs. In the presented approach of the extended Hubbard model and the NEGF method they can be described as GNRs with periodic boundary conditions perpendicular to the ribbon axis. Thus, it is easy to extend the investigations to CNTs.

- In addition to AGNRs and ZGNRs there are a variety of systems with different edge structures that exhibit interesting properties [8]. The flexibility of the presented approach allows to describe any possible lattice geometry.

References

[1]K. S. Novoselov, A. K. Geim, S. V. Morozov, D. Jiang, Y. Zhang, S. V. Dubonos, I. V. Grigorieva, and A. A. Firsov, "Electric field effect in atomically thin carbon films", Science **306**, 666–669 (2004).

[2]X. Wang, L. Zhi, and K. Müllen, "Transparent, conductive graphene electrodes for dye-sensitized solar cells", Nano Letters **8**, 323–327 (2008).

[3]Y. H. Hu, H. Wang, and B. Hu, "Thinnest two-dimensional nanomaterial—graphene for solar energy", ChemSusChem **3**, 782–796 (2010).

[4]I. V. Lightcap and P. V. Kamat, "Graphitic design: prospects of graphene-based nanocomposites for solar energy conversion, storage, and sensing", Accounts of Chemical Research **46**, 2235–2243 (2013).

[5]Y. Song, S. Chang, S. Gradecak, and J. Kong, "Visibly-transparent organic solar cells on flexible substrates with all-graphene electrodes", Advanced Energy Materials **6**, 1600847 (2016).

[6]F. Xia, T. Mueller, Y.-m. Lin, A. Valdes-Garcia, and P. Avouris, "Ultrafast graphene photodetector", Nature Nanotechnology **4**, 839 (2009).

[7]P. Avouris, Z. Chen, and V. Perebeinos, "Carbon-based electronics", Nature Nanotechnology **2**, Review Article, 605 (2007).

[8]M. Dvorak, W. Oswald, and Z. Wu, "Bandgap Opening by Patterning Graphene", Scientific Reports **3**, 2289 (2013).

[9]Y. Zhang, T.-T. Tang, C. Girit, Z. Hao, M. C. Martin, A. Zettl, M. F. Crommie, Y. R. Shen, and F. Wang, "Direct observation of a widely tunable bandgap in bilayer graphene", Nature **459**, 820 (2009).

[10]S. Y. Zhou, G.-H. Gweon, A. V. Fedorov, P. N. First, W. A. de Heer, D.-H. Lee, F. Guinea, A. H. Castro Neto, and A. Lanzara, "Substrate-induced bandgap opening in epitaxial graphene", Nature Materials **6**, Article, 770 (2007).

[11]C. Jeon, H.-C. Shin, I. Song, M. Kim, J.-H. Park, J. Nam, D.-H. Oh, S. Woo, C.-C. Hwang, C.-Y. Park, and J. R. Ahn, "Opening and reversible control of a wide energy gap in uniform monolayer graphene", Scientific Reports **3**, 2725 (2013).

[12]F. Guinea, M. I. Katsnelson, and A. K. Geim, "Energy gaps and a zero-field quantum hall effect in graphene by strain engineering", Nature Physics **6**, 30 (2009).

[13]S.-M. Choi, S.-H. Jhi, and Y.-W. Son, "Effects of strain on electronic properties of graphene", Phys. Rev. B **81**, 081407 (2010).

[14]L. Yang, C.-H. Park, Y.-W. Son, M. L. Cohen, and S. G. Louie, "Quasiparticle energies and band gaps in graphene nanoribbons", Phys. Rev. Lett. **99**, 186801 (2007).

[15]M. Y. Han, B. Özyilmaz, Y. Zhang, and P. Kim, "Energy band-gap engineering of graphene nanoribbons", Phys. Rev. Lett. **98**, 206805 (2007).

[16]J. Bai, X. Duan, and Y. Huang, "Rational fabrication of graphene nanoribbons using a nanowire etch mask", Nano Letters **9**, 2083–2087 (2009).

[17]L. Jiao, X. Wang, G. Diankov, H. Wang, and H. Dai, "Facile synthesis of high-quality graphene nanoribbons", Nature Nanotechnology **5**, 321 (2010).

[18]O. V. Yazyev, "A Guide to the Design of Electronic Properties of Graphene Nanoribbons", Accounts of Chemical Research **46**, 2319–2328 (2013).

[19]A. Kimouche, M. M. Ervasti, R. Drost, S. Halonen, A. Harju, P. M. Joensuu, J. Sainio, and P. Liljeroth, "Ultra-narrow metallic armchair graphene nanoribbons", Nature Communications **6**, 10177 (2015).

[20]R. M. Jacobberger, B. Kiraly, M. Fortin-Deschenes, P. L. Levesque, K. M. McElhinny, G. J. Brady, R. Rojas Delgado, S. Singha Roy, A. Mannix, M. G. Lagally, P. G. Evans, P. Desjardins, R. Martel, M. C. Hersam, N. P. Guisinger, and M. S. Arnold, "Direct oriented growth of armchair graphene nanoribbons on germanium", Nature Communications **6**, Article, 8006 (2015).

[21]S. A. Jensen, R. Ulbricht, A. Narita, X. Feng, K. Müllen, T. Hertel, D. Turchinovich, and M. Bonn, "Ultrafast Photoconductivity of Graphene Nanoribbons and Carbon Nanotubes", Nano Letters **13**, 5925–5930 (2013).

[22]I. Gierz, J. C. Petersen, M. Mitrano, C. Cacho, I. C. E. Turcu, E. Springate, A. Stöhr, A. Köhler, U. Starke, and A. Cavalleri, "Snapshots of non-equilibrium Dirac carrier distributions in graphene", Nature Materials **12**, 1119–1124 (2013).

[23]R. Denk, M. Hohage, P. Zeppenfeld, J. Cai, C. A. Pignedoli, H. Söde, R. Fasel, X. Feng, K. Müllen, S. Wang, D. Prezzi, A. Ferretti, A. Ruini, E. Molinari, and P. Ruffieux, "Exciton-dominated optical response of ultra-narrow graphene nanoribbons", Nature Communications **5**, 5253 (2014).

[24]I. Gierz, F. Calegari, S. Aeschlimann, M. Chávez Cervantes, C. Cacho, R. T. Chapman, E. Springate, S. Link, U. Starke, C. R. Ast, and A. Cavalleri, "Tracking Primary Thermalization Events in Graphene with Photoemission at Extreme Time Scales", Physical Review Letters **115**, 086803 (2015).

[25]G. Soavi, S. D. Conte, C. Manzoni, D. Viola, A. Narita, Y. Hu, X. Feng, U. Hohenester, E. Molinari, D. Prezzi, K. Müllen, and G. Cerullo, "Exciton–exciton annihilation and biexciton stimulated emission in graphene nanoribbons", Nature Communications **7**, 11010 (2016).

[26]B. V. Senkovskiy, A. V. Fedorov, D. Haberer, M. Farjam, K. A. Simonov, A. B. Preobrajenski, N. Mårtensson, N. Atodiresei, V. Caciuc, S. Blügel, A. Rosch, N. I. Verbitskiy, M. Hell, D. V. Evtushinsky, R. German, T. Marangoni, P. H. M. van Loosdrecht, F. R. Fischer, and A. Grüneis, "Semiconductor-to-Metal Transition and Quasiparticle Renormalization in Doped Graphene Nanoribbons", Advanced Electronic Materials **3**, 1600490 (2017).

[27]I. Ivanov, Y. Hu, S. Osella, U. Beser, H. I. Wang, D. Beljonne, A. Narita, K. Müllen, D. Turchinovich, and M. Bonn, "Role of Edge Engineering in Photoconductivity of Graphene Nanoribbons", Journal of the American Chemical Society **139**, 7982–7988 (2017).

[28]P. Hohenberg and W. Kohn, "Inhomogeneous electron gas", Phys. Rev. **136**, B864 (1964).

[29]E. Runge and E. K. Gross, "Density-functional theory for time-dependent systems", Phys. Rev. Lett. **52**, 997 (1984).

[30]S. He, A. Russakoff, Y. Li, and K. Varga, "Time-dependent density-functional theory simulation of local currents in pristine and single-defect zigzag graphene nanoribbons", Journal of Applied Physics **120**, 034304 (2016).

[31]J. Hubbard, "Electron correlations in narrow energy bands", Proceedings of the Royal Society of London A: Mathematical, Physical and Engineering Sciences **276**, 238–257 (1963).

[32]F. H. Essler, H. Frahm, F. Göhmann, A. Klümper, and V. E. Korepin, *The one-dimensional hubbard model* (Cambridge University Press, 2005).

[33]S. R. Manmana, A. Muramatsu, and R. M. Noack, "Time evolution of one-dimensional quantum many body systems", AIP Conference Proceedings **789**, 269–278 (2005).

[34]S. R. White, "Density matrix formulation for quantum renormalization groups", Phys. Rev. Lett. **69**, 2863–2866 (1992).

[35]A. Georges, G. Kotliar, W. Krauth, and M. J. Rozenberg, "Dynamical mean-field theory of strongly correlated fermion systems and the limit of infinite dimensions", Rev. Mod. Phys. **68**, 13 (1996).

[36]M. Bonitz, *Quantum kinetic theory* (Springer, 2016).

[37]K. Balzer and M. Bonitz, *Nonequilibrium Green's Functions Approach to Inhomogeneous Systems*, Vol. 867, Lecture Notes in Physics (Springer, Berlin, Heidelberg, 2013).

[38]G. Stefanucci and R. v. Leeuwen, *Nonequilibrium many-body theory of quantum systems: a modern introduction* (Cambridge University Press, Cambridge, 2013).

[39]C. Leforestier, R. Bisseling, C. Cerjan, M. Feit, R. Friesner, A. Guldberg, A. Hammerich, G. Jolicard, W. Karrlein, H.-D. Meyer, N. Lipkin, O. Roncero, and R. Kosloff, "A comparison of different propagation schemes for the time dependent schrödinger equation", Journal of Computational Physics **94**, 59–80 (1991).

[40]E. Koch, *The Lanczos Method*, https://www.cond-mat.de/events/correl11/manuscripts/koch.pdf.

[41]A. Dolfen, "Massively parallel exact diagonalization of strongly correlated systems", Diploma thesis (Forschungszentrum Jülich, Germany, Oct. 2006).

[42]E. Dagotto, "Correlated electrons in high-temperature superconductors", Rev. Mod. Phys. **66**, 763–840 (1994).

[43]M. Balzer, N. Gdaniec, and M. Potthoff, "Krylov-space approach to the equilibrium and nonequilibrium single-particle Green's function", Journal of Physics: Condensed Matter **24**, 035603 (2012).

[44]A. Messiah and J. Streubel, *Albert Messiah: Quantenmechanik*, Bd. 1 (De Gruyter, 1991).

[45]L. V. Keldysh, "Diagram technique for nonequilibrium processes", Zh. Eksp. Teor. Fiz. **47**, [Sov. Phys. JETP20,1018(1965)], 1515–1527 (1964).

[46]J. Schwinger, "Brownian Motion of a Quantum Oscillator", J. Math. Phys. **2**, 407–432 (1961).

[47]N. Schlünzen, "Nonequilibrium Green functions analysis of electron dynamics in strongly correlated lattice systems", Master thesis (Christian-Albrechts-Universität zu Kiel, Germany, Sept. 2015).

[48]M. Gell-Mann and F. Low, "Bound states in quantum field theory", Phys. Rev. **84**, 350–354 (1951).

[49]A. Fetter and J. Walecka, *Quantum theory of many-particle systems*, Dover Books on Physics (Dover Publications, 2003).

[50]M. Born and V. Fock, "Beweis des Adiabatensatzes", German, Z. Phys. **51**, 165–180 (1928).

[51]P. C. Martin and J. Schwinger, "Theory of many-particle systems. i", Phys. Rev. **115**, 1342–1373 (1959).

[52]D. Kremp, T. Bornath, M. Schlanges, and W. Kraeft, *Quantum statistics of nonideal plasmas*, Springer Series on Atomic, Optical, and Plasma Physics (Springer, Berlin, Heidelberg, 2006).

[53]L. Kadanoff and G. Baym, *Quantum statistical mechanics: Green's function methods in equilibrium and nonequilibrium problems*, Frontiers in physics (W.A. Benjamin, 1962).

[54]S. Hermanns, N. Schlünzen, and M. Bonitz, "Hubbard nanoclusters far from equilibrium", Phys. Rev. B **90**, 125111 (2014).

[55]M. P. von Friesen, C. Verdozzi, and C.-O. Almbladh, "Successes and Failures of Kadanoff-Baym Dynamics in Hubbard Nanoclusters", Phys. Rev. Lett. **103**, 176404 (2009).

[56]M. von Friesen, C. Verdozzi, and C.-O. Almbladh, "Kadanoff-Baym dynamics of Hubbard clusters: Performance of many-body schemes, correlation-induced damping and multiple steady and quasi-steady states", Phys. Rev. B **82**, 155108 (2010).

[57]S. Hermanns, "Nonequilibrium Green functions - Selfenergy approximation techniques", PhD thesis (Christian-Albrechts-Universität zu Kiel, Germany, 2016).

[58]G. Baym, "Self-consistent approximations in many-body systems", Phys. Rev. **127**, 1391–1401 (1962).

[59]G. Stefanucci, Y. Pavlyukh, A.-M. Uimonen, and R. van Leeuwen, "Diagrammatic expansion for positive spectral functions beyond GW: Application to vertex corrections in the electron gas", Physical Review B **90**, 115134 (2014).

[60]A.-M. Uimonen, G. Stefanucci, Y. Pavlyukh, and R. van Leeuwen, "Diagrammatic expansion for positive density-response spectra: Application to the electron gas", Physical Review B **91**, 115104 (2015).

[61]A.-M. Uimonen, "Developments in many-body theory of quantum transport and spectroscopy with non-equilibrium Green's functions and time-dependent density functional theory", eng, Research report / Department of Physics, University of Jyväskylä no. 3/2015. (2015).

[62]Y. Pavlyukh, A.-M. Uimonen, G. Stefanucci, and R. van Leeuwen, "Vertex Corrections for Positive-Definite Spectral Functions of Simple Metals", Physical Review Letters **117**, 206402 (2016).

[63]J. Gukelberger, L. Huang, and P. Werner, "On the dangers of partial diagrammatic summations: benchmarks for the two-dimensional hubbard model in the weak-coupling regime", Phys. Rev. B **91**, 235114 (2015).

[64]P. Romaniello, F. Bechstedt, and L. Reining, "Beyond the GW approximation: Combining correlation channels", Phys. Rev. B **85**, 155131 (2012).

[65]M. Gatti, F. Bruneval, V. Olevano, and L. Reining, "Understanding correlations in vanadium dioxide from first principles", Phys. Rev. Lett. **99**, 266402 (2007).

[66]A. N. Chantis, M. van Schilfgaarde, and T. Kotani, "Quasiparticle self-consistent GW method applied to localized 4f electron systems", Phys. Rev. B **76**, 165126 (2007).

[67]M. Wagner, "Expansions of nonequilibrium green's functions", Phys. Rev. B **44**, 6104–6117 (1991).

[68]D. C. Langreth and J. W. Wilkins, "Theory of spin resonance in dilute magnetic alloys", Phys. Rev. B **6**, 3189 (1972).

[69]P. Lipavský, V. Špička, and B. Velický, "Generalized Kadanoff-Baym ansatz for deriving quantum transport equations", Phys. Rev. B **34**, 6933–6942 (1986).

[70]S. Latini, E. Perfetto, A.-M. Uimonen, R. van Leeuwen, and G. Stefanucci, "Charge dynamics in molecular junctions: Nonequilibrium Green's function approach made fast", Phys. Rev. B **89**, 075306 (2014).

[71]V. Špička, B. Velický, and A. Kalvová, "Long and short time quantum dynamics: I. Between Green's functions and transport equations", Physica E **29**, 154–174 (2005).

[72]M. Eckstein and M. Kollar, "Measuring correlated electron dynamics with time-resolved photoemission spectroscopy", Phys. Rev. B **78**, 245113 (2008).

[73]R. C. Albers, N. E. Christensen, and A. Svane, "Hubbard-U band-structure methods", Journal of Physics: Condensed Matter **21**, 343201 (2009).

[74]M. C. Gutzwiller, "Effect of correlation on the ferromagnetism of transition metals", Phys. Rev. Lett. **10**, 159–162 (1963).

[75]J. Kanamori, "Electron correlation and ferromagnetism of transition metals", Progress of Theoretical Physics **30**, 275–289 (1963).

[76]J. Hubbard, "Electron correlations in narrow energy bands. ii. the degenerate band case", Proceedings of the Royal Society of London A: Mathematical, Physical and Engineering Sciences **277**, 237–259 (1964).

[77]J. Hubbard, "Electron correlations in narrow energy bands iii. an improved solution", Proceedings of the Royal Society of London A: Mathematical, Physical and Engineering Sciences **281**, 401–419 (1964).

[78]R. M. Dreizler and E. K. Gross, "Introduction", in *Density functional theory* (Springer, 1990), pp. 1–3.

[79]N. Schlünzen and M. Bonitz, "Nonequilibrium Green Functions Approach to Strongly Correlated Fermions in Lattice Systems", Contributions to Plasma Physics **56**, 5–91 (2016).

[80]A. Altland and B. D. Simons, *Condensed matter field theory* (Cambridge University Press, 2010).

[81]D. Baeriswyl, D. K. Campbell, J. M. Carmelo, F. Guinea, and E. Louis, *The Hubbard model: its physics and mathematical physics*, Vol. 343 (Springer Science & Business Media, 2013).

[82]A. Montorsi, *The Hubbard Model: A Reprint Volume* (World Scientific, 1992).

[83]A. Tomas, C.-C. Chang, Z. Bai, R. Scalettar, J. Perez, C.-R. Lee, S. Chiesa, I. Yamazaki, M. Jarrell, E. Khatami, C. Varney, W. Chen, E. D'Azevedo, T. Maier, S. Savrasov, and K. Tomko, *Elementary Introduction to the Hubbard Model*, quest.ucdavis.edu/tutorial/hubbard7.pdf.

[84]R. T. Scalettar, *An Introduction to the Hubbard Hamiltonian*, https://www.cond-mat.de/events/correl16/manuscripts/scalettar.pdf.

[85]M. Watanabe and W. P. Reinhardt, "Direct dynamical calculation of entropy and free energy by adiabatic switching", Phys. Rev. Lett. **65**, 3301 (1990).

[86]A. Stan, N. E. Dahlen, and R. van Leeuwen, "Time propagation of the Kadanoff–Baym equations for inhomogeneous systems", J. Chem. Phys **130**, 224101 (2009).

[87]J. C. Butcher, *Numerical methods for ordinary differential equations* (John Wiley & Sons, 2016).

[88]C. Runge, "Ueber die numerische Auflösung von Differentialgleichungen", Mathematische Annalen **46**, 167–178 (1895).

[89]N. Schlünzen, J.-P. Joost, and M. Bonitz, "Comment on "On the unphysical solutions of the Kadanoff-Baym equations in linear response: Correlation-induced homogeneous density-distribution and attractors"", Physical Review B **96**, 117101 (2017).

[90]J. P. Boyd, *Chebyshev and fourier spectral methods* (Courier Corporation, 2001).

[91]G. Dahlquist and Å. Björck, *Numerical methods*, Dover Books on Mathematics (Dover Publications, 2003).

[92]C. Runge, "Ueber empirische Funktionen und die Interpolation zwischen äquidistanten Ordinaten", Zeitschrift für Mathematik und Physik **46**, 20 (1901).

[93]B. Fornberg and J. Zuev, "The runge phenomenon and spatially variable shape parameters in rbf interpolation", Computers & Mathematics with Applications **54**, 379–398 (2007).

[94]J. P. Boyd and F. Xu, "Divergence (runge phenomenon) for least-squares polynomial approximation on an equispaced grid and mock–chebyshev subset interpolation", Applied Mathematics and Computation **210**, 158–168 (2009).

[95]D. Huybrechs, "Stable high-order quadrature rules with equidistant points", Journal of Computational and Applied Mathematics **231**, 933–947 (2009).

[96]J. P. Boyd and J. R. Ong, "Exponentially-convergent strategies for defeating the runge phenomenon for the approximation of non-periodic functions, part two: multi-interval polynomial schemes and multidomain chebyshev interpolation", Applied Numerical Mathematics **61**, 460–472 (2011).

[97]J. P. Boyd, "A comparison of numerical algorithms for fourier extension of the first, second, and third kinds", Journal of Computational Physics **178**, 118–160 (2002).

[98]*CUDA C PROGRAMMING GUIDE*, http://docs.nvidia.com/cuda/pdf/CUDA_C_Programming_Guide.pdf.

[99]Z. Ye, *Matrix multiplication in CUDA*, http://www.es.ele.tue.nl/ mwijtvliet/5KK73/?page=mmcuda.

[100]H. Bethe, "Zur Theorie der Metalle", Zeitschrift für Physik **71**, 205–226 (1931).

[101]E. H. Lieb and F. Y. Wu, "Absence of mott transition in an exact solution of the short-range, one-band model in one dimension", Phys. Rev. Lett. **20**, 1445–1448 (1968).

[102]D. Neilson, A. Perali, and M. Zarenia, "Many-body electron correlations in graphene", en, Journal of Physics: Conference Series **702**, 012008 (2016).

[103]N. Schlünzen, J.-P. Joost, F. Heidrich-Meisner, and M. Bonitz, "Nonequilibrium dynamics in the one-dimensional Fermi-Hubbard model: Comparison of the nonequilibrium Green-functions approach and the density matrix renormalization group method", Physical Review B **95**, 165139 (2017).

[104]R. G. Pereira, K. Penc, S. White, P. D. Sacramento, and J. Carmelo, "Charge dynamics in half-filled hubbard chains with finite on-site interaction", Physical Review B **85**, 165132 (2012).

[105]F. Gebhard, E. Jeckelmann, S. Mahlert, S. Nishimoto, and R. M. Noack, "Fourth-order perturbation theory for the half-filled Hubbard model in infinite dimensions", EPJ B **36**, 491–509 (2003).

[106]S. Hermanns, "Nonequilibrium Green's function approach to Hubbard nano-clusters using the generalized Kadanoff–Baym ansatz", Diploma thesis (Christian-Albrechts-Universität zu Kiel, Germany, Aug. 2012).

[107]A. Stan, "On the unphysical solutions of the Kadanoff-Baym equations in linear response: Correlation-induced homogeneous density-distribution and attractors", Physical Review B **93**, 041103 (2016).

[108]N. D. Mermin and H. Wagner, "Absence of ferromagnetism or antiferromagnetism in one- or two-dimensional isotropic heisenberg models", Phys. Rev. Lett. **17**, 1133–1136 (1966).

[109]A. K. Geim and K. S. Novoselov, "The rise of graphene", Nature Materials **6**, 183 (2007).

[110]K. S. Novoselov, "Nobel lecture: graphene: materials in the flatland", Rev. Mod. Phys. **83**, 837–849 (2011).

[111]P. R. Wallace, "The band theory of graphite", Phys. Rev. **71**, 622–634 (1947).

[112]J. C. Slonczewski and P. R. Weiss, "Band structure of graphite", Phys. Rev. **109**, 272–279 (1958).

[113]G. W. Semenoff, "Condensed-matter simulation of a three-dimensional anomaly", Phys. Rev. Lett. **53**, 2449–2452 (1984).

[114]J.-H. Ahn and B. H. Hong, "Graphene for displays that bend", Nature Nanotechnology **9**, 737 (2014).

[115]F. Withers, O. Del Pozo-Zamudio, A. Mishchenko, A. P. Rooney, A. Gholinia, K. Watanabe, T. Taniguchi, S. J. Haigh, A. K. Geim, A. I. Tartakovskii, and K. S. Novoselov, "Light-emitting diodes by band-structure engineering in van der waals heterostructures", Nature Materials **14**, 301 (2015).

[116]R. Saito, G. Dresselhaus, and M. Dresselhaus, *Physical properties of carbon nanotubes* (Imperial College Press, 1998).

[117]J. Munárriz Arrieta, "Tight-binding description of graphene nanostructures", in *Modelling of plasmonic and graphene nanodevices* (Springer International Publishing, Cham, 2014), pp. 13–23.

[118]D. R. Cooper, B. D'Anjou, N. Ghattamaneni, B. Harack, M. Hilke, A. Horth, N. Majlis, M. Massicotte, L. Vandsburger, E. Whiteway, and V. Yu, "Experimental Review of Graphene", ISRN Condensed Matter Physics **2012**, 56 (2012).

[119]J.-N. Fuchs and M. O. Goerbig, *Introduction to the Keldysh Formalism*, https://www.equipes.lps.u-psud.fr/GOERBIG/CoursGraphene2008.pdf.

[120]V. P. Gusynin, S. G. Sharapov, and J. P. Carbotte, "AC conductivity of graphene: From tight-binding model to 2 + 1-dimensional quantum electrodynamics", International Journal of Modern Physics B **21**, 4611–4658 (2007).

[121]K. Nakada, M. Fujita, G. Dresselhaus, and M. S. Dresselhaus, "Edge state in graphene ribbons: Nanometer size effect and edge shape dependence", Physical Review B **54**, 17954–17961 (1996).

[122]K. Wakabayashi, Y. Takane, M. Yamamoto, and M. Sigrist, "Electronic transport properties of graphene nanoribbons", New Journal of Physics **11**, 095016 (2009).

[123]K. Wakabayashi, K.-i. Sasaki, T. Nakanishi, and T. Enoki, "Electronic states of graphene nanoribbons and analytical solutions", Science and Technology of Advanced Materials **11**, 054504 (2010).

[124]S. Iijima, "Helical microtubules of graphitic carbon", Nature **354**, 56 (1991).

[125]J.-C. Charlier, X. Blase, and S. Roche, "Electronic and transport properties of nanotubes", Reviews of Modern Physics **79**, 677–732 (2007).

[126]K.-i. Sasaki, K. Wakabayashi, and T. Enoki, "Electron Wave Function in Armchair Graphene Nanoribbons", Journal of the Physical Society of Japan **80**, 044710 (2011).

[127]T. W. Ebbesen and P. M. Ajayan, "Large-scale synthesis of carbon nanotubes", Nature **358**, 220 (1992).

[128]T. Boye, J. Oyekale, and G. Arivie, "Carbon nanotubes: a review of the current state-of-the-art material science and technology towards achieving large-scale industrial productions and commercialization", International Journal of Current Research and Review **7**, 12 (2015).

[129]J. Cai, P. Ruffieux, R. Jaafar, M. Bieri, T. Braun, S. Blankenburg, M. Muoth, A. P. Seitsonen, M. Saleh, X. Feng, K. Müllen, and R. Fasel, "Atomically precise bottom-up fabrication of graphene nanoribbons", Nature **466**, 470 (2010).

[130]S. Blankenburg, J. Cai, P. Ruffieux, R. Jaafar, D. Passerone, X. Feng, K. Müllen, R. Fasel, and C. A. Pignedoli, "Intraribbon heterojunction formation in ultranarrow graphene nanoribbons", ACS Nano **6**, 2020–2025 (2012).

[131]T. Winzer, "Ultrafast Carrier Relaxation Dynamics in Graphene", PhD thesis (TU Berlin, Germany, July 2013).

[132]U. Briskot, "Optical and non-equilibrium properties of graphene", PhD thesis (Karlsruhe Institute of Technology, Germany, Oct. 2015).

[133]E. Malic and A. Knorr, *Graphene and carbon nanotubes: ultrafast optics and relaxation dynamics* (John Wiley & Sons, 2013).

[134]N. M. Gabor, "Impact Excitation and Electron–Hole Multiplication in Graphene and Carbon Nanotubes", Accounts of Chemical Research **46**, 1348–1357 (2013).

[135]W. Shockley and H. J. Queisser, "Detailed balance limit of efficiency of p-n junction solar cells", Journal of Applied Physics **32**, 510–519 (1961).

[136]A. Nozik, "Quantum dot solar cells", Physica E: Low-dimensional Systems and Nanostructures **14**, 115–120 (2002).

[137]T. Winzer, A. Knorr, and E. Malic, "Carrier multiplication in graphene", Nano Letters **10**, 4839–4843 (2010).

[138]F. Schulze, M. Schoth, U. Woggon, A. Knorr, and C. Weber, "Ultrafast dynamics of carrier multiplication in quantum dots", Physical Review B **84**, 125318 (2011).

[139]R. Baer and E. Rabani, "Can impact excitation explain efficient carrier multiplication in carbon nanotube photodiodes?", Nano Letters **10**, 3277–3282 (2010).

[140]S. Konabe, N. Onoda, and K. Watanabe, "Auger ionization in armchair-edge graphene nanoribbons", Phys. Rev. B **82**, 073402 (2010).

[141]N. M. Gabor, Z. Zhong, K. Bosnick, J. Park, and P. L. McEuen, "Extremely efficient multiple electron-hole pair generation in carbon nanotube photodiodes", Science **325**, 1367–1371 (2009).

[142]S. Wang, M. Khafizov, X. Tu, M. Zheng, and T. D. Krauss, "Multiple exciton generation in single-walled carbon nanotubes", Nano Letters **10**, 2381–2386 (2010).

[143]W. Kohn and L. J. Sham, "Self-consistent equations including exchange and correlation effects", Phys. Rev. **140**, A1133–A1138 (1965).

[144]M. Ijäs, M. Ervasti, A. Uppstu, P. Liljeroth, J. van der Lit, I. Swart, and A. Harju, "Electronic states in finite graphene nanoribbons: Effect of charging and defects", Physical Review B **88**, 075429 (2013).

[145]Y. Hancock, A. Uppstu, K. Saloriutta, A. Harju, and M. J. Puska, "Generalized tight-binding transport model for graphene nanoribbon-based systems", Physical Review B **81**, 245402 (2010).

[146]V.-T. Tran, J. Saint-Martin, P. Dollfus, and S. Volz, "Third nearest neighbor parameterized tight binding model for graphene nano-ribbons", AIP Advances **7**, 075212 (2017).

[147]P. Giannozzi, *Non-orthonormal basis sets*, http://www.fisica.uniud.it/ giannozz/Corsi/MQ/LectureNotes/mq-cap5.pdf.

[148]P. Löwdin, "On the Non-Orthogonality Problem Connected with the Use of Atomic Wave Functions in the Theory of Molecules and Crystals", The Journal of Chemical Physics **18**, 365–375 (1950).

[149]S. Reich, J. Maultzsch, C. Thomsen, and P. Ordejón, "Tight-binding description of graphene", Physical Review B **66**, 035412 (2002).

[150]R. Kundu, "Tight binding parameters for graphene", arXiv:0907.4264 [cond-mat] (2009).

[151]K. Balzer, N. Schlünzen, and M. Bonitz, "Stopping dynamics of ions passing through correlated honeycomb clusters", Physical Review B **94**, 245118 (2016).

[152]S. Wang, L. Talirz, C. A. Pignedoli, X. Feng, K. Müllen, R. Fasel, and P. Ruffieux, "Giant edge state splitting at atomically precise graphene zigzag edges", Nature Communications **7**, 11507 (2016).

[153]M. Y. Sfeir, F. Wang, L. Huang, C.-C. Chuang, J. Hone, S. P. O'brien, T. F. Heinz, and L. E. Brus, "Probing electronic transitions in individual carbon nanotubes by rayleigh scattering", Science **306**, 1540–1543 (2004).

[154]S. Konabe and S. Okada, "Enhanced photocurrent in single-walled carbon nanotubes by exciton interactions", Applied Physics Letters **102**, 113110 (2013).

Danksagung

Ich möchte die Gelegenheit nutzen, um den Leuten zu danken, ohne die diese Arbeit nicht möglich gewesen wäre.

Zunächst einmal wäre da Prof. Dr. Michael Bonitz, der mich vor nun mehr als 4 Jahren dazu überredet hat, mich in meiner Freizeit mit staubigen Plasmen zu beschäftigen, nur um mich dann vor knapp 2 Jahren doch auf den Weg der Nichtgleichgewichts-Greenfunktionen zu führen. Über all die Jahre hat er es mir ermöglicht, größtenteils selbstständig meinen Forschungsinteressen nachzugehen, woraus am Ende diese Arbeit entstanden ist.

Darüber hinaus gebührt ein besonderer Dank meinem Bürokollegen Niclas Schlünzen, der mir sehr geholfen hat, im Gebiet der Greenfunktionen heimisch zu werden. Nicht nur im Büro sondern auch auf so mancher Konferenz und Tagung durften wir zahlreiche lustige aber auch fachlich anspruchsvolle Diskussionen führen.

Insbesondere danke ich aber meinen Eltern für ihre Unterstützung in dieser stressigen Zeit und meiner zauberhaften Hannah, die so tapfer in der Ferne auf mich gewartet hat und es auch an den trübsten Tagen schaffte, mich zu erheitern.

Erklärung

„Ich erkläre hiermit, dass ich die vorliegende Arbeit selbstständig und ohne unerlaubte fremde Hilfe angefertigt habe, andere als die angegebenen Quellen und Hilfsmittel nicht benutzt habe, die den benutzten Quellen wörtlich oder inhaltlich entnommenen Stellen als solche kenntlich gemacht und die vorliegende Arbeit nicht an anderer Stelle eingereicht habe.“

Kiel, den _____ _____

Jan-Philip Joost